

UNIVERSITY OF NANTES

DOCTORAL THESIS

**Characterization of Intertidal
Vegetation on European Coasts Using
Multi-Scale Remote Sensing in
Response to Natural and
Anthropogenic Pressures**

Author:
Simon Oiry

Supervisors:
Prof. Laurent Barillé,
Dr. Pierre Gernez

*A thesis submitted in fulfillment of the requirements
for the degree of Doctor of Philosophy in Marine Ecology
as part of the*

Remote Sensing, Benthic Ecology and Ecotoxicology team
of the
Institut Des Substances et Organismes de la Mer

UNIVERSITY OF NANTES

Abstract

Sciences & Techniques

Institut Des Substances et Organismes de la Mer

Doctor of Philosophy in Marine Ecology

**Characterization of Intertidal Vegetation on European Coasts Using
Multi-Scale Remote Sensing in Response to Natural and Anthropogenic
Pressures**

by Simon Oiry

To Be Written

Acknowledgements

Integer id risus vel lorem laoreet commodo lobortis quis purus. Cras cursus leo vel dui laoreet pulvinar. Nunc tincidunt metus et ante fermentum lacinia. Proin quam magna, tristique ut viverra at, dapibus eget elit. Quisque eu leo id nisi semper laoreet at ac nulla. Fusce volutpat, metus sed dictum mattis, nisl elit dapibus velit, non porttitor urna urna vel diam. Praesent tortor nulla, rutrum ac magna a, tempor sagittis enim. Praesent pharetra ipsum libero, eu malesuada libero blandit ut. Sed sed venenatis ligula, nec convallis turpis. Nulla iaculis felis eros, eget pharetra lorem cursus quis. Nunc iaculis lobortis magna at malesuada. Nullam elementum elit at urna congue aliquam.

Table of contents

| | |
|---|------------|
| Abstract | iii |
| Acknowledgements | v |
| Preface | 1 |
| Scientific papers | 1 |
| Presentations to International Conferences | 2 |
| Project related to the thesis. | 3 |
| BiCOME | 3 |
| Rewrite | 3 |
| InvaSea | 3 |
| 1 Introduction | 5 |
| 1.1 Coastal Environment | 7 |
| 1.1.1 Ecological and Socio-Economic Importance of Coastal Environments . | 8 |
| 1.1.2 Human Activities in Coastal Areas and their Environmental Impacts | 10 |
| 1.1.3 Tidal flats | 14 |
| 1.1.3.1 Bacillariophyceae, Euglenida and Cyanophyceae | 15 |
| 1.1.3.2 Chlorophyceae | 17 |
| 1.1.3.3 Phaeophyceae | 18 |
| 1.1.3.4 Rhodophyceae | 19 |
| 1.1.3.5 Magnoliopsida | 20 |
| 1.2 Concepts of Remote sensing | 21 |
| 1.2.1 Active Remote Sensing, Example of LiDAR | 23 |
| 1.2.2 Passive Remote Sensing | 26 |
| 1.2.2.1 Spectral and Radiometric resolution | 31 |
| 1.2.2.2 Spatial resolution | 32 |
| 1.2.2.3 Temporal Resolutions | 33 |
| 1.2.2.4 A story of trade-off | 34 |
| 1.2.3 About Drones | 36 |
| 1.2.3.1 History | 36 |
| 1.2.3.2 General presentation | 38 |
| 1.2.3.3 Data acquisition | 39 |
| 1.2.3.4 Data processing | 41 |
| 1.2.4 Machine Learning | 44 |
| 1.2.5 Remote Sensing applied to Coastal monitoring | 48 |
| 1.3 Objectives and Overview | 50 |
| 2 Multispectral and hyperspectral classification of intertidal vegetation using a spectral library for coastal biodiversity remote sensing | 55 |
| 2.1 Introduction | 57 |
| 2.2 Materials and Methods | 60 |

| | | |
|----------------|---|------------|
| 2.2.1 | Spectral Reflectance Acquisition | 60 |
| 2.2.2 | Data Analysis | 62 |
| 2.2.2.1 | Spectral Degradation | 62 |
| 2.2.2.2 | Standardisation | 64 |
| 2.2.2.3 | Statistical Analysis | 64 |
| 2.3 | Results | 65 |
| 2.3.1 | Spectral Signatures at Different Spectral Resolutions | 65 |
| 2.3.2 | Spectral Dissimilarity Between the Taxonomic Classes | 66 |
| 2.3.3 | Accuracy Across Sensors and Importance of Wavelengths | 67 |
| 2.3.4 | Confusion Matrices | 71 |
| 2.4 | Discussion | 72 |
| 2.4.1 | Spectral Library and Vegetation Classification | 72 |
| 2.4.2 | Spectral Discrimination and Pigment Composition | 73 |
| 2.4.3 | Geographical and Temporal Range of Applicability | 76 |
| 2.4.4 | Implications for Coastal Biodiversity Studies | 76 |
| 2.4.5 | Conclusions | 77 |
| 3 | Discriminating Seagrasses from Green Macroalgae in European Intertidal Areas Using High-Resolution Multispectral Drone Imagery | 81 |
| 3.1 | Introduction | 83 |
| 3.2 | Materials & Methods | 85 |
| 3.2.1 | Study sites | 85 |
| 3.2.2 | Field sampling | 87 |
| 3.2.2.1 | Drone acquisition | 87 |
| 3.2.2.2 | Ground Control Points | 88 |
| 3.2.3 | Drone Processing | 89 |
| 3.2.4 | General Workflow | 90 |
| 3.2.4.1 | Training dataset building | 90 |
| 3.2.4.2 | Model building | 91 |
| 3.2.4.3 | Validation | 92 |
| 3.2.5 | Variable Importance | 93 |
| 3.2.6 | Influence of the spatial resolution on classification | 93 |
| 3.2.7 | Impact of mixed vegetation cover on the prediction | 94 |
| 3.3 | Results | 94 |
| 3.3.1 | Reflectance comparison between the two different altitudes | 94 |
| 3.3.2 | Classification | 95 |
| 3.3.3 | Validation of the model | 98 |
| 3.3.4 | Variable importance | 98 |
| 3.3.5 | Effect of spatial resolution on the classification | 100 |
| 3.3.6 | Effect of the percent cover on the prediction | 101 |
| 3.4 | Discussion | 103 |
| 3.4.1 | Vegetation Discrimination | 103 |
| 3.4.2 | Altitude and Temporal Effects on Vegetation Prediction Accuracy . . | 105 |
| 3.4.3 | Impact of Pixel Resolution on the prediction and Implications for Satellite Remote Sensing | 106 |
| 3.4.4 | Towards climate and biodiversity applications | 107 |
| 3.5 | Conclusion | 109 |
| 4 | Spatial and Temporal distributions of the alien invasive <i>Gracilaria vermiculophylla</i> | 111 |

| | | |
|----------|--|------------|
| 4.1 | Introduction | 113 |
| 4.2 | Materiels & Methods | 115 |
| 4.2.1 | Study sites | 115 |
| 4.2.2 | Remote sensing data acquisition and pre-processing | 117 |
| 4.2.2.1 | Hyperspectral measurements | 117 |
| 4.2.2.2 | Drone data | 117 |
| 4.2.3 | Scene classification | 120 |
| 4.2.4 | Historical Presence of <i>Gracilaria vermiculophylla</i> in the Belon estuary | 120 |
| 4.2.5 | Statistical analysis | 121 |
| 4.3 | Results | 122 |
| 4.3.1 | Historical records in the Belon estuary | 122 |
| 4.3.2 | Spectral description | 124 |
| 4.3.3 | Spatial distribution | 124 |
| 4.4 | Discussion | 127 |
| 4.4.1 | Drone mapping of <i>G. vermiculophylla</i> using machine learning approaches | 127 |
| 4.4.2 | <i>G. vermiculophylla</i> spatial distribution and mudflat topography | 129 |
| 4.4.3 | Monitoring <i>Gracilaria vermiculophylla</i> Invasion Dynamics | 130 |
| 4.5 | Conclusion | 132 |
| 4.6 | Annexes | 134 |
| 4.6.1 | Annexes A - Updated training dataset | 134 |
| 4.6.2 | Annexes B - Validation dataset | 135 |
| 4.6.3 | Annexes C - List of historical images records | 136 |
| 4.6.4 | Annexes D - Maps of the Saja estuary, Spain | 137 |
| 5 | The impact of Heatwave on Seagrasses using hyperspectral and multispectral remote sensing | 139 |
| 5.1 | Introduction | 141 |
| 5.2 | Materials & Methods | 143 |
| 5.2.1 | Laboratory Experiment | 143 |
| 5.2.1.1 | Sampling and acclimation of seagrasses | 143 |
| 5.2.1.2 | Experimental design | 144 |
| 5.2.1.3 | Optical measurements | 145 |
| 5.2.2 | Observation of a seagrass bed impacted by a HWs | 147 |
| 5.2.2.1 | Temperature data and HW detection | 148 |
| 5.2.2.2 | Satellite observations | 151 |
| 5.2.2.3 | Emersion time of the seagrass meadow | 151 |
| 5.2.3 | Statistics | 152 |
| 5.3 | Results | 152 |
| 5.3.1 | Laboratory Experiment | 152 |
| 5.3.1.1 | Seagrass spectra variations related to a heatwave | 152 |
| 5.3.1.2 | Evolution of spectral metrics | 153 |
| 5.3.2 | HW of September 2021 in Quiberon, South Brittany | 155 |
| 5.3.2.1 | Spectral changes | 155 |
| 5.3.2.2 | SHSI metric applied to Sentinel-2 | 156 |
| 5.4 | Discussion | 158 |
| 5.4.1 | Physiological impacts of heatwaves on seagrasses | 158 |
| 5.4.2 | Climate change and heatwaves | 162 |
| 5.4.3 | Seagrass resilience to heatwaves | 164 |
| 5.4.4 | Big picture | 166 |
| 5.5 | Conclusion | 167 |

| | |
|---|------------|
| 5.6 Annexes | 169 |
| 5.6.1 Annexes A - Temperatures of the experiment | 169 |
| 6 General conclusions and future perspectives | 171 |
| 6.1 Macrophytes discrimination and associated challenges. | 173 |
| 6.2 Drone and Satellite Interactions | 174 |
| 6.3 Seagrass and Invasive Species Interactions | 176 |
| References | 181 |

List of Figures

| | |
|--|----|
| Figure 1.1: Examples of the diversity of habitat found in coastal environments. A: Upper shore and dunal vegetation of Pen Bron, France, on the 15th of May 2023. B: Rocky shore of the Galician coastline. Picture taken at Baiona, Spain on the 1st of September 2023. C: Tidal flat of the Guadalquivir River, Spain. Picture taken near of Trebujena, Spain on the 22nd of March 2023. D: Submerged seagrass meadows in Greece. Picture taken at Nauplie, Greece on the 29th of October 2023. | 9 |
| Figure 1.2: Global coastal population curve (CoPop curve) expressed as population estimates in 5 km bands. From Cosby et al. (2024) | 10 |
| Figure 1.3: The global trajectory of tidal flats extent, showing areas in which the development of consistent time-series data over 1984–2016 (orange) and 1999–2016 (orange and blue) was possible. b, Change in the extent of tidal flats in 17.1% of the mapped area, 1984–2016 (linear regression, $P = 0.00437$). c, Change in the extent of tidal flats in 61.3% of the mapped area, 1999–2016 (linear regression, $P = 0.1794$). Shading in b and c indicates the standard error of the linear model. From Murray et al. (2019) | 15 |
| Figure 1.4: Main vegetation classes of soft-bottom intertidal areas studied in the work. A: Seagrass meadows (Magnoliopsida) in Cadiz, Spain, on the 21st of March 2023. B: Microphytobenthos (Bacillariophyceae) biofilm patches, Cadiz, Spain, on the 22nd of March 2023. C: Brown algae (Phaeophyceae) in Ria d'Etel, France on the 13th of March 2024. D: Red macroalgae (Rhodophyceae) in the Belon estuary, France on the 10th of April 2024. E: Green macroalgae (Chlorophyceae) colonising the polychaete reef of Noirmoutier Island, France on the 29th of September 2023. | 16 |
| Figure 1.5: Seagrass meadows are habitats containing biodiverse faunal communities such as the following: a) the Spiny Seahorse (<i>Hippocampus guttulatus</i>) in the UK (source N Garrick-Maidment), b) Dogfish (<i>Scyliorhinus canicula</i>) in the UK (source Frogfish Photography), c) the Green Sea Turtle (<i>Chelonia mydas</i>) in the Dutch Antilles, d) Flying Gurnard (<i>Dactylopterus volitans</i>) in Puerto Rico (source Luis R. Rodriguez) and e) shows the proportion of publication each year dedicated to Coral reefs, Mangroves, Seagrasses and Salt marshes. Modified from Unsworth et al. (2019a). | 22 |
| Figure 1.6: Diagram showing several signal-return for a single emitted beam of a LIDAR system. adapted from Wang and Fang (2020) and García-Feced et al. (2011) | 24 |

| | |
|---|----|
| Figure 1.7: Light pathways involved in remote sensing: illustrating the interaction of solar radiation with the atmosphere, vegetation, and water surfaces, highlighting processes such as scattering, absorption, and reflectance contributing to the top-of-atmosphere (TOA) radiance observed by a satellite sensor. | 28 |
| Figure 1.8: The spectral signature of vegetation (green), Water (blue) and bare soil (red). Absorption features of Chlorophyll-a are indicated for the spectra of vegetation. | 29 |
| Figure 1.9: Comparison of spectral resolution between multispectral (A) and hyperspectral (B) sensors in the solar radiance spectrum. Panel C illustrates the impact of spectral resolution on the same spectral signature of <i>Gracilaria vermiculophylla</i> . With hyperspectral resolution (red), absorption features of pigments such as phycocyanin and phycoerythrin are distinguishable, whereas these features are absent in the multispectral resolution provided by Sentinel-2 (green). D is showing examples of different radiometric resolutions for the same band of a Sentinel-2 tile. One is coded in 12 bits (left), and the other in 6 bits (right). | 31 |
| Figure 1.10:Intersection of spectral resolutions (x-axis), temporal resolutions (y-axis), and spatial resolutions (circle size) of the main satellite sensors used to observe coastal areas. | 35 |
| Figure 1.11:One of Neubronner's pigeons (Top), around 1910 equipped with a camera. The bottom shows a picture taken during a pigeon's flight. | 37 |
| Figure 1.12:Schematic representation of image overlapping of a drone | 39 |
| Figure 1.13:Schematic representation of image pre-processing for orthomosaic reconstruction, showing correction of the distortion (A & B) and correction of the vignetting (C & D). | 41 |
| Figure 1.14:Representation of differences between the Digital Surface Model (DSM), the Digital Terrain model (DTM) and the Digital Height Model (DHM). | 43 |
| Figure 1.15:Redo this figure !!!!! | 47 |
| Figure 1.16:Current capabilities of remotely sensed data for measuring Essential Biodiversity Variables (EBVs; Pereira et al. (2013)) for soft-bottom intertidal vegetation. Adapted from Muller-Karger et al. (2018). | 50 |
| Figure 2.1: Examples of taxonomic classes of soft-bottom intertidal vegetation in the field (a: Phaeophyceae (<i>Fucus vesiculosus</i>), b: Magnoliopsida (<i>Zostera noltei</i>), c: Ulvophyceae (<i>Ulva linza</i>), d: Bacillariophyceae (Diatoms) and e: Xanthophyceae (<i>Vaucheria</i> spp.)). Scale bars show approximate scale. | 61 |
| Figure 2.2: Sample collection sites across Europe. | 62 |
| Figure 2.3: Spectral response functions for different hyper- and multi-spectral sensors (ASD, Pleiades, Sentinel-2 (10 m), Sentinel-2 (20 m), Drone, and PRISMA). | 63 |

| | |
|---|----|
| Figure 2.4: Spectral signatures of different vegetation classes at different spectral resolutions (ASD, Pleiades, Sentinel-2 10, Sentinel-2 10-20 m, Drone and PRISMA). Lines show mean signature per wavelength, while shading shows 95% confidence interval. Confidence intervals were consistently small and therefore are hard to distinguish. | 66 |
| Figure 2.5: nMDS ordination showing similarities between vegetation classes at different spectral resolutions (ASD, Pleiades, Sentinel-2 10, Sentinel-2 10-20 m, Drone and PRISMA). Point distances are based on cosine distance, polygons show the minimum convex hull to surround all points. Stress values show the inaccuracy of the 2 dimensional representations. | 67 |
| Figure 2.6: Accuracy metrics (accuracy, Cohen's kappa accuracy, sensitivity and specificity) for different spectral resolutions. | 69 |
| Figure 2.7: The relative importance of different wavelengths for model prediction across spectral resolutions. | 70 |
| Figure 2.8: The relative importance of different wavelengths for ASD model prediction across the spectral bands of the Drone, Sentinel-2 and Pleiades sensors. | 71 |
| Figure 2.9: Confusion matrices for different spectral resolutions. Colour of tiles show proportion of correct predictions across all 20 repetitions with no colour for 0 predictions. Classes were abbreviated Bacillariophyceae as Bac, Bare Sediments as Bar, Magnoliopsida as Mag, Phaeophyceae as Pha and Ulvophyceae as Ulv. Labels with numbers show within class sensitivity and specificity. | 72 |
| Figure 3.1: Location of drone flights in France and Portugal. A: Gulf of Morbihan (Two sites), B: Bourgneuf Bay (Two sites), C: Ria de Aveiro Coastal Lagoon (Three sites). Golden areas represent the intertidal zone. | 86 |
| Figure 3.2: The five taxonomic classes of vegetation used to train the Neural Network model and an example of their raw spectral signatures at the spectral resolution of the Micasense RedEdge Dual MX. A : Magnoliopsida (<i>Zostera noltei</i>) ; B : Phaeophyceae (<i>Fucus sp.</i>) ; C : Rhodophyceae (<i>Gracilaria vermiculophylla</i>) ; D : Chlorophyceae (<i>Ulva sp.</i>) ; E : Bacillariophyceae (Benthic diatoms). The taxonomy was verified following the World Register of Marine Species (WORMS). 89 | 89 |
| Figure 3.3: Schematic representation of the workflow. Parallelograms represent input or output data, and rectangles represent Python processing algorithms. The overall workflow of this study is divided into two distinct parts based on the spatial resolution of the drone flights: high-resolution flights (pixel size: 8 mm) were used for training and prediction of the Neural Network model, whereas lower-resolution flights (pixel size: 80 mm) were solely employed for prediction purposes. Validation has been performed on both high and low-resolution flights. | 90 |

| | |
|--|-----|
| Figure 3.4: Comparison of reflectance retrieved from both low-altitude and high-altitude flights over a common area. The black dashed line represents a 1 to 1 relationship. Left (A) plots raw data and right (B) plots standardized data (Equation 2.1). | 94 |
| Figure 3.5: RGB orthomosaic (Left) and Prediction (Right) of the low altitude flight of Gafanha, Portugal. The total extent of this flight was 3000 m ² with a resolution of 8 mm per pixel. The zoom covers an area equivalent to a 10 m Sentinel-2 pixel size. | 95 |
| Figure 3.6: RGB orthomosaic (Left) and Prediction (Right) of the high-altitude flight of Gafanha, Portugal. The total extent of this flight was about 1 km ² with a resolution of 80 mm per pixel. The yellow outline shows the extent of the low-altitude flight of Gafanha presented in Figure 3.5. The zoom covers an area equivalent to a 10 m Sentinel-2 pixel size. | 96 |
| Figure 3.7: RGB orthomosaic (Top) and Prediction (Bottom) of the flight made in the inner part of Ria de Aveiro Lagoon, Portugal. The total extent of this flight was about 1.5 km ² with a resolution of 80 mm per pixel. The zoom inserts cover an area equivalent to the size of a 10 m Sentinel-2 pixel. | 97 |
| Figure 3.8: RGB orthomosaic (Top) and Prediction (Bottom) of L'Epine, France. The total extent of this flight was about 28 000 m ² with a resolution of 80 mm per pixel. The zoom covers an area equivalent to a 10 m Sentinel-2 pixel size. | 98 |
| Figure 3.9: A global confusion matrix on the left is derived from validation data across each flight, while a mosaic of confusion matrices from individual flights is presented on the right. The labels inside the matrices indicate the balanced accuracy for each class. The labels at the bottom of the global matrix indicate the User's accuracy for each class, and those on the right indicate the Producer's Accuracy. The values adjacent to the names of each site represent the proportion of total pixels from that site contributing to the overall matrix. Grey lines within the mosaic indicate the absence of validation data for the class at that site. The table at the bottom summarizes the Sensitivity, Specificity, and Accuracy for each class and for the overall model. | 99 |
| Figure 3.10: Variable Importance of the Neural Network Classifier for each taxonomic class. The longer the slice, the more important the variable for prediction of each class. The right plot shows the drone raw and standardised reflectance spectra of each class. Each slice represents the Variable Importance (VI) of both raw and standardised reflectance combined. | 100 |
| Figure 3.11: Predicted area loss for different vegetation types (green algae, seagrass, brown algae, red algae) as a function of spatial resolution. Lines represent Generalized Linear Model (GLM) predictions, and shaded areas indicate standard errors. As resolution decreases, predicted area loss increases for all vegetation types, with green algae showing the highest loss and seagrass the smallest at coarser resolutions. | 101 |

| | |
|---|-----|
| Figure 3.12: Kernel density plot showing the proportion of pixel well classified based on the percent cover of the class in high altitude flight pixels of Gafanha, Portugal. Each subplot shows all the pixels of the same classes on the high altitude flight. Percent cover of classes was retrieved using the result of the classification of the low altitude flight of Gafanha, Portugal. | 102 |
| Figure 3.13: Photosynthetic and carotenoid pigments present (Green) or absent (Red) in each taxonomic class present in the Neural Network Classifier, along with their absorption wavelength measured with spectroradiometer, Chl-b: chlorophyll-b, Chl-c: chlorophyll-c, Fuco: fucoxanthin, Zea: zeaxanthin, Diad: diadinoxanthin, Lut: lutein, Neo: neoxanthin, PE: phycoerythrin, PC: phycocyanin; (Cartaxana et al., 2016; Christensen et al., 1977; Douay et al., 2022; Méléder et al., 2013; Ralph et al., 2002). | 104 |
| Figure 3.14: Sample of Figure 3.9 focusing on green macrophytes. The labels inside the matrix indicate the number of pixels. | 104 |
| Figure 4.1: Location of the drone flights. A: Flights made in Aven Estuary, France; B: Flights made in Belon Estuary, France; C: Flights made in the Saja Estuary, Spain. Golden polygons represent intertidal areas. | 116 |
| Figure 4.2: <i>Gracilaria vermiculophylla</i> in the Belon. A: Quadrat of 0.25 m ² with a 100% cover of <i>G. vermiculophylla</i> ; B: Single thallus showing cylindrical branches; C: Landscape view of mudflats covered by monospecific mats of <i>G. vermiculophylla</i> ; D: Recording of the spectral signature of the algae using an ASD FieldSpec HandHeld 2 spectroradiometer. | 118 |
| Figure 4.3: Schematic representation of the workflow. Parallelograms represent input or output data, rectangles represent Python processing algorithms, long rectangle represent instruments used and ovals represent study sites. Red shows Drone data; Orange shows the model training; Blue shows processing performed on the Digital Surface Model; Green shows the validation of the model; Purple shows the statistical analysis. | 121 |
| Figure 4.4: RGB images of the Belon Estuary (Pont de Guilly) showing the colonization of the mudflat by <i>Gracilaria vermiculophylla</i> between 1952 and 2024. | 123 |
| Figure 4.5: Trend of the <i>Gracilaria vermiculophylla</i> cover in the Belon Estuary (at Pont du Guilly). The red vertical line indicates the date of <i>Crassostrea gigas</i> introduction in South Brittany (Grizel and Heral, 1991), while the golden line represents the date of the first documented mention of <i>Gracilaria vermiculophylla</i> presence in Europe which was in the Belon Estuary (Rueness, 2005). | 124 |
| Figure 4.6: Hyperspectral signature of <i>Gracilaria vermiculophylla</i> (A) and its second derivative (B). The black line represents the average spectra, while the shaded area indicates the standard deviation. Dashed lines mark the absorption maxima of Phycoerythrin, Phycocyanin, and Chlorophyll-a, shown in green, orange, and red, respectively. | 125 |

| | |
|--|-----|
| Figure 4.7: Classification of the main classes of intertidal vegetation with a neural network algorithm (A), RGB composition (B), Elevation (C) and mudflat topography (D) of the Belon estuary site in Brittany, France. The total extent of this flight was 21 hectares with a resolution of 8 mm per pixel. Elevation corresponds to the height above mean sea level. | 126 |
| Figure 4.8: DISCOV Prediction (A), RGB composition (B) and Bathymetry (C) of the Belon estuary site in Brittany, France. The total extent of this flight was 21 ha with a resolution of 8 mm per pixel. Bathymetry is represented as the height above mean sea level. | 127 |
| Figure 4.9: Annexe 4.4 - DISCOV Prediction (A), RGB composition (B) and picture of the field campaign of the Saja estuary, Northern Spain. The total extent of this flight was 20.4 ha with a resolution of 8 mm per pixel. | 137 |
| Figure 5.1: Illustration of the experiment. A: Seagrass field sampling using a coring device; B: Intertidal chamber used during the experiment; C: Seagrass sample inside a chamber during the experiment at high tide; D: Treatment sample at the start of the experiment; E: Treatment sample at the end of the experiment, 2 days after the start of the HW event. | 144 |
| Figure 5.2: Temperature variation in the control (left) and treatment (right) intertidal chambers, during the HW experiment. The red line indicates air temperature, and the blue line water temperature. Due to the tidal cycle of immersion / emersion the seagrasses experienced the temperatures represented by solid lines. | 146 |
| Figure 5.3: Computation of the reflectance Seagrass Heat Shock Index (SHSI) for Impacted (A) and Unimpacted (B) seagrass leaves. The dashed line represents the reflectance interpolation between 560 and 842 nm. The red vertical at 740 nm represents the SHSI line height. | 148 |
| Figure 5.4: Location of field observation in a seagrass meadow impacted by a HW that occurred on the 10th of September 2021 in Quiberon, South Brittany, France. The red line indicates the intertidal zone (Zone between high tide and low tide, exposed during low tide), the dark green area indicates the extent of the seagrass meadow and the olive polygons indicate saltmarshes. Green points indicate the location of quadrat pictures over unimpacted seagrasses (i.e. showing a green colour on the field), and orange points indicate the location of quadrats taken over impacted seagrasses (i.e. showing a brown color on the field, Figure 5.5). | 149 |
| Figure 5.5: Illustration of the two colorations of seagrass leaves observed <i>in situ</i> the 10th of September 2021 after a heatwave in Quiberon, South Brittany (France). A: Picture of a zone with both green and brown seagrass; B: Seagrass quadrat with green leaves; C: Seagrass quadrat with brown leaves; D: Picture of a zone where all leaves turned brown. | 150 |

- Figure 5.6: Standardized hyperspectral reflectance signature of *Z. noltei* leaves measured during the HW experiment for both the Control (Left) and the Treatment (Right). Colour denotes the progression along the experiment from the beginning (Day 1: green), middle (Day 2: Yellow) and end (Day 3: Brown). A min-max standardization has been applied to each individual spectrum. 153
- Figure 5.7: Comparison of spectral metrics for detecting reflectance changes of seagrass leaves after a HW. A: Relative difference of the second derivative at 665 nm between the Control and the Treatment over time; B: Relative difference of the NDVI; C: Relative difference of the GLI; D: Relative difference of the SHSI. Points indicate raw data, the line represents a generalized linear model, and the shaded area is the model's standard error. The dashed lines represent no difference between the Control and the Treatment. 154
- Figure 5.8: Median and standard deviation of the Seagrass Heat Shock Index (SHSI) across experimental runs, at each day of the experiment. The green line shows values of the Control group while the orange line indicates values of the Treatment. 155
- Figure 5.9: Intertidal seagrass meadow in South Brittany (France) observed before and during a heatwave (HW). A: RGB colour composition of the Sentinel-2 image of the 1st of September 2021 before the HW; C: RGB colour composition of the Sentinel-2 image of the 6th of September 2021 on the second day of a strong AHW. The circles correspond to Quadrat Points (QPs) collected on the 10th of September 2021, with unimpacted seagrass in green and impacted seagrass in orange; B: Detection of HW events based on both Air Temperature and Sea Surface Temperature (SST). The solid line represents the daily average temperature, while the dashed line indicates the 90th percentile of the climatology. Coloured areas identify HWs (marine in blue and atmospheric in red). The two vertical dashed lines represent the acquisition dates of the two Sentinel-2 images used in this analysis (01-09-2021 and 06-09-2021); D: Sentinel-2 reflectance of seagrass leaves before the HW for both categories of QPs; E: Sentinel-2 reflectance of seagrass leaves during the HW for both categories of QPs. Average spectral signatures were obtained in areas where QPs corresponded to green and brown seagrasses leaves (green and orange circles, respectively) as identified during the field survey. The shaded areas around the reflectance spectra represent the standard deviation. 157
- Figure 5.10: Changes in the relative Seagrass Heat Shock Index (SHSI) estimated from Sentinel-2, before (1st of September 2021), during (6th of September 2021) and after (8th of October 2021) a HW in the seagrass meadow of Quiberon (South Brittany, France). The relative SHSI difference was calculated using the 1st of September as a reference. SHSI was calculated for two categories of Quadrat Points (QPs; Figure 5.9): unimpacted seagrass (green) and impacted seagrass (orange). Points represent the predicted value of the metric using a Generalized Linear Model (GLM), while the error bar represents the 89% confidence interval. 158

| | |
|---|-----|
| Figure 5.11: Sentinel-2 colour composition of the seagrass meadow of Quiberon, South Brittany, France, Before (A), During (B) and After (C) the HW Seagrass Heat Shock Index applied on Sentinel-2 images Before (D), During (E) and After (F) the HW. | 159 |
| Figure 5.12: Relative change of the Seagrass Heat Shock Index (SHSI) before and during the HW events as a function of the daily emersion time of seagrass. The line represents a Generalized Additive Model (GAM) prediction, and the shaded area indicates the standard error. Shaded points represent raw data, each corresponding to a single pixel of the meadow. | 159 |
| Figure 5.13: Annexe 5.1 - Comparison of daily maximum temperatures in August measured using an in-situ sensor (blue) and retrieved from Meteo France (orange). The solid line in the middle of the boxplot represents the median, the two ends of the box represent the 25th and 75th percentiles, and the whiskers represent values that are no more than 1.5 times the interquartile range. | 169 |
| Figure 6.1: Workflow showing process for neural network classification model building and seagrass cover (%) from this classification, with example images showing process from Sentinel-2 Data to Habitat Classification to Seagrass Cover. From Davies et al. (2024a). | 175 |

List of Tables

| | |
|---|-----|
| Table 2.1: Presence and absence of red macroalgae for each drone flight | 61 |
| Table 2.2: Accuracy metrics (accuracy, Cohen's kappa accuracy, sensitivity and specificity) for different spectral resolutions ± standard error. | 69 |
| Table 2.3: Photosynthetic and carotenoid pigments present (1) or absent (0) in each taxonomic class, along with their absorption wavelength measured in vivo and in vitro with an ASD spectroradiometer and by High Performance Liquid Chromatography (HPLC) respectively. Chl b: chlorophyll b, Chl c: chlorophyll c, Fuco: fucoxanthin, Zea: zeaxanthin, Diato: diatoxanthin, Diadino: diadinoxanthin, Neo: neoxanthin. | 75 |
| Table 3.1: List of drone flights, summarising the date, the altitude, and the purpose of each flight. 12 m and 120 m flights have a spatial resolution of 8 and 80 mm respectively. | 88 |
| Table 3.2: Vegetation Classes of the model and the number of pixels used to train and validate each class | 91 |
| Table 4.1: Annexe 4.1 - Class of the Neural Network model, with the number of training pixels used to train that class and the differences with the training dataset of DISCOV v1.0 | 134 |
| Table 4.2: Annexe 4.2 - Presence and absence of red macroalgae for each drone flight | 135 |
| Table 4.3: Annexe 4.3 - Images used to assess the historical presence of <i>Gracilaria vermiculophylla</i> in the Belon estuary. Images from the IGN data source have been retrieved from the “Remonter Le Temps” platform (IGN, 2024b). Drone flight have been performed by the team using a Mavic 3 Entreprise. | 136 |

List of Abbreviations

| | |
|------------|---|
| ASI | Agenzia Spaziale Italiana |
| ANOSIM | Analysis of Similarity |
| AHW | Atmospheric Heatwave |
| BOA | Bottom of Atmosphere |
| BPI | Brown Pigment Index |
| Chla | Chlorophyll-a |
| Chlb | Chlorophyll-b |
| Chlc | Chlorophyll-c |
| CMEMS | Copernicus Marine Environment Monitoring Service |
| dGPS | differential GPS |
| DHM | Digital Height Model |
| DSM | Digital Surface Model |
| DTM | Digital Terrain Model |
| DPA | Diphenylamine |
| DISCOV | Drone Intertidal Substrate Classification Of Vegetation |
| DLS2 | Downwelling Light Sensor |
| EO | Earth Observation |
| EMR | Electromagnetic Radiation |
| EBVs | Essential Biodiversity Variables |
| EOVs | Essential Ocean Variables |
| ESA | European Space Agency |
| EU | European Union |
| EPS | Extracellular Polymeric Substances |
| IGN | Institut National de l'information Géographique et forestière |
| FO | Front Overlap |
| FWHM | Full Width at Half Maximum |
| GAM | Generalized Additive Model |
| GLM | Generalized Linear Model |
| GLMM | Generalized Linear Mixed Model |
| GBIF | Global Biodiversity Information Facility |
| GOOS | Global Ocean Observing System |
| GLI | Green Leaf Index |
| GVA | Gross Value Added |
| HSPs | Heat-Shock Proteins |
| HIDF | Heatwave Intensity Duration Frequency |
| HPLC | High Performance Liquid Chromatography |
| HiRI | High-resolution Imager |
| HW | HeatWave |
| HYC | Hyperspectral Camera |
| ICE CREAMS | Intertidal Classification of Europe: Categorising Reflectance of Emerged Areas of Marine vegetation with Sentinel2 |
| IR | Infrared |

| | |
|-------|---|
| IFOV | I nstantaneous F ield of V iew |
| IGN | I nstitut N ational de l' I nformation G éographique et F orestière (2024a) |
| IPBES | I ntergovernmental S cience- P olicy P latform on Bbiodiversity and Ecosystem Services |
| IAS | I nvasive A lien S pecies |
| LiDAR | L ight D etection and R anging |
| MSFD | M arine S |

List of Symbols

| | |
|---------------------|--|
| FN_i | False negative relative to the class i |
| FP_i | False positive relative to the class i |
| h_{sensor} | Sensor dimension (height) in the flight direction |
| TN_i | True negatives relative to the class i |
| TP_i | True positives relative to the class i |
| L_{down} | Downwelling radiance |
| L_{up} | Upwelling radiance |
| R_{BOA} | Reflectance at the bottom of atmosphere |
| $R_i(\lambda)$ | Reflectance of spectrum i at a specific wavelength λ |
| $R_i^*(\lambda)$ | Standardised R of spectrum i at wavelength λ |
| d_{fl} | Distance between two adjacent flight lines |
| w_{sensor} | Sensor dimension (width) perpendicular to the flight direction |
| L | Radiance |
| $\max(R_i)$ | Maximum reflectance value at spectrum i |
| $\min(R_i)$ | Minimum reflectance value at spectrum i |
| h | Flight altitude above the ground |
| R | Reflectance |
| $R''(\lambda_i)$ | Second derivative at the wavelength i λ_i |
| f | Camera focal length |
| v_g | Ground speed of the drone |
| Δt | Time interval between consecutive photos |
| $\Delta\lambda$ | Uniform spectral sampling interval |
| λ | Wavelength |

Preface

This PhD work was carried out at Nantes University between 2022 and 2024, within the “Remote Sensing, Benthic Ecology and Ecotoxicology” (RSBE²) team of the Institute of Marine Substances and Organisms (ISOMer). This thesis was funded by the Ministry of Research and Higher Education and supervised by the doctoral school “Plant, Animal, Food, Sea, Environment” (VAAME).

Scientific papers

- Barillé, L., Paterson, I. L. R., **Oiry, S.**, Aris, A., Cook-Cottier, E. J., & Nurdin, N. (2025). Variability of *Kappaphycus alvarezii* cultivation in South-Sulawesi (Indonesia) related to the monsoon shift: Water quality, growth and colour quantification. *Aquaculture Reports*, 40, 102557. <https://doi.org/10.1016/j.aqrep.2024.102557>
- **Oiry, S.**, Davies, B. F. R., Sousa, A. I., Rosa, P., Zoffoli, M. L., Brunier, G., Gernez, P., & Barillé, L. (2024). Discriminating Seagrasses from Green Macroalgae in European Intertidal Areas Using High-Resolution Multispectral Drone Imagery. *Remote Sensing*, 16(23), 4383. <https://doi.org/10.3390/rs16234383>
- Román, A., **Oiry, S.**, Davies, B. F. R., Rosa, P., Gernez, P., Tovar-Sánchez, A., Navarro, G., Méléder, V., & Barillé, L. (2024). Mapping intertidal microphytobenthic biomass with very high-resolution remote sensing imagery in an estuarine system. *Science of The Total Environment*, 955, 177025. <https://doi.org/10.1016/j.scitotenv.2024.177025>
- Davies, B. F. R., **Oiry, S.**, Rosa, P., Zoffoli, M. L., Sousa, A. I., Thomas, O. R., Smale, D. A., Austen, M. C., Biermann, L., Attrill, M. J., Roman, A., Navarro, G., Barillé, A.-L., Harin, N., Clewley, D., Martinez-Vicente, V., Gernez, P., & Barillé, L. (2024). Intertidal seagrass extent from Sentinel-2 time-series show distinct trajectories in Western Europe. *Remote Sensing of Environment*, 312, 114340. <https://doi.org/10.1016/j.rse.2024.114340>
- Davies, B. F. R., **Oiry, S.**, Rosa, P., Zoffoli, M. L., Sousa, A. I., Thomas, O. R., Smale, D. A., Austen, M. C., Biermann, L., Attrill, M. J., & others. (2024). A sentinel watching over inter-tidal seagrass phenology across Western Europe and North Africa. *Communications Earth & Environment*, 5(1), 382. <https://doi.org/10.1038/s43247-024-382>
- Nurdin, N., Alevizos, E., Syamsuddin, R., Asis, H., Zainuddin, E. N., Aris, A., **Oiry, S.**, Brunier, G., Komatsu, T., & Barillé, L. (2023). Precision Aquaculture Drone Mapping of the Spatial Distribution of *Kappaphycus alvarezii* Biomass and Carrageenan. *Remote Sensing*, 15(14), 3674. <https://doi.org/10.3390/rs15143674>

- Román, A., Prasyad, H., **Oiry, S.**, Davies, B. F. R., Brunier, G., & Barillé, L. (2023). Mapping intertidal oyster farms using unmanned aerial vehicles (UAV) high-resolution multispectral data. *Estuarine, Coastal and Shelf Science*, 291, 108432. <https://doi.org/10.1016/j.ecss.2023.108432>
- Davies, B. F. R., Gernez, P., Geraud, A., **Oiry, S.**, Rosa, P., Zoffoli, M. L., & Barillé, L. (2023). Multi- and hyperspectral classification of soft-bottom intertidal vegetation using a spectral library for coastal biodiversity remote sensing. *Remote Sensing of Environment*, 290, 113554. <https://doi.org/10.1016/j.rse.2023.113554>
- Zoffoli, M.L., Gernez, P., **Oiry, S.**, Godet, L., Dalloyau, S., Davies, B.F.R. and Barillé, L. (2023), Remote sensing in seagrass ecology: coupled dynamics between migratory herbivorous birds and intertidal meadows observed by satellite during four decades. *Remote Sens Ecol Conserv*, 9: 420-433. <https://doi.org/10.1002/rse2.319>
- Brunier, G., **Oiry, S.**, Lachaussée, N., Barillé, L., Le Fouest, V., & Méléder, V. (2022). A Machine-Learning Approach to Intertidal Mudflat Mapping Combining Multispectral Reflectance and Geomorphology from UAV-Based Monitoring. *Remote Sensing*, 14(22), 5857. <https://doi.org/10.3390/rs14225857>
- Brunier, G., **Oiry, S.**, Gruet, Y., Dubois, S. F., & Barillé, L. (2022). Topographic Analysis of Intertidal Polychaete Reefs (*Sabellaria alveolata*) at a Very High Spatial Resolution. *Remote Sensing*, 14(2), 307. <https://doi.org/10.3390/rs14020307>

Presentations to International Conferences

- Effect of Marine and Atmospheric Heatwaves on Reflectance and Pigment Composition of Intertidal *Zostera noltei* (February 2025); BioSpace25 - Biodiversity insight from Space, Frascati, Italy; Oral presentation
- Discriminating Seagrasses From Green Macroalgae in European Intertidal Areas using High Resolution Multispectral Drone Imagery (17 - 21 June 2024); Word Seagrass Conference, Napoli, Italy; Poster
- Remote Sensing discrimination of seagrass and green macroalgae: hyperspectral library and drone-mounted multispectral camera (22 - 24 November 2023); EC-ESA Joint Earth System Science Initiative, Frascati, Italy; Poster
- Precision aquaculture drone mapping of the spatial distribution of *Kappaphycus alvarezii* biomass and carrageenan (20 - 26 August 2023); 8th European Phycological Congress, Brest, France ; Oral presentation
- Remote Sensing discrimination of seagrass and green macroalgae: hyperspectral library and drone-mounted multispectral camera (20 - 26 August 2023); 8th European Phycological Congress, Brest, France ; Poster
- Remote Sensing discrimination of seagrass and green macroalgae: hyperspectral library and drone-mounted multispectral camera (23 - 27 may 2022); Living Planet Symposium, Bonn, Germany ; Poster

Project related to the thesis.

BiCOME



This thesis has been closely related to the European, ESA funded, project BiCOME. This project, led by the Plymouth Marine Laboratory (PML) in collaboration with the University of Nantes, the German Aerospace Center (Deutsches Zentrum für Luft- und Raumfahrt, DLR) and HYGEOS has started in October 2021 and has ended before the end of this thesis, in October 2023. It aimed to demonstrate that Essential Biodiversity Variables (EBVs), relevant for scientific and monitoring applications, can be obtained from state-of-the-art remotely sensed reflectance close to the shoreline, and that they can be scalable globally.

PML

Plymouth Marine
Laboratory

**Nantes
Université**



HYGEOS

Rewrite



Part of the thesis is related to the REWRITE project, led by Nantes University and funded by the European Union. This project involves 24 partners across 14 countries and focuses on 10 demonstration sites. Its aim is to promote the adaptation of the innovative conservation approach known as 'rewilding' as a nature-based solution for restoring Europe's intertidal areas.

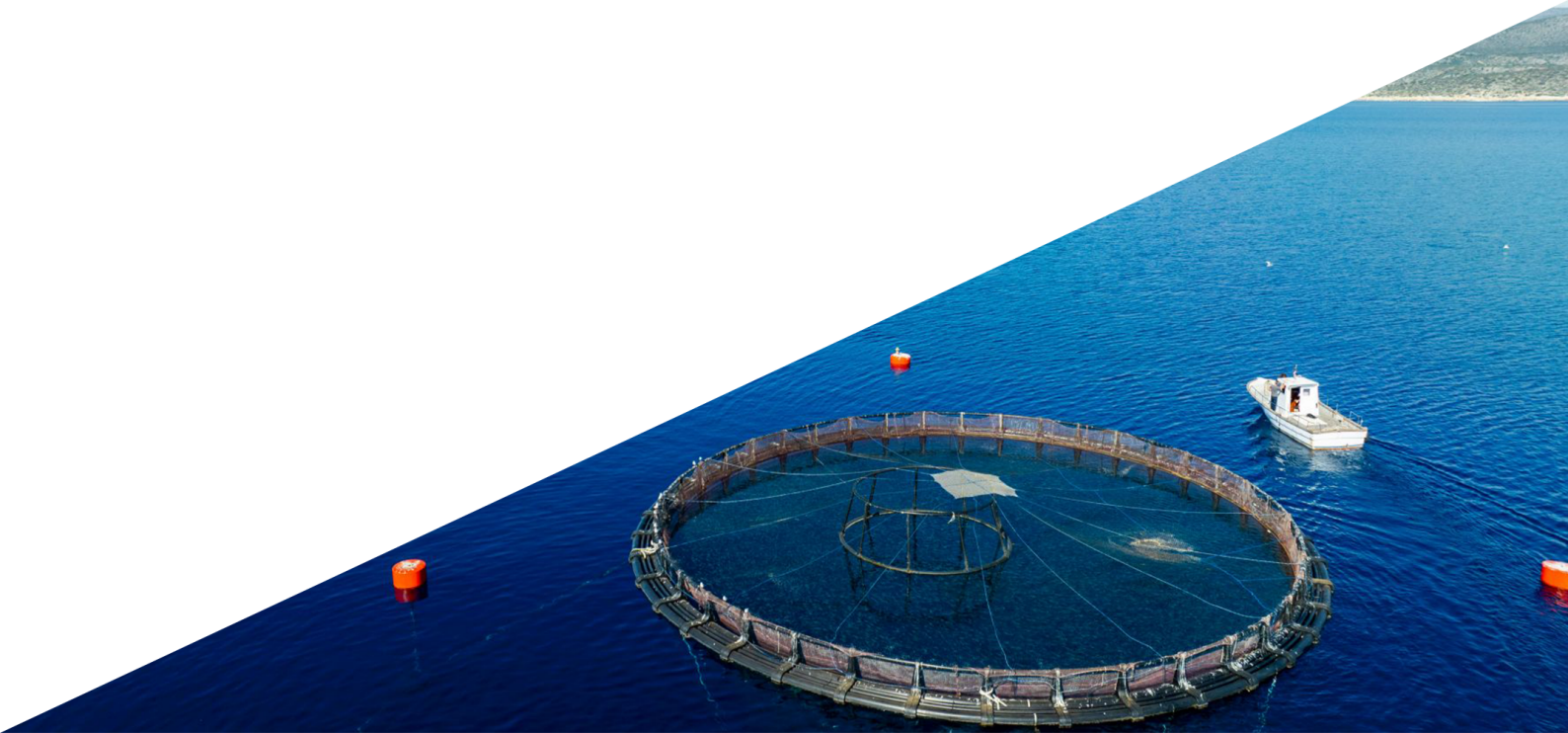
InvaSea

Part of the thesis is related to the InvaSea project, founded by the French National Centre for Space Studies (CNES). It aims to prove the capacity of remote sensing to map the presence of the alien invasive species *Gracilaria vermiculophylla* in French and Spanish estuaries.



1

Introduction



1.1 Coastal Environment

Marine coastal zones are among the most densely populated regions globally, serving as critical hubs for economic activity, transportation, and tourism. These areas support diverse ecosystems and provide essential resources. They also play a pivotal role in global trade and commerce while offering cultural and recreational value. However, their popularity and utility make them highly vulnerable to environmental pressures such as pollution, habitat destruction, and climate change impacts like sea-level rise and coastal erosion (Orth et al., 2006; Valle et al., 2013; Walker and McComb, 1992). Effective management and sustainable practices are crucial to preserving their ecological integrity and ensuring long-term viability.

Marine vegetative habitats in intertidal zones, such as seagrass meadows, microphytobenthos, and macroalgal habitats, face significant hazards from both anthropogenic activities and natural forces. Human-induced threats include coastal development, pollution, overfishing, and habitat modification, which degrade these ecosystems. Seagrass meadows are threatened by various anthropogenic activities (McKenzie et al., 2020), microphytobenthos are affected by the global decline of intertidal mudflats (Murray et al., 2019), and areas colonized by macroalgae may shrink due to the expansion of wild oyster reefs (Le Bris et al., 2016). Additionally, natural factors such as storms, sea-level rise, climatic extreme events and climate change exacerbate these pressures, altering the structure, function, and resilience of vegetated intertidal habitats.

These habitats provide vital ecological functions, including coastal erosion protection through root stabilization and sediment trapping (Bos et al., 2007) , mitigation of eutrophication effects by absorbing excess nutrients and improving water quality (**refs**), atmospheric CO₂ fixation, contributing to carbon sequestration and combating climate change (Krause-Jensen et al., 2018; McRoy and McMillan, 1977; Saderne et al., 2019). They are also biodiversity hotspots that support unique flora and fauna, providing feeding, breeding, and nursery grounds for various species (Sanabria-Fernández et al., 2024; Unsworth et al., 2019b). Despite their ecological significance and the ecosystem services they provide, intertidal habitats, particularly mudflats, remain highly vulnerable yet often overlooked. Tidal flats are challenging to access, and traditional field sampling methods are too time- and labor-intensive for repeated observations over large areas. Moreover, large variations across different temporal

scales in these habitats require frequent monitoring, which is impractical through field surveys alone. This underscores the need for advanced monitoring technologies, effective management practices and targeted conservation strategies to ensure their sustainability and resilience against diverse and evolving pressures.

1.1.1 Ecological and Socio-Economic Importance of Coastal Environments

Coastal environments represent a complex and dynamic interface between terrestrial and marine ecosystems, characterized by exceptional biodiversity, diverse geomorphological structures, and significant socio-economic relevance. These regions span a continuum that includes saltmarshes, beaches, dunes, estuaries, deltas, tidal flats, wetlands, rocky shores, biogenic reefs and lagoons, each shaped by a combination of natural processes and anthropogenic influences (Laignel et al., 2023).

The coastal zone encompasses areas where terrestrial and marine domains intersect, including environments influenced by tidal flows, wave dynamics, and riverine inputs. This transition zone can extend from a few hundred meters inland to several kilometers offshore, depending on local topography and ecological gradients. It incorporates upper shores and dunes, intertidal zones that are periodically submerged and exposed to tidal activity, and subtidal zones that remain submerged permanently (Figure 1.1 ; Laignel et al. (2023)).

As one of the most dynamic and multifaceted regions on Earth, coastal environments host highly diverse and productive habitats. These include both natural ecosystems and managed systems that underpin key economic sectors and urban centers (Hobohm et al., 2021). The functionality of many coastal ecosystems is intrinsically linked to land-sea interactions, as observed in deltas and estuaries (Elliott and Whitfield, 2011). These environments exhibit steep gradients in salinity—from freshwater to hypersaline—and energy levels, ranging from low-energy wetlands to high-energy, wave-dominated shorelines. On a broader scale, coastal regions encompass a spectrum of climatic zones, from tropical to polar, each characterized by unique biogeophysical processes and features (Murray et al., 2019). However, these areas are also exposed to a variety of land-based and marine hazards, including storms, tropical cyclones, storm surges, tsunamis, riverine flooding, shoreline erosion, sea-level rise and biohazards such as algal blooms and pollutants (Mukhopadhyay et al., 2012).

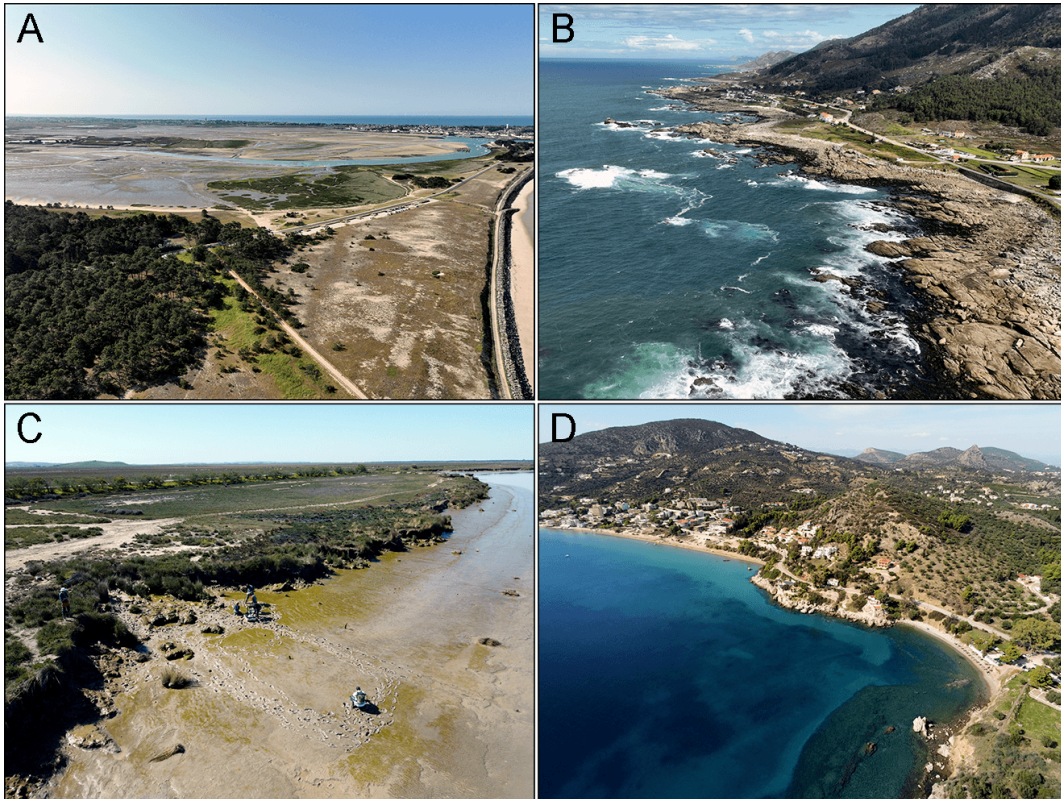


FIGURE 1.1: Examples of the diversity of habitat found in coastal environments. A: Upper shore and dunal vegetation of Pen Bron, France, on the 15th of May 2023. B: Rocky shore of the Galician coastline. Picture taken at Baiona, Spain on the 1st of September 2023. C: Tidal flat of the Guadalquivir River, Spain. Picture taken near of Trebujena, Spain on the 22nd of March 2023. D: Submerged seagrass meadows in Greece. Picture taken at Nauplie, Greece on the 29th of October 2023.

Coastal ecosystems provide a range of ecosystem services that are fundamental to environmental sustainability and human well-being (Barbier et al., 2011). These ecosystems function as natural barriers against storm surges and coastal flooding (Barbier, 2015), thereby mitigating the impacts of such hazards on inland regions and safeguarding human lives and infrastructure (Cooley et al., 2023). They support significant biodiversity, serving as critical habitats and breeding grounds for numerous species, including commercially valuable fish, shellfish, and other marine organisms that sustain global fisheries (Rodrigues-Filho et al., 2023). Coastal vegetation, including mangroves (Alongi, 2012), salt marshes (Connor et al., 2001), and seagrasses (Fourqurean et al., 2012), plays a crucial role in carbon sequestration by capturing and storing atmospheric carbon dioxide, thus contributing to climate change mitigation.

Beyond their role in climate regulation, well-functioning coastal ecosystems enhance

water quality by filtering pollutants, sediments, and excess nutrients, thereby maintaining healthier marine and estuarine systems (Los Santos et al., 2020). These ecosystems are integral to nutrient cycling, ensuring the continued productivity of adjacent marine environments (Nixon, 1981). Additionally, they provide substantial cultural, educational, and recreational opportunities, drawing global attention and fostering an intrinsic human connection to nature (Cao et al., 2022; Lakshmi, 2021). This societal value contributes directly to local and regional economies through industries such as tourism, artisanal fishing, and related enterprises (Martínez et al., 2007; Otrachshenko and Bosello, 2017). Furthermore, coastal ecosystems supply essential natural resources, including seafood and plant-based materials, while supporting sustainable aquaculture practices that promote global food security and bolster local livelihoods (Farmery et al., 2022). Collectively, these functions highlight the indispensable ecological and economic importance of coastal ecosystems.

1.1.2 Human Activities in Coastal Areas and their Environmental Impacts

Coastal areas are among the most significant regions for human habitation due to their strategic geographic position, resource availability, and economic opportunities. Approximately 2 billion people reside within 50 km of coastlines, with nearly 1 billion living within 10 km (Figure 1.2 ; Cosby et al. (2024)).

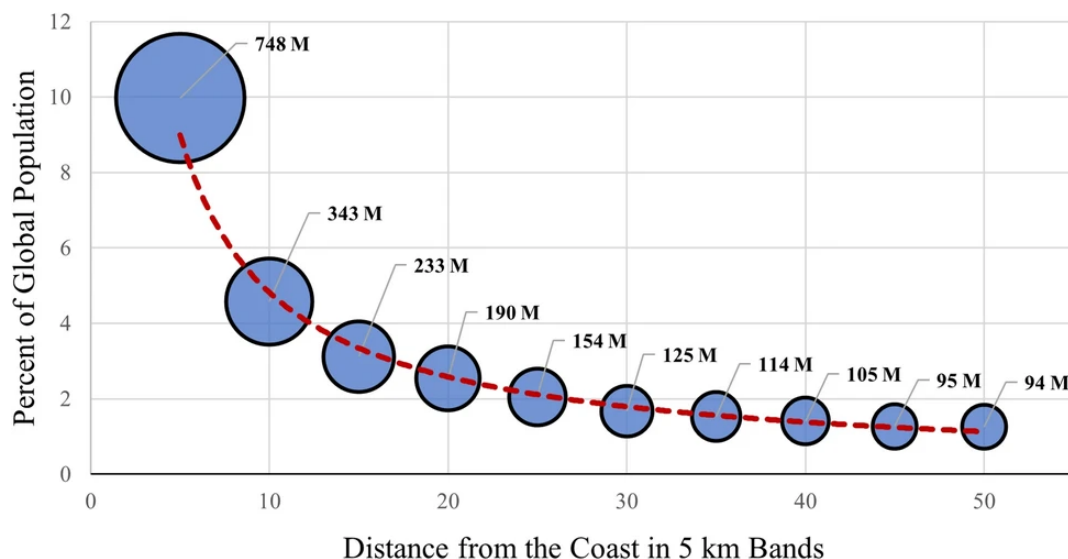


FIGURE 1.2: Global coastal population curve (CoPop curve) expressed as population estimates in 5 km bands. From Cosby et al. (2024)

This represents nearly 15% of the global population occupying only 4% of the Earth's

inhabitable landmass. Projections indicate that coastal populations will continue to rise, potentially reaching 2.9 billion by 2100 under various socioeconomic scenarios (Reimann et al., 2023). These areas offer critical resources such as seafood and freshwater, while their moderate climates often support agricultural activities and other forms of sustainable land use. Proximity to oceans and rivers enables robust trade, transportation, and industrial growth, positioning many coastal cities as pivotal economic hubs on a global scale. The ecological and cultural roles of coastal landscapes further contribute to their appeal, attracting populations for both settlement and economic activities.

Human utilization of coastal areas spans a range of economic and social activities that highlight both the benefits and challenges of these environments. Coastal tourism is a significant driver of economic growth, particularly in regions like the European Union (EU). In 2021, the EU's coastal tourism sector generated approximately €49.9 billion in Gross Value Added (GVA) and employed around 1.9 million people (Eurostat, 2023). Coastal fishing and aquaculture are vital components of the global economy, providing employment to millions and contributing significantly to food security. In 2022, the combined global production of fisheries and aquaculture reached a record 223.2 million tons, with aquaculture alone producing an unprecedented 130.9 million tons. Notably, for the first time, aquaculture surpassed wild capture in aquatic animal production, accounting for 51% of the total (Reuters, 2024). Additionally, maritime shipping is the backbone of international trade, with approximately 80% of global trade by volume and over 70% by value transported via sea routes. This extensive reliance on maritime transport underscores the critical importance of coastal infrastructure, including ports and harbours, in facilitating the movement of goods worldwide (Union, 2025). However, the intensive exploitation of coastal environments for human activities has led to significant ecological challenges.

For instance, marine shipping contributes about 3% of global greenhouse gas emissions, projected to rise by up to 50% by mid-century if stringent measures are not implemented (Faber et al., 2021). Additionally, shipping activities lead to marine pollution, including oil spills, ballast water discharge, underwater noise and light affecting marine life. Oil spills remain a critical environmental concern due to their devastating and long-lasting impacts on marine ecosystems. These spills contaminate

water, harm marine biodiversity, and disrupt food chains, often leading to severe economic losses in fisheries and tourism. In 2023, ten oil spills were recorded globally, releasing over 2,000 tons of oil into the environment, including one major spill exceeding 700 tons in Asia (ITOPF, 2023). While historical trends show a reduction in large spills, from over 20 per year in the 1970s to about 1.3 per year in recent decades, incidents such as the spill that occurred in December 2024 in the Kerch Strait, where 3,700 tons of oil were released, underscore the persistent and significant risks. When writing this thesis, it has been 25 years since the Erika catastrophe. On December 12, 1999, the oil tanker Erika, en route from Dunkirk to Livorno with approximately 31,000 tonnes of heavy fuel oil, encountered severe weather in the Bay of Biscay. The vessel broke in two and sank about 60 miles off the coast of Brittany, France, resulting in the spill of approximately 19,800 tonnes of oil into the sea. The spill polluted nearly 400 kilometers of French coastline, causing extensive environmental damage. The oil contamination had severely impacted marine life, including seabirds and coastal ecosystems (Barillé-Boyer et al., 2004). In response to the disaster, the European Union implemented the Erika I, II, and III legislative packages to enhance maritime safety and prevent future incidents. In 2008, French courts held several parties accountable for the spill, including the oil company Total, the shipowner, and the classification society, imposing fines and damages totaling €192 million. This tragic event remains a turning point in European maritime environmental protection policies.

Such events highlight the necessity for stringent preventive measures and rapid response mechanisms to mitigate the ongoing threat from oil spills to marine environments. Ballast water discharge represents a significant vector for the introduction of invasive aquatic species into new environments. Approximately 40% of introductions of non-indigenous aquatic species have been linked to ballast water release. Underwater noise pollution from shipping activities poses a growing threat to marine life, particularly cetaceans such as whales and dolphins (Reeves et al., 2014). Elevated noise levels can disrupt communication, navigation, and feeding behaviors, leading to increased stress and altered migration patterns (Nowacek et al., 2007). Chronic exposure to underwater noise can also result in physical harm and population-level impacts (Guan and Brookens, 2023). One significant impact of fishing and aquaculture on coastal habitats is the degradation of critical ecosystems such as seagrass beds, coral reefs, and mangroves. Destructive fishing practices, including bottom

trawling and the use of dynamite or cyanide, physically damage the seafloor and associated habitats, resulting in biodiversity loss and the disruption of ecological functions (Desai and Shambaugh, 2021; Ranjan et al., 2023). The expansion of aquaculture operations often involves converting coastal wetlands, into fish or shrimp ponds, or constructing structures over mudflats (Ahmed and Glaser, 2016). These activities usually conflict with ecosystem conservation, as both uses compete for limited space. The change of land-use into aquaculture facilities reduces the availability of essential nursery habitats for marine species and diminishes the ecosystem services provided by these natural habitats, such as carbon sequestration, shoreline stabilization, and water filtration (Hagger et al., 2022). Additionally, aquaculture activities contribute to nutrient enrichment and pollution in adjacent waters through the release of uneaten feed, faeces, and chemical additives, exacerbating eutrophication and altering benthic community structures (Karakassis et al., 2005). Another significant concern is the introduction of alien invasive species into the environment through aquaculture, which can disrupt local ecosystems and biodiversity (Wolff and Reise, 2002). This issue was explored in Chapter 4. Coastal tourism exerts a profound influence on ecosystem integrity, often driving substantial environmental degradation through mechanisms such as habitat destruction, pollution, and resource overexploitation. The construction and expansion of tourist infrastructure frequently lead to the removal or fragmentation of critical habitats, including mangroves, seagrass meadows, and coral reefs, all of which play pivotal roles in maintaining biodiversity and safeguarding coastal resilience. Furthermore, the rapid influx of visitors generates significant volumes of waste and untreated sewage, contributing to water quality deterioration and eutrophication, which disrupt aquatic ecosystems and alter trophic dynamics. The elevated demand for limited resources, notably freshwater and seafood, exacerbates ecological stress, leading to overharvesting and resource depletion.

The dynamic interactions between terrestrial and marine systems are particularly evident in intertidal habitats, which exemplify the transitional nature of coastal zones. The next section will focus on these habitats, exploring their ecological significance, the processes shaping them, and the challenges they face under increasing environmental and anthropogenic pressures.

1.1.3 Tidal flats

The intertidal zone refers to the coastal area between the high and low tide marks, characterized by periodic exposure and submersion due to tidal cycles. This dynamic zone forms the interface between terrestrial and marine ecosystems and is influenced by complex physical, chemical, and biological processes.

Tidal flats, a specific type of intertidal habitat, are defined as expanses of sand, rock, or mud that experience regular tidal inundation. These ecosystems are shaped by sediment deposition driven by tidal currents, wave action, and terrestrial runoff. As transitional ecosystems between terrestrial and marine environments, tidal flats face pressures from both domains. Additionally, they encounter unique threats, including coastal development (Arkema et al., 2013; Hassan et al., 2005), rising sea levels (Lovelock et al., 2017; Passeri et al., 2015), coastal erosion (Nicholls et al., 2007), decreased sediment input from rivers (Blum and Roberts, 2009), and the subsidence and compaction of coastal sediments (Minderhoud et al., 2020).

Globally, tidal flats are experiencing significant declines in extent due to both natural and anthropogenic factors. Murray et al. (2019), using a satellite time series, have shown that tidal flats have declined by approximately 16% from 1984 to 2016, representing a net loss of over 20,000 km² (Figure 1.3).

Regions such as East Asia, the Middle East, and North America have shown the greatest losses. These declines mirror trends observed in other coastal ecosystems, such as mangroves and seagrasses. Despite these losses, some areas have exhibited resilience or even expansion, highlighting the dynamic interplay between sedimentary processes, sea-level rise, and human interventions (Murray et al., 2019).

A potential solution to limit the disappearance of tidal flats is to protect the vegetated ecosystems they host. These ecosystems contribute significantly to nutrient cycling and sediment stabilization, enhancing the overall resilience of tidal flats. By maintaining these biotic communities, the ecological functions of tidal flats can be preserved, buffering them against threats such as erosion and rising sea levels.

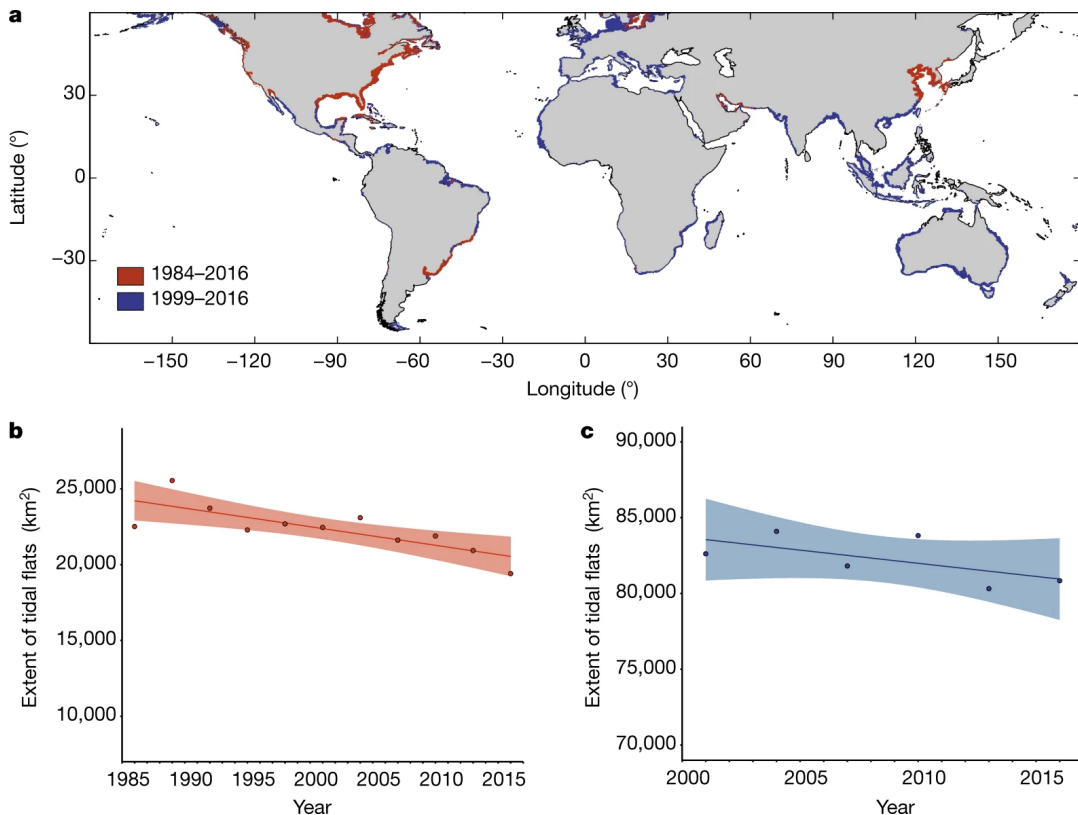


FIGURE 1.3: The global trajectory of tidal flats extent, showing areas in which the development of consistent time-series data over 1984–2016 (orange) and 1999–2016 (orange and blue) was possible. b, Change in the extent of tidal flats in 17.1% of the mapped area, 1984–2016 (linear regression, $P = 0.00437$). c, Change in the extent of tidal flats in 61.3% of the mapped area, 1999–2016 (linear regression, $P = 0.1794$). Shading in b and c indicates the standard error of the linear model.

From Murray et al. (2019)

The main vegetation classes found on tidal flats will be introduced in the following sections, as Chapters 2 and 3 rely specifically on distinguishing between these classes. Here, "classes" is considered in its taxonomic sense, referring to a taxonomic rank that groups related orders of organisms sharing a common ancestor.

1.1.3.1 Bacillariophyceae, Euglenida and Cyanophyceae

Within estuarine biological communities, microphytobenthos (MPB) can contribute up to 50% of total primary production (N-Uptake, 1999). This assemblage comprises unicellular algae—particularly epipsammic diatoms (associated with sand grains) and epipelagic diatoms (free and motile within muddy sediments, Figure 1.4 B)—as well as cyanobacteria and euglenids (MacIntyre et al., 1996). These organisms proliferate on

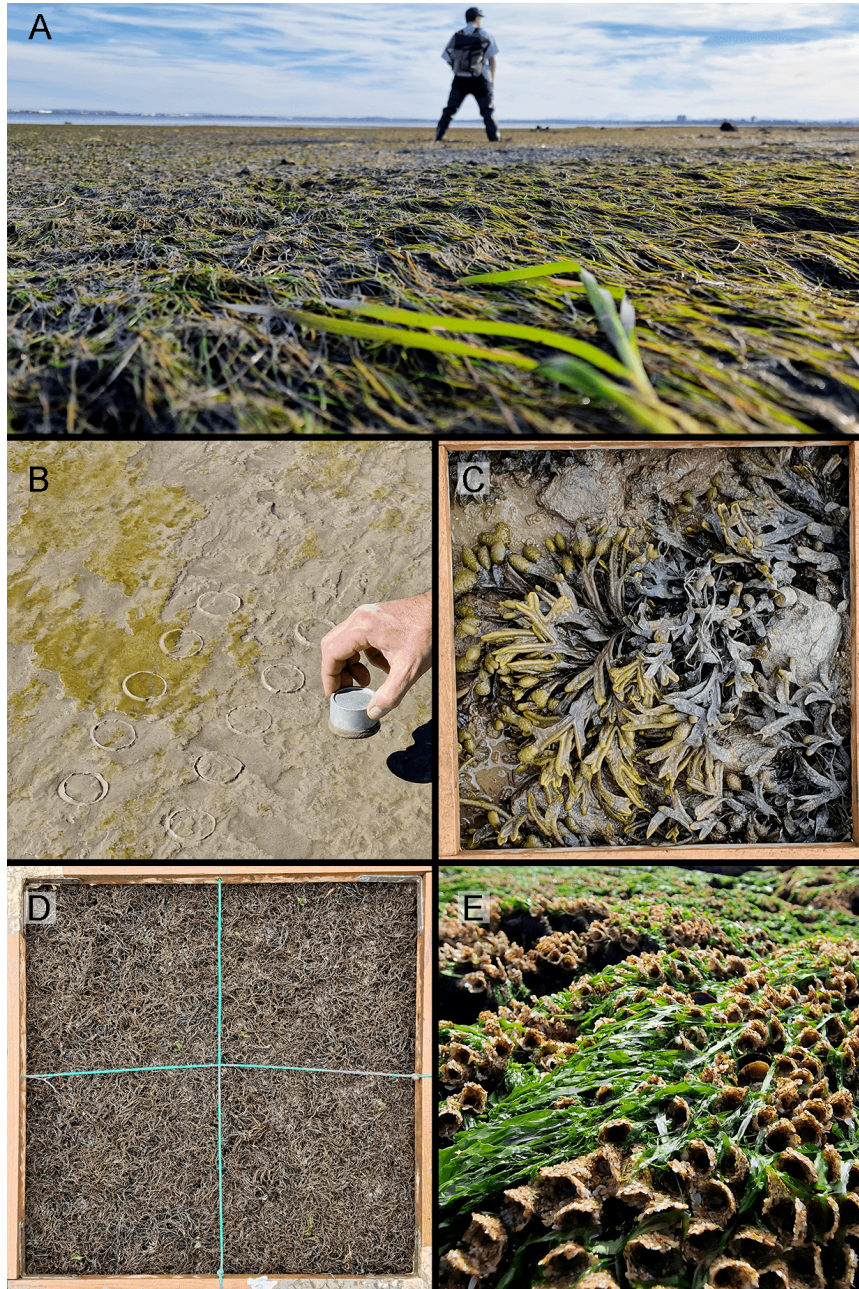


FIGURE 1.4: Main vegetation classes of soft-bottom intertidal areas studied in the work. A: Seagrass meadows (*Magnoliopsida*) in Cadiz, Spain, on the 21st of March 2023. B: Microphytobenthos (*Bacillario-phyceae*) biofilm patches, Cadiz, Spain, on the 22nd of March 2023. C: Brown algae (*Phaeophyceae*) in Ria d'Etel, France on the 13th of March 2024. D: Red macroalgae (*Rhodophyceae*) in the Belon estuary, France on the 10th of April 2024. E: Green macroalgae (*Chlorophyceae*) colonising the polychaete reef of Noirmoutier Island, France on the 29th of September 2023.

sediment surfaces during low tide (Kelly et al., 2001), colonizing intertidal superficial sediments and forming biofilms that can extend over several square kilometers (Benyoucef et al., 2014).

The MPB fulfils both structural and trophic functions within intertidal mudflats. Structurally, microphytobenthic biofilms protect sediment from resuspension and enhance mudflat stability by mitigating erosive processes (Decho, 2000). They also serve as a food resource for deposit-feeding and suspension-feeding invertebrates (Miller et al., 1996). MPB forms the foundation of various food chains, being consumed at low tide by organisms ranging from gastropods (Savelli et al., 2018) to shorebirds (Drouet et al., 2015). Additionally, at high tide, tidal currents and waves can resuspend the MPB, making it available in the water column for suspension feeders and facilitating the export of a portion of its biomass to adjacent ecosystems (De Jorge and Van Beusekom, 1995; Decottignies et al., 2007).

The MPB's role in sediment stabilization is further supported by its production of extracellular polymeric substances (EPS), which enhance sediment cohesion and reduce erosion. Moreover, it contributes to nutrient cycling within coastal ecosystems, influencing the availability of nutrients such as nitrogen and phosphorus, which are essential for primary production. The dynamic nature of MPB communities allows them to adapt to varying environmental conditions, making them integral to the resilience and functioning of coastal habitats.

1.1.3.2 Chlorophyceae

Green macroalgae, belonging to the Class of Chlorophyceae, are a diverse group of multicellular photosynthetic organisms predominantly inhabiting marine environments, though some species are found in freshwater and terrestrial habitats (Figure 1.4 E). They are characterized by green pigmentation, resulting from the dominance of chlorophylls a and b, which play a crucial role in their photosynthetic processes (Cikos et al., 2022).

Ecologically, green macroalgae are significant primary producers of coastal ecosystems. Species such as those in the genus *Ulva* are known for their rapid growth rates and are often indicators of nutrient-rich conditions (Liu et al., 2020).

In addition to their ecological roles, green macroalgae have been utilized in various human applications. They are cultivated for food used in aquaculture and their

potential in biofuel production and as bioindicators for monitoring environmental health is being actively researched (Moreira et al., 2022).

However, under eutrophication conditions —excessive nutrient enrichment—green macroalgae can proliferate excessively, leading to algal blooms. These blooms can have detrimental effects on marine ecosystems, including hypoxia (low oxygen levels) and competition with other important species (Schreyers et al., 2021; Sun et al., 2022).

1.1.3.3 Phaeophyceae

Brown macroalgae, classified under the class Phaeophyceae, are a diverse group of multicellular marine algae predominantly found in temperate and polar coastal regions (Figure 1.4 C). Their characteristic brown coloration arises from the presence of the pigment fucoxanthin, which masks the green color of chlorophylls a and c. This pigmentation is integral to their photosynthetic efficiency, particularly in low-light underwater environments (Cikoš et al., 2022).

Ecologically, brown macroalgae play a pivotal role in marine ecosystems. They form extensive underwater forests, commonly known as kelp forests, which provide habitat, food, and shelter for a multitude of marine organisms, thereby enhancing local biodiversity. These structures influence coastal oceanography by affecting water flow and light penetration. In intertidal areas, they often colonize rocky substrates, creating suitable habitat for various species like sea anemone, limpet and fishes (Eger et al., 2023).

In terms of human utilization, brown macroalgae have been harvested for centuries for various purposes. They are a source of alginates—polysaccharides extracted from their cell walls—widely used as gelling, thickening, and stabilizing agents in the food, pharmaceutical, and cosmetic industries, and they also have the potential to be used in Lithium-ion batteries production (Kovalenko et al., 2011). Additionally, certain species are consumed directly as food, particularly in East Asian cuisines, and are recognized for their nutritional value and health benefits.

Brown macroalgae also contribute to environmental management practices. Their ability to absorb and accumulate heavy metals makes them effective in bioremediation efforts to remove pollutants from marine environments (Davis et al., 2003).

Furthermore, their potential in carbon sequestration positions them as valuable components in strategies aimed at mitigating climate change impacts.

However, brown macroalgae are susceptible to environmental changes. Factors such as ocean warming, pollution, and overfishing can lead to declines in their populations, which in turn affects the broader marine ecosystems they support (Manca et al., 2024). Conservation and sustainable management of these algae are therefore crucial to maintaining the health and productivity of coastal marine environments.

1.1.3.4 Rhodophyceae

Red macroalgae, or Rhodophyta, constitute a diverse group of predominantly marine, multicellular algae characterized by their reddish pigmentation, which results from the presence of phycoerythrin and phycocyanin pigments (Figure 1.4 D). These pigments enable red algae to efficiently absorb blue and green wavelengths of light, facilitating photosynthesis at greater ocean depths compared to other algal groups (Cikoš et al., 2022).

Ecologically, red macroalgae play a vital role in marine environments. They contribute significantly to primary production and serve as foundational species in various marine habitats. Notably, coralline red algae, which secrete calcium carbonate, are instrumental in building and stabilizing coral reef structures, providing habitat complexity that supports diverse marine life (Cornwall et al., 2023).

In terms of human utilization, red macroalgae have been harvested for centuries for their nutritional and industrial value. Species such as *Porphyra* (known as nori in Japan and gim in Korea) and *Palmaria palmata* (dulse) are consumed as food, valued for their high protein content, essential vitamins, and minerals (Stévant et al., 2023; Wei et al., 2023). Additionally, red algae, such as *Kappaphycus alvarezi* or *Eucheuma* spp., are a primary source of phycocolloids like agar and carrageenan, which are extensively used as gelling and stabilizing agents in the food, pharmaceutical, and cosmetic industries (Nurdin et al., 2023; Valderrama et al., 2013). Red macroalgae also possess bioactive compounds with potential therapeutic applications. Research has identified various secondary metabolites in red algae that exhibit antimicrobial, anti-inflammatory, and anticancer properties, highlighting their potential in drug development and functional food ingredients (Ismail et al., 2020).

However, red macroalgae face challenges due to environmental changes. Factors such as climate change, pollution, and habitat destruction can adversely affect their populations and the ecosystems they support. Conservation efforts and sustainable harvesting practices are essential to preserve these ecologically and economically important organisms (Hanley et al., 2024).

1.1.3.5 Magnoliopsida

Intertidal seagrass meadows (Figure 1.4 A), classified under the class Magnoliopsida, consist of flowering plants adapted to the unique challenges of periodic exposure and submersion in the intertidal zone. These meadows stabilize sediments via their root systems, which anchor substrates and mitigate erosion, thereby reducing sediment loss and maintaining substrate integrity (Davies et al., 2024a; Sousa et al., 2019; Zoffoli et al., 2023). Additionally, seagrass meadows provide essential ecosystem services, including acting as habitat, nurseries or feeding location for numerous species (Figure 1.5), many of which are commercially important (Moussa et al., 2020). Their structural complexity offers refuge from predators, supporting juvenile survival and biodiversity. These meadows play a significant role in global carbon sequestration, capturing and storing carbon at rates comparable to, or exceeding, terrestrial forests. Furthermore, they regulate nutrient cycles and improve water quality by trapping sediments and filtering pollutants, thus sustaining the health of adjacent marine environments (Los Santos et al., 2019). By cycling nutrients and contributing organic matter through detritus production, intertidal seagrass meadows enhance tidal flats' ecological productivity and resilience, underscoring their critical role in supporting both ecological functions and socio-economic benefits. Seagrass meadows, like tidal flats, are undergoing significant global decline due to various anthropogenic and natural stressors (Davies et al., 2024a). Despite their critical ecological roles, seagrass ecosystems remain comparatively underrepresented in scientific research within the broader scope of coastal ecosystems. As illustrated in Figure 1.5 (E), the proportion of publications focusing on seagrasses in the context of coastal ecosystem studies is considerably lower than those dedicated to other key habitats such as coral reefs, mangroves. This disparity highlights a critical research gap, underscoring the need for increased scientific attention to better understand and mitigate the factors contributing to the degradation of these vital ecosystems.

Traditional field-based sampling methods have proven to be highly effective for studying coastal environments at localized or small spatial scales, providing detailed insights into species composition, habitat structure, and ecological interactions. However, these approaches face significant limitations when applied to broader spatial extents or temporal scales due to their labor-intensive nature and logistical constraints. This methodological gap poses challenges for evaluating large-scale patterns and long-term changes in coastal ecosystems, such as seagrass meadows, mangroves, and tidal flats. Remote sensing technologies, with their ability to capture high-resolution data across extensive geographic areas and over multiple time periods, offer a powerful complementary tool to address these limitations. Integrating traditional methods with remote sensing approaches allows a more comprehensive understanding of coastal ecosystem dynamics, facilitating the assessment of both localized impacts and global trends. The following section explores how advancements in remote sensing technologies are transforming the study of coastal environments, enabling more efficient and scalable assessments.

1.2 Concepts of Remote sensing

Coastal environments represent highly dynamic and sensitive ecosystems shaped by complex interactions between natural processes and human activities. Remote sensing (RS) technologies are crucial for monitoring these regions, providing detailed data on shoreline erosion, habitat degradation, sediment dynamics, and water quality. This section reviews fundamental concepts and methodologies of RS applied to coastal environments.

RS defines the ability to retrieve information in a non-invasive way, without direct contact with the target. It relies on the propagation of signals, typically optical, acoustic, or microwave, between the target and the sensor. RS provides the basis for Earth observation (EO), where its methodologies facilitate large-scale and long-term data collection. Instruments on satellites, aircraft, and drones provide high-resolution imagery and measurements critical for monitoring environmental changes, mapping natural resources, and assessing land use patterns. These technologies enable systematic data collection over large areas and extended periods, supporting analyses such as deforestation, glacial melting, variations in ocean temperature, and changes

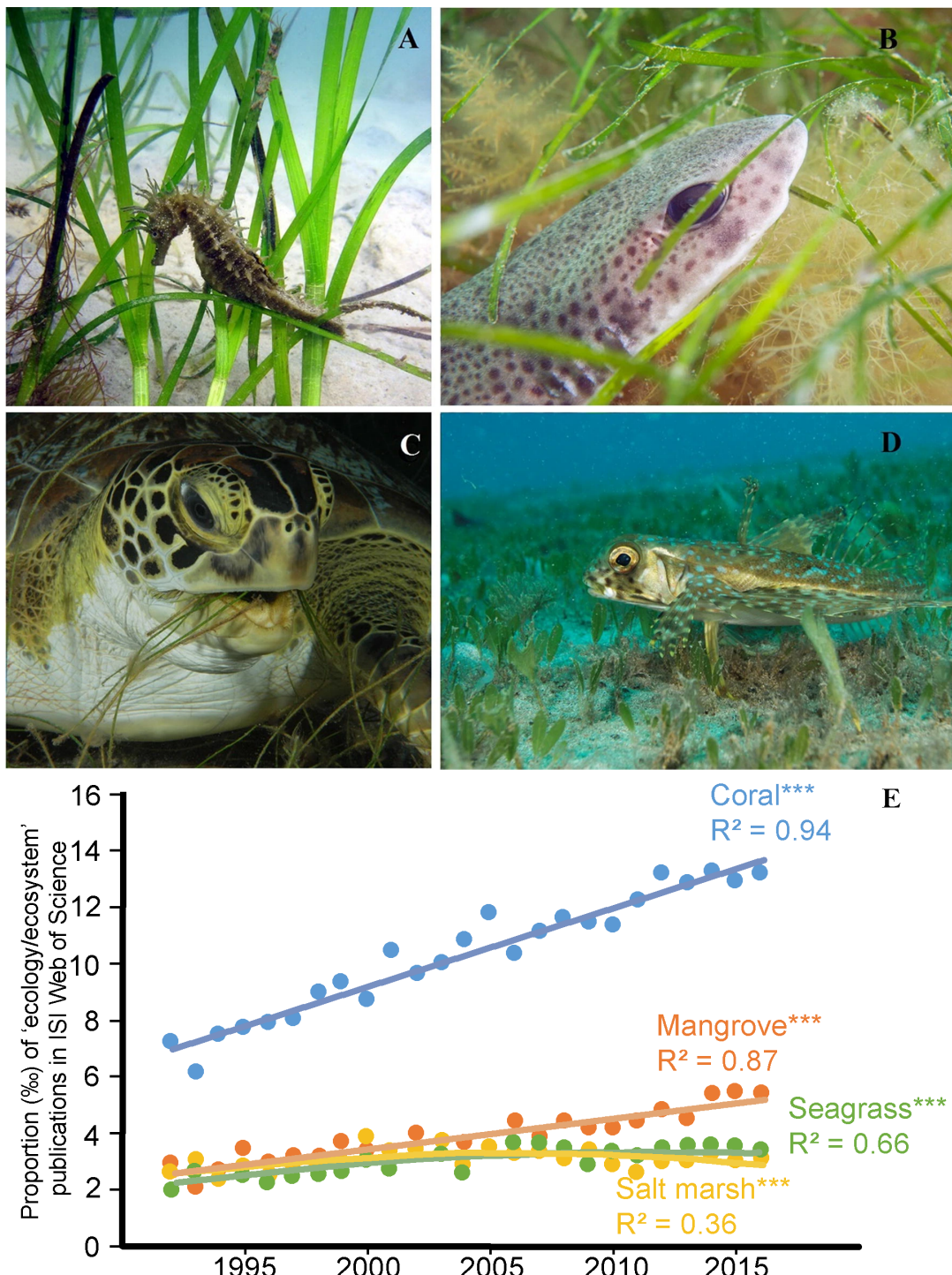


FIGURE 1.5: Seagrass meadows are habitats containing biodiverse faunal communities such as the following: a) the Spiny Seahorse (*Hippocampus guttulatus*) in the UK (source N Garrick-Maidment), b) Dogfish (*Scyliorhinus canicula*) in the UK (source Frogfish Photography), c) the Green Sea Turtle (*Chelonia mydas*) in the Dutch Antilles, d) Flying Gurnard (*Dactylopterus volitans*) in Puerto Rico (source Luis R. Rodriguez) and e) shows the proportion of publication each year dedicated to Coral reefs, Mangroves, Seagrasses and Salt marshes. Modified from Unsworth et al. (2019a).

in land use.

Some technical characteristics of remote RS can directly impact their ability to map coastal ecosystems. The next section explores these characteristics, illustrating their importance with specific use case examples.

1.2.1 Active Remote Sensing, Example of LiDAR

Active RS is a technique in which a sensor emits its own energy—typically in the form of electromagnetic radiation—toward a target and measures the energy reflected or backscattered from it. This method allows for the collection of data regardless of natural light conditions, enabling observations during both day and night and through various weather conditions.

The Light Detection and Ranging (LiDAR) sensor emit laser beams in the ultraviolet (UV), visible or infrared (IR) regions of the electromagnetic spectrum. By analyzing the return signal, they can estimate distances to objects or surfaces, detect optically active constituents in water bodies, and assess aerosols in the atmosphere (Dionisi et al., 2024; Jamet et al., 2019)

LiDAR works by emitting a beam of light and measuring the time it takes for the beam to return to the sensor. This process not only calculates distances but also captures the intensity of the returned signal. In many instances, multiple returns from a single pulse are measured, enabling the mapping of varying objects height within the same x and y coordinates. This capability allows the creation of precise, three-dimensional representations of the environment such as mapping the heights of trees in forests or measuring crop heights in agricultural fields (Figure 1.6). When ground height cannot be directly measured, LiDAR data can generate a digital surface model (DSM), which represents the uppermost layer of the environment. However, if multiple returns are recorded, it becomes possible to create both a DSM and a digital terrain model (DTM), which represents the ground surface, by differentiating between the surface and underlying layers. The difference between DSM and DTM, called Digital Height Model (DHM), can be used to assess living stock or biomass.

Achieving accurate 3D measurements of a target using LiDAR technology requires a high level of precision in assessing each system parameter. The quality of the final output depends on careful calibration and execution at every stage of the process. One

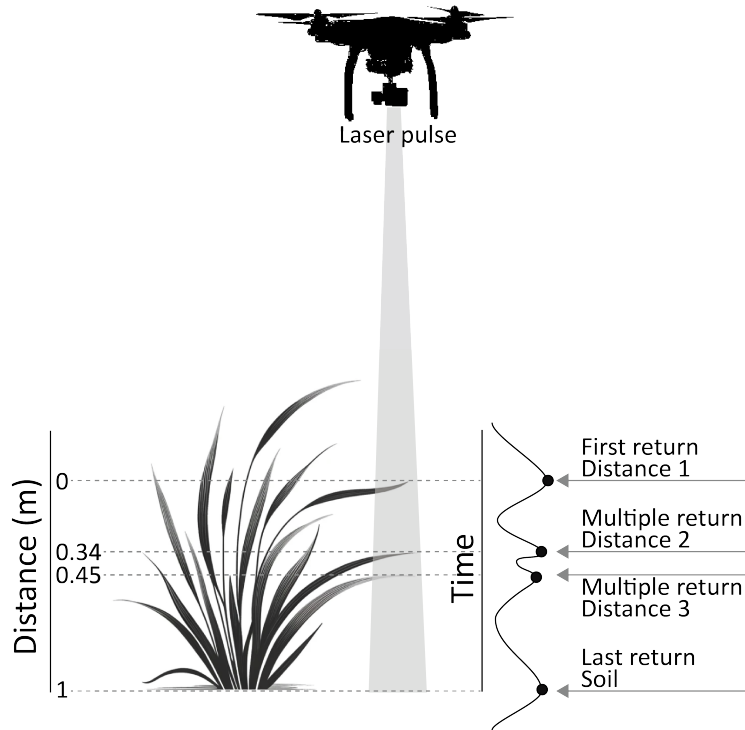


FIGURE 1.6: Diagram showing several signal-return for a single emitted beam of a LiDAR system. adapted from Wang and Fang (2020) and García-Feced et al. (2011)

critical step is ensuring the precise timing of the laser beam's return after it reflects off the target. This timing directly determines the distance calculations that form the basis of the 3D structure. Equally important is the accurate positioning of the LiDAR sensor, which is often mounted on a drone, aircraft, or satellite. The sensor's x, y, and z coordinates must be continuously tracked with high precision. Real-Time Kinematic (RTK) positioning systems are commonly employed to achieve this. These systems enhance the accuracy of the positioning data by providing real-time corrections to the sensor's GPS coordinates, ensuring minimal error and maintaining the integrity of the spatial measurements. Without such stringent measures, the resulting LiDAR data is prone to errors that can lead to distorted and noisy representations of the mapped surface. These inaccuracies diminish the data's reliability and compromise its utility for detailed analysis and decision-making processes.

In coastal environment monitoring, LiDAR systems are classified based on their emitted wavelengths, which determine their performance and application. These systems are categorized into “topographic LiDAR” and “bathymetric LiDAR,” each suited to specific tasks in coastal studies. Topographic LiDAR operates in the near-infrared (NIR) spectrum (approximately 1000 nm) and maps terrestrial features, such as beach

contours, vegetation density, rocky shore structures and man-made installations. Its ability to generate high-density point clouds stems from efficient operation at lower power. Unlike other types of LiDAR, NIR LiDAR requires less power, making it generally more affordable and compact. These attributes allow topographic LiDAR systems to be easily mounted on drone platforms, offering greater flexibility and accessibility for coastal monitoring. In contrast, bathymetric LiDAR, utilizing green (~532 nm) and red wavelengths, penetrates the water column to reveal submerged landscapes, including coral reefs, seagrass meadows, and shallow seabeds. Operating within the visible region of the electromagnetic spectrum, it is more susceptible to atmospheric scattering than NIR LiDAR, making it less suitable for terrestrial applications.

The Litto3D® product (SHOM, n.d.) consists of high-resolution bathymetric and topographic maps in coastal areas created using LiDAR technologies. During airborne missions, the system captures terrestrial and submerged terrain features with high precision. The topographic LiDAR achieves a spatial resolution of 1 m, with vertical accuracy up to 20 cm under optimal conditions, such as minimal atmospheric interference, stable flight paths, and favorable weather. The bathymetric LiDAR maps underwater landscapes to depths of approximately 70 m, depending on water transparency. This dual-mode capability is essential for modeling complex coastal environments, seamlessly integrating terrestrial and marine datasets. The airborne platform enables rapid data acquisition over large areas, overcoming challenges associated with ground-based or shipborne methods. The fusion methodology used by Litto3D® ensures the precise alignment of terrestrial and marine datasets, resolving inconsistencies in elevation data at land-water interfaces. The resulting unified dataset accurately represents coastal environments and supports diverse scientific and practical applications such as coastal risk assessment and ecological studies. Distributed by the Service Hydrographique et Océanographique de la Marine (SHOM, 2024) and the Institut National de l'Information Géographique et Forestière (IGN, 2024a), this dataset is open-source but currently available only for selected coastal regions in France.

In this study, LiDAR data were utilized in **Chapter 4** using a drone-borne NIR LiDAR system. These data were employed to evaluate the elevation and slope of mudflats in French and Spanish estuaries and to map the spatial distribution of

the invasive red macroalga *Gracilaria vermiculophylla*. In **Chapter 5**, the Litto3D product was and a water height dataset were used to assess the emersion time of seagrass meadows in Quiberon, France, during low tide. Since this thesis focuses on intertidal environment, field campaigns were conducted during low tide to ensure optimal conditions for the effective use of NIR LiDAR providing unobstructed access to exposed intertidal zones.

1.2.2 Passive Remote Sensing

Passive RS collects data about the Earth's surface or atmosphere by measuring naturally emitted or sunlight-reflected electromagnetic radiation (EMR) without actively transmitting signals. This technique relies on energy sources external to the instrument, such as sunlight for optical and NIR sensors or Earth's thermal emissions for thermal infrared sensors.

Passive RS is widely utilized in spaceborne satellite missions and has played a pivotal role in programs developed by major space agencies, including the European Space Agency (ESA) and the National Aeronautics and Space Administration (NASA). For instance, Sentinel-2 which provides ESA's highest spatial resolution imagery, employs passive sensors. Data measured by these sensors have been applied to monitor land cover, vegetation dynamics and coastal and in land-water environments.

As sunlight enters the Earth's atmosphere, it interacts with various gases and particles altering its properties. These interactions include scattering, absorption, and refraction. Scattering occurs when atmospheric molecules and aerosols disperse light in different directions, with shorter wavelengths like blue light being more strongly affected. Absorption results from atmospheric constituents such as ozone, water vapor, and carbon dioxide, which absorb energy at specific wavelengths, reducing the intensity of the transmitted light that reaches the Earth's surface. Refraction occurs as light changes direction and speed while passing through atmosphere layers with varying densities (Figure 1.7).

When sunlight reaches the Earth's surface, it exhibits several behaviors, depending on the surface properties and the angle of incidence. These behaviors include:

- **Absorption:** The surface absorbs light, converting it into heat or another form of energy. This process varies based on the biogeochemical characteristics of the surface, with darker surfaces typically absorbing more light.

- Transmission: The light passes through the surface, entering a different medium, such as water or transparent materials. The extent of transmission depends on the material's transparency and refractive index.
- Reflection: Light that is neither absorbed nor transmitted is redirected back in the opposite direction. The amount of reflection depends on the surface's albedo, with bright surfaces like snow reflecting more light compared to darker surfaces such as forests.

Only reflected light can be detected by spaceborne sensors. The most used metric in passive RS, to quantify EMR, is reflectance (R). R is typically measured as the ratio of upwelling radiance L_u to downwelling radiance L_d (Equation 1.1). L is defined as the radiant intensity per unit of projected area in a specified direction and is expressed in units of $\text{W} \cdot \text{m}^{-2} \cdot \text{sr}^{-1}$. R , however, is dimensionless.

$$R(\lambda) = \frac{L_u(\lambda)}{L_d(\lambda)} \quad (1.1)$$

R is defined for each wavelength as a value between 0 and 1. A value of 0 indicates that all light has been absorbed or transmitted by the target, while a value of 1 indicates that all light has been reflected (Figure 1.7).

R at the Top of Atmosphere (TOA), i.e., the magnitude directly measured by spaceborne or airborne sensors contains signals originating from both the atmosphere and the Earth's surface. Therefore, to study targets located on the Earth's surface, R_{TOA} must undergo atmospheric correction processing to transform it into Bottom of Atmosphere (BOA) R , which represents the intrinsic reflectance properties of the surface target. Precise R_{BOA} is crucial for accurately analyzing surface characteristics and for applications like vegetation monitoring, water quality assessment, and land cover classification.

One of the most basic atmospheric correction methods is the “black pixel” method, which assumes that all the signal retrieved over optically deep waters originates entirely from the atmosphere. This information is then used to correct the reflectance across the entire scene. However, this method requires the presence of optically deep water targets within the scene and assumes uniform aerosol concentrations across the scene. Such assumption may be inaccurate, particularly for satellites with a wide

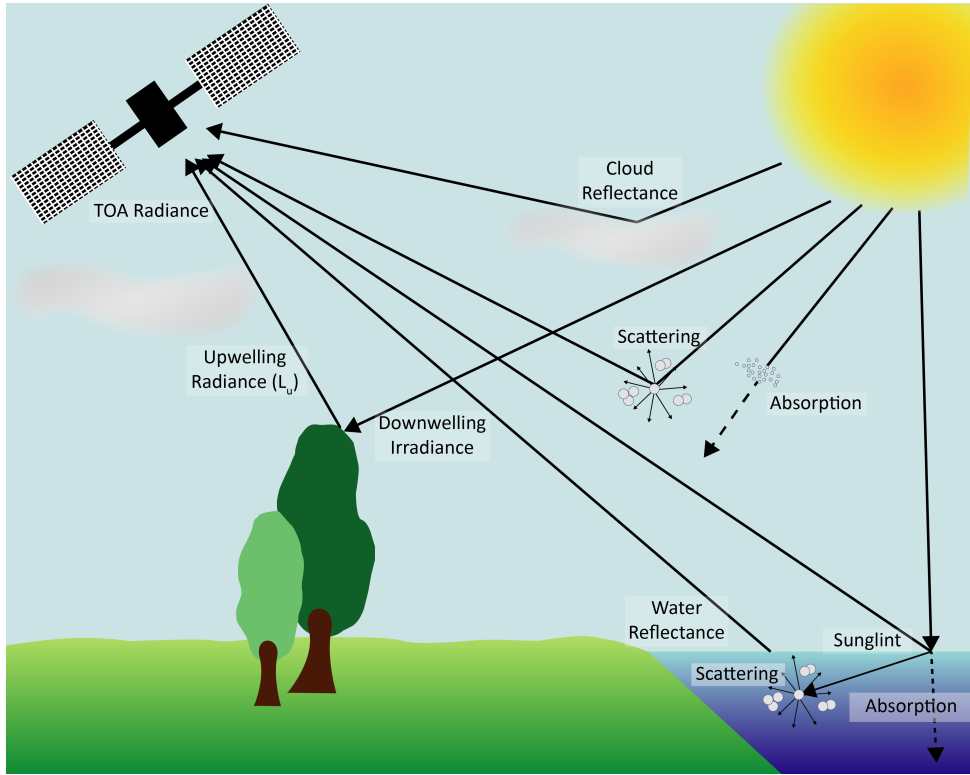


FIGURE 1.7: Light pathways involved in remote sensing: illustrating the interaction of solar radiation with the atmosphere, vegetation, and water surfaces, highlighting processes such as scattering, absorption, and reflectance contributing to the top-of-atmosphere (TOA) radiance observed by a satellite sensor.

field of view, such as MODIS, where a single image can cover a swath of 2,330 km. Limitations to this technique also arise when the target of study is a water body itself. These limitations highlight the need for more advanced correction techniques that account for spatial variability in atmospheric properties.

To address these challenges, sophisticated atmospheric correction algorithms tailored to specific sensors and study areas have been developed. These algorithms account for atmospheric scattering, absorption, and path radiance contributions by leveraging radiative transfer models, auxiliary atmospheric data, and sometimes *in situ* measurements. For example, data from the ESA constellation Sentinel-2 can be processed using Sen2Cor, a correction algorithm designed to produce R_{BOA} by incorporating atmospheric parameters such as water vapor, aerosols, and ozone concentrations. Additionally, some atmospheric correction methods are customized for specific targets, for example, algorithms specifically designed for water bodies, such as POLYMER (Steinmetz et al., 2011) or ACOLITE (Vanhellemond and Ruddick, 2018).

R_{BOA} provides information regarding light reflected by the target across various wavelengths. This phenomenon, referred to as the spectral signature, is a unique feature of each target type. Spectral signatures contain data about the physical and chemical properties of surfaces, forming the basis for RS applications. By analyzing spectral signatures, it is possible to identify and classify surface types, as well as derive insights into environmental changes and land-use dynamics. For example, Chlorophyll-a (Chla), a pigment found in all vegetation cells, plays a key role in defining the spectral signature of plant life. Chla absorbs light in specific regions of the electromagnetic spectrum, particularly in the blue region around 440 nm and the red region near 675 nm. Consequently, healthy vegetation exhibits a spectral signature with low R at 440 and 675 nm. Variations in physiological states and vegetation types result in different spectral patterns, enabling their differentiation and monitoring of ecological conditions over time (Figure 1.8).

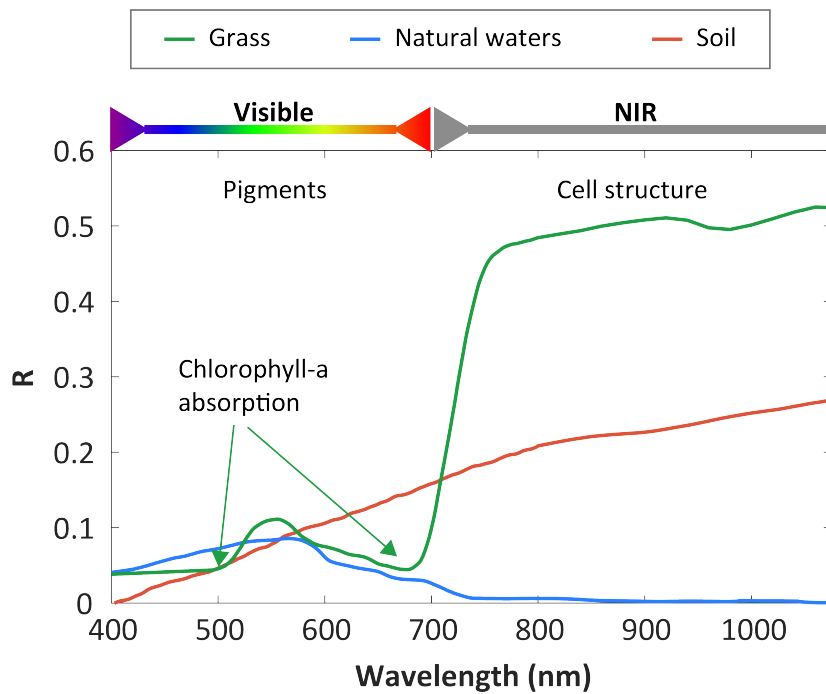


FIGURE 1.8: The spectral signature of vegetation (green), Water (blue) and bare soil (red). Absorption features of Chlorophyll-a are indicated for the spectra of vegetation.

Spectral indices are mathematical combinations of reflectance values at specific wavelengths, designed to maximize particular surface characteristics with simple processing. Vegetation indices, for example, leverage the distinct reflectance patterns of photosynthetic pigments. The Normalized Difference Vegetation Index (NDVI) is a

widely used index based on the normalized difference between R in the NIR and red. It is calculated as:

$$NDVI = \frac{R(NIR) - R(Red)}{R(NIR) + R(Red)} \quad (1.2)$$

where $R(NIR)$ is the reflectance in the NIR region around 800 nm and $R(Red)$ is the reflectance in the red region around 665 nm.

NDVI values range from -1 to 1, with negative values indicating water and higher positive values corresponding to dense healthy vegetation. While NDVI is a proxy for vegetation biomass and photosynthetic activity, its interpretation can be complex in heterogeneous environments, such as areas with overlapping vegetation types or substrates. Some studies propose a simple classification of NDVI based on thresholds to differentiate between distinct types of intertidal vegetation (Méléder et al., 2003b). While this simple first approximation can be useful for delimitating contrasting types of targets, establishing thresholds depends on specific sensor characteristics. This technique often fails in mapping vegetation types with similar pigment content or highly heterogeneous targets. More sophisticated techniques that utilize a greater amount of spectral information are required in such situations (Oiry and Barillé, 2021)

R_{BOA} can be used to identify key absorption features of chemical compounds of the target, by applying derivative analysis to the spectral signature. The second derivative of the R is utilized to enhance the detection of subtle pigment or mineral absorption features. By analyzing the second derivative, these small features are amplified, allowing for more precise identification of pigment presence and estimation of their concentrations. This approach is particularly effective for identifying accessory pigments with weaker absorption features than Chla (Jesus et al., 2014).

Some technical characteristics of RS sensors can directly impact their ability to map coastal ecosystems. The next section explores these characteristics, illustrating their importance with examples of specific use cases.

1.2.2.1 Spectral and Radiometric resolution

The detection of pigments absorption features necessitates measuring light reflectance at fine spectral resolution. However, measuring detailed spectral signatures depends on the sensor's characteristics.

Spectral resolution is defined by three main components: the number of spectral bands, the bandwidth (Full Width at Half Maximum, FWHM), and the spectral sampling interval. Sensors with higher spectral resolution can distinguish between closely spaced wavelengths within the electromagnetic spectrum, enabling precise characterization of spectral features (Figure 1.9).

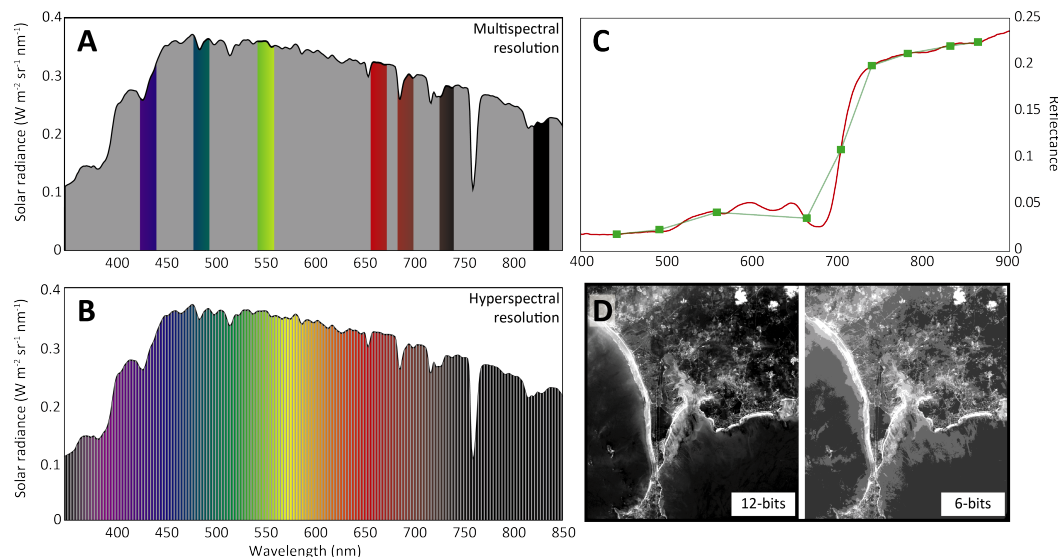


FIGURE 1.9: Comparison of spectral resolution between multispectral (A) and hyperspectral (B) sensors in the solar radiance spectrum. Panel C illustrates the impact of spectral resolution on the same spectral signature of *Gracilaria vermiculophylla*. With hyperspectral resolution (red), absorption features of pigments such as phycocyanin and phycoerythrin are distinguishable, whereas these features are absent in the multispectral resolution provided by Sentinel-2 (green). D is showing examples of different radiometric resolutions for the same band of a Sentinel-2 tile. One is coded in 12 bits (left), and the other in 6 bits (right).

RS sensors are generally classified into two categories based on their spectral resolution: multispectral and hyperspectral sensors. Multispectral sensors are characterized by a limited number of broad spectral bands, with a bandwidth generally exceeding 20 nm. The spectral sampling interval is relatively large, resulting in a coarser spectral resolution that provides a broad overview of the spectral characteristics of a scene. In contrast, hyperspectral sensors are equipped with hundreds of narrow, contiguous

spectral bands. Small spectral sampling intervals separate these bands, often just a few nanometers, which results in a much finer spectral detail. High spectral resolutions, capturing subtle variations in absorption features and spectral shapes, allow distinguishing between targets with similar spectral characteristics, such as vegetation with similar pigment profile. Multispectral sensors, while less detailed, are efficient for general spectral analyses where fine discrimination is not required. Another specification of sensors in the spectral discrimination is the radiometric resolution. It refers to the precision at which the sensor records the data. It is defined by the number of discrete levels, or bits, used to represent the energy recorded for each pixel in an image. Higher radiometric resolution enables finer distinctions in brightness levels, which is particularly important for detecting subtle differences in reflectance and ensuring accurate analysis of surface features. For example, an 8-bit sensor can record 256 levels of intensity, while a 12-bit sensor can capture 4,096 levels, providing greater detail and dynamic range in the captured imagery (Figure 1.9 D).

1.2.2.2 Spatial resolution

Spatial resolution, defined as the smallest discernible detail a sensor can detect on Earth's surface, is another fundamental characteristic of RS sensors. It is typically represented by the ground area covered by a single pixel in an image and is influenced by the sensor's instantaneous field of view (IFOV), which determines the angle of view and, consequently, the ground area visible to the sensor. A smaller IFOV or lower sensor altitude results in finer spatial resolution, enabling the detection of smaller features. For the same IFOV, sensors mounted on satellites can cover larger areas compared to those on drones, albeit with reduced detail.

Spatial resolution can range widely depending on the research objective and sensor platform. For instance, moderate-resolution sensors like MODIS aboard Terra and Aqua capture data at spatial resolutions of 250 m, 500 m, and 1 km, making them suitable for large-scale environmental monitoring. In contrast, Sentinel-2 provides higher spatial resolutions—10 m for visible and NIR bands, 20 m for red-edge and shortwave infrared bands, and 60 m for atmospheric correction bands—facilitating detailed observations for applications such as vegetation and land-use mapping. At the finer end, high-resolution sensors on platforms like Pleiades-Neo achieve sub-meter resolutions (e.g., 30 cm per pixel), ideal for precise Earth observations.

Unmanned Aerial Vehicles (UAVs), equipped with high-resolution cameras, offer even finer spatial resolutions, often down to a few cm, even mm, depending on flight altitude and sensor specifications. This ultra-high resolution is particularly advantageous for heterogeneous site mapping. Chapter 3 will show that an ultra-high spatial resolution can be valuable for machine learning model training. However, such a high resolution requires increased data storage and processing capacity, illustrating the trade-off between detail and operational feasibility (Section 1.2.3.2).

In scenarios involving mixed vegetation types or intricate landscape features, coarse-resolution sensors may fail to capture fine-scale heterogeneity, limiting the accuracy of ecological or land-use analyses. Conversely, high-resolution imagery excels in such contexts but demands significant computational resources. Selecting the appropriate spatial resolution depends on specific research objectives and the spatial scale of the phenomena under investigation, underscoring the necessity of aligning sensor capabilities with study requirements.

1.2.2.3 Temporal Resolutions

Another key characteristic of RS sensors is their temporal resolution, defined as the time interval between successive image acquisitions over the same study site. Temporal resolution is critical for monitoring dynamic environments, such as coastal ecosystems, where conditions can change rapidly due to tides, weather events, or human activity.

The temporal resolution of a satellite sensor may vary from hours to days, depending on whether the platform orbit is geostationary or sun-synchronous. Geostationary satellites provide continuous coverage over a fixed location, while sun-synchronous orbits follow sun illumination, allowing image acquisition at the same time of the day for a location. This consistency is particularly important for visible-infrared sensors, as it ensures usable images and maximizes the temporal resolution of the sensor by avoiding night-time acquisitions. On the other hand, airborne platforms exhibit more variable temporal resolutions, ranging from days to years, depending on mission planning. For example, the Sentinel-2 constellation, composed of two satellites, offers a temporal resolution of 5 days at the equator. This revisit time improves to approximately 3 days at higher latitudes, such as in France, due to the overlap in satellite paths. Such frequent revisits make Sentinel-2 an excellent choice for

applications requiring consistent monitoring, such as vegetation health assessments, sediment transport studies, or vegetation phenology estimations. Certain missions, like Sentinel-3, achieve even shorter revisit times. Equipped with sensors designed for ocean and land monitoring, Sentinel-3 provides near-daily coverage, making it particularly suited for applications that require high temporal frequency, such as tracking phytoplankton blooms, which can appear and disappear within a few days, or surface temperature variations. This capability is crucial for capturing fast-evolving phenomena and ensuring timely data delivery for decision-making.

Usually, temporal resolution is highly dependent on the spatial resolution of the sensor. Higher spatial resolution often corresponds to lower temporal resolution, although geostationary platforms and pointable sensors can be exceptions to this trend (Figure 1.10).

In contrast, some sensors are operated on-demand, with data acquisition triggered directly by the user. This is characteristic of drones and specialized satellite missions like Pleiades or the italiano Precursore IperSpectrale della Missione Applicativa (PRISMA). While these systems may lack consistent temporal archives for a given study site, they provide unmatched flexibility for high-resolution data collection. Such sensors are invaluable for addressing specific research objectives, including acquiring detailed imagery immediately after extreme weather events or capturing localized features with high spatial precision, complementing routine satellite-based monitoring programs.

1.2.2.4 A story of trade-off

RS involves inherent trade-offs between spatial, temporal and spectral resolutions, and coverage area, which influence the suitability of sensors for different applications (Figure 1.10). High spatial resolution sensors, capable of capturing fine-scale details, are essential for precise tasks like urban infrastructure mapping or site-specific ecological studies. In coastal environments, high-resolution sensors are invaluable for identifying small-scale features such as intertidal vegetation patterns, sediment deposition dynamics. However, these sensors typically have lower temporal resolution and smaller coverage areas, limiting their utility for monitoring dynamic or widespread phenomena, such as tracking algal bloom events across entire coastal regions.

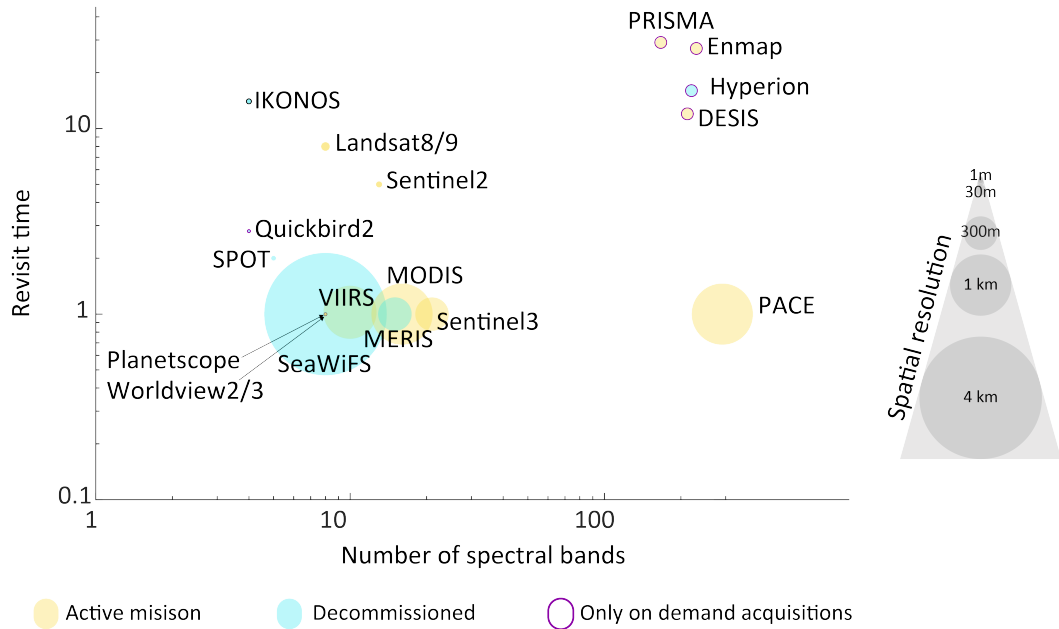


FIGURE 1.10: Intersection of spectral resolutions (x-axis), temporal resolutions (y-axis), and spatial resolutions (circle size) of the main satellite sensors used to observe coastal areas.

In contrast, sensors with coarser spatial resolution offer extensive coverage and higher revisit frequencies, making them ideal for tracking large-scale environmental changes. For coastal areas, these sensors can effectively monitor phenomena such as Sea Surface Temperature (SST) variability, coastal erosion trends, and seasonal changes in primary productivity over larger geographic extents. For example, instruments like MODIS or VIIRS are well-suited for observing ocean color and Chla concentrations, critical for understanding broader ecosystem health in coastal zones.

Intermediate-resolution sensors provide a compromise, offering sufficient spatial detail for regional studies while maintaining adequate temporal resolution for periodic monitoring. These are particularly useful for applications such as mapping coastal vegetation transitions, estuarine dynamics, and changes in sediment plumes from rivers into the ocean over time. Instruments like Sentinel-2 or Landsat provide this balance, making them key assets for monitoring coastal ecosystems at scales relevant to regional management.

The selection of an appropriate sensor depends on the specific requirements of the study, balancing the need for detail, frequency, and geographic extent. Coastal zone management, for instance, often benefits from using a combination of sensors to

capture both fine-scale spatial patterns and broader temporal trends, ensuring comprehensive monitoring of these dynamic environments.

While satellite acquisitions are essential for covering large areas, heterogeneous habitats often require finer spatial resolutions, positioning drones as the most suitable observation tool. Drone-based studies can also serve as proof-of-concept techniques to refine and develop methodologies later applicable to satellite data.

Although this work builds upon many of the concepts introduced in the previous sections, one critical RS technique warrants further discussion in this introduction. This technique, characterized by its adaptability and technical precision, provides essential insights and complements the methods already outlined. The next section will introduce drones, focusing on their application as a RS tool and detailing the associated techniques and data analysis methods.

1.2.3 About Drones

1.2.3.1 History

At the beginning of the 20th century, Julius Neubronner, a German apothecary, faced a logistical challenge in his professional practice. Neubronner regularly relied on carrier pigeons to deliver and retrieve small, urgent medical packages, such as medications or prescriptions, between his pharmacy and a sanatorium located several kilometers away. This method, though efficient for short distances, often left Neubronner curious about the exact routes taken by the pigeons and the environmental conditions they encountered during their flights. Motivated by both practical concerns and a spirit of innovation, Neubronner sought a way to monitor and document the journeys of his pigeons. He developed a lightweight, auto-triggering camera that could be strapped to the pigeons' chests (Figure 1.11 Top). The camera was designed to automatically take photographs at regular intervals during the birds' flights. It had two lenses and a pneumatic system; it was activated by inflating the left chamber. As the air slowly escaped from the capillary at the bottom, the piston moved back triggering the exposure. Neubronner ensured that the camera was light enough not to impede the pigeons' ability to fly (Simic Milas et al., 2018).

The resulting aerial photographs offered a novel perspective, capturing bird's-eye views of landscapes, towns, and natural features (Figure 1.11 Bottom). These images



FIGURE 1.11: One of Neubronner's pigeons (Top), around 1910 equipped with a camera. The bottom shows a picture taken during a pigeon's flight.

not only satisfied Neubronner's initial curiosity about the pigeons' routes but also demonstrated the broader potential of aerial photography for cartography, reconnaissance, and environmental observation. His innovative work garnered widespread attention, paving the way for further developments in RS and aerial imaging. Neubronner's experiments illustrated the practical applications of aerial imaging at a time when such perspectives were almost entirely unavailable, highlighting his contributions to science and art.

Julius Neubronner's early vision exemplifies how innovative thinking can overcome barriers in data collection. For many years, the practical limitations of RS technologies, particularly regarding spatial and temporal resolution or the high costs and delays in data acquisition, constrained their applicability in various fields. However, innovations like drones have significantly addressed these challenges. Much like Neubronner's pigeons, modern drones are not only accessible and affordable but also

offer users the freedom to determine when and where to deploy them, providing unparalleled control over spatial and temporal data collection. Neubronner's ingenuity in developing lightweight aerial cameras for pigeons paved the way for these advancements, demonstrating the enduring impact of pioneering solutions in expanding the potential applications of RS.

Modern drone history has its roots in military applications, where the need for unmanned surveillance and targeted operations drove the initial technological advancements. Early drone systems, such as the use of radio-controlled aircraft in World War II, laid the foundation for what would become an essential tool in both civilian and military contexts. The transition to civilian applications gained momentum in the late 20th century, particularly with the advent of lightweight materials, improved battery technologies, and advances in GPS and RS capabilities. Today, drones are integral to various industries, from precision agriculture and infrastructure inspection to environmental monitoring and emergency response. This evolution reflects the growing accessibility and versatility of drone technology, making it a transformative element in modern data acquisition and analysis.

1.2.3.2 General presentation

Drones, also known as Unmanned Aerial Vehicles (UAVs), are aircraft systems operated without a human pilot onboard. They are often embedded with GPS and can be remotely controlled or fly autonomously through software-controlled flight plans. These devices have become indispensable tools in modern RS, offering high accuracy, on-demand data acquisition, and access to previously unreachable locations. The growing use of drones in various fields, from environmental monitoring to urban planning, underscores their versatility and importance.

While drones are not inherently functional on their own, they become highly effective tools when integrated with various sensors. These include hyperspectral sensors (Suomalainen et al., 2021), multispectral sensors (Nurdin et al., 2023; Román et al., 2023), RGB cameras (Sweet et al., 2022), thermal cameras (Speth et al., 2022), LiDAR systems (Krček et al., 2020; Lee et al., 2023), as well as gas and chemical sensors.

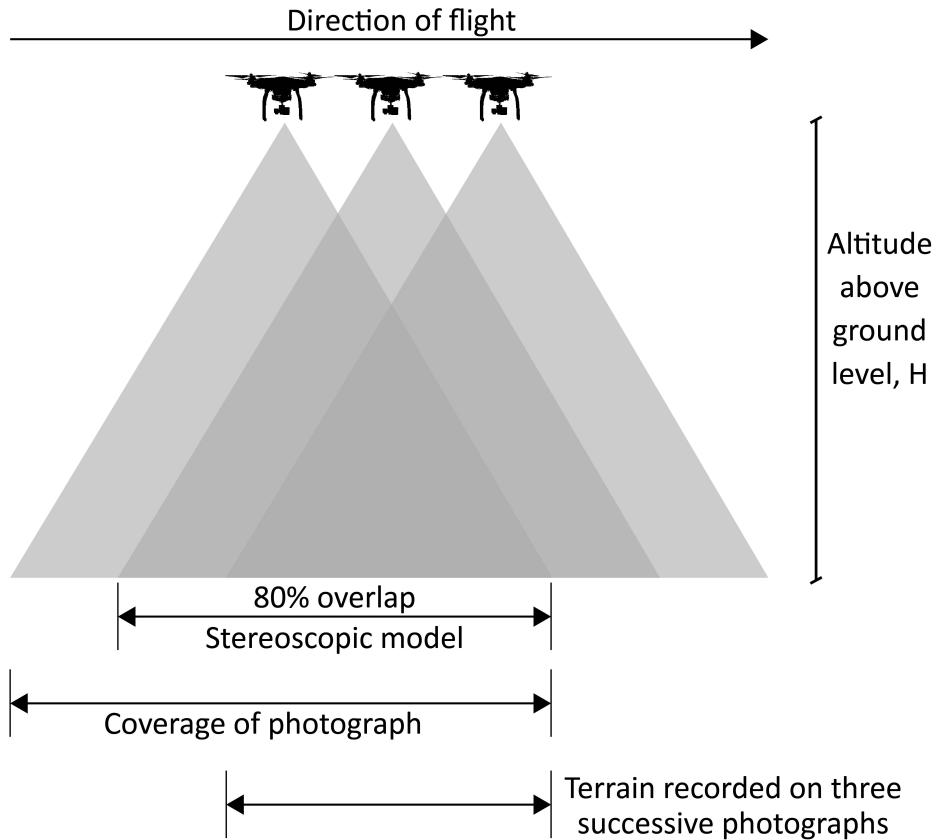


FIGURE 1.12: Schematic representation of image overlapping of a drone

1.2.3.3 Data acquisition

A key parameter in drone-based image acquisition is the overlap between images (Figure 1.12). This is categorized as front overlap (FO), which refers to the overlap between consecutive images along the same flight path, and side overlap (SO), which pertains to the overlap between images from adjacent flight paths. Ensuring sufficient overlap is essential for accurate reconstruction of orthomosaics through photogrammetric processes. Typically, 80% front overlap and 70% side overlap are considered optimal to achieve reliable results. The mathematical definitions of FO and SO are as follows:

$$FO = \left(1 - \frac{v \times \Delta t}{\frac{H \times h_{\text{sensor}}}{f}} \right) \times 100$$

$$SO = \left(1 - \frac{d_{\text{flight_line}}}{\frac{H \times w_{\text{sensor}}}{f}} \right) \times 100$$

Where:

- FO: Forward Overlap (in %)
- SO: Side Overlap (in %)
- v : Ground speed of the drone (m/s)
- Δt : Time interval between consecutive photos (s)
- H : Flight altitude above the ground (m)
- h_{sensor} : Sensor height in the flight direction (mm)
- w_{sensor} : Sensor width perpendicular to the flight direction (mm)
- f : Camera focal length (mm)
- $d_{\text{flight_line}}$: Distance between adjacent flight lines (m)

These equations show that for a given sensor (e.g., for known f , h_{sensor} , w_{sensor} , and Δt), the only parameters that can be adjusted to ensure sufficient overlap are the flight speed or the altitude of flights. If the user chooses to set H (directly linked to the spatial resolution of the final product), then v will be automatically fixed by the system. The higher the flight altitude, the higher the flight speed, or conversely, if the user chooses to set v (directly linked to the total time of the mission), then the altitude will be locked by the system, resulting in a higher v corresponding to a higher flight height.

The area that a drone can cover during a mission grows exponentially as the flight height increases. However, while the maximum flight height drones can technically reach is not inherently limited, it is strictly regulated by law. In Europe, for instance, the maximum permitted flight height is 120 m. This restriction can be a limiting factor for certain applications, particularly when the area to be covered exceeds several square kilometers. For instance, the largest intertidal seagrass meadow in France is located in the Bassin d’Arcachon and covers an area of nearly 40 km² (Cognat et al., 2018). Using a Micasense RedEdge-MX DUAL multispectral sensor mounted on a drone flying at 120 m altitude at 10 m.s⁻¹, this area would take approximately 44 hours of flight time to cover entirely. The total time required to map this entire area at low tide could be further extended when accounting for constraints such as daylight hours, tide cycles, battery recharging, potential weather-related delays, and the need

for the operator to frequently reposition themselves due to regulatory restrictions that limit the drone's distance to 1 km from the drone pilot.

1.2.3.4 Data processing

Satellite products produced by space agencies are often provided to users after extensive preprocessing steps, including orthorectification, precise georeferencing, radiometric calibration. Similarly, these preprocessing steps are crucial for utilizing drone-acquired data effectively. Nowadays, user-friendly software, such as Agisoft Metashape and Pix4D, enables users to perform these essential steps efficiently, making advanced data processing accessible even to non-expert users. Steps to obtain an orthoimage from a bunch of single images will be described now in more details.

1.2.3.4.1 Image pre-processing

The first step is to correct each individual image acquired by the drone from optical distortion that occurred during its acquisition (Figure 1.13). Photogrammetric software typically addresses lens distortion and vignetting through a combination of camera calibration and radiometric adjustments.

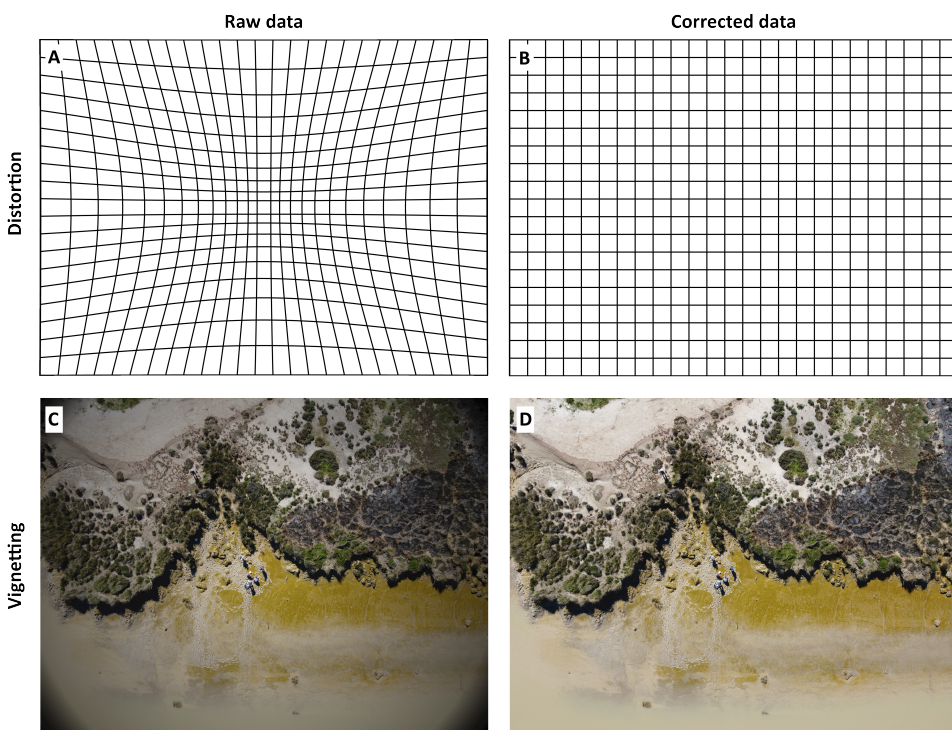


FIGURE 1.13: Schematic representation of image pre-processing for orthomosaic reconstruction, showing correction of the distortion (A & B) and correction of the vignetting (C & D).

During calibration, the software refines intrinsic parameters such as focal length, principal point offsets, and radial/tangential distortion coefficients (called k1, k2, k3, p1, p2) by matching features across overlapping images in a bundle adjustment process. Some camera manufacturers provide sensor-specific metadata, including correction factors, which can further enhance calibration accuracy. Vignetting, which manifests as reduced brightness near the image edges, is often corrected via additional vignetting coefficients or automated radiometric calibration routines that normalize illumination across photos. These corrections are essential for ensuring both geometric precision in the 3D reconstruction and radiometric consistency in the final orthomosaic.

1.2.3.4.2 Initial Image Alignment / Aerial Triangulation

Once corrected, each image can be aligned. During the initial image alignment phase, the photogrammetry software relies on Structure from Motion (SfM) algorithms to identify unique tie points in overlapping images and triangulate their 3D positions. These tie points are then matched across the dataset, and a bundle adjustment is performed to optimize camera parameters (position, orientation, and intrinsic calibration). Often referred to as aerial triangulation, this step produces a sparse point cloud that underpins all subsequent stages. Its accuracy is critical, as it defines the precision of the final 2D and 3D outputs.

1.2.3.4.3 Dense Point Cloud Generation

Building upon the camera geometry established by SfM, the software uses Multi-View Stereo (MVS) techniques to compute dense depth maps for each overlapping image pair. These depth maps are merged to create a dense point cloud containing millions—or even billions—of points, capturing high-resolution details of the scene’s geometry. Although computationally intensive, this phase lays the groundwork for generating accurate surface models and textured 3D representations later in the workflow.

1.2.3.4.4 Digital Surface Model (DSM) / Digital Terrain Model (DTM)

From the dense point cloud, a DSM is derived by capturing the highest elevation values within each pixel or grid cell, thereby representing above-ground features like buildings and vegetation. Alternatively, a DTM can be produced by classifying and removing non-ground points to approximate the bare-earth surface. Both models are

typically exported as raster files and used in various analytical applications, such as hydrological modeling, viewshed analysis, and volume calculations. Their accuracy depends on the quality of the dense cloud and effective point classification techniques. The difference between the DSM and the DTM is called a Digital Height Model (DHM, Figure 1.14).

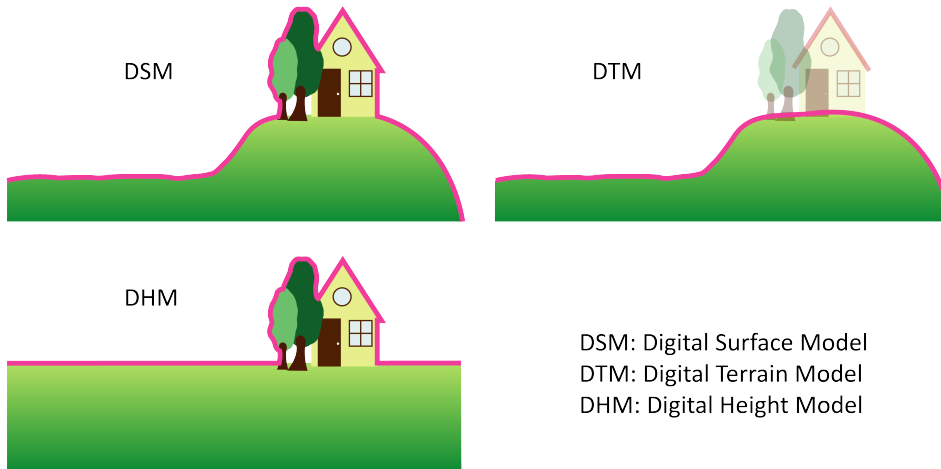


FIGURE 1.14: Representation of differences between the Digital Surface Model (DSM), the Digital Terrain model (DTM) and the Digital Height Model (DHM).

1.2.3.4.5 Orthorectification and Orthomosaic Creation

During orthorectification, the software projects each image onto the DSM or DTM to correct for camera tilt and terrain distortions, ensuring consistent spatial alignment. Afterwards, overlapping images are seamlessly blended—often balancing color and brightness variations—to form a georeferenced orthomosaic. This final 2D product is dimensionally accurate and vital for cartographic and analytic tasks, offering a reliable visual representation of the surveyed area.

1.2.3.4.6 Optional steps

Following the creation of a dense point cloud (Section 1.2.3.4.3), photogrammetric software can convert millions of data points into a continuous 3D surface known as a mesh. This process involves triangulating the points to form a polygonal framework that captures the shape and features of the surveyed scene. Once the mesh is generated, the software projects the original imagery onto the surface to create a photorealistic texture. This textured 3D model provides an immersive visualization, enabling more detailed analysis of structures, terrain, and other elements than would

be possible through a 2D map alone. During data acquisition, the drone's camera can be oriented at a 45° angle to capture detailed features of the target's vertical structure. This approach ensures that the texture of these features is detailed.

Another optional step, depending on the dataset, is the radiometric calibration of the data. However, this step becomes mandatory for multispectral and hyperspectral datasets, as it ensures the accuracy and usability of radiometric information by compensating for sensor-specific biases and environmental conditions during data acquisition.

The high-resolution maps generated through photogrammetry provide an essential basis for understanding spatial patterns and environmental features. However, to extract meaningful information from these datasets and address specific research or management questions, advanced analytical methods are required. The next section will focus on the machine learning techniques used to process and interpret these maps, transforming raw data into valuable insights for a range of applications.

1.2.4 Machine Learning

Machine learning, a subfield of artificial intelligence (AI), involves the creation of computer systems capable of executing tasks that traditionally require human cognition, such as reasoning, problem-solving, and decision-making (Sarker, 2021). It encompasses the simulation of human-like intelligence in machines, enabling them to identify patterns and make data-driven predictions. The field originated in the mid-20th century, rooted in pattern recognition and the formulation of adaptive algorithms that refine their operations through iterative learning. Early contributions by pioneers such as Alan Turing and Arthur Samuel established the conceptual and practical foundation of the discipline. Alan Turing's development of the Turing Machine in 1936 represents one of the earliest instances of computational models capable of executing algorithmic processes. The Turing Machine was designed as a theoretical construct to simulate the logic of any computer algorithm, utilizing a tape for memory and a set of rules for operations. While initially intended as a tool for exploring the limits of computation, the principles behind the Turing Machine laid the groundwork for modern machine learning and deep learning (Malekmohamadi Faradonbe et al., 2020). Turing's emphasis on computation and learning inspired

subsequent advancements in artificial intelligence, including the design of systems capable of adaptive and predictive behaviors. Notably, Samuel's development of a checkers-playing program in the 1950s demonstrated a machine's ability to improve its performance autonomously through learning processes.

At its core, machine learning involves the development of models—mathematical representations of data relationships—that can identify structures and trends within datasets. These models are trained on data using various techniques. Supervised learning is a method wherein models are trained on labeled datasets, with each input paired to a specific output. This framework enables the algorithm to establish explicit mappings between inputs and their corresponding outcomes. Applications include classification tasks, such as categorizing images or text, and regression, where the objective is to predict continuous variables like temperature or stock prices. The accuracy of supervised models depends significantly on the quality and quantity of labeled data available for training.

Unsupervised learning, on the other hand, functions without labeled data, enabling models to discern patterns or structures inherent in the dataset. It is often applied in clustering, where similar data points are grouped together, and in dimensionality reduction, which simplifies datasets by highlighting their most significant features. This approach is particularly valuable in domains where labeled data is scarce or costly to generate, offering a means to uncover underlying patterns and relationships within complex datasets.

A notable example of supervised machine learning is the Random Forest algorithm, developed by Leo Breiman in 2001 (Breiman, 2001). This learning technique constructs multiple decision trees during training by drawing random subsets of the training data with replacement (a process known as bagging) and selecting a random subset of features at each split. Each tree independently outputs a class prediction (in classification tasks) or a mean prediction (in regression tasks), and the Random Forest aggregates these predictions by majority voting or averaging. This approach enhances the robustness of the model by reducing variance and mitigating overfitting (Figure 1.15 X). Additionally, Random Forest provides a measure of feature importance, which can be leveraged to identify the most influential variables in a dataset. Random Forest is widely recognized for its robustness, ability to handle high-dimensional data, and resistance to overfitting, making it particularly effective

in domains such as remote sensing and bioinformatics. However, the algorithm has its limitations. Random Forest can be computationally intensive, especially with large datasets or a high number of trees, which may increase training time and resource requirements. Additionally, Random Forest can face challenges with highly imbalanced datasets, as it tends to favor the majority class unless specific measures, such as resampling techniques or adjusting class weights, are implemented to address the imbalance effectively. Ensuring a balanced dataset or applying these corrective strategies is crucial for improving the model's performance in such scenarios (Zhu, 2020). Furthermore, while Random Forest provides feature importance measures, these can sometimes be biased toward variables with more levels or higher variability, potentially misleading the interpretation of results. Finally, the model's ensemble nature makes it less interpretable compared to simpler models like individual decision trees.

Neural networks, an essential component of deep learning, are inspired by the structure and function of biological neural networks in the human brain (Abiodun et al., 2018). These computational models consist of interconnected nodes, or neurons, organized into layers that process and transform data through weighted connections. Originating in the mid-20th century with early work by researchers such as Warren McCulloch (McCulloch and Pitts, 1943) and Walter Pitts (Pitts, 1943), neural networks initially struggled with computational limitations and theoretical challenges. The development of backpropagation in the 1980s, a method for optimizing weights by minimizing error, marked a significant breakthrough (Werbos, 1974).

Neural networks are particularly novel due to their ability to model complex, non-linear relationships in data (Mienye et al., 2024). They operate through an input layer that receives data, one or more hidden layers that extract features and learn representations, and an output layer that delivers predictions or classifications (Werbos, 1974). Each connection between neurons forms the basis of neural computation, where neurons are the fundamental units inspired by biological nerve cells. In artificial neural networks, a neuron receives input signals, processes them using a mathematical function, and transmits the output to connected neurons. This process is governed by adjustable weights that determine the strength of connections, and an activation function introduces non-linearity, enabling the network to model complex relationships within data. The learning rate, a crucial hyperparameter, dictates how much the model adjusts its weights in response to the error during training. Choosing an

appropriate learning rate is essential; a rate that is too high may cause the model to converge erratically or not at all, while a rate that is too low results in slow training and potential stagnation in local minima.

The learning curve, which represents the model's performance over time, provides critical insights into training dynamics. A steep decline in training loss paired with a significant gap between training and validation loss often signals overfitting, where the model memorizes training data but fails to generalize to unseen data. Conversely, a flat learning curve with high training and validation losses indicates underfitting, where the model is too simplistic to capture underlying patterns. Addressing overfitting often involves techniques such as regularization, dropout, and early stopping, whereas underfitting may require enhancing model complexity, increasing data volume, or improving data quality. By carefully monitoring and tuning these aspects, neural networks can achieve robust performance across diverse applications.

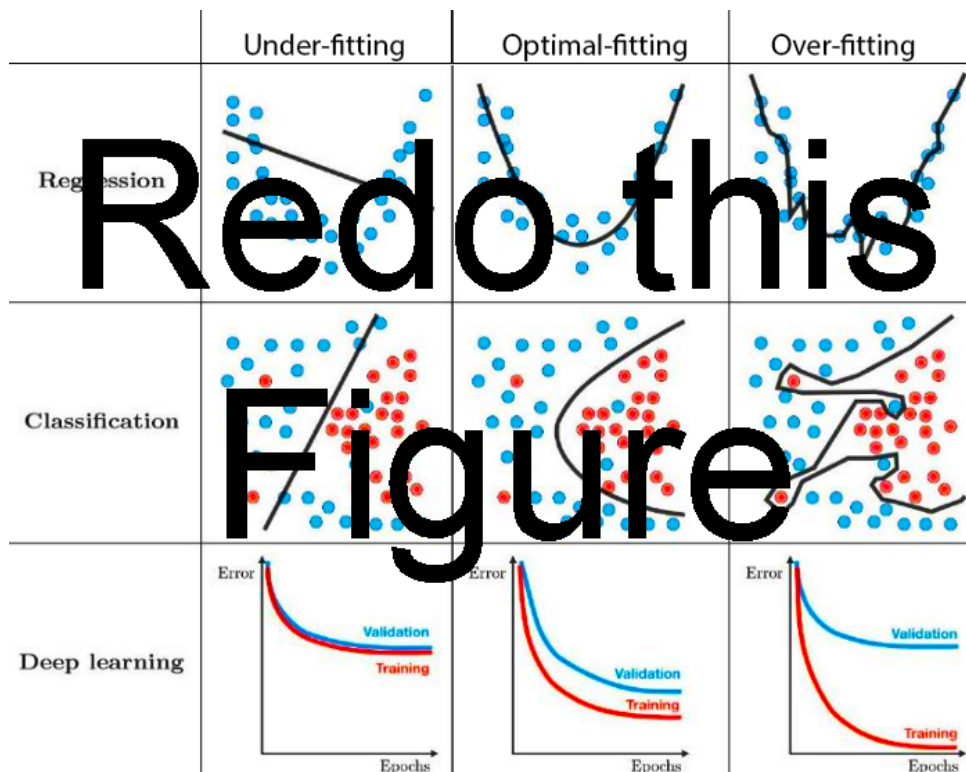


FIGURE 1.15: Redo this !!!!!

The primary advantage of neural networks lies in their versatility and performance across a wide range of tasks, from image recognition to natural language processing. They are capable of learning directly from raw data, reducing the need for extensive feature engineering. However, their application is not without limitations (Cheng

and Titterington, 1994; Kattenborn et al., 2021; Yuan et al., 2021). Neural networks are computationally intensive, requiring significant processing power and large datasets for effective training. They are also prone to overfitting, especially with small datasets, and their decision-making processes can be opaque, often referred to as the “black box” problem. Despite these challenges, advancements in architectures, such as convolutional and recurrent neural networks, and optimization techniques continue to expand their applicability and effectiveness across domains.

Over the decades, the field has undergone remarkable transformations, driven by increases in computational power, the availability of large datasets, and theoretical advancements. Initially, traditional machine learning methods, such as decision trees and support vector machines, dominated the landscape. However, the past two decades have seen the rise of deep learning, a subset of machine learning characterized by its use of neural networks with multiple layers. This paradigm shift has enabled significant breakthroughs, particularly in areas such as image recognition, natural language processing, and autonomous systems.

The utility of machine learning lies in its adaptability and scalability across disciplines. From enabling predictive analytics in healthcare to enhancing environmental monitoring through remote sensing, machine learning has become an indispensable tool for extracting actionable insights from complex datasets. This section provides a foundation for understanding how machine learning techniques are applied to convert data, such as those obtained through drone mapping, into informative and usable outputs.

1.2.5 Remote Sensing applied to Coastal monitoring

Coastal environments represent highly dynamic and sensitive ecosystems shaped by complex interactions between natural processes and human activities. RS technologies are crucial for monitoring these regions, providing detailed data on shoreline erosion, habitat degradation, sediment dynamics, and water quality. High-resolution satellite imagery and drone-based platforms facilitate the detection of fine-scale changes in intertidal zones, mangroves, coral reefs, and other critical coastal habitats. These observations enable quantification of spatial and temporal variations, informing evidence-based conservation and sustainable management strategies.

Essential Biodiversity Variables (EBVs) and Essential Ocean Variables (EOVs) constitute a framework for systematically monitoring and understanding ecological and oceanographic changes. Based on the model of Essential Climate Variables (ECVs), EBVs provide a standardized set of biodiversity metrics to detect and analyze changes across spatial and temporal scales (Bojinski et al., 2014; Miloslavich et al., 2018; Pereira et al., 2013). These variables act as an interface between raw ecological data and the biodiversity indicators required for global reporting and policy-making. Similarly, EOVs focus on the biological and ecological characteristics of marine systems, emphasizing metrics such as plankton diversity and biomass, fish populations, and the spatial extent of habitats like coral reefs and seagrass meadows. By standardizing biodiversity and oceanic assessments, EBVs and EOVs enhance consistency and comparability across studies and regions (Muller-Karger et al., 2018, Figure 1.16).

These frameworks address the need for scalable and harmonized observations, aligning with international directives like the Water Framework Directive (WFD, 2000/60/EC) and the Marine Strategy Framework Directive (MSFD), which use habitat diversity as an indicator of aquatic health (Borja et al., 2013; E. Papathanasopoulou et al., 2019; Zoffoli et al., 2021). Beyond enabling environmental monitoring, EBVs and EOVs provide a foundation for conservation strategies by addressing knowledge gaps and promoting coordinated action among stakeholders. However, evaluating the ecological status of a large number of water bodies using exclusively field observations turned out to be extremely challenging, and the status of many sites has still not been assessed (Oiry and Barillé, 2021; E. Papathanasopoulou et al., 2019)

Developments in RS have further improved the applicability of EBVs and EOVs (Pereira et al., 2013; Skidmore et al., 2015). Drone and satellite technologies enable large-scale, frequent observations of biodiversity and marine parameters, facilitating the detection of environmental changes. These technologies support tracking habitat extent, species distribution, and functional traits, incorporating these frameworks into conservation policies. The integration of EBVs and EOVs with RS tools advances ecological monitoring and decision-making at local, regional and global scales. However, past and current satellite missions lack optimal technical specifications (spatial, spectral, and temporal resolution) for full operational capability (Muller-Karger et al., 2018). For some habitats, multispectral resolution may be adequate under certain conditions (Zoffoli et al., 2020), although risks of classification errors remain. For

| | | Intertidal benthic communities in sediment shores (beaches, estuaries, mudflats) | | |
|-----------------------|------------------------------|--|------------|-------------------|
| EVB class | EVB | Seagrass | Macroalgae | Microphytobenthos |
| Genetic composition | Population genetic diversity | | | |
| Species population | Distribution | | | |
| | Abundance | | | |
| | Size/Vertical distribution | | | |
| Species traits | Pigments | | | |
| | Phenology | | | |
| Community composition | Taxonomic diversity | | | |
| Ecosystem structure | Functional type | | | |
| | Fragmentation heterogeneity | | | |
| Ecosystem function | Primary production | | | |

FIGURE 1.16: Current capabilities of remotely sensed data for measuring Essential Biodiversity Variables (EBVs; Pereira et al. (2013)) for soft-bottom intertidal vegetation. Adapted from Muller-Karger et al. (2018).

others, higher spectral resolution is necessary to distinguish taxonomically distinct groups of organisms (Fyfe, 2003; Launeau et al., 2018; Méléder et al., 2018). Identification relies partly on the presence of visible absorption bands associated with photosynthetic and accessory pigments, which can be detected and quantified using high-performance liquid chromatography (Bargain et al., 2013; Jesus et al., 2014; Méléder et al., 2005, 2003a).

1.3 Objectives and Overview

Intertidal habitats are particularly complex to map accurately due to their dynamic nature, influenced by tidal cycles, sediment deposition, and erosion processes. The presence of multiple vegetation types interspersed across these habitats further complicates mapping efforts. Several of these vegetation types share similar pigment compositions, including Chla, Chlorophyll-b (Chlb), and accessory carotenoids. This similarity results in spectral signatures that are nearly indistinguishable, complicating their differentiation through remote sensing.

Hyperspectral sensors can detect subtle variations in spectral signatures that are

unique to individual vegetation types. These sensors operate by capturing reflectance data across a broad range of wavelengths, enabling the identification of minor differences in spectral patterns. However, multispectral sensors, which record data across fewer and broader wavelength bands, face considerable challenges in distinguishing vegetation types with overlapping spectral features.

Intertidal areas often consist of closely interspersed vegetation types that create mixed spectral signals, a phenomenon known as spectral mixing. This spectral blending occurs when the sensor records reflectance from multiple vegetation types within a single pixel, causing the resulting signature to represent a composite rather than distinct categories. The problem of spectral mixing is further exacerbated as the spatial resolution of the sensor decreases. For instance, Sentinel-2 sensors, with a spatial resolution of 10 meters, are effective only in scenarios where tidal flats are vegetated by a single dominant species. In mixed habitats, this resolution is insufficient to capture smaller patches of vegetation types, which often play a crucial role in biodiversity and ecosystem dynamics.

This limitation has practical implications for the use of remote sensing data in intertidal mapping. The inability to accurately classify vegetation types in mixed habitats reduces the overall effectiveness of such data for ecological monitoring and conservation planning. Smaller vegetation patches, despite their ecological importance, may go undetected, leading to incomplete assessments of habitat distribution and species diversity. These gaps in data can hinder efforts to understand critical ecological interactions, such as nutrient cycling and habitat connectivity, which are often mediated by the spatial distribution of intertidal vegetation. Addressing these challenges requires not only advancements in sensor technology but also the integration of sophisticated classification algorithms capable of disentangling mixed spectral signals.

The application of advanced machine-learning techniques offers a means to enhance the mapping accuracy of sensors with low spatial and/or spectral resolution. These techniques leverage computational algorithms that can identify complex patterns in the data, enabling the differentiation of vegetation types even in challenging spectral conditions. By training these models on sufficiently large and diverse datasets, which include examples from various geographic regions and environmental conditions, they adapt to a wide range of scenarios. This adaptability allows for the creation of robust predictive models capable of handling mixed spectral signals that result from

the overlapping vegetation types commonly found in intertidal zones. Furthermore, these algorithms incorporate feature selection and optimization processes to identify the most informative spectral bands, thereby improving classification accuracy. They have demonstrated their utility in generating habitat maps over extensive areas, offering a scalable solution for ecological monitoring.

The principal objective of this work is to demonstrate the effectiveness of remote sensing for mapping intertidal habitats and the environmental pressures they face by developing advanced methodologies for accurate vegetation classification and ecosystem monitoring.

This goal will be reached through specific objectives proposed as follow:

- analysing the potential of multispectral spectral sensors for the discrimination of macrophytes from low tide soft-bottom intertidal areas.
- Building an algorithm that discriminates the most common taxonomic classes of vegetation found on soft bottom intertidal sediment.
- Investigate the capacity of remote sensing to monitor intertidal vegetation under abiotic and biotic pressures.

Chapter 2 establishes the foundation by analyzing a spectral library to assess the feasibility of distinguishing different types of vegetation using RS. It demonstrated that all taxonomic classes could be discriminated, in particular green macroalgae from seagrasses. By employing multi- and hyperspectral datasets, the study identifies the number of spectral bands and specific wavelengths that maximize classification accuracy, showcasing the potential of remote sensing for detailed habitat mapping.

Building upon this result, **Chapter 3** focuses on developing a robust algorithm called DISCOV v1.0, capable of automating the discrimination of green macrophytes in heterogeneous intertidal habitats. Utilizing high-resolution multispectral drone imagery and advanced machine-learning techniques, this chapter addresses the spatial complexity of these environments. The algorithm's validation across diverse geographic and ecological settings ensures its applicability beyond the initial study sites. This advancement underscores the critical role of cutting-edge RS technologies in ecological monitoring.

In **Chapter 4**, the methodology evolves to include red macroalgae, specifically targeting the invasive species *Gracilaria vermiculophylla*. By updating the algorithm in its v2.0, this study extends its application to a different taxonomic group, demonstrating the flexibility and scalability of the approach. Additionally, this chapter integrates LiDAR-based topographical data to examine the relationship between habitat characteristics and macroalgal distribution. The insights gained from mapping and modeling the spatial dynamics of *G. vermiculophylla* provide valuable implications for managing invasive species and conserving native biodiversity.

Chapter 5 examines the physiological impacts of environmental stressors, specifically marine and atmospheric heatwaves, on seagrass reflectance. Through controlled laboratory experiments and field validations, this chapter highlights the spectral responses of *Zostera noltei* under heatwave conditions. Well-established spectral indices such as the NDVI and GLI are employed, and a new index, the Seagrass Heat Shock Index (SHSI), is developed to specifically identify heatwave-impacted seagrasses. These indices provide metrics to detect and quantify stress-induced changes. These findings emphasize the role of RS in assessing the resilience and vulnerability of intertidal ecosystems under climate change.

Finally, the **General conclusions and future perspectives** section will close the work, discussing the broader implication of this work and suggesting future directions for research and application. This section will synthesize the key findings from each chapter, highlighting how the advancements in RS methodologies contribute to improved habitat monitoring and management of intertidal ecosystems. It will also emphasize the potential for adapting these approaches to other coastal and marine environments, supporting biodiversity conservation and ecosystem resilience in the face of global environmental changes. Future perspectives will explore opportunities to enhance further RS techniques, such as integrating additional data sources like satellite imagery, and advanced field validation methods. Additionally, potential applications for policy-making, ecosystem restoration, and long-term environmental monitoring will be discussed, emphasizing the critical role of technology in addressing ecological challenges and guiding sustainable coastal management practices.

2

Multispectral and hyperspectral classification of intertidal vegetation using a spectral library for coastal biodiversity remote sensing

2.1 Introduction

Soft-bottom intertidal ecosystems support a diversity of habitats (seagrass meadows, honeycomb worm reefs, oyster reefs, mudflats) and biological communities worldwide (Mouritsen and Poulin, 2002; Murray et al., 2019; Van Der Maarel, 2003). The richness and diversity these habitats contain help to provide numerous ecosystem services, such as protection against coastal erosion, carbon regulation, oxygen production, seasonal habitat for migratory birds (Zoffoli et al., 2023), and reserves and nurseries for fisheries (Gardner and Finlayson, 2018). However, the significant roles of intertidal areas for biodiversity and the ecosystem services they provide are not universally known (Reddin et al., 2022; Unsworth et al., 2022, 2019b, 2019a). Like the majority of coastal ecosystems worldwide, intertidal areas are exposed and vulnerable to anthropogenic pressures, particularly more so due to their closer proximity to potentially destructive human activity (Green et al., 2021; Murray et al., 2019). Global warming, sea-level rise and the rising frequency of extreme climatic events lead to a reduction of their surface (Masson-Delmotte et al., 2021), and to a diminution of their capability to recover from perturbations (Schiel et al., 2021). The effects of climate change impact intertidal habitats inconsistently; declines of certain species and the proliferation of others (Bryndum-Buchholz et al., 2019). Intertidal areas are also directly degraded by human activities, such as coastal urbanization (Momota and Hosokawa, 2021), use of various biochemical contaminants (Durou et al., 2007; Hope et al., 2021), eutrophication (Cardoso et al., 2004), land reclamation (Sedano et al., 2021), and shellfish farming (Garmendia et al., 2021). These pressures impact intertidal biodiversity (Beltrand et al., 2022) and the ecosystem services it provides (Brondízio et al., 2019; Gardner and Finlayson, 2018).

To reduce these impacts and improve the protection of intertidal areas, several measures have been implemented over the past decades in Europe, such as the WFD (Parliament and Council, 2001), and the Marine Strategy Framework Directive MSFD (Parliament and Council, 2008). However, according to the Intergovernmental Science-Policy Platform on Biodiversity and Ecosystem Services (IPBES, Brondízio et al., 2019), current efforts are insufficient to reach the objectives of ecosystem conservation and sustainable exploitation. The ecological status of many intertidal areas have never been evaluated, with many areas uncharacterised. Even in documented areas, there are many socio-environmental challenges to implementing

efficient protection and sustainable exploitation (Unsworth et al., 2019b). Providing updated and accurate maps of intertidal areas is a prerequisite to addressing such challenges (McKenzie et al., 2020). However, the traditional methods for mapping rely on field surveys to estimate species abundance, biomass and habitat surface, which are time-consuming and labor-intensive (Nijland et al., 2019; Olmedo-Masat et al., 2020). The collected data are also limited by sampling constraints, as many intertidal areas are difficult to access. Remote sensing can overcome these issues by acquiring temporally and spatially resolved observations of coastal areas (Eleni Papathanasopoulou et al., 2019; Veettil et al., 2020). Likewise, the use of drones can increase the surveyed area compared to traditional survey methods while providing greater spatial resolution and flexibility than satellite imagery (Gomes et al., 2018).

Marine vegetation, defined as any species of plant that, at any time in its life, must inhabit water, other than freshwater, includes a wide range of highly important intertidal species, such as seagrasses, mangroves and marine algae. In the visible and near-infrared range (VNIR), exposed intertidal vegetation can be identified by its spectral reflectance (Douay et al., 2022; Olmedo-Masat et al., 2020). Solar irradiance is absorbed by plant pigments in the visible spectral range (400 to 700 nm: Hallik et al., 2017), while in the NIR range (700 to 900 nm), light is reflected by tissues in pluricellular organisms (Ustin and Jacquemoud, 2020), and by the sediment background for biofilms composed of unicellular photoautotrophs (Barillé et al., 2011). The spectral signature or lack thereof can be used as a marker of the different classes of organisms (Thorhaug et al., 2007). Reflectance is increasingly being used to measure EBVs in coastal ecosystems, such as species traits or ecosystem structure and function (Muller-Karger et al., 2018; Pereira et al., 2013). Time-series derived from satellite observations also make it possible to study changes in biodiversity metrics and environmental drivers over decades, as demonstrated recently for the monitoring of seagrass status (Lizcano-Sandoval et al., 2022; Zoffoli et al., 2021), or macroalgae invasions (Hu et al., 2017; Santos et al., 2020). Most satellite sensors are multispectral (Joyce et al., 2009; Xue and Su, 2017), and generally measure the reflectance using three to ten spectral bands in the VNIR spectral domain. Depending on the band numbers and characteristics, the discrimination of different types of marine vegetation can be limited (Casal et al., 2013; Kutser et al., 2006). Hyperspectral missions such as PRISMA, or EnMAP acquiring data along a large number of narrow spectral bands could improve habitat identification accuracy (Hestir et al., 2015; Ustin et al.,

2004). However, these sensors often provide relatively low spatial and temporal resolutions (Veettil et al., 2020), can contain high levels of noise per spectral band, and are not openly available resources (e.g. PRISMA imagery: 30 m pixel size, 29 day orbit repeat cycle and are only available on prior request or EnMAP imagery: 30 m pixel size and a 27 day orbit repeat cycle).

Mapping intertidal habitats of ecological importance, such as seagrass beds, can be achieved with a multispectral resolution in the case of exposed monospecific meadows observed during low tide (Zoffoli et al., 2023, 2020). However, when seagrass are mixed with other green vegetation, discrimination with multi- or even hyperspectral sensors (*in situ* and satellite) is challenging (Phinn et al., 2018; Veettil et al., 2020). Green macroalgae and more specifically the taxonomic class of Ulvophyceae share the same pigmentary composition with seagrass and should be *a priori* more complex to discriminate (Oiry and Barillé, 2021). Other taxonomic classes common in intertidal soft-bottom environments such as Xanthophyceae and Bacillariophyceae could also be confused with seagrass when present at low cover (Zoffoli et al., 2020). It is generally agreed that the identification at broad taxonomic levels (eg. class level) is more precise than at the species level (Casal et al., 2013; Kutser et al., 2006). Assessing the ability of a sensor to discriminate seagrass meadows from other intertidal vegetation can be explored with spectral libraries. They have been used to study the spectral discrimination between macroalgal species (Casal et al., 2013; Chao Rodríguez et al., 2017; Dierssen et al., 2015; Douay et al., 2022; Mcilwaine et al., 2019; Olmedo-Masat et al., 2020), and to identify different seagrass species (Fyfe, 2003) or to differentiate seagrass from other nearshore vegetation types (Légaré et al., 2022). By applying to *in situ* spectra collected with a spectroradiometer the spectral responses function of multi- and hyperspectral sensors, it is possible to investigate their abilities to classify intertidal green macrophytes. In particular, the possibility to discriminate seagrass from green macroalgae at a multispectral resolution remains to be studied using machine learning (ML) approaches.

This study aimed at analysing the potential of multi- and hyperspectral satellite missions (Pleiades, Sentinel-2, and PRISMA), as well as a multispectral drone sensor, for the discrimination of green macrophytes from low tide soft-bottom intertidal areas when exposed using RS. A spectral library of the spectral signatures of seagrass, green macroalgae, and other intertidal vegetation was compiled from measurements

performed with a field spectroradiometer. This library represents a novel taxonomic and spatial coverage with spectra from a wide array of exposed soft-bottom intertidal habitats collected across almost 15 degrees of latitude. High-resolution spectra were degraded to each sensor spectral resolution. A combination of multivariate and ML algorithms was then performed to compare the ability of the different spectral resolution data at distinguishing the main taxonomic classes of intertidal vegetation. The wavelengths which best discriminated green macrophytes were identified and recommendations given on potential future satellite sensors.

2.2 Materials and Methods

2.2.1 Spectral Reflectance Acquisition

Spectral reflectance data were collected from a range of macroalgal, microphytobenthic and seagrass dominated soft-bottom intertidal areas. Samples were grouped at the class level: Magnoliopsida (Seagrasses), Ulvophyceae (Green Macroalgae), Phaeophyceae (Brown Macroalgae), Xanthophyceae (Yellow Algae) and Bacillariophyceae (Diatoms: Table 2.1 & Figure 2.1). Brown macroalgae growing on rocky substrates were added as they are often found stranded in the intertidal zone. Spectral reflectance were also recorded from sediment areas without clear vegetation, hereafter referred to as “bare sediment” for the sake of simplicity. Scientific names and taxonomy were based on the World Register of Marine Species (WORMS). Species were identified *in situ* when recently exposed but not covered by a layer of water.

Multiple field campaigns taking place from 2 hours prior to 2 hours post minimum tide were carried out across temperate intertidal areas along the Western Atlantic coastline during the summer months (Figure 2.2). The campaigns took place in France in Bourgneuf Bay (Barillé et al., 2011, 2010; Zoffoli et al., 2020), Marennes-Oléron Bay, Auray Estuary, Mont-Saint-Michel Bay, Morbihan Gulf and Traict of Merquel, in Spain in Bolonia Beach (Roca et al., 2022) and Bay of Cadiz (Zoffoli et al., 2020), and in Portugal in the Tagus Estuary and Aveiro Lagoon.

TABLE 2.1: Presence and absence of red macroalgae for each drone flight

| Class | Species | Number of Spectra | Site | Reference |
|--------------------------|------------------------------|-------------------|---|-------------------------------------|
| Magnoliopsida | | | | |
| | <i>Zostera noltei</i> | 58 | Bourgneuf Bay, Marennes-Oléron Bay, Cadiz Bay, Tagus Estuary, Aveiro Lagoon and Traict of Merquel | Zoffoli et al., 2020 and this study |
| | <i>Zostera marina</i> | 23 | Bourgneuf Bay | This study |
| Ulvophyceae | | | | |
| | <i>Ulva sp.</i> | 16 | Bourgneuf Bay, Auray Estuary, MSM, Tagus Estuary, Aveiro Lagoon and Traict of Merquel | Barillé et al., 2010 and this study |
| | <i>Ulva ramosa</i> | 3 | Bourgneuf Bay | This study |
| | <i>Ulva linza</i> | 33 | Traict of Merquel | This study |
| | <i>Chaetomorpha sp.</i> | 21 | Morbihan Gulf | This study |
| | <i>Cladophora sp.</i> | 11 | Morbihan Gulf | This study |
| | <i>Ulva lactuca</i> | 34 | Morbihan Gulf | This study |
| | <i>Codium fragile</i> | 3 | Morbihan Gulf | This study |
| Xanthophyceae | | | | |
| | <i>Vaucheria sp.</i> | 33 | Bourgneuf Bay | This study |
| Phaeophyceae | | | | |
| | <i>Fucus vesiculosus</i> | 27 | MSM, Bourgneuf Bay, Morbihan Gulf, Tagus Estuary and Aveiro Lagoon | This study |
| | <i>Fucus serratus</i> | 6 | MSM | This study |
| | <i>Fucus spiralis</i> | 13 | Morbihan Gulf | This study |
| | <i>Ascophyllum nodosum</i> | 13 | MSM, Auray Estuary, Morbihan Gulf | This study |
| | <i>Rugulopteryx okamurae</i> | 5 | Bolonia Beach | Roca et al., 2022 |
| Bacillariophyceae | | | | |
| | <i>Navicula ramosissima</i> | 10 | Bourgneuf Bay | Barillé et al., 2011 |
| | <i>Entomeis paludosa</i> | 21 | Bourgneuf Bay | Barillé et al., 2011 |
| | <i>Gyrosigma limosum</i> | 2 | Bourgneuf Bay | Barillé et al., 2011 |

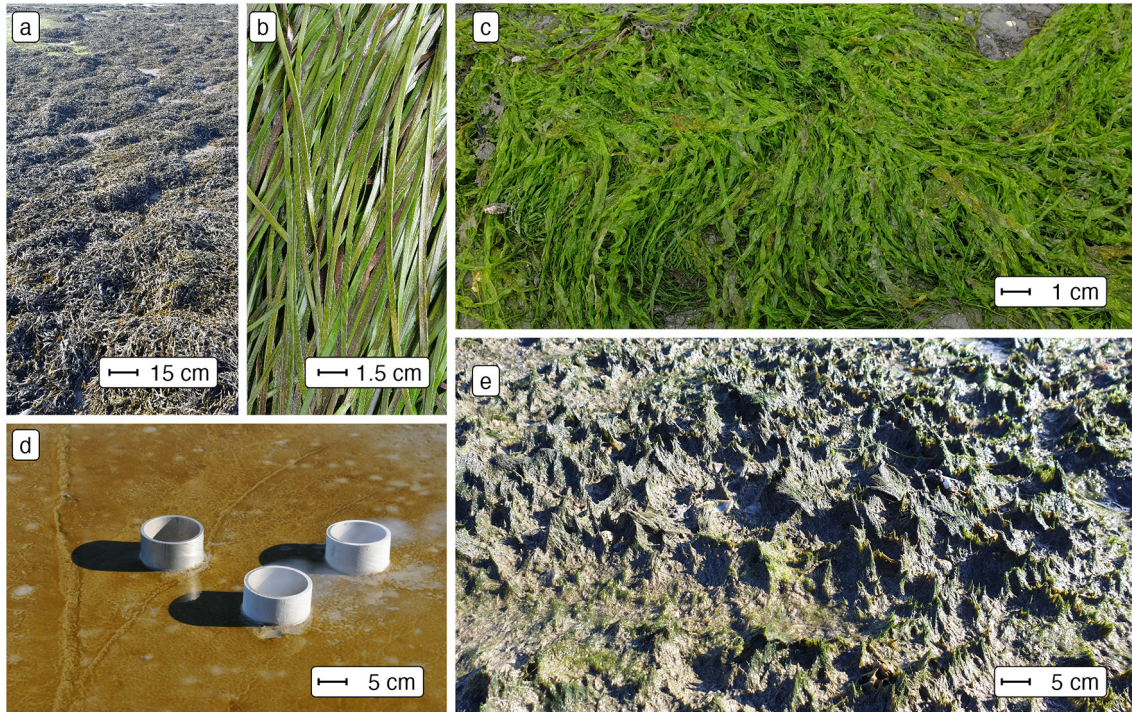


FIGURE 2.1: Examples of taxonomic classes of soft-bottom intertidal vegetation in the field (a: Phaeophyceae (*Fucus vesiculosus*), b: Magnoliopsida (*Zostera noltei*), c: Ulvophyceae (*Ulva linza*), d: Bacillariophyceae (Diatoms) and e: Xanthophyceae (*Vaucheria* spp.)). Scale bars show approximate scale.

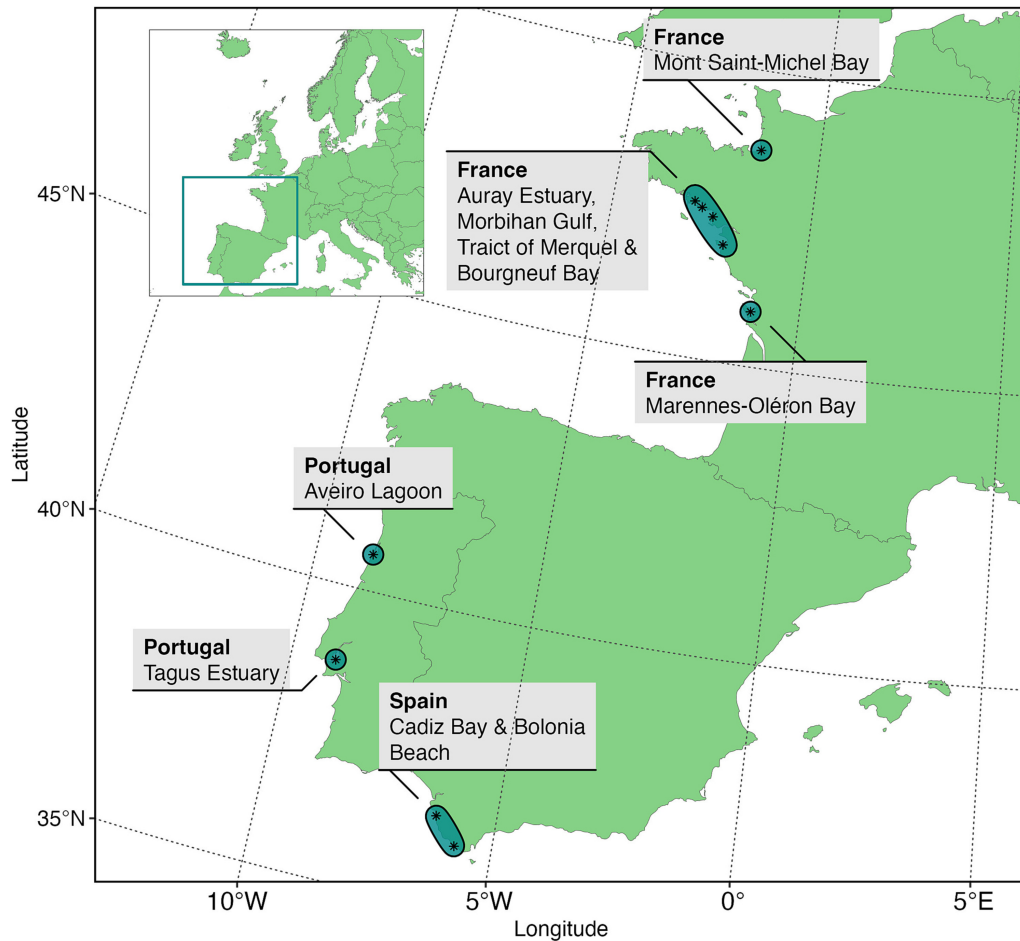


FIGURE 2.2: Sample collection sites across Europe.

2.2.2 Data Analysis

2.2.2.1 Spectral Degradation

The efficacy, efficiency and ability of classifying intertidal soft-bottom vegetation were assessed for a variety of remote-sensing sensors, including two multispectral satellite sensors (the high-resolution imager (HiRI) onboard Pleiades and the multi-spectral instrument (MSI) onboard Sentinel-2), one hyperspectral satellite sensor (the hyperspectral camera (HYC) onboard PRISMA satellite) and one airborne multispectral sensor (MicaSense RedEdge MX-dual Sensor on board a DJI Matrice 200 drone). These sensors cover a gradient of spectral resolution from multispectral to hyperspectral (Figure 2.3). The spectral response functions of Pleiades and Sentinel-2 were used to degrade the hyperspectral library to the respective resolution of each sensor. The highest spatial resolution of Sentinel-2 (10 m) consists of 4 spectral bands while the 20 m sensor has 4 additional bands in the VNIR spectral range (total 8 bands).

Sentinel-2 spectral bands, such as at 443 nm, were not used because its spatial resolution (60 m) is too coarse for intertidal seagrass mapping (Zoffoli et al., 2020). To degrade the ASD library to the PRISMA spectral resolution, only central wavelengths and bandwidths (from 400 to 900 nm) were obtained from the Agenzia Spaziale Italiana (ASI, n.d.). Likewise, central wavelengths with bandwidths were available for the Micasense (“Drone” henceforth). Therefore, the mean of the reflectance values included in the bandwidth of each PRISMA and Drone function band were computed. Across all sensors, a moving average was applied to the ASD spectral library with a 5 nm smoothing window to reduce instrument-induced noise in the data.

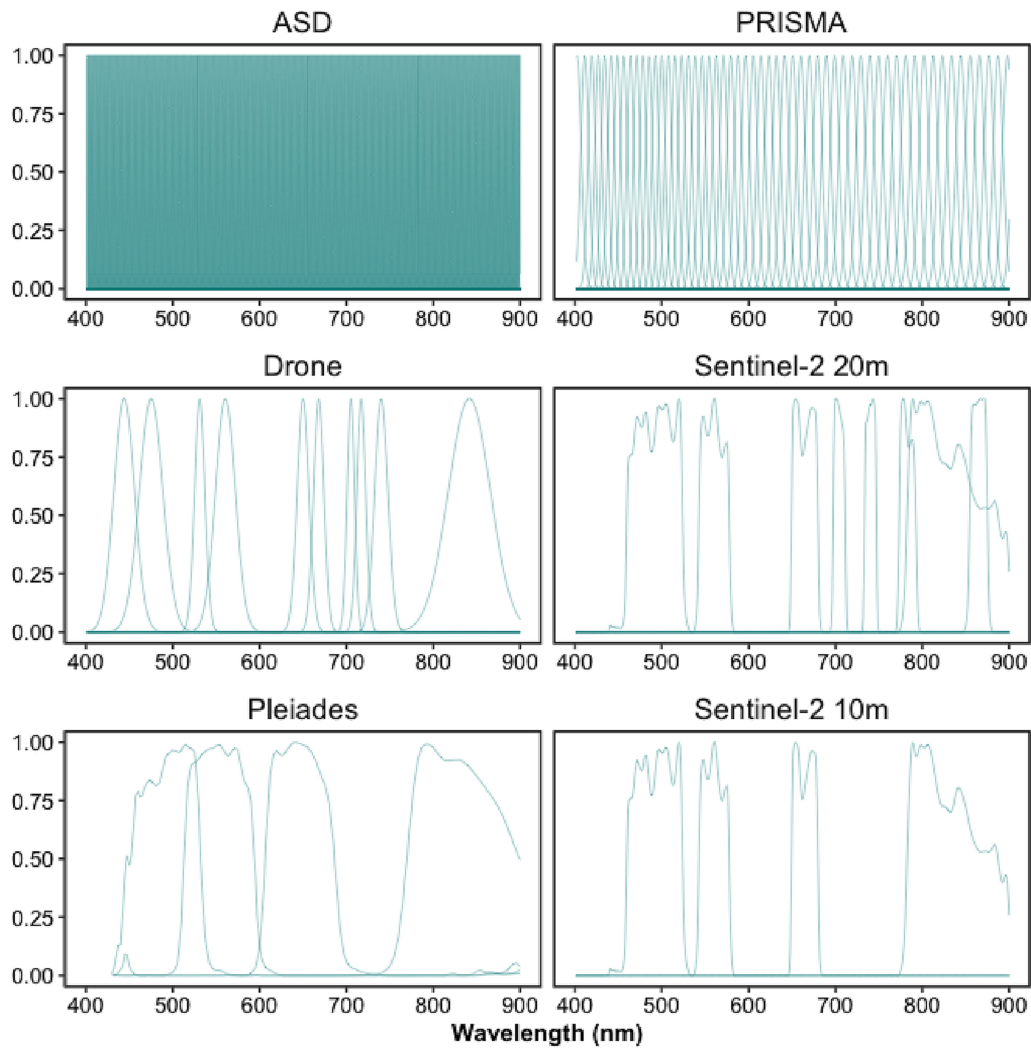


FIGURE 2.3: Spectral response functions for different hyper- and multi-spectral sensors (ASD, Pleiades, Sentinel-2 (10 m), Sentinel-2 (20 m), Drone, and PRISMA).

2.2.2.2 Standardisation

All spectra were standardised to reduce the effect of variable biomass, density or thickness of sample, with a Min-Max transformation (Cao et al., 2017). This calculation emphasised the spectral shapes in the visible range associated with the pigment composition (Douay et al., 2022):

$$R_i^*(\lambda) = \frac{R_i(\lambda) - \min(R_i)}{\max(R_i) - \min(R_i)} \quad (2.1)$$

where $R_i(\lambda)$ is the reflectance at a specific wavelength (λ) for a specific spectrum (i), where $\min(R_i)$ and $\max(R_i)$ are the corresponding minimum and maximum values.

2.2.2.3 Statistical Analysis

To visually assess the differences between classes across different spectral resolutions dissimilarity matrices were computed for all vegetative classes, with the cosine distance to compute a Spectral Angle Mapper (SAM). The SAM algorithm considers that each spectrum is a vector in n -dimensions space, n being the number of bands, and measures the angle between two spectra to determine their dissimilarity (Kruse et al., 1993). The difference between classes were visualised and statistically assessed with non-metric Multi-Dimensional Scaling (nMDS) ordination and Analysis of Similarity (ANOSIM) from the ‘vegan’ package within the programming language R (Oksanen et al., 2024). ANOSIM was carried out on the SAM distance matrix using 999 permutations.

To assess the ability of different sensors at classifying intertidal vegetative and non vegetative classes (bare sediments, Bacillariophyceae, Magnoliopsida, Phaeophyceae, Ulvophyceae & Xanthophyceae) from their spectral reflectance data, supervised Machine Learning (ML) algorithms were applied from the “tidymodels” ecosystem of packages within the programming language R (Kuhn and Wickham, 2020; R Core Team, 2023). Multiple models were developed (Random Forest, XGBoost and Multi-nomial Classifiers) with relatively similar results. The model described here was an ensemble decision tree classification approach; Random Forest from the “ranger” package (Wright and Ziegler, 2017). As Random Forest employs randomisation of trees, 20 repetitions of the analysis were carried out to avoid over or under representation of specific samples. Spectral data were split into training and testing sets

using a proportion of 0.75 to 0.25 using the response variable to stratify samples and reduce group imbalance. Training data were then further split into 30 training and validation datasets using bootstrap resamples to allow hyper-parameter tuning from the “rsample” package (Frick et al., 2024). Class was modelled as a function of all available features (standardised reflectance of each wavelength), where all features displaying zero variance across all classes were removed before model tuning as zero variance values would provide no additional information for the models. This meant only the first three bands of Pleiades and Sentinel-2 at 10 m were evaluated as their highest bands in the NIR showed no variance. Models were tuned to maximise the Area Under the Curve of the Receiver Operating Characteristic (ROC), which measures the diagnostic ability of a classifier based on the ratio of false positive and true positive rate. Accuracy, Cohen’s kappa (an accuracy measure that takes into account class size discrepancy), sensitivity and specificity were calculated using the ‘yardstick’ package, while the ‘vip’ package was used to calculate variable importance (Greenwell and Boehmke, 2020; Kuhn et al., 2024). Variable importance will show the relative importance of different wavelengths and was calculated by the prediction error, using permuted out-of-bag data and comparing differences to the prediction error of permuted predictor variables.

2.3 Results

2.3.1 Spectral Signatures at Different Spectral Resolutions

At hyperspectral resolution (ASD, PRISMA), the differences among vegetative habitats were obvious, with the highest dissimilarities observed from 550 – 650 nm and from 700 – 850 nm (Figure 2.4). In particular, the spectral characteristics among the classes were more conspicuous in the green - red spectral range, such as reflectance peaks at 550 nm (Magnoliopsida, Ulvophyceae, Xanthophyceae), 600 nm (Bacillariophyceae), and 650 nm (Xanthophyceae and Bacillariophyceae). The absorption band at 675 nm, present in every class, corresponded to Chla while at 630 nm a smaller absorption band for the Bacillariophyceae and the Xanthophyceae corresponded to Chlorophyll-c (Chlc). Phaeophyceae was the class showing the lowest reflectance in the visible range. All classes but the Ulvophyceae had a positive slope in the NIR. The degradation to a multispectral resolution made these spectral features harder and or impossible to distinguish. The differences between vegetation classes were more

pronounced for the drone and Sentinel-2 20 m sensors (8 - 10 spectral bands) than for the Pleiades and Sentinel-2 10 m sensors (4 spectral bands).

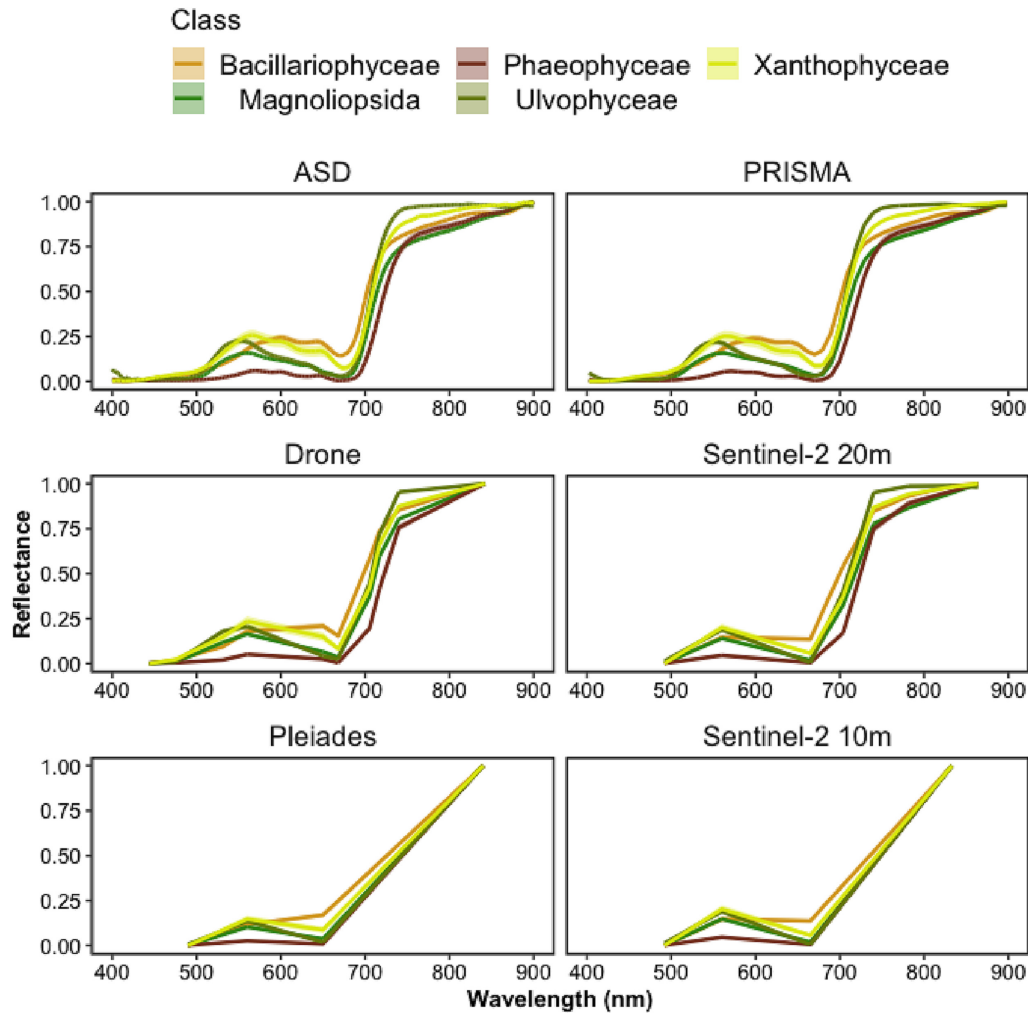


FIGURE 2.4: Spectral signatures of different vegetation classes at different spectral resolutions (ASD, Pleiades, Sentinel-2 10, Sentinel-2 10-20 m, Drone and PRISMA). Lines show mean signature per wavelength, while shading shows 95% confidence interval. Confidence intervals were consistently small and therefore are hard to distinguish.

2.3.2 Spectral Dissimilarity Between the Taxonomic Classes

The nMDS ordinations calculated with a cosine distance showed that all vegetation classes could be distinguished with a hyperspectral sensor (ASD, PRISMA), despite some overlaps between the Magnoliopsida, Ulvophyceae and Xanthophyceae (Figure 2.5). Interestingly, similar ordination patterns were also observed for the multispectral sensors with the highest number of bands (i.e., Drone, Sentinel-2 20 m). The greatest dissimilarity between classes was observed for the ASD ($R = 0.638$ & $p = 0.001$). The differences between PRISMA, the Drone and Sentinel-2 at 20 m were

very similar (PRISMA: $R = 0.611$ & $p = 0.001$, Drone: $R = 0.588$ & $p = 0.001$ & Sentinel-2 at 20 m), while Pleiades and Sentinel-2 at 10 m were far lower (Pleiades: $R = 0.49$ & $p = 0.001$ & Sentinel-2 at 10 m). Strong overlaps were observed between the classes Magnoliopsida and Ulvophyceae at the low spectral resolution of Pleiades and Sentinel-2 10 m.

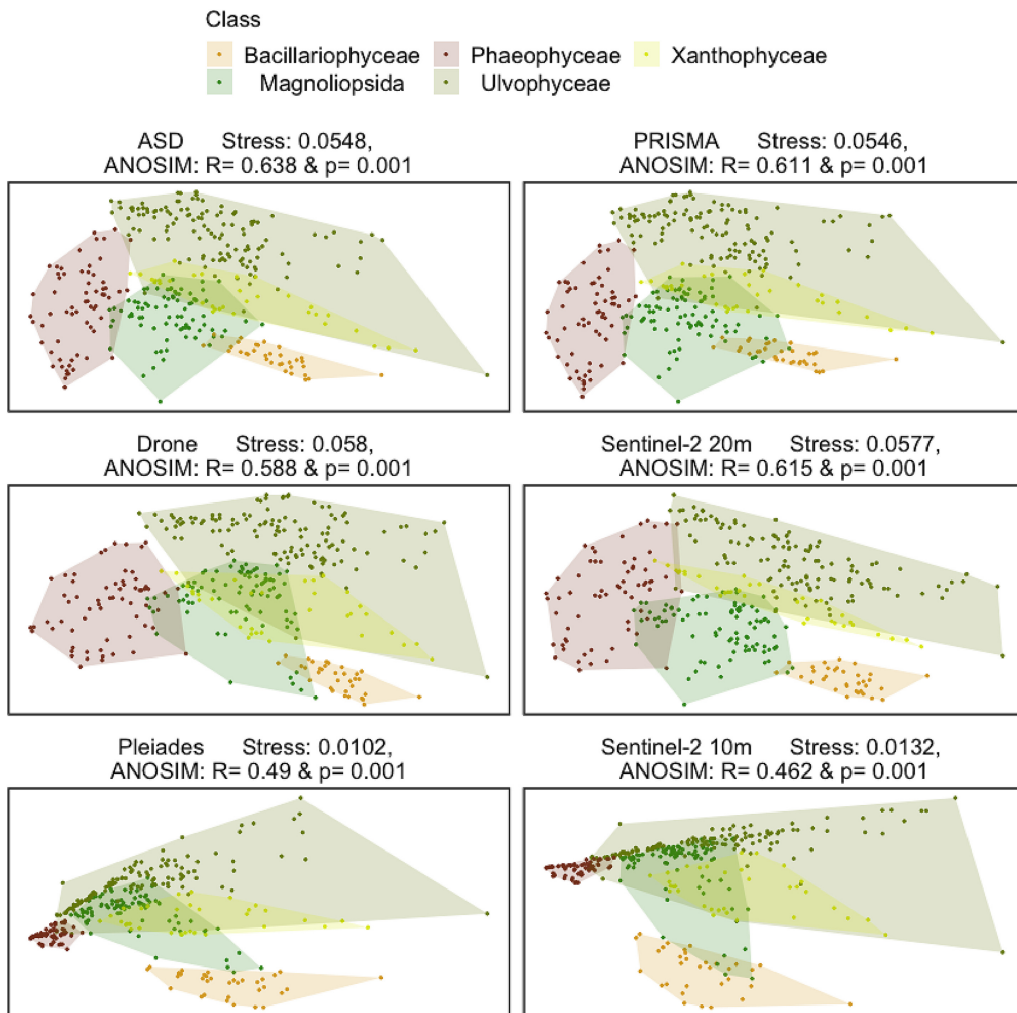


FIGURE 2.5: nMDS ordination showing similarities between vegetation classes at different spectral resolutions (ASD, Pleiades, Sentinel-2 10, Sentinel-2 10-20 m, Drone and PRISMA). Point distances are based on cosine distance, polygons show the minimum convex hull to surround all points. Stress values show the inaccuracy of the 2 dimensional representations.

2.3.3 Accuracy Across Sensors and Importance of Wavelengths

When assessed by Random Forest modelling, accuracy metrics of different spectral resolutions showed that Sentinel-2 20 m and Drone spectra gave high mean accuracy regardless of accuracy metric (Accuracy: 0.95 ± 0.004 for Sentinel-2 20 m & 0.948 ± 0.004 for Drone. Cohen's Kappa Accuracy: 0.935 ± 0.006 for Sentinel-2 20 m &

0.934 ± 0.005 for Drone: Figure 2.6 & Table 2.2). Above a spectral resolution of 10 bands, there was no gain in mean accuracy even with large increases in spectral resolution (Accuracy: 0.95 ± 0.005 for ASD & 0.951 ± 0.006 for PRISMA. Cohen's Kappa Accuracy: 0.936 ± 0.006 for ASD & 0.938 ± 0.008 for PRISMA). The sensors with the lowest spectral resolution (Pleiades and Sentinel-2 10 m) showed the lowest accuracy, yet still were accurate around 80 to 90% of the time (Accuracy: 0.861 ± 0.006 for Pleiades & 0.835 ± 0.008 for Sentinel-2 10 m. Cohen's Kappa Accuracy: 0.821 ± 0.008 for Pleiades & 0.792 ± 0.005 for Sentinel-2 10 m). Likewise, model specificity and sensitivity showed the greatest values from 8 spectral bands and above, but no increase was shown from 10 to 300 bands (Sensitivity: 0.948 ± 0.006 for Sentinel-2 20 m, 0.941 ± 0.006 for Drone, ± 0.006 for PRISMA & 0.938 ± 0.008 for ASD; Specificity: 0.989 ± 0.001 for Sentinel-2 20 m, 0.989 ± 0.001 for Drone, ± 0.001 for PRISMA & 0.989 ± 0.001 for ASD). Below 8 spectral bands, mean sensitivity and specificity were lowest, yet still around 85% (Sensitivity: 0.847 ± 0.008 for Pleiades & 0.844 ± 0.008 for Sentinel-2 10 m; Specificity: 0.97 ± 0.001 for Pleiades & 0.966 ± 0.002 for Sentinel-2 10 m). Standardised variable importance, the relative amount the inclusion of a variable in the model affected its' performance, showed the wavelengths the model considered most important (Fig. 7). Consistently across all spectral resolutions, wavelengths 517–556 nm were shown to be highly important. When present, wavelengths around 722–754 nm were the most important. When the variable importance of the ASD was overlaid on the response functions for the different multispectral sensors, the ability of each sensor to effectively sample the wavelengths of interest become clearer (Fig. 8). The Drone and Pleiades sensors effectively sample the top of the peak in importance from 517 to 556 nm, while Sentinel-2 (10 m and 20 m) is only sampling the edges of the peak. Both Pleiades and Sentinel-2 at 10 m did not sample the highest peak of importance from 722 to 754 nm, while the Drone and Sentinel-2 at 20 m only sampled one side of this peak. Generally, the Drone is sampling all the major and minor peaks of importance apart from one minor peak around 780 nm.

Standardised variable importance, the relative amount the inclusion of a variable in the model affected its' performance, showed the wavelengths the model considered most important (Figure 2.7). Consistently across all spectral resolutions, wavelengths 517–556 nm were shown to be highly important. When present, wavelengths around 722–754 nm were the most important.

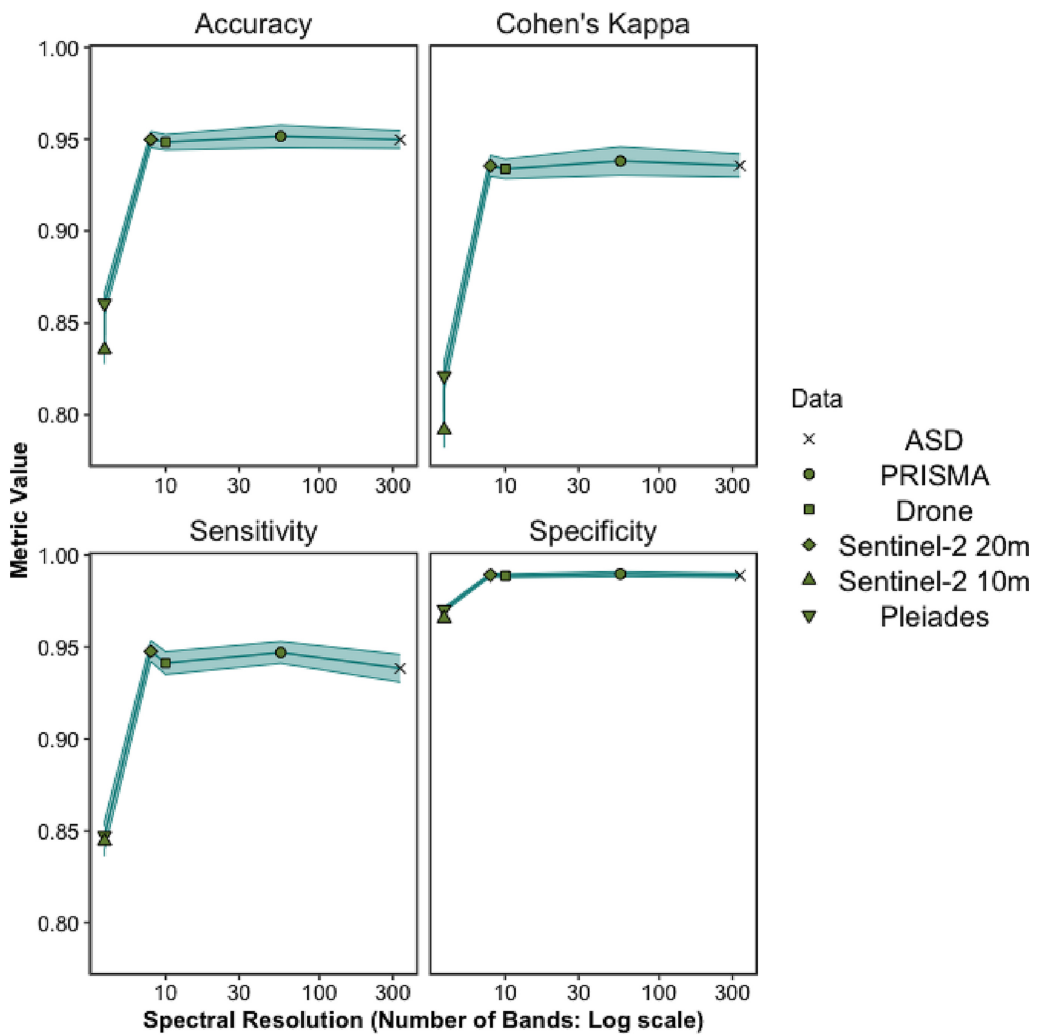


FIGURE 2.6: Accuracy metrics (accuracy, Cohen's kappa accuracy, sensitivity and specificity) for different spectral resolutions.

TABLE 2.2: Accuracy metrics (accuracy, Cohen's kappa accuracy, sensitivity and specificity) for different spectral resolutions \pm standard error.

| Sensor | Accuracy | Cohen's Kappa | Sensitivity | Specificity |
|--------------------------|-----------------|---------------------|-----------------|-----------------|
| Sentinel-2 10m (4 bands) | 83.5 ± 0.76 | 0.792 ± 0.0096 | 84.4 ± 0.81 | 96.6 ± 0.16 |
| Pleiades (4 bands) | 86.1 ± 0.61 | 0.821 ± 0.00773 | 84.7 ± 0.76 | 97 ± 0.13 |
| Sentinel-2 20m (8 bands) | 95.2 ± 0.44 | 0.935 ± 0.00577 | 94.8 ± 0.57 | 98.9 ± 0.1 |
| Drone (10 bands) | 94.8 ± 0.42 | 0.934 ± 0.00535 | 94.1 ± 0.62 | 98.9 ± 0.09 |
| PRISMA (56 bands) | 95.1 ± 0.61 | 0.938 ± 0.00778 | 94.7 ± 0.6 | 99 ± 0.13 |
| ASD (335 bands) | 95.2 ± 0.48 | 0.936 ± 0.00624 | 93.8 ± 0.75 | 98.9 ± 0.11 |

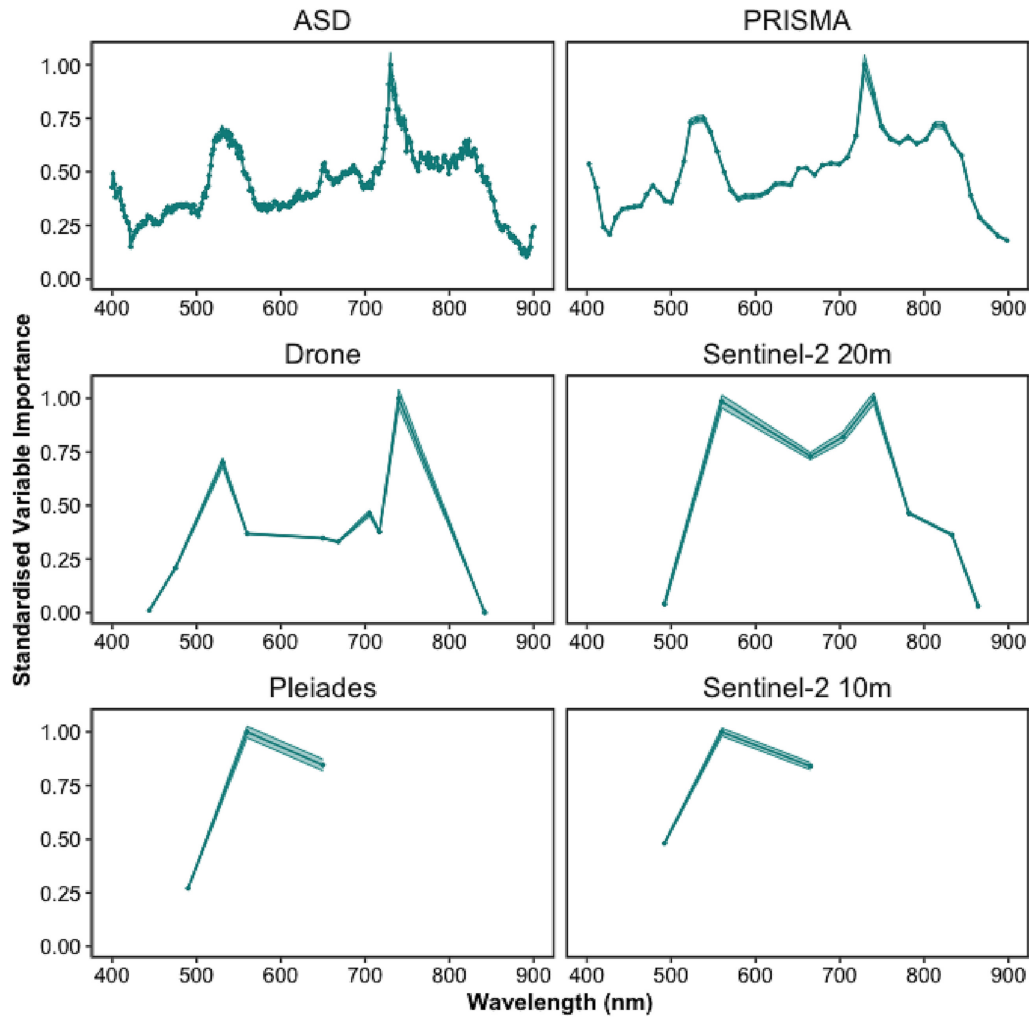


FIGURE 2.7: The relative importance of different wavelengths for model prediction across spectral resolutions.

When the variable importance of the ASD was overlaid on the response functions for the different multispectral sensors, the ability of each sensor to effectively sample the wavelengths of interest become clearer (Fig. 8). The Drone and Pleiades sensors effectively sample the top of the peak in importance from 517 to 556 nm, while Sentinel-2 (10 m and 20 m) is only sampling the edges of the peak. Both Pleiades and Sentinel-2 at 10 m did not sample the highest peak of importance from 722 to 754 nm, while the Drone and Sentinel-2 at 20 m only sampled one side of this peak. Generally, the Drone is sampling all the major and minor peaks of importance apart from one minor peak around 780 nm.

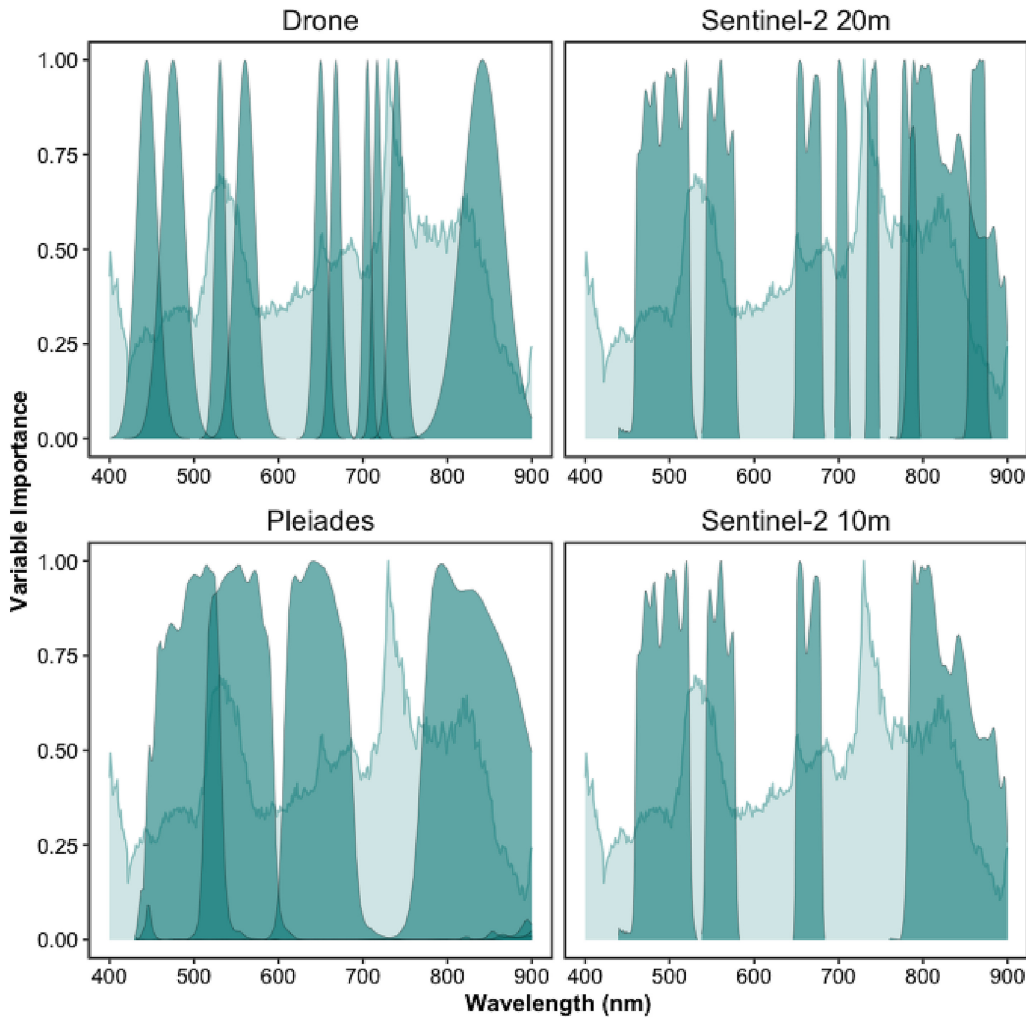


FIGURE 2.8: The relative importance of different wavelengths for ASD model prediction across the spectral bands of the Drone, Sentinel-2 and Pleiades sensors.

2.3.4 Confusion Matrices

Models accurately classed bare sediments consistently, regardless of spectral resolution (Figure 2.9). Ulvophyceae appeared to be mislabeled the most, while Magnoliopsida and Phaeophyceae showed consistently high prediction accuracy, especially by the Drone data. Across all spectral resolutions a small number of Magnoliopsida samples were mislabeled as Bacillariophyceae, Xanthophyceae and Ulvophyceae. A few Bacillariophyceae and Ulvophyceae samples were incorrectly labeled as Magnoliopsida. Likewise, identification of Xanthophyceae was consistently poor across all spectral resolutions apart from Sentinel-2 at 20 m (Sensitivity: 0.79 ASD, 0.87 PRISMA, 0.76 Drone, 0.93 Sentinel-2 at 20 m, 0.7 Sentinel-2 at 10 m and 0.5 Pleiades and Specificity: 0.84 ASD, 0.84 PRISMA, 0.86 Drone, 0.82 Sentinel-2 at 20 m, 0.57 Sentinel-2 at 10 m and 0.53 Pleiades). Pleiades and Sentinel-2 at 10 m had the worst

Magnoliopsida classification (Sensitivity: 0.66 Sentinel-2 at 10 m and 0.75 Pleiades; Specificity: 0.79 Sentinel-2 at 10 m and 0.8 Pleiades).

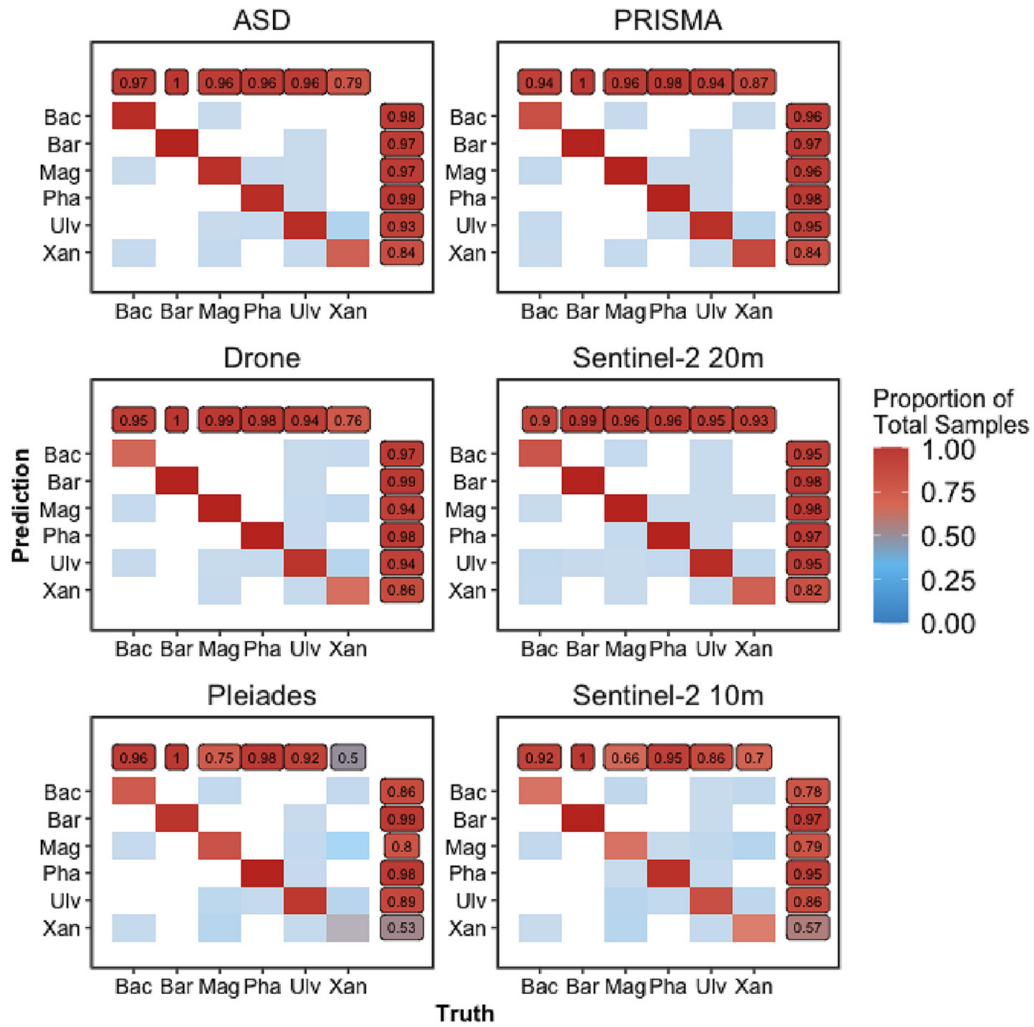


FIGURE 2.9: Confusion matrices for different spectral resolutions. Colour of tiles show proportion of correct predictions across all 20 repetitions with no colour for 0 predictions. Classes were abbreviated Bacillariophyceae as Bac, Bare Sediments as Bar, Magnoliopsida as Mag, Phaeophyceae as Pha and Ulvophyceae as Ulv. Labels with numbers show within class sensitivity and specificity.

2.4 Discussion

2.4.1 Spectral Library and Vegetation Classification

Spectral libraries have been used in coastal areas to analyse the capacity of hyperspectral sensors to discriminate macrophytes at different taxonomic resolutions (Diruit et al., 2022; Douay et al., 2022; Mcilwaine et al., 2019; for earlier references see Chao Rodríguez et al., 2017) or to estimate the background contribution on benthic diatoms reflectance spectra (Barillé et al., 2011). The spectral library built up for this work was

used to study the discriminatory ability of exposed soft-bottom intertidal vegetation at a class taxonomic level for a variety of remote-sensing instruments. Importantly, the classifier was designed to be applicable to both multi- and hyperspectral sensors, which is an advantage compared to classification methods only designed for hyperspectral sensors, such as derivative spectral analysis (Mcilwaine et al., 2019). The discrimination accuracy of the vegetation classes increased with spectral resolution, yet showed diminishing returns for resolutions above ~10 spectral bands. The main result of this study was the capacity to discriminate seagrass from green macroalgae at a multispectral resolution with ten bands when using ML classification techniques. As expected, this discrimination was also possible with hyperspectral sensors. Sensors with a spectral resolution of four bands, such as Pleiades and Sentinel 2 (10 m), were poorer at accurately discriminating between green macroalgae and seagrass, as their spectral shapes were too similar (Figure 2.4 & Figure 2.6). The importance of effective seagrass classification is considerable, with seagrass conservation and restoration contributing to 16 of the 17 United Nations Sustainable Development Goals (SDGs: Unsworth et al., 2022). A practical restraint of this analysis is the necessity for non-submerged samples. However, the main challenge in mapping seagrass through RS stems from confusion between similarly pigmented green algae, leading to high levels of uncertainty in current seagrass extent (McKenzie et al., 2020). Vegetation classes were consistently distinguishable from bare sediments, as found elsewhere between bare rock and algae (Douay et al., 2022). Likewise, random forest models were successfully able to discriminate between habitats (Légaré et al., 2022; See also: Oiry and Barillé, 2021), with generally lower accuracy at lower spectral resolution, yet even at the lowest spectral resolutions (Pleiades and Sentinel-2 10 m) there was a mean test accuracy of 86.1% and 83.5% respectively (82.1% and 79.2% respectively when class imbalance was considered with Cohen's kappa).

2.4.2 Spectral Discrimination and Pigment Composition

Two wavelength regions, respectively in the green (~517–556 nm) and NIR (~722–754 nm) spectral domains, were identified for their importance to the random forest model as contributing most to the discrimination between taxonomic classes (Figure 2.7). The wavelength window around 530 nm has already been recommended to distinguish different species of seagrass (Fyfe, 2003), and brown from green macroalgae (Mcilwaine et al., 2019). The spectral differences in the visible range between the classes

are partially explained by their difference of pigment composition (Table 2.3). Pigments have different optical properties and absorption wavelengths, which influence the reflectance spectra shapes. Chlc and fucoxanthin absorb light at 636 nm and 550 nm respectively (Méléder et al., 2013). Those pigments are present amongst diatoms and brown macroalgae, but absent in green macrophytes. Xanthophyceae also contain Chlc, but no fucoxanthin (Table 2.3). Chlorophylls and carotenoids absorptions can thus be used as diagnostic features to identify vegetation types that do not share the same pigmentary composition (Casal et al., 2012; Douay et al., 2022; Méléder et al., 2013). In this work, spectral differences have been observed between two classes having a similar pigment composition, the Magnoliopsida and the Ulvophyceae (Table 2.3). This indicates that the pigment concentrations and relative proportions, which can vary inside the main vegetation groups (Bargain et al., 2013; Beach et al., 1997), contribute to the spectral discrimination between taxonomic classes sharing the same pigment composition. Variations in the configuration of photosynthetic and accessory pigments in the 3D pigment-protein complexes within cells can also change the absorption features of taxa sharing the same pigments (Kirk, 1994), while 3D disposition of the plants as a whole can alter the magnitude of reflectance (Hedley et al., 2018). As pigment absorptions correspond to narrow spectral bands (Douay et al., 2022; Méléder et al., 2013), discriminating the different types of intertidal vegetation relies on access to these specific absorption wavelengths, which explains why the hyperspectral sensors are generally more accurate than the multispectral sensors. For the latter, the lack of relevant spectral bands and the large width of the available ones does not permit to capture the diagnostic absorption features. NIR wavelengths have long been recognized as relevant for the spectral discrimination of terrestrial plant diversity (Schmidt and Skidmore, 2003). At these wavelengths, spectral signatures are mainly a function of light scattering determined by the internal structure of leaves for angiosperms or thallus for macroalgae (Guyot, 1990). Fyfe (2003) showed that seagrass species could be separated using NIR wavelengths, with a significant change in the slopes between 700 and 900 nm. In our study, the min-max standardization preserved the slope changes for this spectral domain while removing the difference related to biomass variations (Bargain et al., 2012). Within the NIR, the ~722-754 nm wavelength range was identified in our work as the most discriminant for the spectral separation of the taxonomic classes of intertidal macrophytes. The better

TABLE 2.3: Photosynthetic and carotenoid pigments present (1) or absent (0) in each taxonomic class, along with their absorption wavelength measured *in vivo* and *in vitro* with an ASD spectroradiometer and by High Performance Liquid Chromatography (HPLC) respectively. Chl b: chlorophyll b, Chl c: chlorophyll c, Fuco: fucoxanthin, Zea: zeaxanthin, Diato: diatoxanthin, Diadino: diadinoxanthin, Neo: neoxanthin.

| Class | Chl b | Chl c | Fuco | Zea | Diato | Diadino | Neo | Lutein | Source |
|------------------------------|---------------------|---------------------|-------------|-------------|-------------|---------------------|---------------------|---------------------|--------------------------|
| Magnoliopsida | 1 | 0 | 0 | 1 | 0 | 0 | 1 | 1 | Ralph et al., 2002 |
| Ulvophyceae | 1 | 0 | 0 | 1 | 0 | 0 | 1 | 1 | Douay et al., 2022 |
| Xanthophyceae | 0 | 1 | 0 | 1 | 1 | 1 | 0 | 0 | Christensen et al., 1977 |
| Phaeophyceae | 0 | 1 | 1 | 1 | 0 | 0 | 0 | 0 | Douay et al., 2022 |
| Bacillariophyceae | 0 | 1 | 1 | 0 | 1 | 1 | 0 | 0 | Cartaxana et al., 2016 |
| Absorption wavelength (ASD) | 650 | 636 | 550 | 489 | 496 | 496 | - | 500 | Méléder et al., 2013 |
| Absorption wavelength (HPLC) | 458, 596, 646 | 442, 573, 630 | 451, 465 | 452, 478 | 453, 481 | 420, 447, 477 | 414, 437, 466 | 421, 446, 474 | Méléder et al., 2013 |

results obtained with the Drone and Sentinel-2 (20 m) bands suggest that a multispectral sensor with 10 relevant VNIR spectral bands could discriminate the main classes considered in this study. Furthermore, the wavelengths of importance for distinguishing the taxonomic classes here showed that the sensor used by Sentinel-2 could be greatly improved by the inclusion of a band at the main peaks of importance (517–556 nm and 722–754 nm). Both Pleiades and Sentinel-2 at 10 m miss the peak of highest importance. Furthermore, the marginally higher performance of the Pleiades sensor compared to that of the Sentinel-2 at 10 m could be linked to the overlap of two Pleiades bands over the 517–556 nm peak, while Sentinel-2 at 10 m only has bands either side of this peak. Thus, future satellite missions aiming to provide information on global habitat cover, especially including intertidal habitats, should aim to provide sensors with spectral patterns that cover the important wavelengths shown here. Dekker et al. (2018) highlighted the utility multispectral sensors could have for monitoring a wide range of aquatic systems, recommending ~26 bands between 380 and 780 nm, specifically 684 nm to capture Chla fluorescence. From the current analysis focusing on intertidal habitats, the most important wavelengths to cover would be around 530 & 730 nm. The main reason for this difference with the recommendations of Dekker et al. (2018) is that their work was specifically focused on submerged vegetation and addressed a broader range of objectives. For an effective monitoring system, specific and broad objectives of the satellite will ideally dictate the spectral coverage of the sensors used.

2.4.3 Geographical and Temporal Range of Applicability

The present spectral library aimed to represent a diversity of soft-bottom intertidal vegetation, with the main objective of discriminating seagrass from green macroalgae. However, it has a greater diversity of green macrophytes, making unbalanced among classes. Green macroalgae represent around 33% % of the library with 121 spectra out of 366, while the yellow macroalgae only have 33 spectra. Such a difference has an impact on the statistical analysis and the discrimination results, as some species are over-represented and others underrepresented. Yet, use of Cohen's kappa, which is an accuracy metric taking into consideration this imbalance, gave minimal difference to global accuracy. This library was built with data collected on the Atlantic coasts of France, Spain and Portugal and could be improved by the addition of new species or spectra from the existing species from other sites, both across Europe and globally.

As advised by Bajjouk et al. (2019), *Z. noltei* spectral data were collected at their development peak (June to September), as it is known that these macrophytes have a seasonal pigment variation (Bargain et al., 2013). Likewise, Légaré et al. (2022) found that depending on the season, spectral reflectance from intertidal habitats can vary significantly. As such, the current spectral library should not be used outside a late spring and summer period for Western Europe, as the varying pigment content can affect the reflectance spectral shapes. Seagrass spectral analysis could also be refined by taking into account the presence of epiphytes on their leaves, which was not done in this study. Epiphytes on seagrass leaves are known to have an impact on the shape of the reflectance spectra (Fyfe, 2003), as they are composed of diatoms and brown algae. This might explain the proximity between some seagrass and brown macroalgae spectra and the overlap between the diatoms and the seagrass (Figure 2.5). The presence of epiphytes could alter the relevance of the most discriminative wavelengths between seagrass and other macroalgae. Furthermore, this library was created using 100% cover of taxonomic classes. This homogeneity is often rare at the satellite pixel scales (10 - 60 m), meaning future work should assess the spectral signatures of mixed intertidal vegetation to best predict extent of heterogeneous intertidal vegetation.

2.4.4 Implications for Coastal Biodiversity Studies

The importance of long term monitoring of ecosystems is becoming more acknowledged, especially when monitoring human impacts that may affect EBVs, such as

important habitats, species, or the functioning of those species or habitats (B. F. Davies et al., 2022; Davies et al., 2021; El-Hacen et al., 2020; Lengyel et al., 2008; Livore et al., 2021; Perera-Valderrama et al., 2020). This is becoming even more apparent with the acceleration of human induced climate change, which is likely to exacerbate or accelerate the effects of many other human impacts (Cramer et al., 2018; Sage, 2020). Yet, *in situ* long term monitoring of EBVs is rare (Edwards et al., 2010). This rarity is due to a range of factors, most of which are driven by financial cost, especially if multiple fieldwork campaigns per year are required to capture seasonal variation (Condal et al., 2012). Furthermore, many human impacts can rarely be predicted *a priori*, so the ability to monitor their impact with sufficient previous data is circumstantial (B. F. R. Davies et al., 2022; Sheehan et al., 2021). This prior data is imperative to properly monitor human impacts and subsequently manage the activities leading to those impacts appropriately (Edgar et al., 2004; Fox et al., 2017; Underwood, 1992). The extent, both temporally and spatially, of EO from satellite data alongside its accessibility means it has been used to study long term anthropogenic impacts (Hu et al., 2017; Lizcano-Sandoval et al., 2022; Santos et al., 2020; Zoffoli et al., 2021). Unlike *in situ* monitoring data, past EO data are easily available, meaning that the long term manifestation of novel phenomena can be assessed effectively (Mahrad et al., 2020). Here, it was shown that spectral reflectance measurements from a relatively low spectral resolution sensor (8-10 bands: e.g. sensor of Sentinel-2 at 20 m resolution) could effectively and accurately classify soft-bottom intertidal vegetative habitats. However, the importance of spectral coverage has also been highlighted; when EO is being utilised, the specific response functions of sensors need to be aligned effectively with the objectives of the analysis. These considerations, alongside the temporal and spatial scales; revisit times of satellites, and the ability for satellites sensors to effectively observe important spectral differences after atmospheric correction is applied, will dictate the most appropriate satellites to be included in a Global Ocean Observing System (GOOS) for optimal monitoring and understanding of the EOVs in coastal ecosystems studies.

2.4.5 Conclusions

Here, the ability to distinguish between five different vegetative intertidal habitats was assessed by analysing their spectral reflectance signatures. Around 366 spectra were compiled across the European Atlantic coast, from Southern Spain to Northern

France. The spectral library was analysed at different multi- and hyperspectral resolutions with the emphasis on comparing commonly used satellite and drone sensors. This analysis not only highlighted the ability of a random forest spectral classification model to distinguish between differently pigmented habitats but also between similarly pigmented classes (green algae and seagrass). This approach could aid with ongoing efforts to accurately estimate global seagrass extent, alongside common methods such as NDVI that can provide proxies for vegetation coverage, such as monospecific intertidal seagrass meadow (Zoffoli et al., 2020). In particular, our work demonstrated the potential of discriminating intertidal seagrass from *Ulvophyceae* using satellite RS, therefore unlocking a strong limitation for seagrass mapping in heterogeneous environments. High accuracy at distinguishing habitats was found for hyperspectral sensors as well as multispectral sensors consisting of >8 bands in the visible and NIR (ASD, PRISMA, Sentinel-2 at 20 m resolution and the MicaSense RedEdge MX-dual Drone sensor). As climate change alongside other anthropogenic activities continue to impact community stability and functions, and potentially altering ecosystem services, monitoring of habitats becomes ever more important. Intertidal habitats are a vital link between terrestrial and coastal marine ecosystems, yet due to their dynamic nature and inaccessibility are difficult to assess. Therefore, the ability to monitor these ecosystems over time with high spatial and temporal resolution is important. This research provides the evidence that soft-bottom intertidal green macrophytes can be accurately classified at spectral resolutions currently available from satellite missions, assuming consistency after atmospheric correction, thus offering new perspectives for EO biodiversity studies of intertidal ecosystems. It further provides advice for the next generation of satellite missions in terms of optimal spectral resolution and important wavelengths.



3

Discriminating Seagrasses from Green Macroalgae in European Intertidal Areas Using High-Resolution Multispectral Drone Imagery



3.1 Introduction

Coastal areas are vital hotspots for marine biodiversity, with intertidal seagrass meadows playing a crucial role at the interface between land and ocean (Unsworth et al., 2022). Seagrass meadows provide a myriad of ecosystem services, including carbon sequestration, oxygen production, protection against sea-level rise and coastline erosion, and mitigation of eutrophication (Sousa et al., 2019; Unsworth et al., 2022). They serve as vital habitats for a diverse array of marine and terrestrial species, providing living, breeding, and feeding grounds (Gardner and Finlayson, 2018; Jankowska et al., 2019; Zoffoli et al., 2023). Due to the concentration of human activities in coastal zones, seagrass meadows are directly exposed to and impacted by anthropogenic pressures. Global regression and fragmentation of seagrass meadows are currently observed due to climate change, diseases, urbanization, land reclamation, dredging, competition with alien species, and reduction in water quality (Chefaoui et al., 2018; Duffy et al., 2019; Lin et al., 2018; Nguyen et al., 2021; Orth et al., 2006; Rasheed and Unsworth, 2011; Soissons et al., 2018; Sousa et al., 2019). Both habitat fragmentation and reduction, in turn, can severely compromise the effectiveness of ecosystem services provided by seagrass meadows. While improvements in water quality and hydrodynamics have been recently reported in Europe, allowing an overall recovery of seagrass ecosystems at local and European scales, many coastal waters worldwide are still subjected to strong eutrophication processes (Los Santos et al., 2019; Sousa et al., 2019; Zoffoli et al., 2021). Coastal eutrophication has been associated to excessive accumulation of green macroalgae, so-called green tides (Devlin and Brodie, 2023). Green tides produce shade and suffocation over seagrass individuals, thus threatening the health of seagrass ecosystems (Wang et al., 2022).

The importance of seagrass meadows and the variety of ecosystem services they provide have led to the enhancement of both global and regional programs to monitor EOVs such as seagrass composition (Miloslavich et al., 2018), as well as EBVs such as seagrass taxonomic diversity, species distribution, population abundance, and phenology (Pereira et al., 2013). Traditionally, indicators of seagrass status have been quantified using *in situ* measurements. However, the acquisition of field measurements in intertidal zones is notoriously challenging. Intertidal seagrass meadows are only exposed during low tide and can be situated in difficult-to-reach mudflats, potentially leading to inaccurate and limited estimations with conventional sampling

techniques (Nijland et al., 2019). Satellite observations have been proven effective in complementing *in situ* sampling, allowing for near real-time and consistent retrieval of seagrass EOVS and EBVs over extensive meadows (Coffer et al., 2023; Davies et al., 2024a, 2024b; Traganos and Reinartz, 2018; Xu et al., 2021; Zoffoli et al., 2021).

While satellite RS provides temporally consistent observations over large spatial scales, its utilization over intertidal areas is limited by several constraints. Satellite missions with a high temporal resolution (e.g. daily MODIS observation) are limited by too coarse spatial resolution (>100 m) to accurately map patchy seagrass meadows. Missions with a high spatial resolution such as Sentinel-2 (10 m) or Landsat8/9 (30 m) can be limited by low spectral resolution. The limited number of spectral bands challenges accurate discrimination of seagrass from other co-existing macrophytes. In particular, Chlorophyceae (green algae) and marine Magnoliopsida (seagrass) share the same pigment composition (Douay et al., 2022; Ralph et al., 2002), resulting in a similar spectral signature in terms of reflectance, especially in the visible range (Bannari et al., 2022; Davies et al., 2023a). Recently, using advanced machine-learning algorithms trained with a large hyperspectral library of more than 300 field reflectance spectra, Davies et al. (2023a) demonstrated that it was possible to discriminate Magnoliopsida from Chlorophyceae using reflectance spectra at Sentinel-2's spectral resolution. However the application of this approach to satellite RS remains to be validated. Moreover patches of green algae can develop at small spatial scales that are not observable using Sentinel-2 and/or Landsat-8/9 images (Tuya et al., 2013), especially during the initial stage of a green tide.

Drones (UAVs) can potentially fill the data gaps left by satellite RS and *in situ* measurements, due to their ability to provide spatially-explicit observations at very high spatial resolutions (pixel size from mm to cm) while capturing data at multi-spectral resolution (Fairley et al., 2022; Oh et al., 2017). The versatility of drones allows for their application across a diverse thematic range, from coastal zone management (Adade et al., 2021; Angnuureng et al., 2022; Casella et al., 2020) to mapping species distribution (Brunier et al., 2022a; Joyce et al., 2023; Roca et al., 2022; Román et al., 2021; Sousa et al., 2019; Tallam et al., 2023). However, when applied to coastal habitat mapping, previous case studies were mostly limited to a low number of drone flights over a single study site, restricting the generalizability of their application over wider geographical scales (Brunier et al., 2022a; Collin et al., 2019; Román et

al., 2021; Rossiter et al., 2020). These studies have demonstrated the capability of drones to map intertidal habitats, including seagrasses; however a broader generalization of these findings is still lacking. The current paper uniquely expands the spatial and methodological scope of drone-based RS for intertidal habitat mapping across a broad biogeographical range. It demonstrates the feasibility of accurately classifying diverse macrophyte types across various study sites, with a particular focus on distinguishing Magnoliopsida (seagrasses) and Chlorophyceae (green algae). Unlike previous studies, our approach integrates multiple spatial scales by simulating satellite resolutions and quantifying the impact of spatial resolution on classification accuracy. Nine drone flights were performed over soft-bottom intertidal areas along the Atlantic coastlines of two European countries (France and Portugal), covering a wide range of habitats, from monospecific seagrass meadows to meadows mixed with green, or red macroalgae. A deep learning algorithm was trained and validated for macrophyte discrimination, emphasizing applicability across diverse sites without losing prediction accuracy. The classification maps obtained at a very high spatial resolution with the drone were spatially degraded to satellite resolutions, making it possible to assess the effect of spatial resolution on classification accuracy, and provide insights for coastal habitat mapping using satellite remote sensing. This study is, therefore, among the first to quantify the effects of spatial resolution on the accuracy of drone-based macrophyte classification across a wide geographical scale, providing a framework to better understand satellite-based classification challenges.

3.2 Materials & Methods

3.2.1 Study sites

Seven study sites distributed between France and Portugal were selected for their extensive intertidal seagrass beds. Two sites were located in the Gulf of Morbihan, France (Figure 3.1 A : 47.5791°N, 2.8018°W). This gulf covers an area of 115 km² and is only connected to the sea through a 900 m wide channel. A total of 53 small islands are scattered across the gulf leading to 250 km of shorelines. Patchy seagrass meadows can be found on many of these islands. One of the sites within the gulf was on one its islands (Arz) and the other was located further south on a mainland beach area (Duer). The Gulf of Morbihan is a Natura 2000 site and a Regional Protected Area due to its rich biodiversity, including its seagrass meadows,

and is also classified as a RAMSAR site, which highlights its significance as a wetland of international importance. Two other sites were located in Bourgneuf Bay, France (Figure 3.1 B : 46.9849°N, 2.1488°W) which is a 340 km² semi-enclosed macrotidal bay, protected from waves by Noirmoutier Island. Bourgneuf bay hosts a large intertidal seagrass meadow of about 6 km² (Zoffoli et al., 2021). Within this meadow, the sites observed by drones (L'Epine and Barbatre) contained monospecific beds of *Zostera noltei* (dwarf eelgrass) with very little mixing with other macrophytes. Bourgneuf Bay is also part of the Natura 2000 network and serves as a RAMSAR site due to its critical habitat for migratory bird species and its extensive seagrass meadows (Zoffoli et al., 2023).

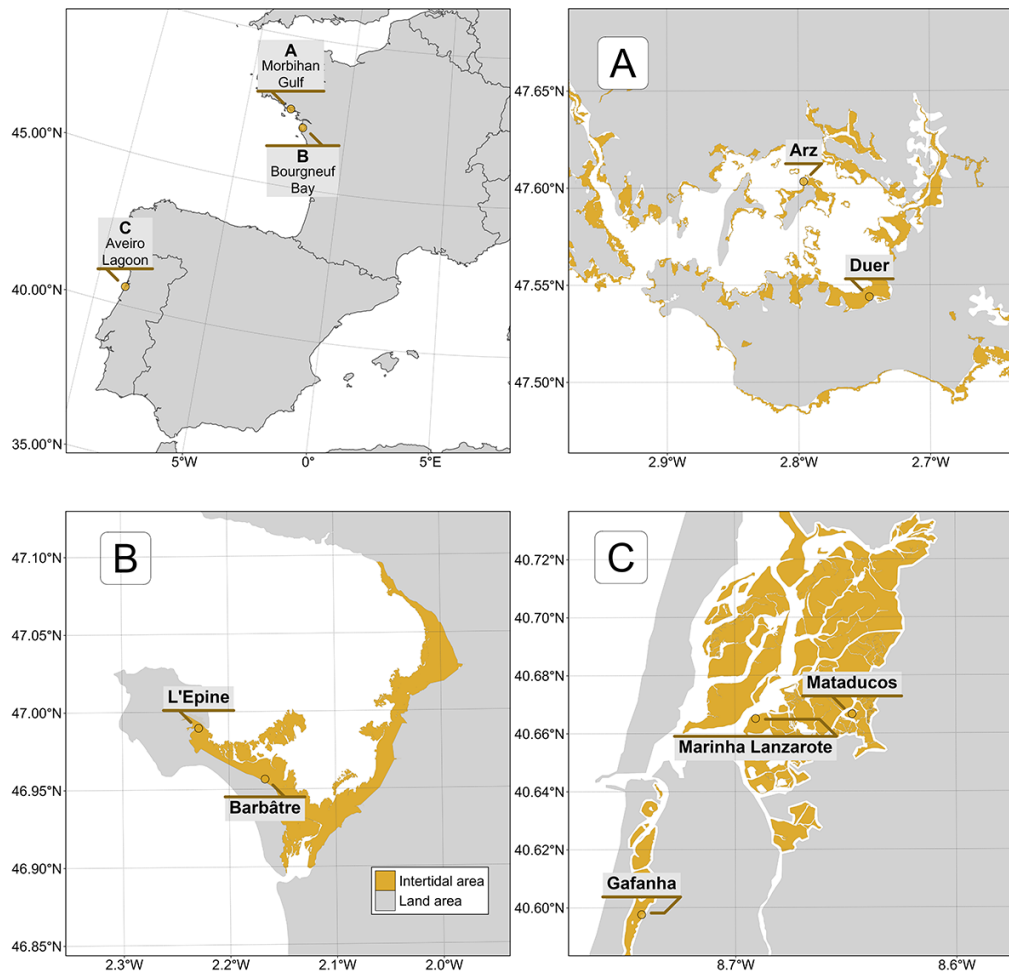


FIGURE 3.1: Location of drone flights in France and Portugal. A: Gulf of Morbihan (Two sites), B: Bourgneuf Bay (Two sites), C: Ria de Aveiro Coastal Lagoon (Three sites). Golden areas represent the intertidal zone.

Three sites were surveyed in the Ria de Aveiro Coastal Lagoon in Portugal (Figure 3.1

C : 40.6887°N, 8.6810°W). The extent of this lagoon is ~83 km² (at low tide) with many narrow channels, large salt marshes and many mudflats that uncover at low tide (Sousa et al., 2017). It is connected to the open sea through a single channel, with a tidal lag between the North and the South of the lagoon. The southernmost site (Gafanha) is a mudflat located in the Mira channel (one of the four main channels of the lagoon) whereas the two other sites (Mataducos and Marinha Lanzarote) were situated in the middle of the lagoon and only accessible by boat. These Portuguese sites are characterized by a more diverse intertidal vegetation, where patches of seagrass intermingle with red, brown, and green macroalgae. The Aveiro Lagoon, like the other study areas, is a Natura 2000 site and a RAMSAR wetland, recognized for its rich mosaic of habitats and importance for biodiversity, including migratory bird species and intertidal vegetation.

3.2.2 Field sampling

3.2.2.1 Drone acquisition

At each location, a DJI Matrice 200 quadcopter drone equipped with a Micasense RedEdge Dual MX multispectral camera was flown to take 1.2 million pixel reflectance photographs with ten spectral bands ranging from the blue to the NIR: 444, 475, 531, 560, 650, 668, 705, 717, 740 and 840 nm. To ensure consistent lighting conditions across flight paths, the drone's trajectory was aligned to maintain a solar azimuth angle of 90 degrees. An overlap of 70% and 80% (side and front respectively) between each image was set for each flight. A downwelling light sensor (DLS2) was used to acquire irradiance data concomitantly with the camera measurements. Raw data were calibrated in reflectance using a calibration panel reflective at ~50% provided by the manufacturer. Across all sites, flights were made at two different altitudes : 12 m or/and 120 m, with a spatial resolution of 8 mm and 80 mm, respectively (Table 3.1). Low-altitude flights, with a spatial resolution of 8 mm, were used to build the training dataset for the neural network, as this high resolution allowed for precise photo-interpretation of vegetation classes. In contrast, high-altitude flights were used for validation purposes.

TABLE 3.1: List of drone flights, summarising the date, the altitude, and the purpose of each flight. 12 m and 120 m flights have a spatial resolution of 8 and 80 mm respectively.

| Country | Site | Name | Altitude | Utility | Date |
|----------|------------------|-------------------|----------|------------|------------|
| France | Gulf of Morbihan | Arz Island | 12m | Training | 29/09/2022 |
| | | Duer | 12m | Training | 14/07/2022 |
| | | Duer | 120m | Validation | 14/07/2022 |
| | Bourgneuf Bay | Barbâtre | 120m | Validation | 07/09/2021 |
| Portugal | Aveiro Lagoon | L'Epine | 120m | Validation | 08/07/2021 |
| | | Marinha Lanzarote | 120m | Validation | 17/06/2022 |
| | | Mataducos | 120m | Validation | 16/06/2022 |
| | | Gafanha | 120m | Validation | 15/06/2022 |
| | | Gafanha | 12m | Training | 15/06/2022 |

3.2.2.2 Ground Control Points

Before each flight, targets used as ground control points were distributed over the study site and georeferenced with a Trimble © Geo XH 6000 differential GPS (dGPS). Ground control points were used to correct georeferencing imprecision of orthomosaics with a horizontal and vertical accuracy of 10cm. A dGPS was also used to georeference quadrats of 0.25 m², which assessed the presence or absence of five key taxonomic classes of intertidal vegetation: Bacillariophyceae (benthic diatoms forming biofilms at the sediment surface during low tide with biofilm's size ranging from small patches (m²) to entire mudflats (km²); henceforth: Benthic diatoms), Phaeophyceae (brown macroalgae generally attached to rocks or other substrates able to form dense beds in the intertidal zone; henceforth: Brown macroalgae), Magnoliopsida (seagrasses, rooted flowering marine plants able to form extensive meadows on soft sediments; henceforth: Seagrasses), Chlorophyceae (green macroalgae, typically found attached to rocks or washed ashore; henceforth: Green macroalgae), and Rhodophyceae (red macroalgae, attached to hard substrates but can also be found on soft-bottom substrate; henceforth: Red macroalgae). Only homogeneous vegetation patches extending over several meters were selected as ground control points. Pictures of each quadrat were uploaded online to the open-portal Global Biodiversity Information Facility (GBIF) platform (Davies et al., 2023b). Each photograph was also processed to estimate the percent cover of each type of vegetation using an image processing software (ImageJ, Schneider et al., 2012). Hyperspectral reflectance signatures of

each vegetation class were recorded using an ASD FieldSpec HandHeld 2 spectroradiometer, which acquires reflectance between 325 and 1075 nm, with 1 nm of spectral resolution. Hyperspectral signatures served dual purposes: they validate the radiometric calibration of drone data and contribute to misclassification reduction in photo interpretations.

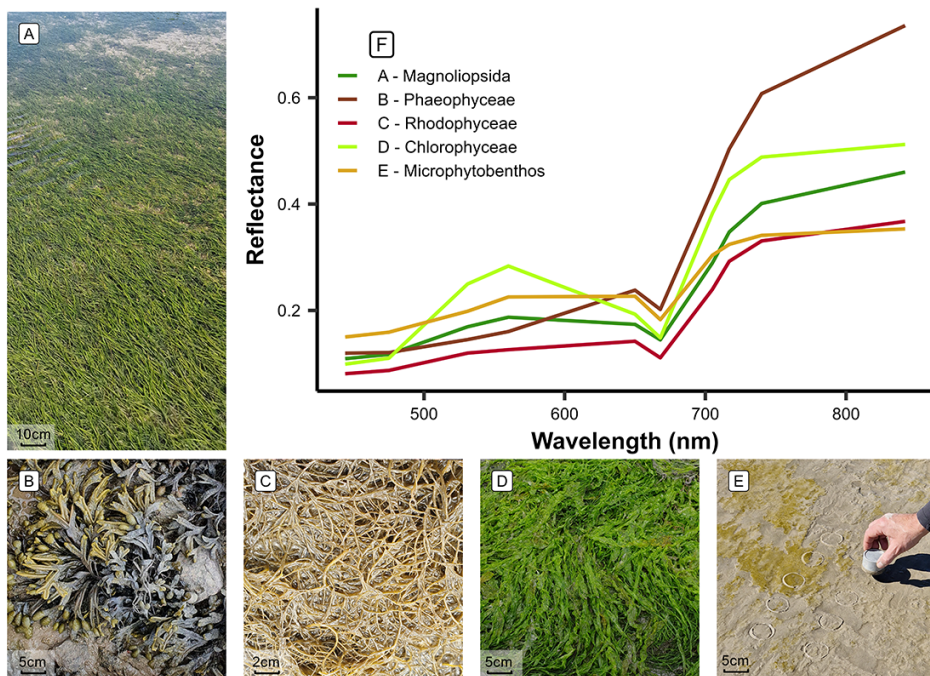


FIGURE 3.2: The five taxonomic classes of vegetation used to train the Neural Network model and an example of their raw spectral signatures at the spectral resolution of the Micasense RedEdge Dual MX. A : Magnoliopsida (*Zostera noltei*) ; B : Phaeophyceae (*Fucus sp.*) ; C : Rhodophyceae (*Gracilaria vermiculophylla*) ; D : Chlorophyceae (*Ulva sp.*) ; E : Bacillariophyceae (Benthic diatoms). The taxonomy was verified following the World Register of Marine Species (WORMS).

3.2.3 Drone Processing

A structure-from-motion photogrammetry software (Agisoft Metashape, Agisoft, 2019) was used to process images to obtain multispectral orthomosaics of each flight. The process for orthomosaicking was identical for every flight. First, key tying points were detected inside each image and between overlapping images in order to obtain a sparse point cloud. This cloud was cleaned using a reprojection accuracy metric to remove noisy points. A dense point cloud was then produced using a structure from motion algorithm. A surface interpolation of this dense point cloud was made to obtain a DSM, used to reconstruct the multispectral ortho-image (Nebel et al.,

2020). Low-altitude drone flights produced ortho-images with a very high spatial resolution (8 mm per pixel), making it efficient to visually distinguish between the various types of vegetation. High-altitude flights allowed to cover larger areas and produced images with a pixel size of 80 mm (Table 3.1).

3.2.4 General Workflow

The spectral similarities of the reflectance signatures at the spectral resolution of the Micasense senor between intertidal green macrophytes (*Magnoliopsida* and *Chlorophyceae*) make their discrimination challenging using simple classification algorithms (Figure 3.2 F). To overcome this challenge, a deep learning classification method was trained, validated, and applied to each drone flight (Figure 3.3).

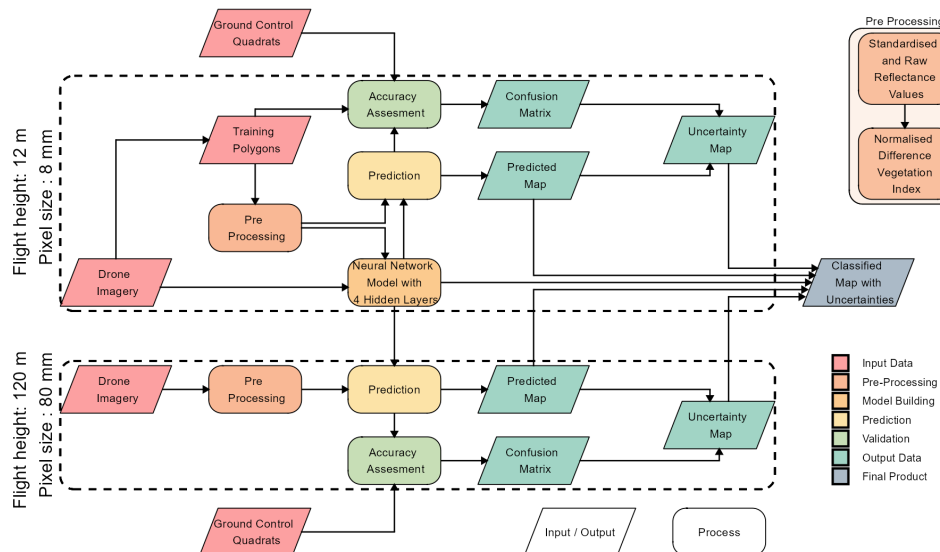


FIGURE 3.3: Schematic representation of the workflow. Parallelograms represent input or output data, and rectangles represent Python processing algorithms. The overall workflow of this study is divided into two distinct parts based on the spatial resolution of the drone flights: high-resolution flights (pixel size: 8 mm) were used for training and prediction of the Neural Network model, whereas lower-resolution flights (pixel size: 80 mm) were solely employed for prediction purposes. Validation has been performed on both high and low-resolution flights.

3.2.4.1 Training dataset building

A dataset containing photo-interpreted drone reflectance pixels was built to train a Neural Network model. The training pixels were categorized into seven different classes, representing the various habitats encountered at the different study sites:

TABLE 3.2: Vegetation Classes of the model and the number of pixels used to train and validate each class

| Name | Taxonomic Class | Training Pixels | Validation Pixels |
|------------------|-------------------|-----------------|-------------------|
| Benthic diatoms | Bacillariophyceae | 4,475 | 9,807 |
| Green macroalgae | Chlorophyceae | 17,140 | 25,910 |
| Seagrass | Magnoliopsida | 221,065 | 179,119 |
| Brown macroalgae | Phaeophyceae | 169,936 | 82,161 |
| Red macroalgae | Rhodophyceae | 5,771 | 10,054 |
| Water | - | 83,677 | 76,612 |
| Sediment | - | 95,126 | 57,299 |

sediment, water, green macroalgae, seagrasses, Benthic diatoms, brown macroalgae and red macroalgae. Only data from the low-altitude flights (Table 3.1) were used for training because their 8 mm spatial resolution allowed to avoid spectral sub-pixel mixing and to accurately identify vegetation classes. In the field, seagrasses displayed two types of color, most seagrass had green leaves, brownish leaves were also observed due to senescence or photo-degradation. Careful attention was given to incorporating training pixels from both color types into the training dataset for the seagrass class. This approach was consistently applied to all classes within the model. More than 418,000 pixels at 8 mm resolution from the 3 training flights were used to train the model (Table 3.2). For model training, 21 variables were used as predictors: the ten raw spectral bands of the Micasense RedEdge Dual MX multispectral camera (ranging from 444 nm to 840 nm), the same ten spectral bands standardized using a min/max transformation Equation 2.1 and the Normalized difference vegetation index (NDVI, Equation 1.2). Standardisation of spectral bands is commonly used to eliminate the scaling differences between spectra and to limit the effect of biomass on the spectra shape (Davies et al., 2023a; Douay et al., 2022).

3.2.4.2 Model building

A neural network classification model was built using the fastai workflow (Howard et al., 2018). This model was composed of 2 hidden layers and has a total of 26 054 trainable parameters. Parameters have been fine-tuned using 12 epoch to minimize the error rate. This model has been called DISCOV, standing for Drone Intertidal Substrate Classification Of Vegetation.

3.2.4.3 Validation

The workflow of this study revolves around two distinct flight heights (12 and 120 m, Figure 3.3) where ensuring consistency between reflectance at both heights is crucial. This comparison was conducted at sites where low and high-altitude flights overlapped. To compare reflectance of both flights, the low-altitude flights were resampled to the same spatial resolution and grid as the high-altitude flights using a median resampling method. Reflectance values were then extracted, and a scatterplot was generated. The Root Mean Square Error (RMSE) was computed to compare the difference between the raw and standardised reflectance.

The classification model was applied to all flights at both 12 and 120 m of altitude. *In situ* information on georeferenced class type and percent cover, acquired over homogeneous vegetation patches at the same time as drone flights was used to assess the model accuracy. These images were used to construct a validation dataset indicating the presence or absence of each class. Additionally, to the quadrat-based validation dataset, polygons of each class were photo interpreted in order to increase the number of pixels of the validation dataset. A total of 536,000 pixels were used to validate the Neural Network classifier. The sites with the lowest and highest number of validation data were Gafanha Low (17,316 pixels) and Marinha Lanzarote (159,713 pixels) respectively. A confusion matrix, along with precision metrics such as global accuracy, sensitivity, specificity, F1 score, and Kappa coefficient, were generated for each site. These metrics were computed as follow :

$$\text{Global accuracy} = \frac{\sum_{i=1}^k \text{TP}_i}{\sum_{i=1}^k (\text{TP}_i + \text{FP}_i + \text{FN}_i)}$$

$$\text{Sensitivity}_i = \frac{\text{TP}_i}{\text{TP}_i + \text{FN}_i}$$

$$\text{Specificity}_i = \frac{\text{TN}_i}{\text{TN}_i + \text{FP}_i}$$

$$\text{F1}_i = \frac{2 \cdot \text{TP}_i}{2 \cdot \text{TP}_i + \text{FP}_i + \text{FN}_i}$$

Where TP_i , TN_i , FN_i and FP_i represent the true positives, true negatives, false negatives and false positives relative to the class i.

All validation matrices were then aggregated to create an overall matrix

3.2.5 Variable Importance

Variable Importance Plots (VIP) serve as a method to identify which predictors are important for predicting a specific class. Out of the 21 predictors used in this study, Variable Importance was computed only for the raw and standardized values of the 10 spectral bands captured by the MicaSense camera. This is achieved by repeatedly predicting the same dataset while randomly shuffling one predictor at a time. The benchmark score obtained after each iteration is then compared to the benchmark score obtained without shuffling any variables. The greater the difference between these two benchmark values, the more important the variable is for the model (Wei et al., 2015).

3.2.6 Influence of the spatial resolution on classification

To assess the impact of spatial resolution on the model's output, we resampled the drone orthomosaics from their native resolution (8 cm for high-altitude flights) using the “average” method from the terra package in R. The rasters were resampled to 32 different resolutions, ranging from 10 cm to 30 m. DISCOV was then applied to these resampled rasters, and the results were compared to the original model predictions. For each resolution and vegetation class, we calculated the predicted area loss, where a score of 0 indicates no area loss during spatial resampling, and a score of 100 indicates complete loss of the vegetation class.

We used a Generalized Linear Model (GLM) with a Beta distribution to examine the relationship between pixel resolution, vegetation class, and their interaction on the loss of vegetation. The loss of vegetation was modelled as function of the interaction between pixel resolution and vegetation class (Benthic diatoms, brown macroalgae, seagrass, green macroalgae and red macroalgae). Sample vs fitted residuals and quartile-quartile graphics were assessed visually, to ensure assumptions of the models used were met.

3.2.7 Impact of mixed vegetation cover on the prediction

The key aspect of the workflow adopted in the present study is the mapping at two different altitudes (12 and 120 m), resulting in two distinct resolutions for the same area (8 and 80 mm; respectively). The high-resolution flight was used to estimate the sub-pixel composition for each pixel of the lower-resolution flight. Consequently, within each pixel of the high-altitude flights, the contribution of each vegetation class (% cover) was obtained, and a kernel density plot was generated. This plot provided a visual representation of the model's behaviour in mixed vegetation scenarios. It helped to understand the minimum vegetation cover of a given class within a pixel necessary for the model to confidently predict that class.

3.3 Results

3.3.1 Reflectance comparison between the two different altitudes

In this study, drone flights were conducted at two different altitudes (12 and 120 m) to construct the neural network model. At the sites where the flights at both altitudes overlapped, the reflectance was compared. Overall there was a good agreement between the two altitudes (RMSE : 0.027 ; Figure 3.4).

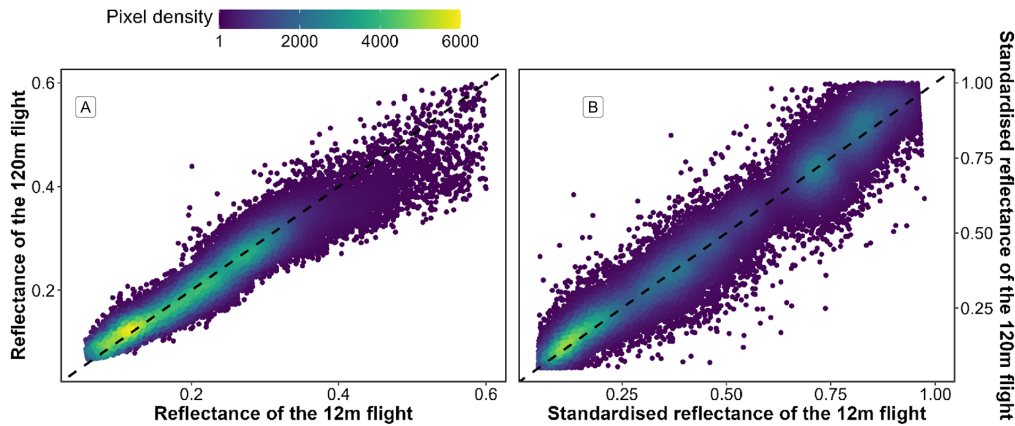


FIGURE 3.4: Comparison of reflectance retrieved from both low-altitude and high-altitude flights over a common area. The black dashed line represents a 1 to 1 relationship. Left (A) plots raw data and right (B) plots standardized data (Equation 2.1).

There was a slight underestimation of raw reflectance values in the high-altitude flight, particularly for higher reflectance values (Figure 3.4 A). Since both flights were conducted over vegetated areas, the highest reflectance values correspond to the

IR part of the spectrum. This difference was not present when the reflectance has been standardized (Equation 2.1 ; Figure 3.4 B).

3.3.2 Classification

Each drone flight was used to produce a prediction map, as well as a probability map that indicates the model-derived probability of the selected class for every pixel. The low-altitude flight conducted in Gafanha, Portugal, represented the site with the highest complexity (Figure 3.5). Among the five vegetation classes on which the model was trained, four were present on this site, with green and red macroalgae mixed with a seagrass meadow. There were also benthic diatoms biofilms on sediment surface. Although the seagrass was solely composed of a single species, *Zostera noltei*, two colours of this species could be observed: dark green (corresponding to healthy leaves) and brown (when leaves are senescent or have an altered pigment composition). Regardless of the variation of colour, the class Magnoliopsida (seagrass) was accurately predicted by the model (F1 score of 0.96 at that site).

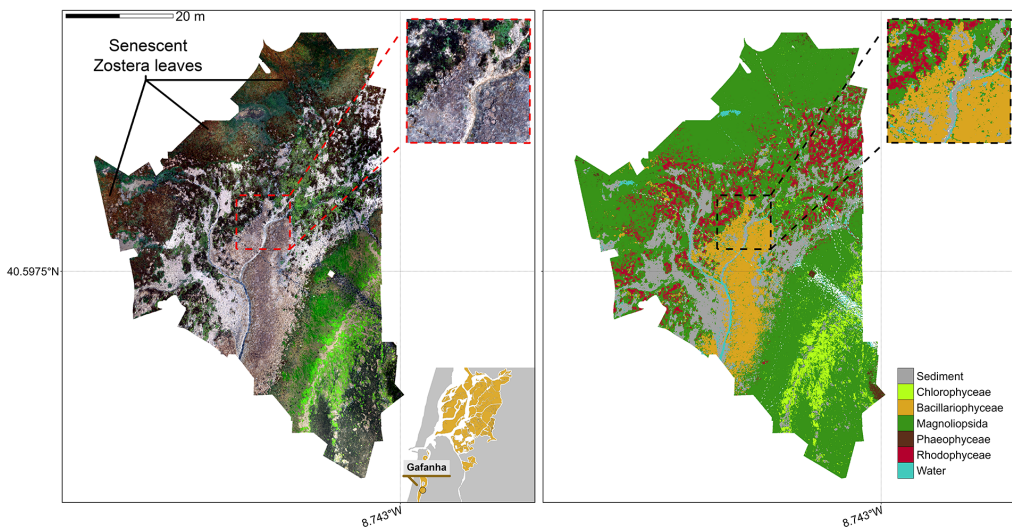


FIGURE 3.5: RGB orthomosaic (Left) and Prediction (Right) of the low altitude flight of Gafanha, Portugal. The total extent of this flight was 3000 m² with a resolution of 8 mm per pixel. The zoom covers an area equivalent to a 10 m Sentinel-2 pixel size.

The high-altitude flight over Gafanha covered a total area of ~1 km² (Figure 3.6). A channel contouring a small island was masked in the prediction map. Most of the vegetation area was classified as seagrass by the model, including patches with brown leaves. Only a few pixels were classified as green macroalgae (F1 score of 0.55). Patches of red macroalgae were correctly classified (F1 score of 0.85). In the northern

part of the site and near the land edges, patches of the shore angiosperm *Sporobolus maritimus* (syn. *Spartina maritima*) were misclassified, either as seagrass or as brown algae (F1 score of 0.77 and 0.71, respectively).

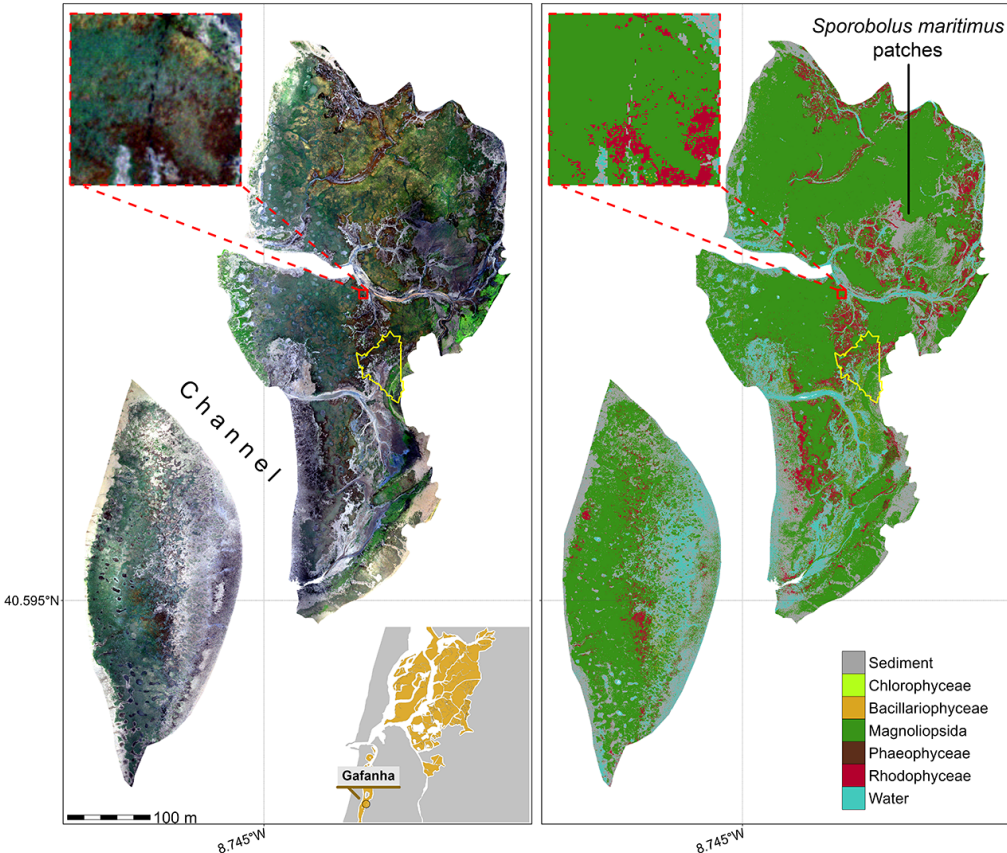


FIGURE 3.6: RGB orthomosaic (Left) and Prediction (Right) of the high-altitude flight of Gafanha, Portugal. The total extent of this flight was about 1 km² with a resolution of 80 mm per pixel. The yellow outline shows the extent of the low-altitude flight of Gafanha presented in Figure 3.5. The zoom covers an area equivalent to a 10 m Sentinel-2 pixel size.

Among the high altitude flights, the one acquired over the inner part of Ria de Aveiro coastal lagoon covered the largest area with approximately 1.5 km² (Figure 3.7). The vegetation present at the site was dominated by seagrass and red macroalgae. The classification provided consistent results, with a patchy seagrass meadow mixed with red macroalgae on the eastern part of the site. As shown in the zoom (Figure 3.7), the edges of the meadow were mixed with green macroalgae (*Ulva* sp.), which the model agreed with (F1 score of 0.89 for green algae, 0.97 for seagrass and 0.98 for red algae).

The flight over L'Epine in Noirmoutier Island, France (Figure 3.8) was conducted near a dike, which crossed the northern part of the site from West to East. Alongside this

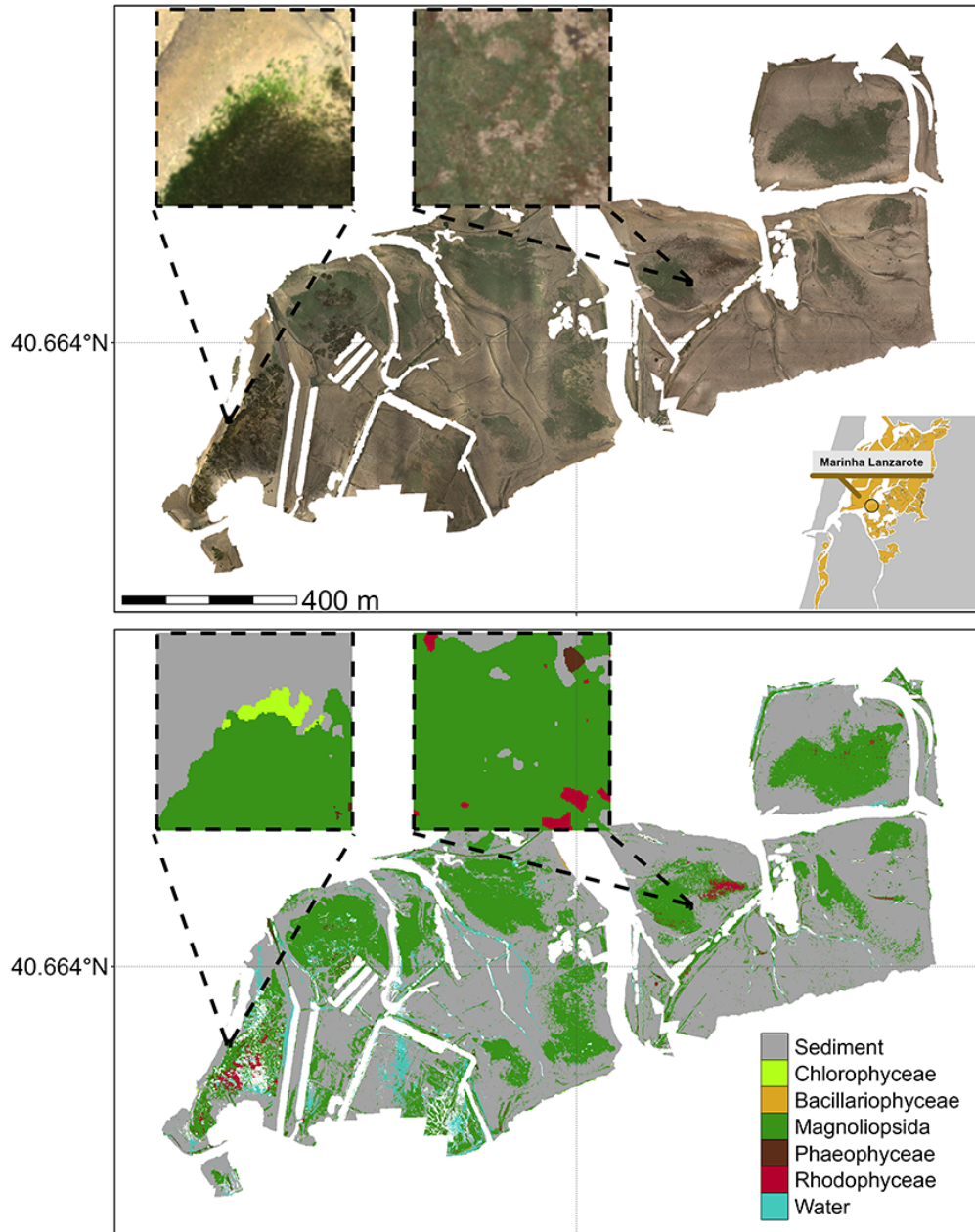


FIGURE 3.7: RGB orthomosaic (Top) and Prediction (Bottom) of the flight made in the inner part of Ria de Aveiro Lagoon, Portugal. The total extent of this flight was about 1.5 km^2 with a resolution of 80 mm per pixel. The zoom inserts cover an area equivalent to the size of a 10 m Sentinel-2 pixel.

dike, Fucale brown macroalgae (*Fucus spp.*, *Ascophyllum nodosum*) were attached to sparse rocks, and stranded green algae (*Ulva spp.*) could be observed, which was correctly reproduced by the prediction (Figure 3.8 Bottom). This site was characterized by a high mixture between green macroalgae and seagrass but these two classes were correctly discriminated by the classifier (F1 score of 0.97 and 0.98 respectively).

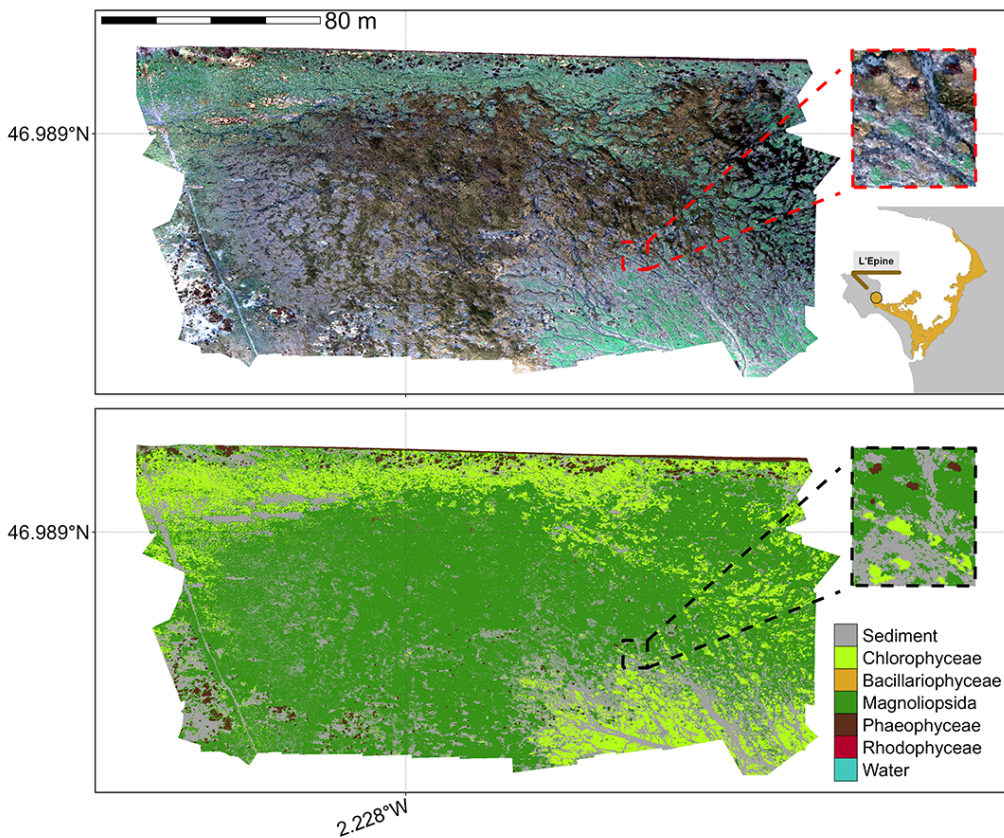


FIGURE 3.8: RGB orthomosaic (Top) and Prediction (Bottom) of L'Epine, France. The total extent of this flight was about 28 000 m² with a resolution of 80 mm per pixel. The zoom covers an area equivalent to a 10 m Sentinel-2 pixel size.

3.3.3 Validation of the model

With all drone flights combined, the model's global accuracy was 94.26%, with a Kappa coefficient of 0.92 (Figure 3.9).

The lowest-performing site was Gafanha High (global accuracy of 75.45%), whereas Mataduços was the site with the most accurate prediction (global accuracy of 98.05%). Overall, the classes Phaeophyceae, Magnoliopsida, Sediment, and Rhodophyceae were correctly classified with a balanced accuracy of 1, 0.96, 0.96, and 0.91, respectively. Bacillariophyceae was the least accurate class (accuracy of 0.72), mainly due to confusion with Magnoliopsida and Sediment.

3.3.4 Variable importance

The computation of the variable importance made it possible to identify which bands were the most useful for class prediction (Figure 3.10).

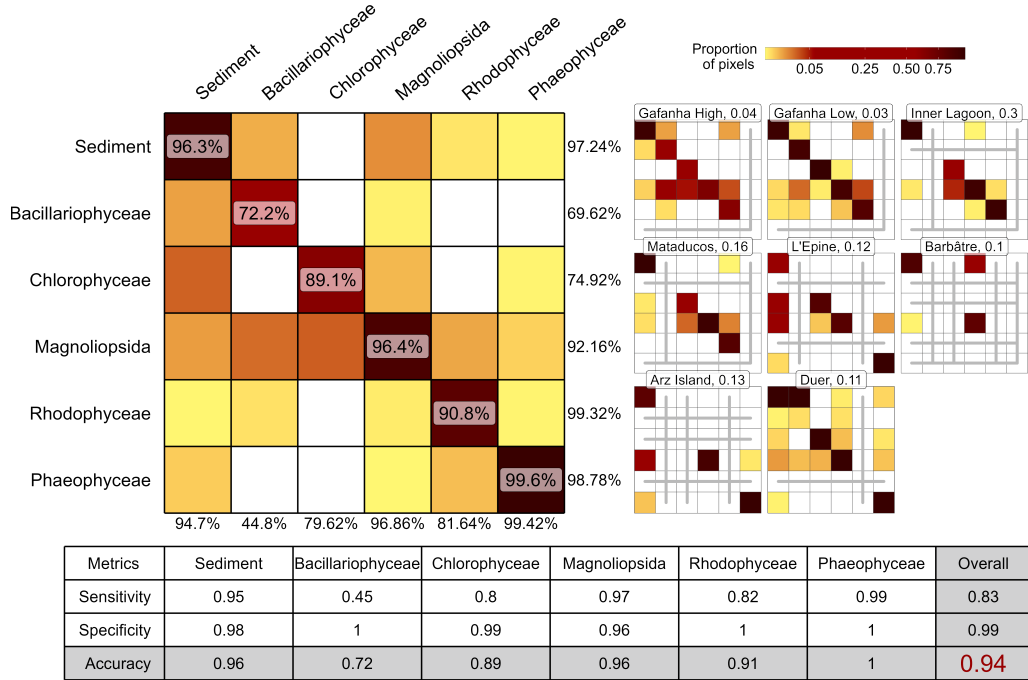


FIGURE 3.9: A global confusion matrix on the left is derived from validation data across each flight, while a mosaic of confusion matrices from individual flights is presented on the right. The labels inside the matrices indicate the balanced accuracy for each class. The labels at the bottom of the global matrix indicate the User’s accuracy for each class, and those on the right indicate the Producer’s Accuracy. The values adjacent to the names of each site represent the proportion of total pixels from that site contributing to the overall matrix. Grey lines within the mosaic indicate the absence of validation data for the class at that site. The table at the bottom summarizes the Sensitivity, Specificity, and Accuracy for each class and for the overall model.

The spectral bands at 444, 717 and 842 nm of the Micasense camera did not provide important information to discriminate any of the vegetation classes. The band at 531 nm was the most important predictor by far for the classifier to accurately predict Chlorophyceae. In fact, at this wavelength, the Chlorophyceae spectra showed the highest reflectance among all vegetation classes (Figure 3.10). The bands at 531 and 740 nm were the most important predictors for Phaeophyceae, corresponding to the lowest reflectance among all classes. Bands at 475 and 560 nm were the most important predictors for Bacillariophyceae and Rhodophyceae, respectively. Four predictors, ranging from the green (560 nm) to the RedEdge (705 nm) bands were important to accurately predict Magnoliopsida.

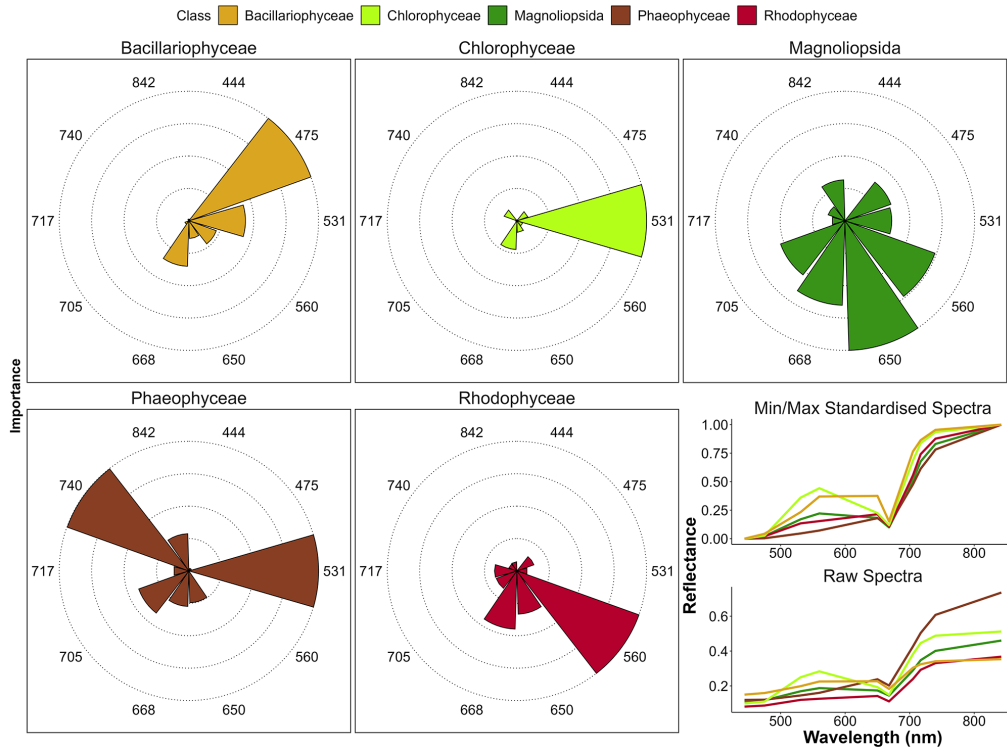


FIGURE 3.10: Variable Importance of the Neural Network Classifier for each taxonomic class. The longer the slice, the more important the variable for prediction of each class. The right plot shows the drone raw and standardised reflectance spectra of each class. Each slice represents the Variable Importance (VI) of both raw and standardised reflectance combined.

3.3.5 Effect of spatial resolution on the classification

Clear differences were seen in vegetation loss across spatial resolutions and vegetation classes (Figure 3.11). At a fine resolution of 1m, changes in the retrieved area for each vegetation type are minimal. Green macroalgae show the highest loss, with 1.2% area lost compared to the native resolution (80 mm). As the resolution coarsens to 10m, vegetation loss becomes more pronounced, with green macroalgae again experiencing the greatest reduction (12% compared to 8cm) and seagrass showing the smallest loss (1.3%). All green macroalgae have been lost at a resolution of 30m (100% compared to 8cm), while seagrass experiences a relatively small reduction of 11%. Brown and red macroalgae show lower declines, with losses at 30m resolution reaching approximately 37% and 59%, respectively.

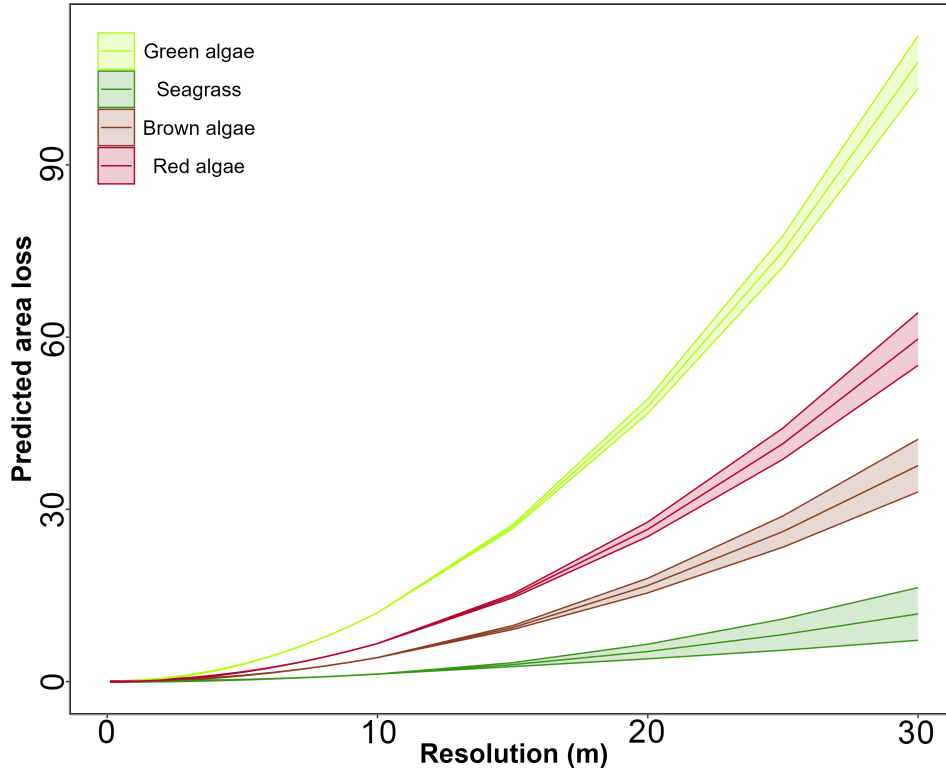


FIGURE 3.11: Predicted area loss for different vegetation types (green algae, seagrass, brown algae, red algae) as a function of spatial resolution. Lines represent Generalized Linear Model (GLM) predictions, and shaded areas indicate standard errors. As resolution decreases, predicted area loss increases for all vegetation types, with green algae showing the highest loss and seagrass the smallest at coarser resolutions.

3.3.6 Effect of the percent cover on the prediction

Using the very high-resolution low-altitude flight (8 mm pixels), we determined the minimal percent cover required to correctly classify a given class within the corresponding high-altitude flight (8cm pixel resolution ; Figure 3.12).

A cover of at least 80% was sufficient to have all the 80 mm pixels correctly classified, except for Magnoliopsida, which required a higher cover ($>90\%$) to be accurately classified. Concerning the probability of each class, there is a linear relationship between the percent cover and the confidence of the model to predict the class. To predict green macroalgae with a model likelihood of 0.85, a cover of 93% was needed, 90% for seagrass, 92% for red macroalgae, and 97% for benthic diatoms. When the vegetation cover of a given class was 100%, coarser high-flight pixels were correctly classified for all the classes except for bare sediment, which was only correctly classified 80% of the time. This phenomenon may be attributed to the time gap between the two flights,

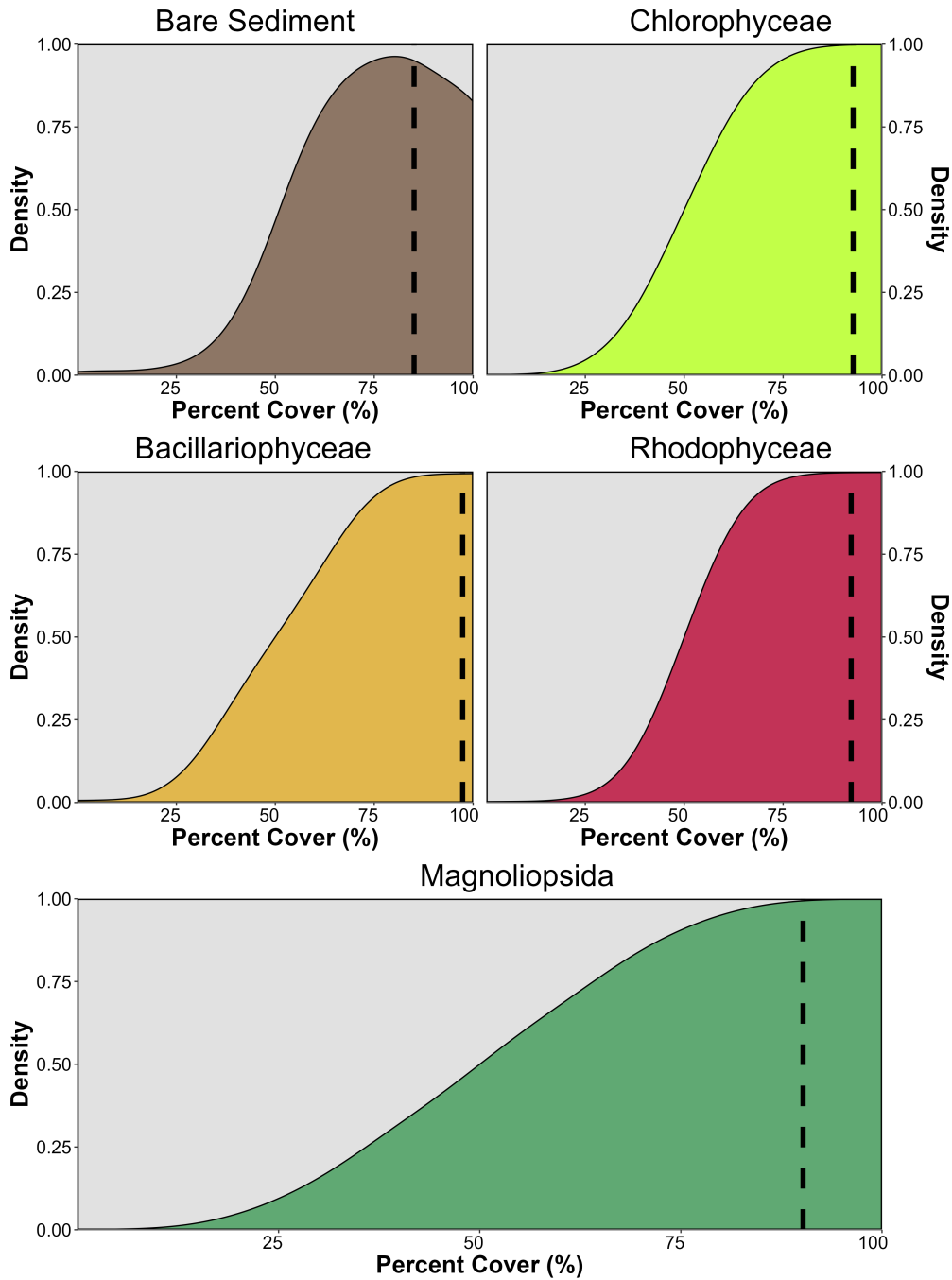


FIGURE 3.12: Kernel density plot showing the proportion of pixel well classified based on the percent cover of the class in high altitude flight pixels of Gafanha, Portugal. Each subplot shows all the pixels of the same classes on the high altitude flight. Percent cover of classes was retrieved using the result of the classification of the low altitude flight of Gafanha, Portugal.

allowing for MPB migration to the sediment surface during low tide, consequently altering the model's classification from bare sediment to Bacillariophyceae.

3.4 Discussion

3.4.1 Vegetation Discrimination

The primary objective of this study was to develop a method for the accurate classification of emerged macrophytes observed during low tide on tidal flats, specifically focusing on distinguishing between Chlorophyceae (green macroalgae) and marine Magnoliopsida (seagrasses) using a multispectral resolution. The discrimination between seagrasses and green macroalgae is challenging due to their optical similarity in the visible range (Bannari et al., 2022; Oiry and Barillé, 2021; Veettil et al., 2020). These two macrophytes share a similar pigment composition: Chla, Chlb (an additional photosynthetic pigment), and accessory carotenoids such as zeaxanthin, lutein and neoxanthin (Figure 3.13). Their spectral responses could be close, particularly at a multispectral resolution. Seagrass and green macroalgae frequently co-occur in intertidal areas, and can intermingle within a RS pixel if the spatial resolution is too low. Here, the issue of intra-pixel mixing was resolved thanks to the very high spatial resolution of the drone (from 8 to 80 mm). In this study the risk of spectral confusion was avoided with a machine-learning approach exploiting a neural networks classifier. Our drone flights and a recent study based on *in situ* radiometry, suggested that a sensor with at least eight spectral bands ranging from 500 to 850 nm, and including a green band at 530 nm and a RedEdge band at 730 nm, was crucial to accurately discriminate green macroalgae from seagrasses (Davies et al., 2023a).

Meeting these two criteria, the Micasense RedEdge-MX DUAL camera used in this study, enabled the classifier to achieve 97% accuracy between these two classes (Figure 3.14). Even if their pigment composition is similar, differences in the spectral shape can be observed, with green algae having a higher reflectance peak at 560 nm as well as a higher NIR plateau than seagrass (Figure 3.2). Such differences were previously attributed to differences in pigments concentration and/or ratios (Bargain et al., 2013), cellular structure as well as in the orientation of the plant at the sediment surface (Beach et al., 1997; Hedley et al., 2018; Kirk, 1994).

The variable importance analysis (Figure 3.10) identified that the band at 531 nm

| | Chl-b | Chl-c | Fuco | Zea | Diad | Lut | Neo | PE | PC |
|-----------------|-------|-------|------|-------|-------|-------|-------|-------|-------|
| Magnoliopsida | Green | Red | | Green | Red | Green | | Red | |
| Chlorophyceae | Green | Red | | Green | Red | Green | Green | Red | Red |
| Bacillariophy. | Red | Green | | Red | Green | Red | | Red | Red |
| Phaeophyceae | Red | Green | | Green | Red | Red | Red | Red | Red |
| Rhodophyceae | Red | Red | Red | Red | Red | Red | Red | Green | Green |
| Absorption (nm) | 650 | 636 | 550 | 489 | 496 | 490 | 450 | 566 | 615 |

FIGURE 3.13: Photosynthetic and carotenoid pigments present (Green) or absent (Red) in each taxonomic class present in the Neural Network Classifier, along with their absorption wavelength measured with spectroradiometer, Chl-b: chlorophyll-b, Chl-c: chlorophyll-c, Fuco: fucoxanthin, Zea: zeaxanthin, Diad: diadinoxanthin, Lut: lutein, Neo: neoxanthin, PE: phycoerythrin, PC: phycocyanin; (Carraxana et al., 2016; Christensen et al., 1977; Douay et al., 2022; Méléder et al., 2013; Ralph et al., 2002).

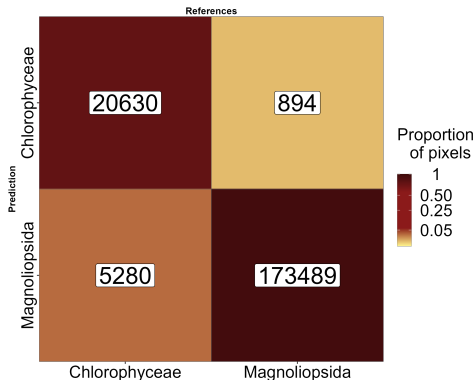


FIGURE 3.14: Sample of Figure 3.9 focusing on green macrophytes. The labels inside the matrix indicate the number of pixels.

was the most important for accurately identifying Chlorophyceae. In fact, at this wavelength, Chlorophyceae exhibited the highest reflectance among all other classes, highlighting the difference in carotenoid to Chla ratios between seagrasses and green macroalgae (Repolho et al., 2017). Concerning Phaeophyceae, the thick cell walls of these macroalgae (Charrier et al., 2021) make it more reflective in the IR part of the spectrum (Slaton et al., 2001), while the presence of fucoxanthin and zeaxanthin result in a low reflectance in the visible region (Figure 3.10 ; Figure 3.13). These two key features have been identified by the Neural Network as the two principal predictors to accurately identify brown algae (Figure 3.10). Similarly, the presence of

phycoerythrin and phycocyanin in Rhodophyceae contributes to the lowest reflectance among all classes in the spectral range from 560 to 615 nm (Figure 3.10). Indeed the band at 560 nm has been identified as important for identifying this class, likely due to phycoerythrin absorption at this wavelength. Regarding Bacillariophyceae, 475 nm was the most important predictor for this class (Figure 3.10). Indeed, the reflectance at 475 nm was higher for Bacillariophyceae than for any other vegetation class (Figure 3.2), very likely due to the low biomass (and associated concentration of blue-absorbing pigments) of these unicellular organisms compared to seagrass and macroalgae.

3.4.2 Altitude and Temporal Effects on Vegetation Prediction Accuracy

The ability to differentiate between various types of vegetation plays a critical role in ecological monitoring and coastal management (European-Commission, n.d.). By distinguishing between seagrasses and macroalgae, our approach facilitates targeted conservation strategies, enabling more effective preservation and restoration efforts in coastal ecosystems. While comparing the reflectance at two different altitudes (12 m and 120 m with a spatial resolution of 8 and 80 mm, respectively), a nearly one-to-one relationship was observed, with a RMSE of 0.02 (Figure 3.4). This result indicates that the reflectance measured by RS sensors was not significantly influenced by pixel size for these two altitudes. This finding is valuable for integrating drone-based data into larger-scale mapping projects (e.g., combining satellite and drone mapping in side-by-side analyses). The consistency of reflectance across altitudes suggests that drones can be effectively used for finer-scale mapping without compromising data accuracy when merging with other platforms. However, it was observed that there is an underestimation of the IR part of the spectra in the high-altitude dataset (Figure 3.4). Such disparity in IR reflectance may stem from temporal differences between the flights, possibly resulting in a slightly drier intertidal area and consequently higher IR reflectance. This disparity poses an issue for the methodology followed in the present study, relying solely on one flight height for training. To address this issue, we employed min/max standardized reflectance spectra as predictors for the model Equation 2.1. This approach allowed us to eliminate the slight reflectance difference between the flights (Figure 3.4 B) and to focus on the shape of the spectra in the visible domain (400 to 700 nm). At these wavelength different pigments are associated

with taxonomic diagnostic features. In contrast to subtidal seagrasses, which maintain relatively constant biomass throughout the year, intertidal seagrasses, like the one studied in this work, exhibit strong seasonal phenology (Davies et al., 2024b). At some sites, they completely disappear during the winter and reach their peak above-ground biomass in the summer and early autumn. Along with these seasonal changes in biomass, the pigment composition and ratios also vary throughout the year, reflecting the plants' adaptations to different environmental conditions (Bargain et al., 2013; Légaré et al., 2022). Standardization of spectral signatures helps to mitigate the impact of changing biomass on the spectral profile, enabling the development of a model that can reliably predict vegetation across different geographical locations and seasons. This approach allows for consistent classification of vegetation despite variations in biomass and fluctuations in light conditions, providing a robust tool for monitoring and predicting vegetation dynamics (Costa et al., 2021; Fyfe, 2003; Piaser et al., 2023). However, due to the strong phenology of intertidal seagrass meadows in Europe, the period when a meadow is well-established can be temporally restricted, limiting the ideal window for accurate detection.

3.4.3 Impact of Pixel Resolution on the prediction and Implications for Satellite Remote Sensing

Pixel resolution plays a critical role in accurately retrieving vegetation areas from RS data. As pixel size increases, we found a consistent decline in area retrieval across all vegetation types, with more pronounced effects for certain types, such as green algae (Figure 3.11). This highlights the sensitivity of spatial resolution in detecting smaller or more fragmented vegetation features. Green algae, being particularly patchy across all study sites, showed the steepest decline in areal agreement as pixel size increases, which aligns with expectations given the limitations of coarser resolution in capturing fine-scale details.

This resolution-area relationship has important implications for satellite missions like Sentinel-2 and Landsat, which are commonly used in marine and coastal vegetation studies. Both satellites offer high-resolution imagery, with pixel sizes of 10m and 30m, respectively. While these resolutions are suitable for broad-scale environmental monitoring, they may be too coarse to capture finer-scale heterogeneity, as it was observed with green macroalgae in this study. Our findings suggest that, while the 30m resolution of Landsat may be adequate for homogeneous vegetation types, such

as seagrass, a higher resolution is essential for accurately mapping patchy vegetation like green algae. These findings have direct implications for environmental management and conservation planning. Overlooking fine-scale vegetation features, such as those seen in green algae, could result in inadequate protection or restoration efforts, particularly in ecologically sensitive coastal zones, as the early stages of green tides could be challenging to detect at coarse resolutions.

Very high-resolution imagery offers more accurate vegetation mapping but comes with trade-offs. As resolution increases, data costs rise, and processing becomes more resource-intensive due to the larger file sizes and computational demands. Consequently, high-resolution data requires more storage and can slow down real-time applications. For large-scale monitoring of homogeneous vegetation types, 10 m resolution of S2/MSI or even the 30 m of Landsat/OLI is often sufficient. However, when mapping vegetation like macroalgae with heterogeneous distribution, the precision provided by higher-resolution imagery is crucial, despite the additional costs and processing challenges it imposes.

3.4.4 Towards climate and biodiversity applications

Climate change, global warming, eutrophication, alien and invasive species development, coastal erosion, and sea level rise are expected to continue impacting coastal ecosystems in the future (Holon et al., 2018; Marquet et al., 2024; Schibalski et al., 2022) and the demand for meaningful and efficient monitoring of coastal habitats has never been higher (Muller-Karger et al., 2018; Oiry and Barillé, 2021; Villalobos Perna et al., 2023). Our findings, particularly the improved discrimination of intertidal seagrass and green macroalgae from other intertidal vegetation classes, highlight the potential of drone-based RS to support diverse applications, from the conservation of biodiversity to climate change adaptation strategies.

Due to increasing coastal eutrophication, macroalgal blooms are becoming increasingly common in many regions around the world (Sutton et al., 2011; Ye et al., 2011). These blooms can have negative impacts on human health and local economic activities, including human health, fishing and aquaculture, tourism, and recreational activities (Villares et al., 1999; Ye et al., 2011). The first green tide events (*i.e.* bloom of green macroalgae of the genus *Ulva*) were reported in Brittany, France, in the 1970s and have since been a concern for local stakeholders and economic activities

(Ménesguen, 2018). Some regions of the world have witnessed an increase in brown macroalgae blooms, predominantly involving algae of the genus *Sargassum* washing along the Caribbean coastlines (Louime et al., 2017), and more recently *Rugulopteryx okamurea* in southern Europe (Roca et al., 2022). Satellite RS has proven to be a valuable tool for mapping the spatial and temporal extent of macroalgal blooms worldwide. However, due to limitations in spatial resolution, it can only effectively map well-developed blooms (Haro et al., 2023; Klemas, 2012). High spatial resolution drone imagery, coupled with an accurate classification algorithm, could be used to map the early stages of macroalgal blooms in areas known to have regular blooms or in new sites. Indeed, this approach could provide early warning alerts to local managers and complimentary to traditional sampling methods to monitor coastal ecosystems. These methods are generally time and resource-intensive, and the findings are often difficult to scale up when applied alone. EO can bridge this gap and meet the need for systematic monitoring of coastal ecosystems over large areas (E. Papathanasopoulou et al., 2019). The retrieval of EBVs and EOVs through satellite observations has been increasingly common, enabling comprehensive monitoring of entire ecosystems over extended time periods (Ratnarajah et al., 2023; Zoffoli et al., 2021). The WFD mandates the achievement and maintenance of “good ecological status” for all European waters, which necessitates a comprehensive understanding and monitoring of aquatic ecosystems, including coastal habitats like seagrass beds (Foden and Brazier, 2007; Nordlund et al., 2024; Zoffoli et al., 2021).

Effective and efficient monitoring tools are essential for identifying the impacts of human activities and natural changes on coastal ecosystems. On-demand, multispectral drone observations at very high spatial resolution provide a novel and powerful tool to rapidly and accurately acquire ground truth data, which can be used to develop ML algorithm for satellite sensors (Davies et al., 2024a). Spatially resolved data are indeed critical for calibrating and validating satellite RS observations, thereby enhancing our capacity to monitor vast coastal areas. The integration of drone technology facilitates a scalable approach to environmental surveillance while taking into account the patchiness of vegetation, offering significant advancements in the spatial and temporal resolution of data collection. This, in turn, supports the EU WFD’s objectives by enabling more informed and timely management decisions for the conservation and restoration of aquatic ecosystems.

3.5 Conclusion

The utilization of very high spatial resolution (from 8 to 80 mm) drone-based RS coupled with ML techniques has proven to be an effective method for the discrimination of intertidal seagrasses from green macroalgae with a multispectral resolution sensor. Standardized reflectance was incorporated in the Neural Network model allowing for a better discrimination of spectral features related to pigment absorption in the visible region of the spectrum. There was a striking difference between the variable of importance to discriminate Magnoliopsida from Chlorophyceae. The latter was essentially identified with the 451 nm spectral band while more spectral bands were needed to identify the former, notably 650, 560, 668, and 705 nm. As the spectral bands of the Micasense RedEdge Dual sensor are very similar to those of Sentinel-2/MSI, we suggest that multispectral satellite data have the potential to perform this discrimination between these green macrophytes. The findings underscore the importance of adopting advanced RS tools in ecological studies and environmental monitoring, providing a foundation for future research and policy implementation aimed at ecosystem conservation and restoration.



4

Spatial and Temporal distributions of the alien invasive *Gracilaria vermiculophylla*



4.1 Introduction

The introduction of Non-Indigenous Species (NIS) in terrestrial, freshwater, and marine ecosystems is one of the major threats to biodiversity worldwide. In particular, the proliferation and rapid spread of Invasive Alien Species (IAS) can radically change the structure and functioning of marine ecosystems, requiring effective assessment and monitoring programs (Massé et al., 2023). In Europe, 874 NIS have been introduced to the marine environment so far (i.e. until 2020) and it is expected that the rate of biological invasions will continue to increase in the coming years (Zenetos et al., 2022). Macroalgae represent more than 40 % of the NIS introduced to Europe waters, with many species native to the Temperate Northern Pacific (Williams and Smith, 2007).

Amongst all invasive macroalgae, *Gracilaria vermiculophylla* (Papenfuss, 1967) (original name *Gracilaria vermiculophylla* (OHMI, 1956); also known as *Agarophyton vermiculophyllum* (Gurgel et al., 2018)), has spread extensively from its native distribution range in Japan and Korea (Terada and Yamamoto, 2002). This spread has occurred across temperate estuaries in North America, Europe, and other regions, facilitated by aquaculture and maritime activities (Krueger-Hadfield et al., 2017; Rueness, 2005; Weinberger et al., 2008).

In regions like the Baltic Sea and the eastern United States, it can affect native fucoid macroalgae and seagrasses negatively (Firth et al., 2024; Thomsen et al., 2013; Van Katwijk, 2003). It can also alter sediment composition (Nyberg et al., 2009), and disrupts trophic interactions (Ginneken et al., 2018). However *G. vermiculophylla* create new habitats for invertebrates and juvenile fish in a soft-bottom environment (Davoult et al., 2017) and, more generally, can positively enhance ecosystem processes (Ramus et al., 2017). The negative and positive effects of this species (Thomsen et al., 2009), which now dominate some coastal ecosystems, underscore the importance of monitoring and managing its population, particularly as climate change and anthropogenic pressures continue to facilitate biological invasions. *G. vermiculophylla* success as an invader stems from its tolerance to a wide range of environmental conditions, including temperature (Sotka et al., 2018), nutrient variability (Abreu et al., 2011), and salinity (Weinberger et al., 2008). Its growth capacity at low salinities (Nyberg, 2007; Rueness, 2005) explains its presence in the brackish waters of the Baltic Sea (Weinberger et al., 2008) but also in the mesohaline sheltered part of estuaries

of the Atlantic coast of Europe (**Surget et al., 2017**). It is also present in confined areas of lagoons characterized by low hydrodynamism (Abreu et al., 2011; Sfriso et al., 2012). In Europe, it was first observed in 1996 in the Belon estuary (France) and later in many other estuaries on the coasts of Franch Brittany (Rueness, 2005). It can be found on hard substrates such as invertebrate's tubes and shells providing a substratum (Thomsen et al., 2007) or attached to pebbles and rocks (Terada and Yamamoto, 2002) but the largest populations are colonizing soft-bottom sediment and particularly estuarine intertidal mudflats (**Surget et al., 2017**). In this habitat, extensive dark red mats are observed at low tide, covering vast areas that have largely been unquantified in most studies. Therefore, *G. vermiculophylla* can establish populations in soft-bottom sediment habitats, previously devoid of macroalgae (Ramus et al., 2017). These mats are usually monospecific, with the alga thalli partially buried in the mud (Rueness, 2005; Surget, 2017). Intertidal mats can, however, be temporarily overgrown by ephemeral green macroalgae (Weinberger et al., 2008). In the European estuaries where *G. vermiculophylla* was first documented, large monospecific mats were reported to be confined to the upper intertidal zones (Rueness, 2005); however, their spatial distribution relative to the mudflat topography and elevation had not been quantitatively assessed. In coastal lagoons of the East Atlantic coast, Besterman et al. (2021) have shown that the mudflat topography was a significant predictor of its abundance. In fact, *G. vermiculophylla* has never been mapped using RS techniques, and existing descriptions of its distribution lack spatially explicit mapping (Abreu et al., 2011; Sfriso et al., 2012; Thomsen et al., 2007; Weinberger et al., 2008).

RS has revolutionized our ability to monitor and manage coastal ecosystems, offering efficient and scalable methods for detecting environmental changes in intertidal vegetation across a wide range of spatio-temporal scales (Calleja et al., 2017; Davies et al., 2024a, 2024b; Valle et al., 2015; Zoffoli et al., 2021). Among remote-sensing technologies, drone-based imagery has recently emerged as a particularly promising tool for studying the spatial distribution of intertidal primary producers such as benthic microalgae (Román et al., 2024, 2021), seagrass (Chand and Bolland, 2021; Duffy et al., 2018; Oiry et al., 2024; Román et al., 2021) and macroalgae (Diruit et al., 2022; Peidro-Devesa et al., 2024). While it lacks the temporal consistency of satellite missions, drone RS makes it possible to acquire images at extremely high spatial resolution (i.e. cm-scale), rapidly target specific areas of interest, and provide observations

in overcast conditions. In particular, the potential of drone RS for monitoring the surface area occupied by IAS has been demonstrated (Roca et al., 2022). Drone-based photogrammetry also makes it possible to characterize the distribution of intertidal vegetation together with mudflat geomorphology, thus improving our understanding of primary producers patterning (Brunier et al., 2022b; Douglas et al., 2024).

This study applied a drone-based RS approach to map *G. vermiculophylla* spatial distribution at a very-high spatial resolution (centimeter) in intertidal estuaries of European Atlantic coast. We adapted a neural network classification model, Drone Intertidal Substrate Classification Of Vegetation (DISCOV, (Oiry et al., 2024)) by re-training the model with new pixels of *G. vermiculophylla*. An *in situ* data validation dataset was obtained from French and Spanish sites to estimate the classification accuracy. LiDAR data were concurrently acquired to map accurately the intertidal elevation. A Generalized Linear Mixed Model (GLMM) was used to examine the relationship between *G. vermiculophylla* spatial distribution and information on the mudflat topography. We expected the presence of *G. vermiculophylla* in mudflats to be associated with a specific height range as well as being more closely related to flat areas of the intertidal zone. In the Belon estuary (South Brittany, France) where it was first observed in Europe, a time-series of aerial images, from 1952 to 2024, was analysed to describe the temporal changes of its distribution over the last seventy years.

4.2 Materiels & Methods

4.2.1 Study sites

Field campaigns were conducted at three study sites across France and Spain. At each site, two locations were investigated (Figure 4.1). The Aven & Belon estuaries in South Brittany, France (Figure 4.1 A & C) are dynamic ria-type systems hosting diverse habitats, including tidal flats and subtidal zones with coarse, marine-origin sediments (Castaing and Guilcher, 1995; Michel et al., 2021). These habitats support key benthic species such as *Scrobicularia plana*, *Cerastoderma edule*, and *Tellina tenuis*, which play essential roles in sediment bioturbation and nutrient cycling (Blanchet et al., 2014; Tankoua et al., 2011). These estuaries serve as a nursery for juvenile fish and a feeding ground for migratory birds, with their ecological productivity driven by a mix of euryhaline and marine species adapted to salinity gradients (Blanchet et al.,

2014). Oyster farming, particularly *Crassostrea gigas*, is a dominant activity, altering sediment dynamics and local biodiversity (Michel et al., 2021). Despite its ecological richness, the estuary faces pressures from nutrient loading and physical alteration (Tankoua et al., 2011).

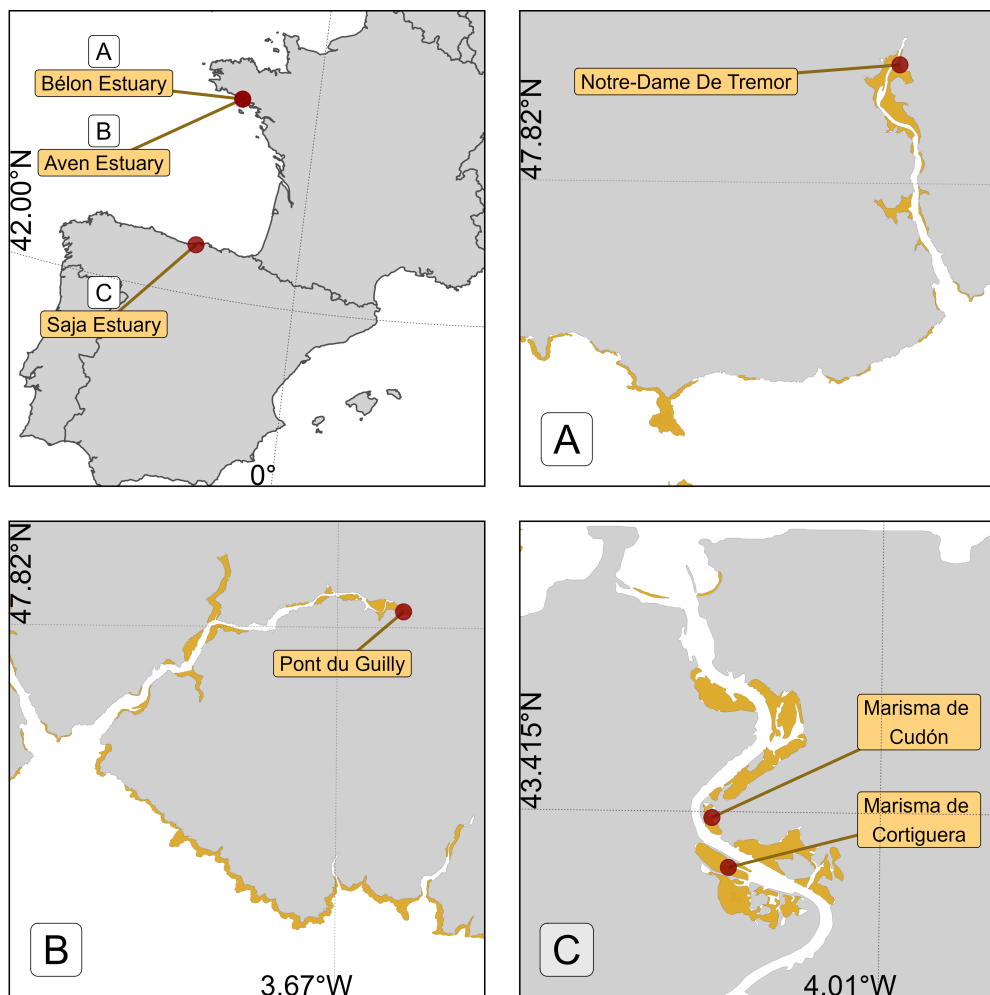


FIGURE 4.1: Location of the drone flights. A: Flights made in Aven Estuary, France; B: Flights made in Belon Estuary, France; C: Flights made in the Saja Estuary, Spain. Golden polygons represent intertidal areas.

The Saja-Besaya Estuary, situated along the Cantabrian Coast in northern Spain, is characterized by the confluence of the Saja and Besaya rivers near Torrelavega (Figure 4.1 C). The estuary, also known as San Martín de la Arena or Suances Estuary, has been subject to significant anthropogenic pressures, including industrial developments throughout the 20th century. These activities have led to contamination from mining, paper manufacturing, and carbonate discharges, classifying the estuary as highly polluted near its upper reaches (Ortega et al., 2005). This contamination

impacted the water quality and biodiversity, with minimal aquatic life and sparse riverbank vegetation in its lower sections (Romero et al., 2008).

4.2.2 Remote sensing data acquisition and pre-processing

4.2.2.1 Hyperspectral measurements

At each location, hyperspectral reflectance signatures were recorded using an ASD FieldSpec HandHeld 2 spectroradiometer (Malvern Panalytical, Worcestershire, UK), which measures reflectance from 325 to 1075 nm with a spectral resolution of approximately 1 nm (Figure 4.2 D). Each spectrum was subsequently smoothed using a Savitzky–Golay filter (Savitzky and Golay, 1964) with a third-order polynomial and an 11-point window, selected to minimize noise while preserving salient spectral features. After this initial smoothing, the first and second derivatives were computed using a central difference approximation (Equation 4.1).

$$R''(\lambda_i) \approx \frac{R(\lambda_{i+1}) - 2R(\lambda_i) + R(\lambda_{i-1})}{(\Delta\lambda)^2} \quad (4.1)$$

where $R(\lambda_i)$ is the reflectance at wavelength λ_i and $\Delta\lambda$ is the uniform spectral sampling interval.

4.2.2.2 Drone data

A total of four drone flights were conducted across the three study sites. All flights were performed at an altitude of 120 m and a speed of 10 m · s⁻¹. Two flights were carried out in the Saja Estuary on June 25, 2024, covering areas of 20.4 hectares (Marisma de Cortiguera) and 8.4 hectares (Marisma de Cudón), respectively (Figure 4.1). The other two flights took place in the Belon and Aven estuaries on April 11, 2024, covering areas of 21.3 hectares and 26.7 hectares, respectively.

4.2.2.2.1 Multispectral data

At each location, reflectance images with of 1.2 million pixels were captured using a DJI Matrice 300 quadcopter drone equipped with a Micasense RedEdge Dual MX multispectral camera. The camera recorded data across ten spectral bands, spanning from blue to NIR wavelengths (444, 475, 531, 560, 650, 668, 705, 717, 740, and 840 nm). To ensure consistent lighting conditions, the drone's flight trajectory was

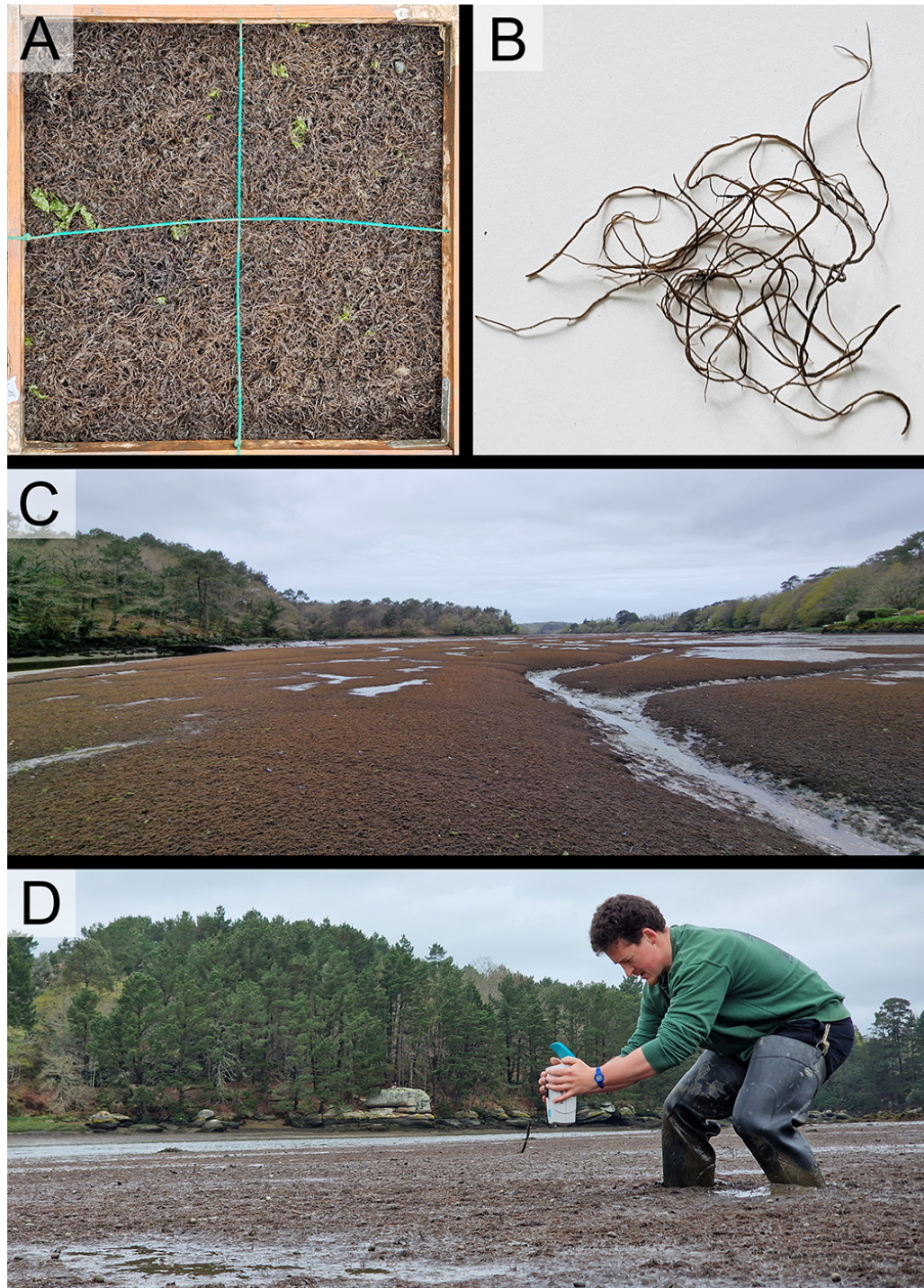


FIGURE 4.2: *Gracilaria vermiculophylla* in the Belon. A: Quadrat of 0.25 m² with a 100% cover of *G. vermiculophylla*; B: Single thallus showing cylindrical branches; C: Landscape view of mudflats covered by monospecific mats of *G. vermiculophylla*; D: Recording of the spectral signature of the algae using an ASD FieldSpec HandHeld 2 spectroradiometer.

aligned to maintain a solar azimuth angle of 90 degrees. Image acquisition was carried out with an overlap of 70% between side-by-side images and 80% between successive images along the flight path. A downwelling light sensor (DLS2) was used to measure real-time irradiance, enabling the correction of reflectance values for variations in light intensity caused by changing cloud cover during the flight. The raw image data were subsequently calibrated to reflectance using a calibration panel with ~50% reflectivity, provided by the camera's manufacturer. Images were processed using structure-from-motion photogrammetry software (Agisoft, 2019) to generate multispectral ortho-mosaics for each flight. The ortho-mosaicking workflow was consistent across all flights. Initially, key tie points were identified within each image and across overlapping images to create a sparse point cloud. This point cloud was refined by removing noisy points using a reprojection accuracy metric. Subsequently, a dense point cloud was generated using a structure-from-motion algorithm. A digital surface model (DSM) was then created through surface interpolation of the dense point cloud, which served as the basis for reconstructing the multispectral ortho-image (Nebel et al., 2020). The resolution of the multispectral ortho-mosaic obtained was 8 cm per pixel.

4.2.2.2.2 LiDAR data

Using the Matrice 300 Series Dual Gimbal Connector, a DJI Zenmuse L1 LiDAR and RGB sensor was mounted on the drone alongside the multispectral camera. This setup enabled the simultaneous capture of LiDAR point clouds, high-resolution RGB images, and multispectral images collected by the MicaSense RedEdge Dual MX during the same flight. The same processing workflow as Section 4.2.2.1 was applied to process LiDAR RGB images, resulting in ortho-mosaic with a resolution of 2.5 cm per pixel. Since the mapping focused solely on surfaces without dense vegetation, the LiDAR measured only a single return. Operating in repetitive scanning mode with a sampling rate of 240 kHz, the system achieved a point density of 350 points per square meter. The LiDAR point cloud was extracted and converted into LAS format using DJI Terra software. The LAS point cloud was then imported into Agisoft Metashape (Agisoft, 2019) to generate a DSM with a resolution of 2.5 cm. From the DSM, the inclination angle of each pixel based on a grid of 8 surrounding pixels was computed using the terrain function of the 'terra' package in R (Hijmans, 2024). The angle

of the mudflat was categorized into three classes: Flat (angle < 10°), Angled (10° angle – 40°), and Steep (angle > 40°).

4.2.3 Scene classification

In a previous study we developed a neural network classification model (DISCOV; Oiry et al. (2024)), which was successfully applied to Micasense reflectance data for mapping intertidal vegetation along the Portuguese and French Atlantic coasts. In this study, the DISCOV v1.0 algorithm architecture and training dataset were utilized and enhanced (Figure 4.3) to create DISCOV v2.0. Initially, DISCOV v1.0 model was trained with 5771 Rhodophyceae pixels, constituting only 3% of the training dataset (Oiry et al., 2024). To address this limitation, the training dataset for DISCOV v2.0 was expanded with 427.000 (Section 4.6.1) new training pixels collected from the four drone flights over *G. vermiculophylla*-dominated sites (Section 4.2.2).

To validate the DISCOV V2.0 model, a user-friendly Shiny app was developed. This app enabled independent users to photo-interpret snapshots of the ortho-mosaic from each drone flight (Chang et al., 2024; Oiry, 2024). Users could select on various parts of the snapshots to indicate the type of vegetation they believed was present. Using this method, three independent users helped create a validation dataset of 6755 pixels across 79 snapshots distributed among the four drone flights (Section 4.6.2). The validation dataset was then simplified into binary categories: the presence or absence of red macroalgae (Figure 4.3).

4.2.4 Historical Presence of *Gracilaria vermiculophylla* in the Belon estuary

To assess the historical presence of *G. vermiculophylla* in the Belon Estuary, aerial imagery from flight campaigns was obtained via the French “Institut National de l’information Geographique et forestiere” (IGN) platform “Remonter Le Temps” (IGN, 2024b). Nine images were selected between 1952 and 2012 from the IGN platform and an additional one has been added for the year 2024 (Section 4.6.3). As most of the images obtained from “Remonter Le Temps” were digitized versions of physical photographs, initial georeferencing was conducted manually using QGIS software (QGIS Development Team, 2024).

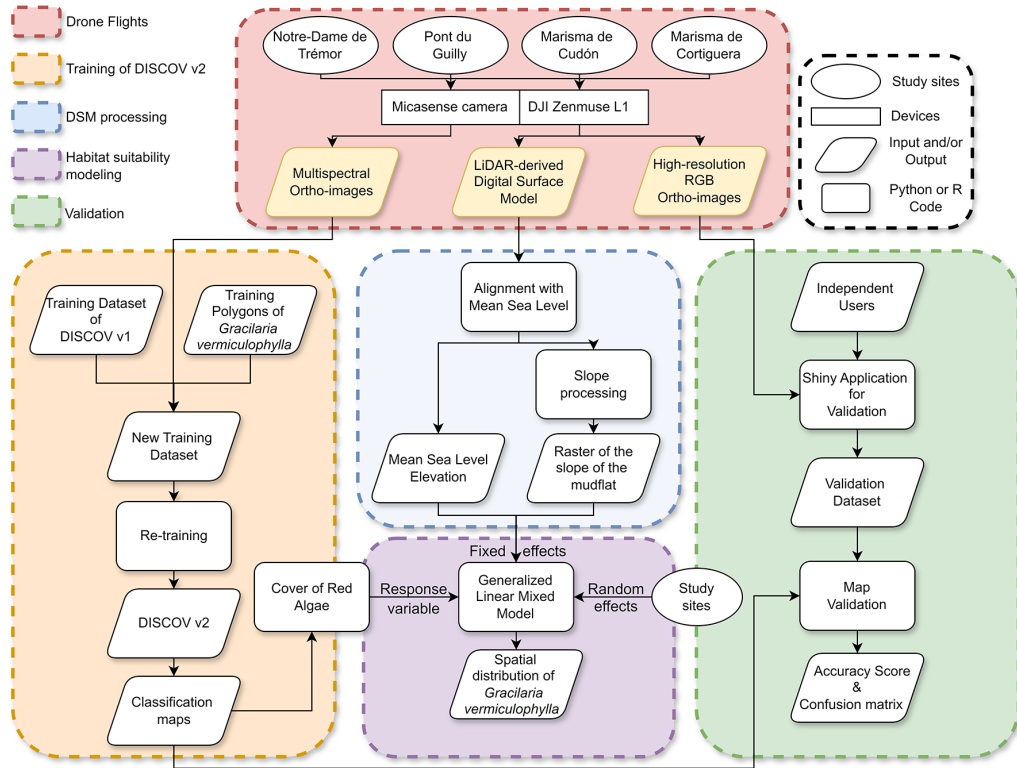


FIGURE 4.3: Schematic representation of the workflow. Parallelograms represent input or output data, rectangles represent Python processing algorithms, long rectangle represent instruments used and ovals represent study sites. Red shows Drone data; Orange shows the model training; Blue shows processing performed on the Digital Surface Model; Green shows the validation of the model; Purple shows the statistical analysis.

For each date, polygons have been drawn around *G. vermiculophylla* patches by visual photo-interpretation. These polygons were used to calculate the total area of the mudflat covered by macroalgae within a common extent of 30 hectares in Pont de Guilly, located in the Belon Estuary, South Brittany, France.

4.2.5 Statistical analysis

We used a GLMM within a Bayesian framework using the ‘brms’ package in R (Bürkner, 2021, 2018, 2017). The response variable, the cover of *G. vermiculophylla*, was modelled using a Beta distribution as a function of bathymetry elevation and the angle of the mudflat (categorized as Flat, Angled, Steep). A random intercept for site was included to account for potential hierarchical variation among sampling sites. The Beta distribution was chosen because the response variable was continuous and constrained between 0 and 1. We visually assessed sample vs. fitted residuals and quartile-quartile (Q-Q) plots to ensure that the model assumptions, including

appropriate model fit and absence of patterns in residuals, were satisfied.

4.3 Results

4.3.1 Historical records in the Belon estuary

A clear shift from bare sediment to vegetated mudflats has been observed over the past 70 years, corresponding to the colonization of the Belon Estuary by *G. vermiculophylla* (Figure 4.4). In the 50s, the tidal flats showed no detectable presence of vegetation. During the 70s some darkening of the sediment became discernible, but the first clear and unambiguous presence of *G. vermiculophylla* was recorded in 1982. During the subsequent decades, the cover of algae increased and in 2024, the high-resolution drone mapping showed that the mudflat was exclusively colonised by monospecific mats of *G. vermiculophylla*.

From the early recordings in the 1950s through the late 1970s, *Gracilaria vermiculophylla* coverage remained effectively at 0% (Figure 4.4). Shortly after the introduction of *Crassostrea gigas* in the estuary, in 1971-1972 (see vertical red dashed line in the figure), the first detectable presence of *G. vermiculophylla* emerged. By 1976, it covered 2.5% (0.7 ha) of the Pont du Guilly area, and by 1978 it had increased slightly to 3.0% (0.9 ha). From 1982 onward, coverage expanded more rapidly, increasing from 6.6% (2.0 ha) in 1982 to 14.7% (4.5 ha) in 1992 and nearly 30% (9.0 ha) by 1997. This upward trend continued into the 21st century, peaking at 41.2% (13.3 ha) in 2012. Although coverage fluctuated somewhat thereafter (40.6% in 2019 and 41.8% in 2024), it remained consistently high, indicating sustained and widespread colonization.

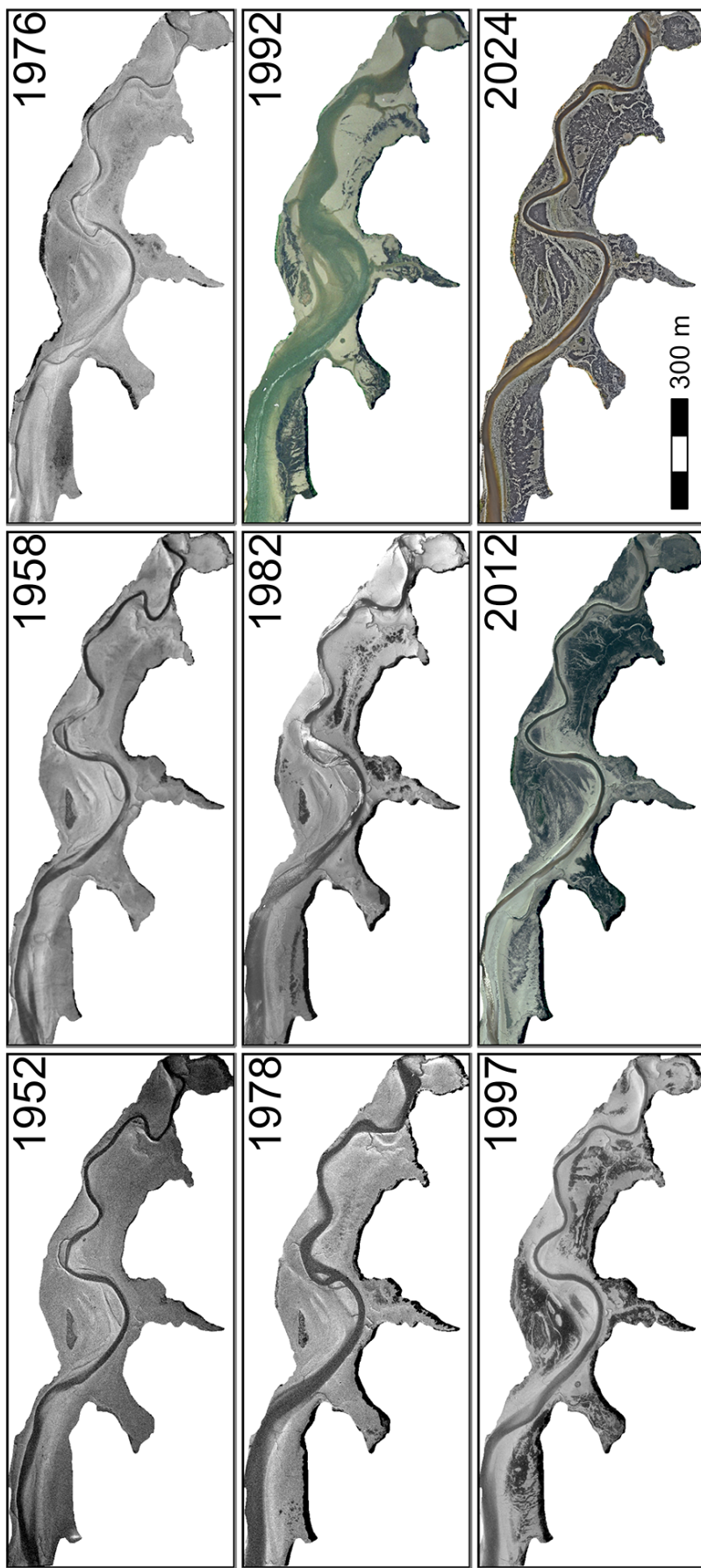


FIGURE 4.4: RGB images of the Belon Estuary (Pont de Guilly) showing the colonization of the mudflat by *Gracilaria vermiculophylla* between 1952 and 2024.

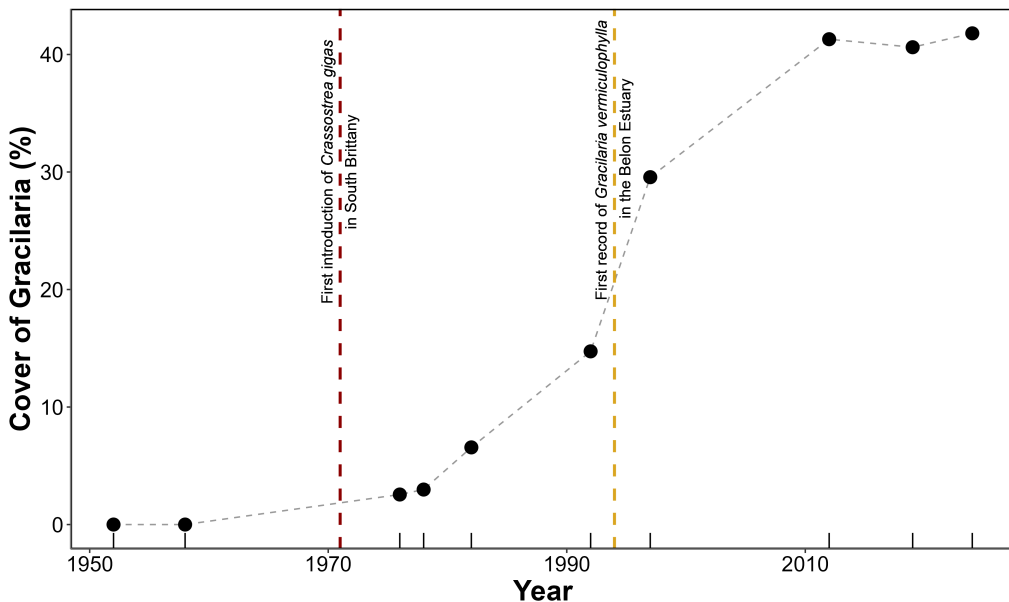


FIGURE 4.5: Trend of the *Gracilaria vermiculophylla* cover in the Belon Estuary (at Pont du Guilly). The red vertical line indicates the date of *Crassostrea gigas* introduction in South Brittany (Grizel and Heral, 1991), while the golden line represents the date of the first documented mention of *Gracilaria vermiculophylla* presence in Europe which was in the Belon Estuary (Rueness, 2005).

4.3.2 Spectral description

The spectral signature of *G. vermiculophylla* was characterized by a reflectance pattern in the visible region of the spectrum shaped by the photosynthetic and accessory pigments common to all rhodophytes (Figure 4.6 A). This pattern was primarily driven by phycoerythrin and phycocyanin, which exhibited maximum absorption peaks at approximately 565 nm and 620 nm, respectively. An additional absorption feature around 495 nm was likely attributable to carotenoid pigments. The most pronounced absorption peak occurred at 675 nm, corresponding to Chla absorption. The second derivative analysis clearly highlighted the inflection points corresponding to the main absorption peaks at 495, 565, 620, and 675 nm, allowing for more precise identification of the wavelength associated with these pigments (Figure 4.6 B).

4.3.3 Spatial distribution

The classification map obtained from the neural network algorithm is shown for the Belon estuary (Figure 4.7 A). Among the main classes of the intertidal vegetation,

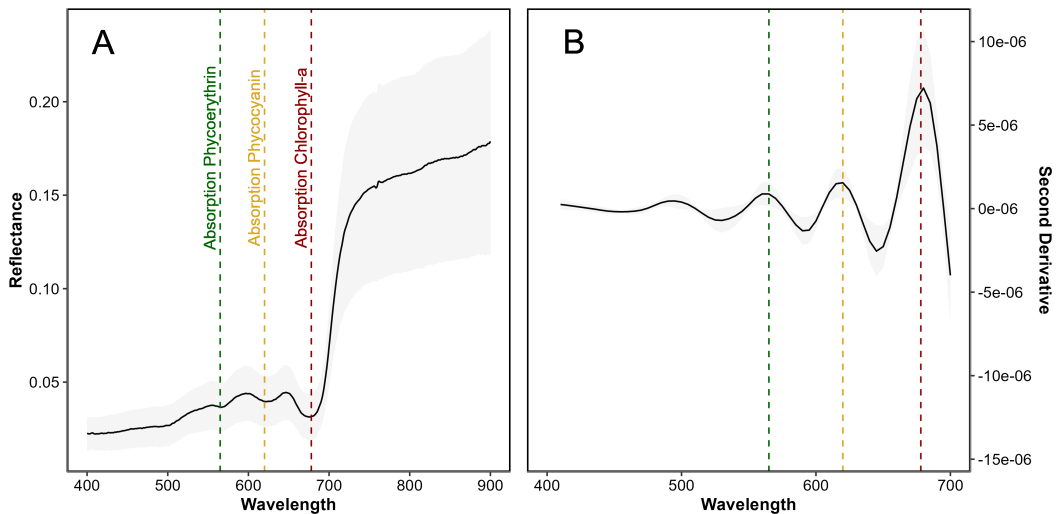


FIGURE 4.6: Hyperspectral signature of *Gracilaria vermiculophylla* (A) and its second derivative (B). The black line represents the average spectra, while the shaded area indicates the standard deviation. Dashed lines mark the absorption maxima of Phycoerythrin, Phycocyanin, and Chlorophyll-a, shown in green, orange, and red, respectively.

Rhodophyceae (red macroalgae) represented the dominant class cover, forming extensive, continuous patches colonizing almost the entire mudflat. In contrast, Bacillariophyceae (diatoms biofilm) and Chlorophyceae (Green macroalgae) exhibited more localized distributions, typically restricted to smaller, fragmented patches. A few areas covered by Phaeophyceae (brown macroalgae) were confined to small patches in the upper intertidal attached to rocks. In the Saja estuaray, Rhodophyceae cover was more sparse, due to a strong Chlorophyceae presence on this site (Annexe D: Section 4.6.4).

Across all study sites the presence/absence of *G. vermiculophylla* was classified with a global accuracy of 91.1 %, a sensitivity of 96.5 % and a specificity of 71.5 %.

The elevation map showed that the main mats of *G. vermiculophylla* were located between 1 and 2 m above mean sea level (Figure 4.7 C). The presence of red macroalgae was strongly influenced by the elevation, with lower intertidal zones closer to the tidal channel consistently exhibiting reduced cover. Most of the intertidal flats exhibited angle below 10° (Violet, (Figure 4.7 D). Angled surfaces ($10^\circ < \text{angle} < 40^\circ$) often found adjacent to tidal channels, exhibited almost no vegetation cover.

Overall, the percent cover of *G. vermiculophylla* increased with elevation, as shown by the general relationship (Figure 4.8, black line), which rises from approximately

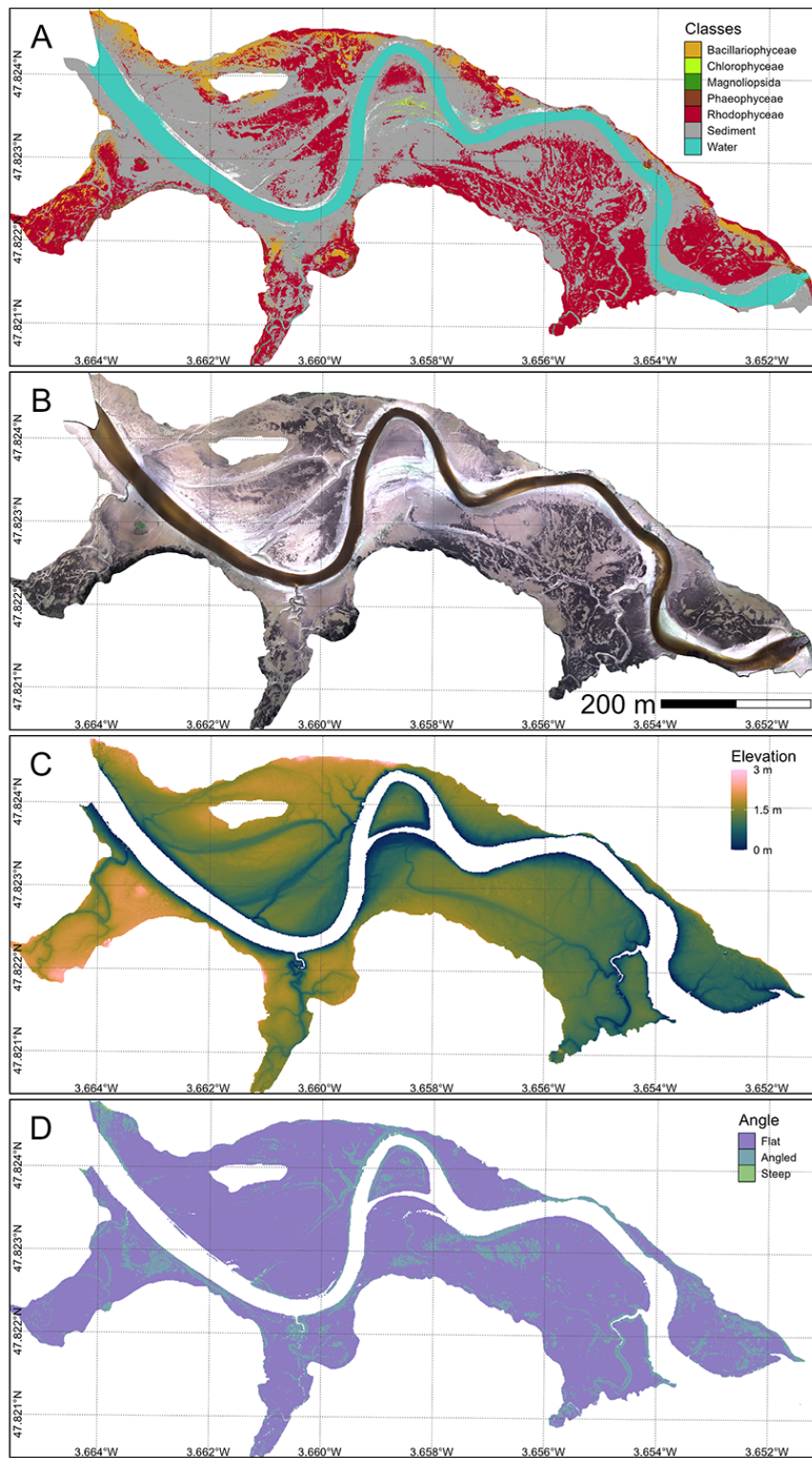


FIGURE 4.7: Classification of the main classes of intertidal vegetation with a neural network algorithm (A), RGB composition (B), Elevation (C) and mudflat topography (D) of the Belon estuary site in Brittany, France. The total extent of this flight was 21 hectares with a resolution of 8 mm per pixel. Elevation corresponds to the height above mean sea level.

16% at the lowest elevation to about 30% at the highest elevation. This indicates a consistent positive association between elevation and algal cover.

When accounting for the slope angle, it was demonstrated that the angle influences the coverage, the percent cover of *G. vermiculophylla* increasing as angles became flatter. Specifically, for flat angles, the cover ranged from approximately 20% at the lowest elevation to nearly 38% at the highest elevation. In contrast, the increase was less pronounced for angled slopes, ranging from around 16% to 32%. The lowest cover was observed on steep angles, starting at about 15% and rising only slightly above 30% at the highest elevation (Figure 4.8).

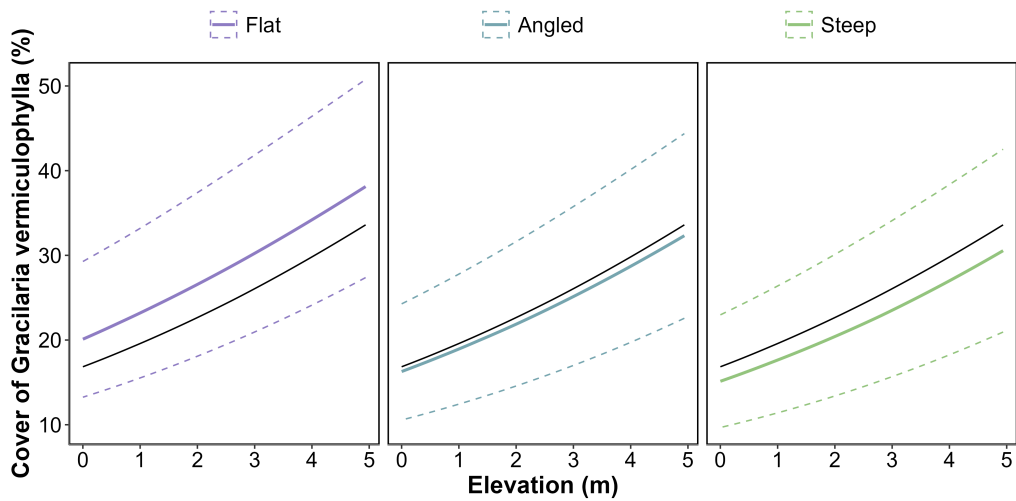


FIGURE 4.8: DISCOV Prediction (A), RGB composition (B) and Bathymetry (C) of the Belon estuary site in Brittany, France. The total extent of this flight was 21 ha with a resolution of 8 mm per pixel. Bathymetry is represented as the height above mean sea level.

4.4 Discussion

4.4.1 Drone mapping of *G. vermiculophylla* using machine learning approaches

In this study, we produced the first spatial distribution maps of the invasive red alga *Gracilaria vermiculophylla* using a multispectral drone survey conducted at low tide in Atlantic estuaries, representing varied environmental conditions. In French Brittany, the species formed monospecific mats, while in the Spanish Cantabrian region, it was intermixed with other intertidal vegetation. Distinguishing among these vegetation types was a key prerequisite for the analysis.

To achieve this, we developed a new version of the deep learning-based classification model DISCOV (Oiry et al., 2024). DISCOV v2.0 was based on an improved training dataset, which included a larger number of pixels on red algae covering approximately 26 % of one million pixels and allowed the model to achieve an accuracy of 91.1 % on predicting *G. vermiculophylla* presence.

Rhodophytes possess unique phycobilin pigments, enabling their spectral distinction from other macroalgal groups (Douay et al., 2022; Mcilwaine et al., 2019; Olmedo-Masat et al., 2020). Even with the ten-band multispectral sensor used in our study, it remained feasible to discriminate the major classes of intertidal vegetation (Davies et al., 2023a; Oiry et al., 2024; Román et al., 2021). Note that DISCOV V2.0 identifies *G. vermiculophylla* at the class level (Rhodophyceae) rather than at the species level. Although it is unlikely that *Gracilaria* can be precisely distinguished at species level using standard multispectral sensors (Douay et al., 2022; Olmedo-Masat et al., 2020), hyperspectral data may allow mapping on a finer taxonomic resolution.

Ecological factors also aided in identifying *G. vermiculophylla*. Unlike many other macroalgae that require hard substrates, *G. vermiculophylla* establishes itself on soft-bottom sediments. In fact, it is commonly found on mudflats, anchoring its thalli in the top 10 cm of mud (Surget, 2017), and inhabiting the upper intertidal zone—an unusual trait for a Rhodophyte (Abreu et al., 2011; Davoult et al., 2017). By effectively detecting *G. vermiculophylla* in these soft-substrate, upper intertidal habitats, our method provides a framework for identifying niche conditions that favour its spread. This information may provide managers with early-warning indicators to control its expansion before it reaches nuisance levels. Therefore, integrating spectral data with sediment characteristics serves as a strong indicator of *G. vermiculophylla* presence in European Atlantic estuaries, complementing the physical variables already used in species distribution modelling (Mendoza-Segura et al., 2023).

In addition, the scalability of drone-based surveying facilitates repeat mapping to detect temporal shifts in the distribution and abundance of *G. vermiculophylla*. Such continuous monitoring could capture seasonal patterns of colonization, allowing researchers and environmental managers to evaluate the effectiveness of mitigation measures, track long-term ecological impacts, and anticipate future shifts in habitat suitability under changing climate conditions.

4.4.2 *G. vermiculophylla* spatial distribution and mudflat topography

The spatial distribution of *G. vermiculophylla* across intertidal zones reveals a distinct relationship with mudflat topography, which significantly influences algal density and coverage. Our results show that higher elevations within the intertidal zone support greater densities of *G. vermiculophylla*. A pattern that aligns with findings by Thomsen et al. (2009), where elevated areas provided optimal conditions for algal survival. *G. vermiculophylla* demonstrates remarkable physiological plasticity, enabling it to tolerate a broad spectrum of environmental conditions, including temperature fluctuations (Sotka et al., 2018), nutrient variability (Abreu et al., 2011), and a wide range of salinities (Weinberger et al., 2008). Its capacity for sustained growth under low salinity conditions (Nyberg, 2007; Rueness, 2005) underpins its successful establishment and persistence within polyhaline and mesohaline estuarine environments. A strong constrain, however, for the algae is the hydrodynamism. Unlike seagrasses, another type of marine plant that can also colonize soft sediment, which possess rhizomes allowing for a robust anchorage, *G. vermiculophylla* lacks such specialized structures. Its attachment to the substrate relies solely on its buried thalli, which embed into the upper layers of soft sediment. This mode of anchorage renders the alga particularly vulnerable to high hydrodynamic conditions, as it lacks the structural stability needed to withstand strong currents or wave action. To partially bury its thalli into the sediment, *G. vermiculophylla* requires areas with high sedimentation rates. These conditions are typically found in the upper regions of estuarine systems or in proximity to other macrophytes, such as *Sporobolus* spp. (commonly known as small cordgrass), which reduce current velocity and promote sediment deposition (Mudd et al., 2010). This may explain the localization of one of the first areas colonized by *G. vermiculophylla* in the Belon estuary, observed in 1982-1992 near a patch of salt marsh (*Figure 4.4*). As a result, *G. vermiculophylla* compensates for its vulnerability to hydrodynamic forces by forming dense mats, which enhance its stability and facilitate its persistence and proliferation in intertidal and estuarine environments with low to moderate hydrodynamic conditions (Surget, 2017).

The negative relationship between angle steepness and the density of *G. vermiculophylla* can be explained by the physical and ecological characteristics of steeper mudflat areas. Steeper angles are typically associated with higher rates of water runoff

during tidal exchanges, resulting in stronger hydrodynamic forces. These forces can lead to increased sediment erosion, reduced sedimentation, and less stable substrate conditions, which are unfavourable for *G. vermiculophylla* to anchor its thalli effectively (Besterman et al., 2021). Furthermore, steeper angles may limit the retention of organic matter and nutrients, reducing the availability of essential resources needed for algal growth. In contrast, flatter areas within the intertidal zone are more likely to accumulate fine sediments and retain water for longer periods during low tides, creating a more stable and nutrient-rich environment conducive to *G. vermiculophylla* proliferation as well reduce desiccation effects. In turn, these conditions may favour the formation of dense algal mats, which further stabilize the sediment and promote growth.

4.4.3 Monitoring *Gracilaria vermiculophylla* Invasion Dynamics

The invasive red alga *G. vermiculophylla* represents a significant example of delayed recognition and documentation in biological invasions. Historical aerial imagery and photo-interpretation analyses from the Bélon Estuary suggest the initial presence of this species in 1976 (*Figure 4.4*), preceding by two decades its first formal description in European waters in 1996 (Rueness, 2005). This delay likely stems from insufficient early monitoring frameworks and limited awareness of its ecological impacts, which often characterize the early stages of invasive species colonization. It also arises from the fact that other red macroalgae species, resembling *G. vermiculophylla* and native to this area (e.g. *Gracilaria gracilis*) were already present at sites where *G. vermiculophylla* was introduced, further complicating its detection. This lag highlights challenges associated with the detection, monitoring, and reporting of invasive species and their ecological impacts during early colonization.

The appearance of *G. vermiculophylla* in 1976 coincides with the introduction of the Pacific oyster (*Crassostrea gigas*) into the estuary, a few years before, between 1971 and 1975, which was pointed as a potential the introduced the algae in Europe (Grizel and Heral, 1991; Rueness, 2005). Aquaculture practices, such as the transfer of oyster spat and equipment between regions, facilitate the unintentional transport of invasive algal fragments. For instance, *G. vermiculophylla* may have attached to shells or nets used in oyster farming, enabling its spread to new estuarine habitats. After initial establishment, in the 70's and early 80's (*Figure 4.4*), the alga progressively occupied suitable habitats, consistent with theoretical invasion dynamics involving a lag phase

followed by rapid spread in the 90's (Arim et al., 2006). The establishment of *G. vermiculophylla* likely induced changes in sediment characteristics, trophic interactions, and habitat structure prior to formal recognition (BenDor and Metcalf, 2006). Such shifts are comparable to documented impacts in similar systems (Crowl et al., 2008; Gallardo et al., 2016), yet remain difficult to quantify without early monitoring data. RS using multispectral drone mapping can provide high-resolution, spatially explicit data, but it must be combined with repeated, *in situ* field measurements to maximize its potential (Chadwick et al., 2020; Zoffoli et al., 2023, 2021). Temporal repetition makes it possible to assess dynamic processes, and integrating these mapping approaches with *in situ* analyses of local infauna, carbon cycling, riverine inputs, and sedimentology yields valuable data for local managers. Such an integrated approach can determine how the invasive algae affects the local ecosystem and, more broadly, forecast its potential impact on other estuarine environments facing similar invasion events.

The temporal gap between the first presence and documentation reflects limitations in early surveillance, potentially underestimating ecological and economic impacts during the initial colonization phase. Studies on invasion dynamics demonstrate that early detection is crucial for effective containment and management, particularly before an invasion reaches the exponential spread phase, which complicates control efforts (Arim et al., 2006; BenDor and Metcalf, 2006; Elton, 2020). Specific practices, such as the removal of early-stage algal mats, implementation of physical barriers to prevent further spread, and public awareness campaigns, could mitigate the impacts during this critical phase (Green and Grosholz, 2021; Jones et al., 2021; Simberloff, 2021). In the Belon Estuary, *G. vermiculophylla* appears to have thrived under ecological conditions favourable to its proliferation, enabling the formation of dense mats in about 6 years (between 1976 and 1982; *Figure 4.4*) after its first detection in the estuary. This undocumented growth likely contributed to substantial changes in the estuarine ecosystem. Historical aerial imagery has provided valuable insights into long-term invasion patterns by enabling the retrospective identification of shifts in habitat characteristics. Modern drone-based systems enhance this capacity through high spatial and temporal resolution, enabling the rapid detection of invasive species at early stages of establishment. By capturing detailed data on the spatial distribution and habitat preferences of species such as *G. vermiculophylla*, RS facilitates timely

interventions, allowing stakeholders to take rapid measures to limit the invasion. Integrating these tools into routine monitoring programs offers a scalable and efficient means to track invasive species dynamics and inform targeted management strategies, such as habitat restoration, removal of invasive mats, and prevention of further spread through targeted interventions. Expanding these methodologies to lower-cost RGB-based detection would further democratize access to monitoring tools, enabling more widespread application for early detection and rapid response. These tools could also be integrated into community-driven management programs, empowering local stakeholders to monitor invasive species and implement timely control measures.

4.5 Conclusion

In this study, we demonstrated the potential of high-resolution drone-based multispectral RS to map the spatial and temporal distribution of the invasive red macroalga *G. vermiculophylla* in European estuaries. By releasing the DISCOV v2.0 model, updated to include an extensive dataset of Rhodophyceae pixels, we achieved a classification accuracy of 91.1%. Our analysis revealed a clear spatial relationship between *G. vermiculophylla* and intertidal topography retrieved from LiDAR, with its cover consistently higher in flat, elevated mudflats compared to lower and steeper areas. The remarkable physiological plasticity of *G. vermiculophylla* enabling it to thrive in diverse environmental conditions, further underscores its adaptability and invasive potential. However, its reliance on sediment stability and vulnerability to hydrodynamic forces delineate its preferred habitat with the intertidal zones.

The temporal progression, derived from a historical dataset spanning over seven decades, highlights the progressive establishment and expansion of the algae. Notably, our aerial imagery analysis confirmed the presence of *G. vermiculophylla* in the Belon Estuary approximately 20 years before its first scientific description, emphasizing the value of retrospective mapping.

This historical analysis provided crucial insights into the dynamics of *G. vermiculophylla*'s invasion, revealing a lag phase followed by rapid colonization. This expansion coincided with the development of oyster aquaculture, suggesting a potential link between human activities and the proliferation of this invasive species. These findings underscore the crucial role of RS in ecological research, particularly in studying invasive species. By leveraging high-resolution, scalable technologies, we can not only

map current distributions but also uncover historical patterns that would otherwise remain unknown. The identification of *G. vermiculophylla* decades prior to its formal description exemplifies this capability. This discovery provides a compelling basis for re-evaluating historical data to understand the broader implications of invasive species dynamics. Moving forward, integrating hyperspectral sensors could enhance species-level discrimination, while adopting low-cost RGB-based methods could extend monitoring capacities to a broader range of stakeholders. Incorporating these advancements into environmental management frameworks can enable proactive monitoring, timely interventions, and habitat restoration efforts. These advancements will be crucial for informing management strategies, fostering community engagement, and preserving estuarine biodiversity in the face of ongoing ecological changes.

| Name | Taxonomic Class | Training Pixels | Difference with DISCOV v1.0 |
|------------------|-------------------|-----------------|-----------------------------|
| Benthic Diatoms | Bacillariophyceae | 62,436 | x13.95 |
| Green macroalgae | Chlorophyta | 92,585 | x5.4 |
| Seagrass | Magnoliopsida | 221,065 | - |
| Brown macroalgae | Phaeophyta | 169,936 | - |
| Red macroalgae | Rhodophyta | 268,637 | x46.55 |
| Sediment | - | 117,956 | x1.24 |
| Water | - | 91,614 | x1.09 |

TABLE 4.1: Annexe 4.1 - Class of the Neural Network model, with the number of training pixels used to train that class and the differences with the training dataset of DISCOV v1.0

4.6 Annexes

4.6.1 Annexes A - Updated training dataset

| Site | Absent | Present | Total |
|-----------------------|--------|---------|-------|
| Marisma de Cortiguera | 1,531 | 483 | 2,014 |
| Marisma de Cudón | 1,237 | 136 | 1,373 |
| Notre-Dame De Tremor | 1,073 | 463 | 1,536 |
| Pont de Guilly | 1,389 | 443 | 1,832 |
| Total | 5,230 | 1,525 | 6,755 |

TABLE 4.2: Annexe 4.2 - Presence and absence of red macroalgae for each drone flight

4.6.2 Annexes B - Validation dataset

4.6.3 Annexes C - List of historical images records

TABLE 4.3: Annexe 4.3 - Images used to assess the historical presence of *Gracilaria vermiculophylla* in the Belon estuary. Images from the IGN data source have been retrieved from the “Remonter Le Temps” platform (IGN, 2024b). Drone flight have been performed by the team using a Mavic 3 Entreprise.

| Date | Type | Data Source | Resolution (cm per Pixel) |
|------------|-----------------|--------------|---------------------------|
| 1952-04-26 | Black and White | IGN | 10 |
| 1958-04-22 | Black and White | IGN | 90 |
| 1976-07-? | Black and White | IGN | 4 |
| 1978-08-22 | Black and White | IGN | 44 |
| 1982-08-11 | Black and White | IGN | 44 |
| 1992-05-17 | True Colour | IGN | 70 |
| 1997-04-11 | Black and White | IGN | 64 |
| 2012-07-24 | True Colour | IGN | 18 |
| 2024-04-11 | True Colour | Drone Flight | 3 |

4.6.4 Annexes D - Maps of the Saja estuary, Spain

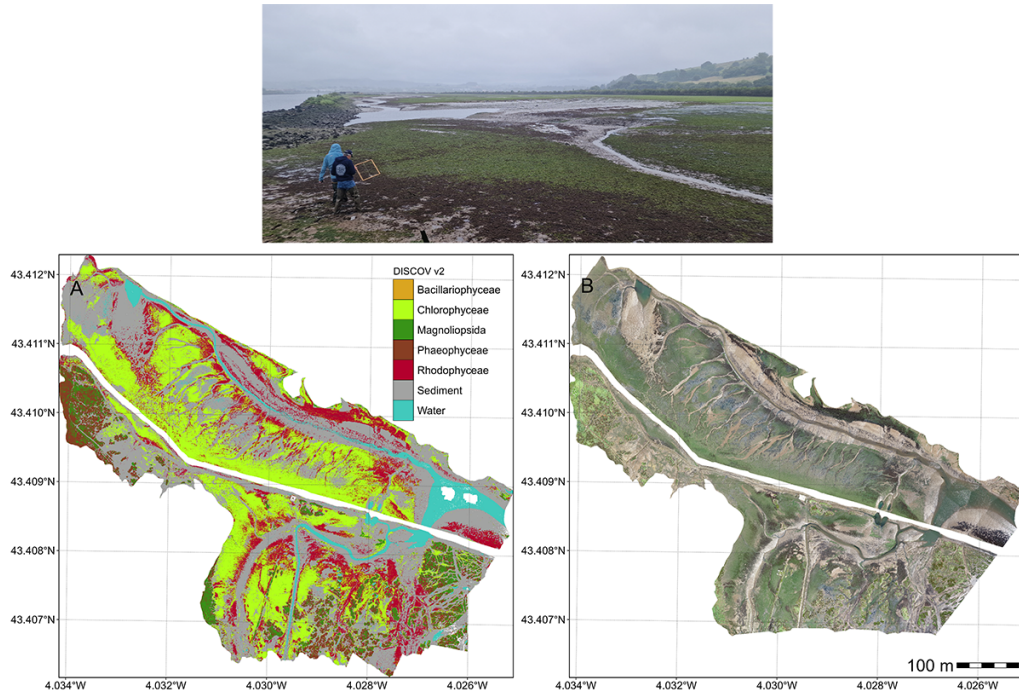


FIGURE 4.9: Annexe 4.4 - DISCOV Prediction (A), RGB composition (B) and picture of the field campaign of the Saja estuary, Northern Spain. The total extent of this flight was 20.4 ha with a resolution of 8 mm per pixel.

5

**The impact of Heatwave on Seagrasses using
hyperspectral and multispectral remote sensing**

5.1 Introduction

Seagrasses play a crucial role in coastal ecosystems by providing habitats and feeding grounds for various marine species, supporting marine biodiversity, and contributing to primary production and carbon sequestration (Sousa et al., 2019; Unsworth et al., 2022). Seagrasses are essential for several ecological functions, such as sediment stabilization (Infantes et al., 2022) or eutrophication mitigation by consuming nutrients (Gladstone-Gallagher et al., 2018). This justifies their use as indicators of environmental changes due to their sensitivity to water quality variations (Zoffoli et al., 2021). The interactions between seagrass meadows and their associated herbivores further enhance the delivery of ecosystem services, including coastal protection, fisheries support and provision of habitat and resources for birds (Gardner and Finlayson, 2018; Jankowska et al., 2019; Unsworth and Butterworth, 2021; Zoffoli et al., 2023). Understanding and preserving seagrass is vital for maintaining the biodiversity and productivity of coastal regions (Ramesh and Mohanraju, 2020; Scott et al., 2018).

Despite their crucial role in marine ecosystems, seagrasses face numerous threats that compromise their health and functionality. These habitats are subjected to a combination of aquatic and aerial conditions, facing impact from terrestrial and aquatic stressors. Coastal development and human activities are primary threats, reducing the available habitat for seagrasses and increasing water turbidity, limiting light penetration and photosynthesis (Waycott et al., 2009). Seagrasses are also threatened by runoff from agricultural fields and urban areas leading to nutrient enrichment. Eutrophication promotes the growth of seaweed in coastal waters, causing macroalgal blooms that compete with seagrasses for light and nutrients (Oiry et al., 2024; Thomsen et al., 2023). Pollution from industrial and agricultural sources introduces harmful chemicals and heavy metals into coastal waters, posing toxic risks to seagrass health (Bastos et al., 2023; Green et al., 2021; Zahoor and Mushtaq, 2023). Among manifold anthropogenic stressors, heatwaves (HWs), exacerbated by climate change, pose a severe threat to seagrasses, with catastrophic dieback events observed worldwide (Carlson et al., 2018; Marbà and Duarte, 2010; Moore and Jarvis, 2008; Strydom et al., 2020; Thomson et al., 2015).

Marine Heatwaves (MHWs) are defined by Hobday et al. (2016) as prolonged discrete anomalously warm water events while Atmospheric Heatwaves (AHW) are defined by

Perkins and Alexander (2013) as periods of at least three consecutive days with temperatures exceeding the 90th percentile of a time series covering at least 30 years. In shallow waters, subtidal seagrass meadows are exposed to MHWs, whereas at the interface between land and ocean, intertidal seagrasses are exposed to both MHWs and AHWs. HWs profoundly impact seagrass physiology, with effects varying between species and geographic location. Widespread seagrass species such as *Zostera marina* exhibits high susceptibility to elevated SST during winter and spring, leading to advanced flowering, high mortality rates, and reduced biomass (Sawall et al., 2021). Similarly, *Cymodocea nodosa* shows increased photosynthetic activity during HWs but suffers negative effects on photosynthetic performance and leaf biomass during recovery (Deguette et al., 2022). Additionally, different populations of *Zostera marina* along the European thermal gradient exhibit varied photophysiological responses during the recovery phase of HWs, indicating differential adaptation capabilities among populations (Winters et al., 2011). These events intensify other stressors, such as overgrazing and seed burial, compromising recruitment (Guerrero-Meseguer et al., 2020).

The increased occurrence of extreme climate events calls for the implementation of monitoring strategies able to provide detailed and spatially explicit assessments of HWs effects on seagrass meadows. In such context, RS, whose ability to map seagrass distribution over a variety of spatio-temporal scales has been demonstrated (Davies et al., 2024b, 2024a; Oiry et al., 2024; Román et al., 2021), proved useful to study the changes in seagrass coverage caused by extreme HW event (Strydom et al., 2020). In complement to its ability to measure the spatial distribution of post-heatwave seagrass loss, we hypothesize that RS has the potential to detect more subtle changes, such as the browning of seagrass leaves. The pigment composition of plants, such as chlorophylls, carotenoids, and anthocyanins, significantly influences their spectral signature in the visible range due to their specific light absorption properties (Davies et al., 2023a; Douay et al., 2022; Olmedo-Masat et al., 2020; Ustin and Jacquemoud, 2020). During senescence phase, the degradation of Chla and the unmasking of accessory pigments result in noticeable changes in leaf coloration and reflectance, including increased reflectance in the red and green wavelengths and shifts in the red-edge position (Boyer et al., 1988; Mariën et al., 2019; Peñuelas et al., 2004). Leaf browning, often observed after stress events, produces reflectance changes similar to those caused by senescence, enabling the detection of vegetation stress through

RS (Boyer et al., 1988; Peñuelas et al., 2004). Spectral indices such as the Brown Pigment Index (BPI) and the Photochemical Reflectance Index (PRI) have been developed to assess changes in terrestrial plant physiological status, including oxidative and drought stress (Garbulsky et al., 2011; Skendzic, 2023). While these effects are well-documented in terrestrial plants, the spectral reflectance changes associated with senescence and stress events such as MHWs or AHWs remain poorly studied on intertidal seagrasses.

This study aims to experimentally test the hypothesis that HWs alter the reflectance of the intertidal seagrass *Zostera noltei*. Controlled experiments in intertidal chambers were conducted to evaluate the direct impact of heat stress on seagrass reflectance. The findings were then applied to satellite RS images, providing critical insights into the spatial extent and temporal dynamics of HW effects on seagrass meadows. By linking experimental results with large-scale observations of seagrass leaves' browning, the study underscores the potential of RS to enhance our understanding of seagrass responses to extreme thermal events across diverse settings and timescales.

5.2 Materials & Methods

5.2.1 Laboratory Experiment

5.2.1.1 Sampling and acclimation of seagrasses

Seagrass samples were taken in summer 2024, at low tide, from a *Zostera noltei* (dwarf eelgrass) meadow located in Bourgneuf Bay, France (46°57'32.0"N, 2°10'37.0"W). A metal sampling box was used to sample seagrass from an area of 30x15 cm and 5 cm deep, maintaining the sediment structure and avoiding damage to seagrass rhizomes and leaves (Figure 5.1 A). This sampling box reduced the variability between each sample replicates. Samples including seagrass, sediment, meiofauna, and macrofauna, were placed in plastic trays. Keeping the entire biota allowed for natural interactions between components and reduced stress on the seagrass. Seawater was added to each tray to avoid hydric stress caused by insufficient moisture during transportation (1h drive from the laboratory). Simultaneously, seawater was sampled from a nearby site and transported to the lab, where it was filtered using a 0.22 µm nitrocellulose filter to remove suspended particulate matter. The filtered seawater was used in the acclimation tank and the intertidal chambers. The seagrasses were acclimated during

one week with a water temperature of 17°C, matching the *in situ* temperature during sampling, and a Photosynthetically Active Radiation (PAR) of 150 $\mu\text{mol.s}^{-1}.\text{m}^{-2}$. (Akbar et al., 2020).

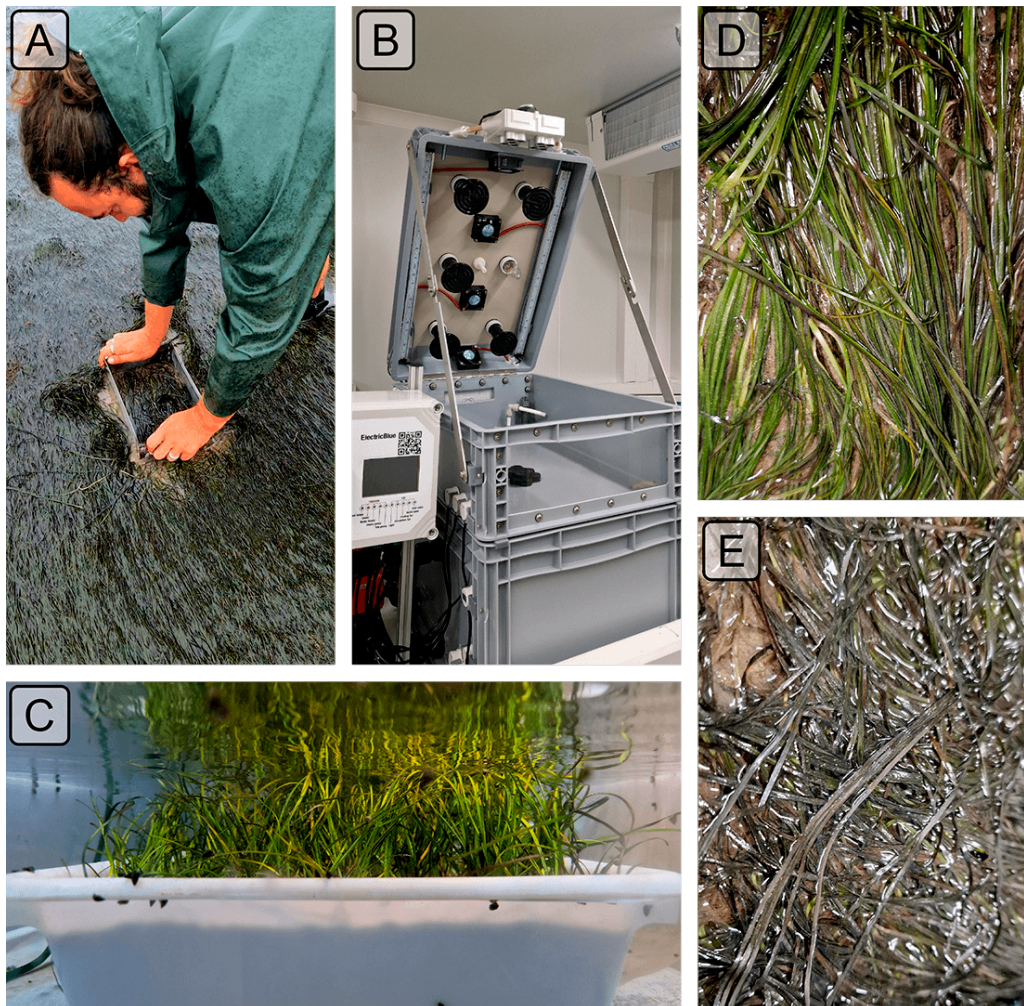


FIGURE 5.1: Illustration of the experiment. A: Seagrass field sampling using a coring device; B: Intertidal chamber used during the experiment; C: Seagrass sample inside a chamber during the experiment at high tide; D: Treatment sample at the start of the experiment; E: Treatment sample at the end of the experiment, 2 days after the start of the HW event.

5.2.1.2 Experimental design

A tidal cycle (i.e. regularly alternating 6h of low tide and 6h of high-tide) was simulated in the laboratory using an intertidal chamber system from ElectricBlue® (Electric Blue, 2023). The transition between low tide and high tide is binary and took about 15 minutes to be completed when initiated. During the phase of high tide, a volume of 30 L of filtered seawater was pumped and circulated through the chamber (Figure 5.1 B, C). During low tide, the seagrass sample was emerged. The acclimated

seagrasses were split into two subsets and placed in two independent chambers used in parallel, with one chamber used for control and the other for the experimental treatment. The intertidal chambers were equipped with LED lights that emitted low red and IR radiation. To achieve a PAR intensity of up to $400 \text{ mol} \cdot \text{m}^{-2} \cdot \text{s}^{-1}$, a filament bulb was added inside the chambers. During the diurnal phase of the experiment, the PAR was kept constant in both intertidal chambers. To follow the circadian cycle, light was turned on and off each day, at the time of sunrise and sunset, respectively.

Air temperature and water temperature were controlled inside the experiment chambers, in order to reproduce the range of variability observed in the field. Field temperature was measured using *in situ sensors* (T7.3 EnvLoggers from ElectricBlue®) deployed at the sampling site in August 2024. In complement, the temperature daily maxima recorded *in situ* were compared with measurements from the nearest Météo France weather station (Annexe A1, Section 5.6.1). The control chamber was kept at temperatures representing typical seasonal conditions, with water temperatures at 18°C and air temperatures from 19°C to 23°C , following natural daily temperature fluctuations (Figure 5.2). For the experimental treatment, the air temperature was adjusted to mimic an AHW that affected the seagrass meadow in Quiberon, South Brittany, France ($47^\circ 35' 40.0''\text{N}$, $3^\circ 07' 30.0''\text{W}$), from September 2 to September 6, 2021. Air temperature in the experimental chamber was set to vary from 23°C (at night) to 35°C (daytime) during the first day of the experiment, and increase by 1°C daily during three consecutive days. Water temperature in the experimental chamber was adjusted to mimic MHW conditions, starting at the seasonal baseline (18°C) and rising incrementally by 0.5°C daily to simulate the increasing temperatures during the event. This aimed to reproduce the thermal stress experienced by the seagrass meadow during a MHW (Figure 5.2). The experiment was repeated three times to obtain replicates (hereafter referred to as “Run”).

5.2.1.3 Optical measurements

5.2.1.3.1 Hyperspectral reflectance measurements

Throughout the experiment, the hyperspectral reflectance, $R(\lambda)$, of both the control and treatment seagrasses was measured using an ASD HandHeld 2 equipped with a fiber optic extension placed inside the chamber. The measurement set up made it possible to automatically acquire $R(\lambda)$ without opening the chamber. An average of

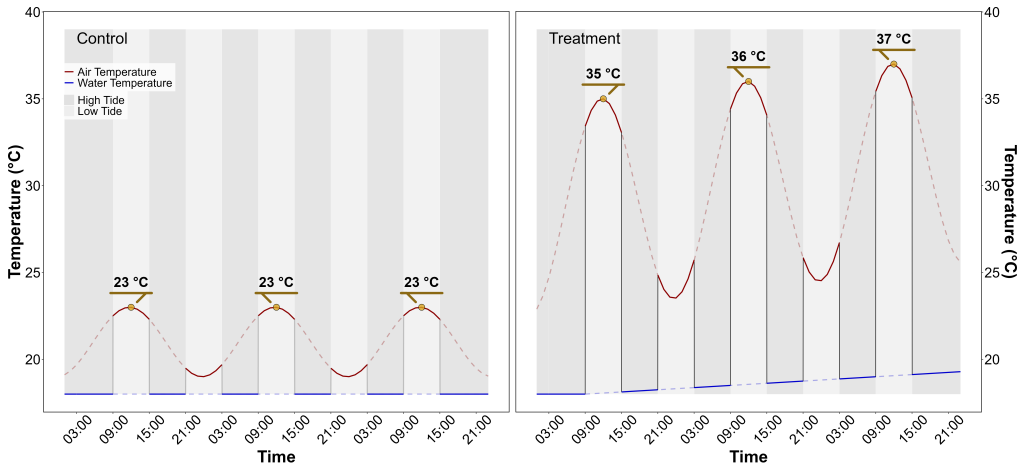


FIGURE 5.2: Temperature variation in the control (left) and treatment (right) intertidal chambers, during the HW experiment. The red line indicates air temperature, and the blue line water temperature. Due to the tidal cycle of immersion / emersion the seagrasses experienced the temperatures represented by solid lines.

five $R(\lambda)$ spectra, each with an integration time of 544 ms, was taken every minute during daytime (Malvern Panalytical, 2023). Every 10 minutes, the fiber optic was switched from one intertidal chamber to the other, in order to measure $R(\lambda)$ in both the treatment and control. Light conditions were controlled inside of the chambers and the reflectance calibration was performed each morning at the very first moment of low tide using a Spectralon white reference with 99% Lambertian reflectivity.

5.2.1.3.2 Spectrum post-processing

A Savitzky-Golay smoothing function with a 5 nm moving window was applied to each spectrum using the “hsdar” package in R (Lehnert et al., 2017). The second derivative at 665 nm, showing the highest variability between the control and the treatment, was tested as an indicator of the spectral changes following HWs

The effect the HW on $R(\lambda)$ was also quantified using two radiometric indices:

- The Normalized Difference Vegetation Index (NDVI, Rouse et al., 1974), a proxy of Chla concentration (Equation 1.2)
- The Green Leaf Index (GLI, Louhaichi et al. (2001)), a quantification of the seagrass leaves greenness (Equation 5.1)

$$GLI = \frac{[R(550) - R(668)] + [R(550) - R(450)]}{(2 \times R(550)) + R(668) + R(450)} \quad (5.1)$$

where $R(550)$ and $R(450)$ are the reflectance in the green (at 550 nm) and in the blue (at 450 nm) spectral bands, respectively. (Davies et al., 2023a) Based on the observed spectral changes in seagrasses exposed to HWs, we developed a new radiometric index to better detect the radiometric caused by the HW. The browning of the leaves was characterized by substantial radiometric changes in both the green and red-edge spectral regions. The seagrass Heat Shock Index (SHSI) was introduced as the reflectance line height at 740 nm, compared to the 560 - 842 nm baseline (Figure 5.3). Namely the SHSI subtract the reflectance observed at 740 nm to the interpolated reflectance between 560 and 842 nm, so that the index is positive in the case of brown, HW-impacted seagrass leaves, and negative in the case of green, non-impacted leaves:

$$\text{SHSI} = I_{SHSI} - R(740) \quad (5.2)$$

where :

$$I_{SHSI} = R(560) + \tau[R(842) - R(560)]$$

and :

$$\tau = \frac{740 - 560}{842 - 560}$$

where $R(560)$, $R(740)$, and $R(842)$ represent the reflectance at 560, 740, and 842 nm, respectively. These wavelengths were selected to align with the spectral resolution of satellites missions such as Sentinel-2, for broader RS application.

5.2.2 Observation of a seagrass bed impacted by a HWs

Field measurements were taken the 10th of September 2021 after an AHW and MHW in order to assess the impact of heat stress on seagrass. The study site was a seagrass meadow near Quiberon (France : 46°57'32.0"N, 2°10'37.0"W, Figure 5.4). Brown seagrass leaves were observed over large patches of the meadow alongside areas covered by green seagrass (Figure 5.5). A total of 96 Quadrat Points (QPs) were collected as georeferenced quadrat images across the meadow. These images allowed for visual assessment of vegetation type, density, and coloration. The quadrats were then divided into two categories: green seagrasses (henceforth: QPs unimpacted) and brown

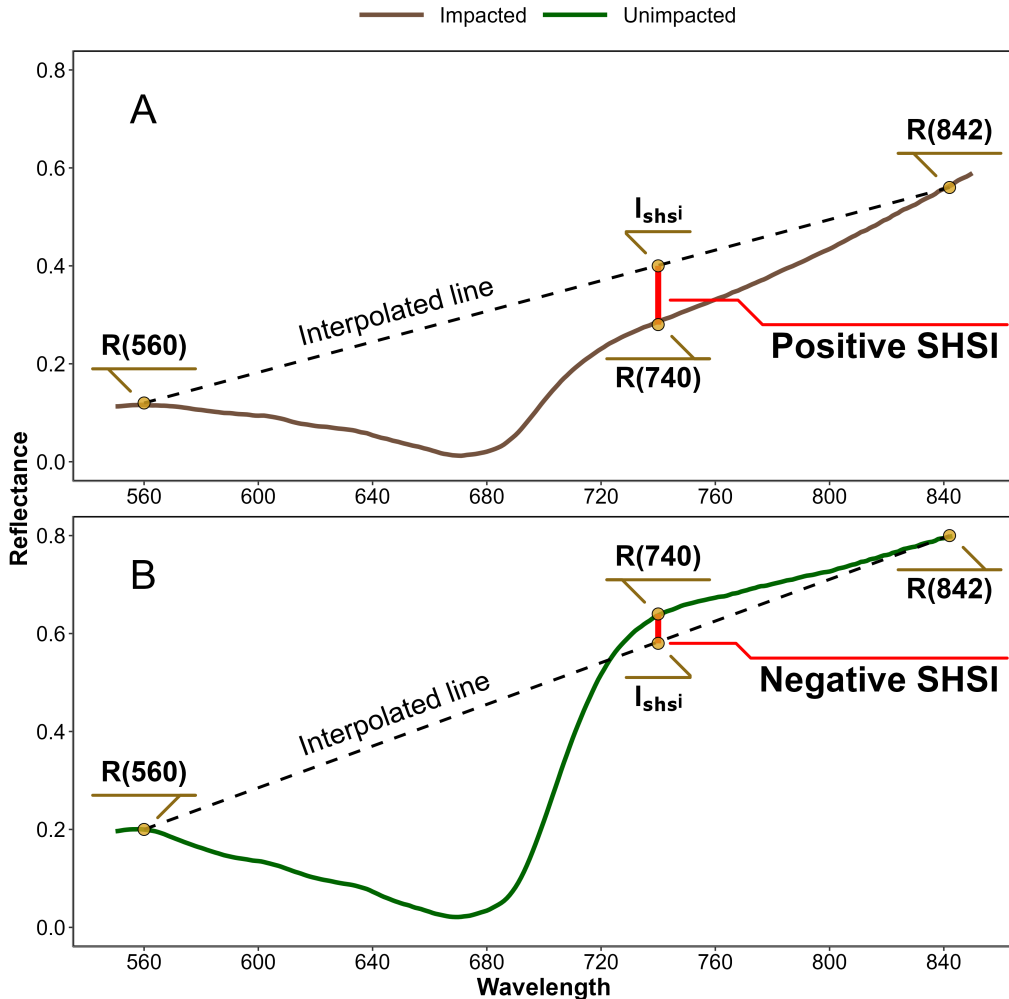


FIGURE 5.3: Computation of the reflectance Seagrass Heat Shock Index (SHSI) for Impacted (A) and Unimpacted (B) seagrass leaves. The dashed line represents the reflectance interpolation between 560 and 842 nm. The red vertical at 740 nm represents the SHSI line height.

seagrasses (henceforth: QPs impacted), based on a visual estimation of the leaf coloration (Figure 5.4).

5.2.2.1 Temperature data and HW detection

5.2.2.1.1 Air temperature

Since 2024, Meteo France weather data has been freely and openly accessible. Hourly air temperature data from a nearby weather station (Lorient-Lann Bihoue, 47°45'46"N 3°26'11"W) was retrieved using a custom script as no API was available at the time of this study. For this station more than 395,000 hourly observations were available since 1952.

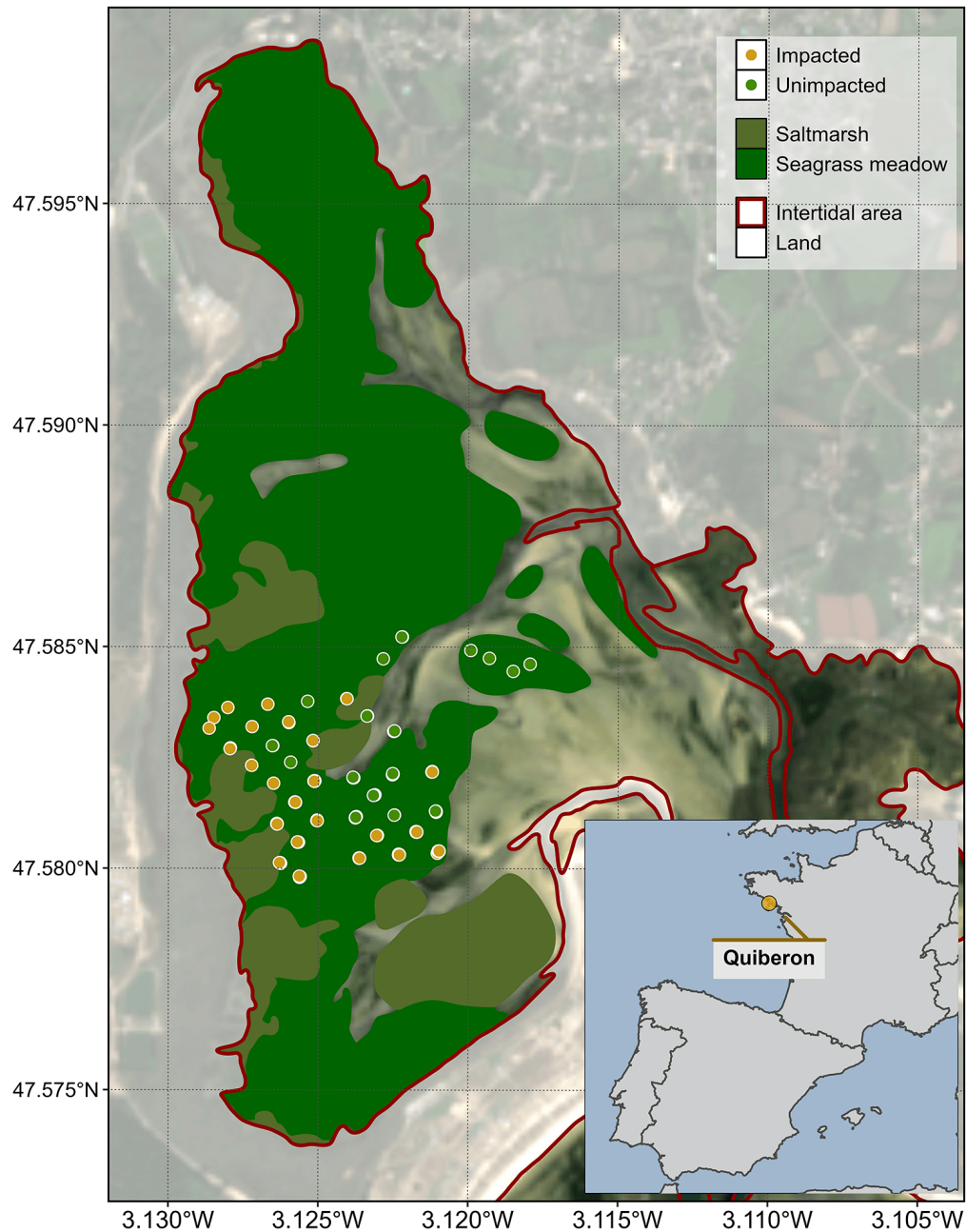


FIGURE 5.4: Location of field observation in a seagrass meadow impacted by a HW that occurred on the 10th of September 2021 in Quiberon, South Brittany, France. The red line indicates the intertidal zone (Zone between high tide and low tide, exposed during low tide), the dark green area indicates the extent of the seagrass meadow and the olive polygons indicate saltmarshes. Green points indicate the location of quadrat pictures over unimpacted seagrasses (i.e. showing a green colour on the field), and orange points indicate the location of quadrats taken over impacted seagrasses (i.e. showing a brown color on the field, Figure 5.5).

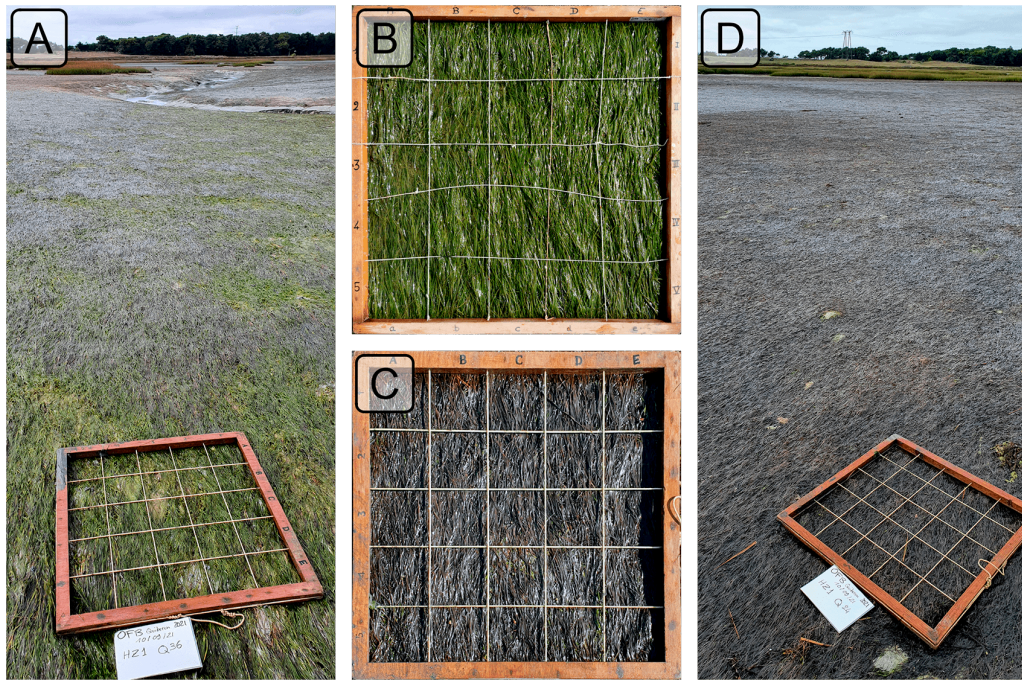


FIGURE 5.5: Illustration of the two colorations of seagrass leaves observed *in situ* the 10th of September 2021 after a heatwave in Quiberon, South Brittany (France). A: Picture of a zone with both green and brown seagrass; B: Seagrass quadrat with green leaves; C: Seagrass quadrat with brown leaves; D: Picture of a zone where all leaves turned brown.

5.2.2.1.2 Water temperature

SST data from 1982 -2022 was downloaded from the Copernicus Marine Data Store (Copernicus Marine Environment Monitoring Service, CMEMS (2024)) over the Quiberon coastal area. An area of 2700 km² was extracted and analysed. This area was large enough to minimize missing values caused by cloud cover and small enough to limit the influence of offshore SST stability.

5.2.2.1.3 Heatwave detection and characterization

Marine and Atmospheric Heatwave detection was performed using the HeatwaveR package in R (Schlegel and Smit, 2018). This package utilizes the methodology proposed by Hobday et al. (2016) to detect HW events. The annual climatology of both air and water temperature was computed. HWs were defined as events when the temperature exceeded the 90th percentile of the climatology during three consecutive days. The severity of each event has been assessed using the methodology proposed by Hobday et al. (2018).

5.2.2.2 Satellite observations

Three Sentinel-2 images of the study site were selected in 2021 to assess the effect of the HW on the seagrass meadow: the first image was taken 5 days before the HW (1st of September 2021), the second image during the HW (6th of September 2021) and the third image one month later (8th of October 2021). Level-2 data was downloaded from the Copernicus open access hub (ESA, 2024a) provided by the ESA. Level-2 images consist of orthorectified surface reflectance corrected from the effect of the atmosphere using ESA standard correction (i.e., Sen2cor, ESA (2024b)).

The seagrass heat shock index (SHSI, Equation 5.2) was computed and mapped for each image. For the pixel containing a field QP (Figure 5.4), the satellite-derived reflectance was extracted, and compared before and after the HW event.

5.2.2.3 Emersion time of the seagrass meadow

The post-HW seagrass discoloration is likely related to the emersion time and intertidal topography. The spatial distribution of seagrass emersion time during low tide was estimated using bathymetric and water level data. High resolution bathymetry data (Litto3D® product) for the Quiberon intertidal meadow was sourced from the “Service Hydrographique et Océanographique de la Marine” (SHOM, n.d.). This product is a three-dimensional land-sea elevation database with 1m of spatial resolution, accurately depicting the coastal terrain of the French shores. It uses the NGF/IGN69 reference “zero”, which corresponds to the mean sea level recorded at the Marseille tide gauge between 1885 and 1897, commonly known as the “Terrestrial Altimetric Zero”.

Water level at one-minute intervals data during the HW event were downloaded from the Intergovernmental Oceanographic Commission data portal (IOC, n.d.), using measurements from the nearest tide gauge at Le Crouesty. In this dataset, the reference “zero” corresponds to the lowest astronomical tide, also known as the Hydrographic Zero.

Before calculating the emersion time, both datasets were inter-calibrated to a common altitude reference. This involved applying a correction factor to the Litto3D data to align it with the Hydrographic zero. SHOM annually publishes a document called

“Références Altimétriques Marines” (RAM, SHOM, 2022), which provides the correction factors for each station of reference along the French coastline. The correction factor for Le Crouesty port data for 2022 was 2.85 m.

Once aligned, the corrected elevation was compared to water height for each pixel and each time step during the HW event. The emersion time was then calculated as the daily total time each pixel remained exposed along the duration of the AHW.

5.2.3 Statistics

General Linear Models (GLMs) were used to assess relative differences over time in response variables (Spectral Indices) with different treatments (Impacted vs Unimpacted). To analyse the effect of HW on the reflectance indices observed during the lab experiment, the relative change was modelled as function of Days (1-3: Discrete) with Replicate (henceforth Runs; 1-3: Factor) and Timestep within Run (1-6: Factor) as cross random factors. Satellite-derived indices were modelled as function of Date (1-3: Discrete) and Treatment (Impacted vs Unimpacted: Categorical). A Generalised Additive Model (GAM) was used to assess the relationship between relative SHSI change with emersion time. SHSI was modelled as a function of emersion time with a basis spline. All model parameters were estimated with a Bayesian framework using the “brms” and “RStan” packages in R to leverage the stan language (Bürkner, 2021; Carpenter et al., 2017; R Core Team, 2023; Stan Development Team et al., 2020). The response variables were modelled assuming a Gaussian distribution, with weakly informative priors (Student-T(3,0,2.5)). Model parameters were estimated using Markov Chain Monte Carlo (MCMC) sampling, with 4 chains of 5000 iterations and a warm-up of 500.

5.3 Results

5.3.1 Laboratory Experiment

5.3.1.1 Seagrass spectra variations related to a heatwave

In the Control group, reflectance remained relatively stable over time, with only minimal changes in magnitude and spectral features (Figure 5.6). Overall, the Control group’s reflectance spectra displayed a peak at 560 nm (green region), low values at

665 nm (indicative of strong Chla absorption), and a high plateau in the NIR, beyond 705 nm (Figure 5.6, left).

In contrast, the Treatment group simulated HW showed more pronounced changes in reflectance throughout the experiment (Figure 5.6, right). At the beginning (Day 1), reflectance values were comparable to those in the Control group, especially in the visible region, with a notable peak around 560 nm and a pronounced trough at 665 nm. However, starting from day 2, reflectance began to decrease across all wavelengths, particularly around 560 nm and in the NIR. At day 3, the NIR reflectance appeared to stabilize at values like those observed during day 2. In the green region, however, reflectance continued to decline slightly until the experiment's conclusion.

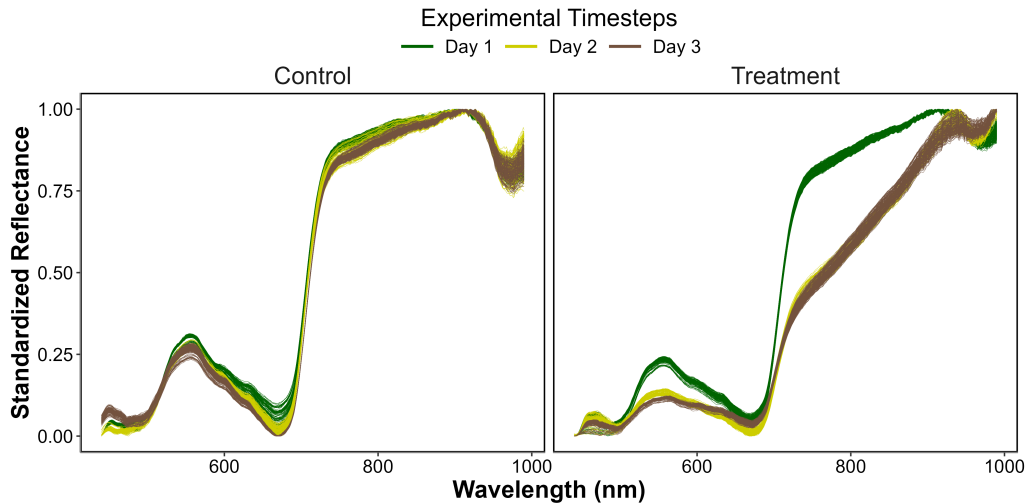


FIGURE 5.6: Standardized hyperspectral reflectance signature of *Z. noltei* leaves measured during the HW experiment for both the Control (Left) and the Treatment (Right). Colour denotes the progression along the experiment from the beginning (Day 1: green), middle (Day 2: Yellow) and end (Day 3: Brown). A min-max standardization has been applied to each individual spectrum.

5.3.1.2 Evolution of spectral metrics

Similar patterns were found for the ($R''_{665\text{ nm}}$), NDVI and GLI, where the indices started similar to the control and consistently decline over the three days of experiment (Figure 5.7 A, B and C)

At the start of the experiment (day 1) $R''_{665\text{ nm}}$, NDVI and GLI in the Treatment group were on average 13% greater, 3% lower and 2% lower, respectively, than that of the Control. However, by day 2, the Treatment showed a rapid decrease of approximately

27%, 17% and 28%, eventually reaching a total decline of 68%, 31% and 54% by day 3.

Unlike the other metrics, at the start of the experiment (day 1), the SHSI for the Treatment group was on average 55 % greater than that of the Control. By day 2, the SHSI for the Treatment exhibited a rapid decrease of approximately 241 %, eventually reaching a cumulative decline of 420 % by day 3 (Figure 5.7 D).

With a maximum deviation of 420 %, SHSI emerges as the most sensitive index for detecting seagrass browning. Consequently, only this index was considered for the next steps of this study.

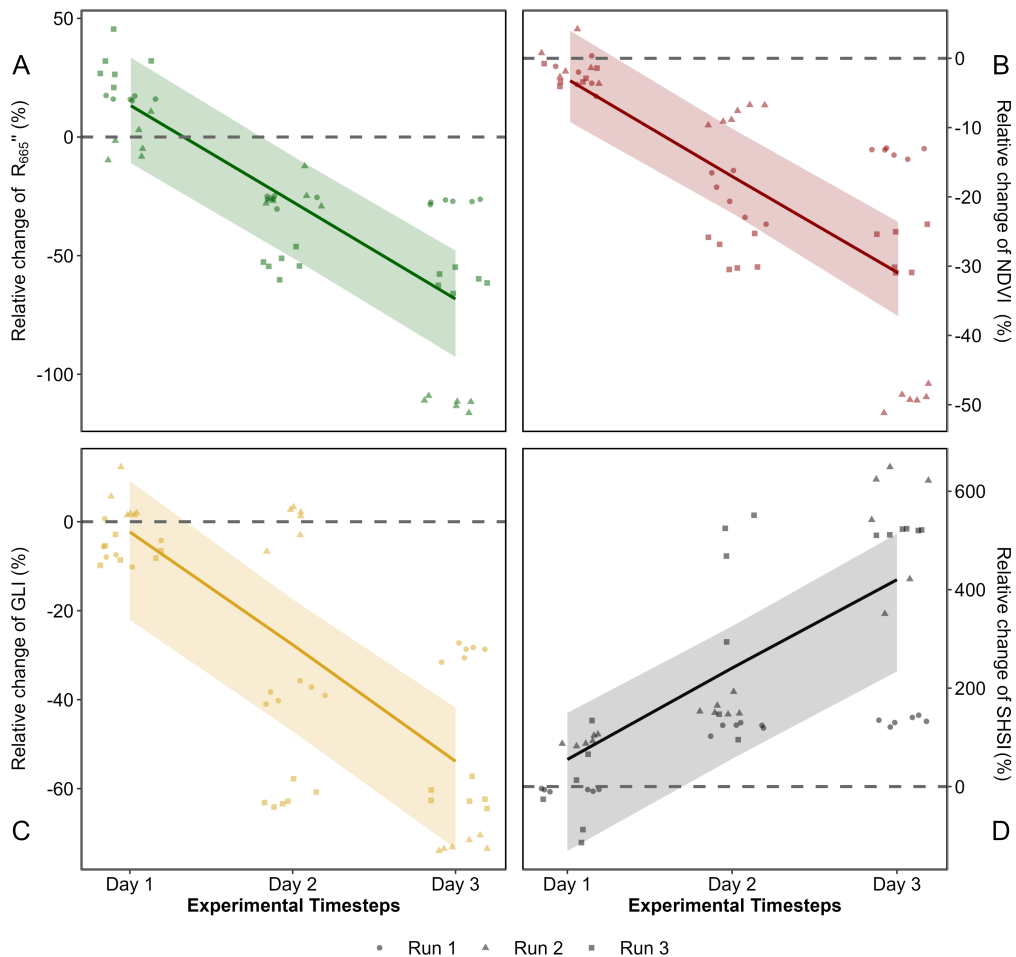


FIGURE 5.7: Comparison of spectral metrics for detecting reflectance changes of seagrass leaves after a HW. A: Relative difference of the second derivative at 665 nm between the Control and the Treatment over time; B: Relative difference of the NDVI; C: Relative difference of the GLI; D: Relative difference of the SHSI. Points indicate raw data, the line represents a generalized linear model, and the shaded area is the model's standard error. The dashed lines represent no difference between the Control and the Treatment.

Looking at raw SHSI values revealed clear distinctions between the Control and Treatment groups (Figure 5.8). At day 1, the SHSI of the Control and Treatment groups are comparable, with median values of -0.11 and -0.08, respectively. By the end of the experiment, seagrasses in the Treatment group exhibited a median SHSI of 0.15, consistent with their visibly darkened appearance. In contrast, the Control group retained a green appearance throughout the experiment, with a median SHSI of -0.07.

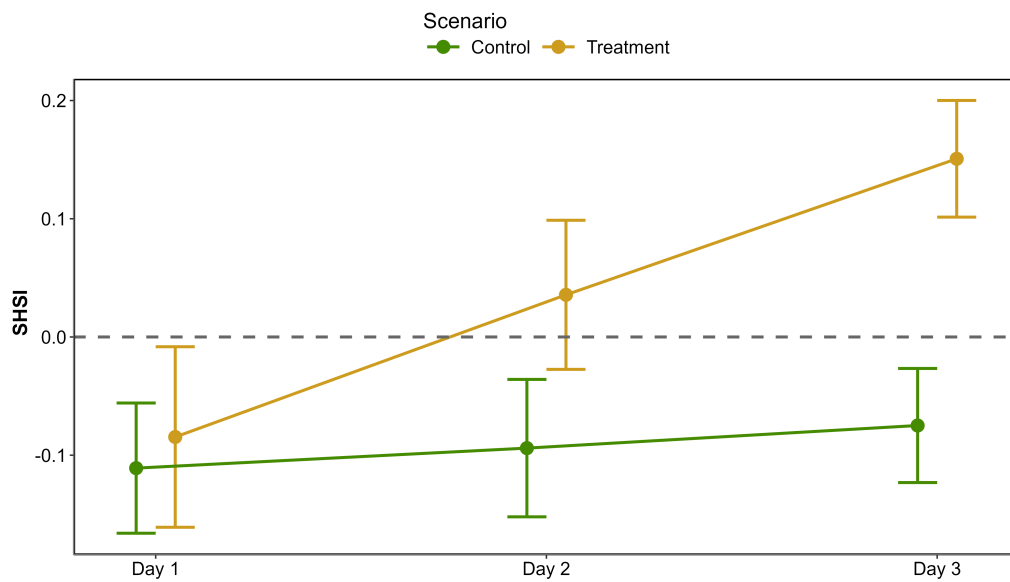


FIGURE 5.8: Median and standard deviation of the Seagrass Heat Shock Index (SHSI) across experimental runs, at each day of the experiment. The green line shows values of the Control group while the orange line indicates values of the Treatment group.

5.3.2 HW of September 2021 in Quiberon, South Brittany

5.3.2.1 Spectral changes

The Sentinel-2 images analysed in this study corresponded to acquisitions on the 1st of September 2021 and the 6th of September 2021 (Figure 5.9 A and C, respectively). The Atmospheric Heat Wave (AHW) started on the 4th of September and lasted until the 7th of September, while the Marine Heat Wave (MHW) started on the 3rd of September and ended on the 8th of September 2021 (Figure 9 B). Both air and water temperatures experienced a sharp increase. Between September 1st and 6th, the daily average air temperature rose from 22.2 to 30.8 while the daily average water temperature increased from 17.7 to 19.3 °C. During this period, the 90th percentile temperatures were 25.3 °C for air and 18.8 °C for water. The air temperature anomaly

of 9.9 °C classified the AHW as a strong event, whereas the 1.7 °C anomaly in water temperature classified the MHW as a moderate event.

The Sentinel-2 image from the 6th of September, captured two days after the start of the AHW already revealed brown seagrass leaves in the true-colour composition (Figure 5.9 C). This contrasts with the reference image from the 1st of September 2021, taken before the HW began (Figure 5.9 A), where no brown patches can be observed. Before the event, all QPs appeared green on the Sentinel-2 image, with similar reflectance spectra, typical of green seagrass leaves (Figure 5.9 A and D). Their reflectance spectra showed a peak at 560 nm (in the green part of the spectra), low values at 665 nm and a high IR plateau (> 705 nm). However, on the 6th of September, QPs classified as impacted during the field campaign, showed significant differences in their reflectance spectral shape compared to unimpacted QPs (Figure 5.9 C and E). The reflectance spectra of brown seagrass were characterized by the loss of the reflectance peak at 560 nm and a decrease in the IR plateau, which was replaced by a steadily increasing slope up to 940 nm. The darkening of large areas within the meadow could also be observed in the true colour composition (Figure 5.9 C)

5.3.2.2 SHSI metric applied to Sentinel-2

Using Sentinel-2 data and the QPs, SHSI was calculated for green seagrass unimpacted by the HW (QPs unimpacted Figure 5.9 C), showing minimal changes of 3 % between the 1st and the 6th of September (Figure 5.10). In contrast, seagrass impacted by the HW and turned brown (QPs impacted Figure 5.9 C) exhibited significant SHSI changes, showing an increase of 97 % during the HW exposure (Figure 5.10). One month after the event, on the 8th of October 2021, the SHSI of unimpacted seagrass had increased by 14 % compared to the 1st of September. Regarding impacted seagrass, one month after the event, the SHSI decreased to values comparable to those of unimpacted seagrass. This change reflects an increase of 15 % compared to values recorded on the 1st of September.

Using the SHSI (Equation 5.2), we detected large darkened seagrass patches in the meadow at the 6th of September (Figure 5.11). A total of 26.9 ha of seagrass turned brown between the 1st and the 6th of September. The largest brown patch covered nearly 8 hectares. Overall, 24 % of the total seagrass meadow area showed signs of darkening between the 1st and 6th of September 2021. Comparing the spatial

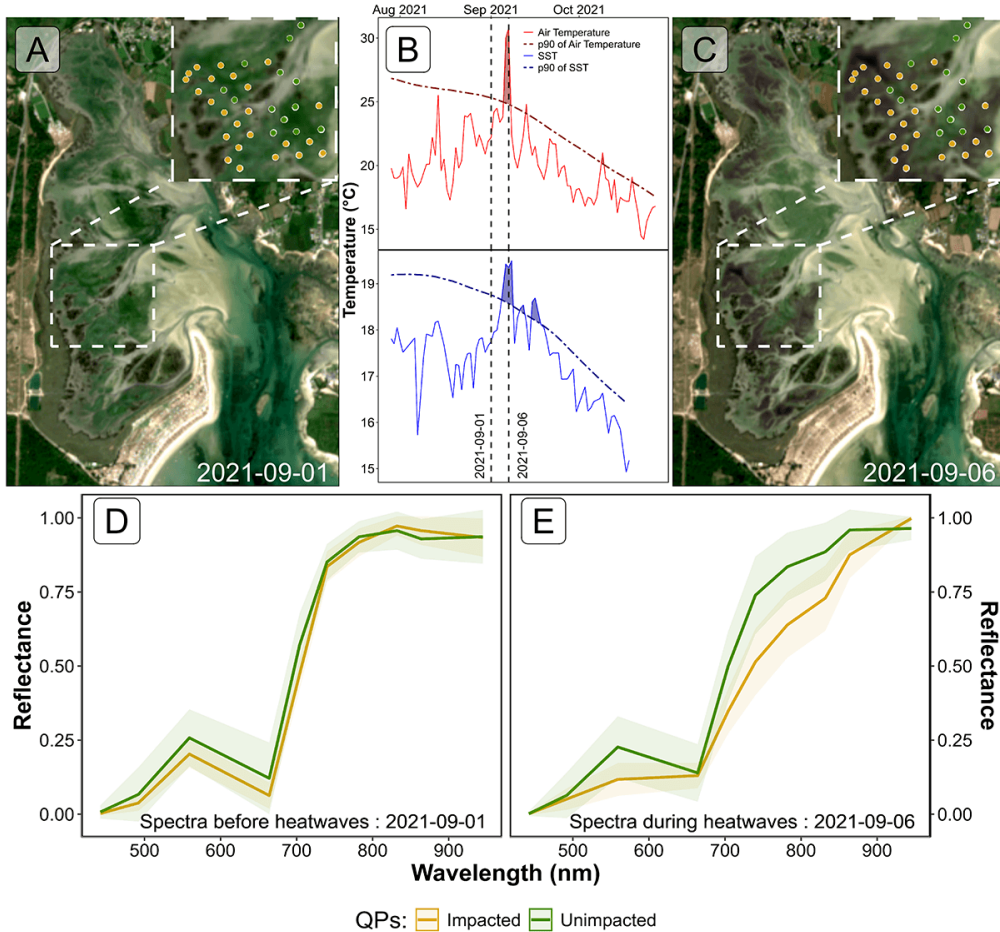


FIGURE 5.9: Intertidal seagrass meadow in South Brittany (France) observed before and during a heatwave (HW). A: RGB colour composition of the Sentinel-2 image of the 1st of September 2021 before the HW; C: RGB colour composition of the Sentinel-2 image of the 6th of September 2021 on the second day of a strong AHW. The circles correspond to Quadrat Points (QPs) collected on the 10th of September 2021, with unimpacted seagrass in green and impacted seagrass in orange; B: Detection of HW events based on both Air Temperature and Sea Surface Temperature (SST). The solid line represents the daily average temperature, while the dashed line indicates the 90th percentile of the climatology. Coloured areas identify HWs (marine in blue and atmospheric in red). The two vertical dashed lines represent the acquisition dates of the two Sentinel-2 images used in this analysis (01-09-2021 and 06-09-2021); D: Sentinel-2 reflectance of seagrass leaves before the HW for both categories of QPs; E: Sentinel-2 reflectance of seagrass leaves during the HW for both categories of QPs. Average spectral signatures were obtained in areas where QPs corresponded to green and brown seagrasses leaves (green and orange circles, respectively) as identified during the field survey. The shaded areas around the reflectance spectra represent the standard deviation.

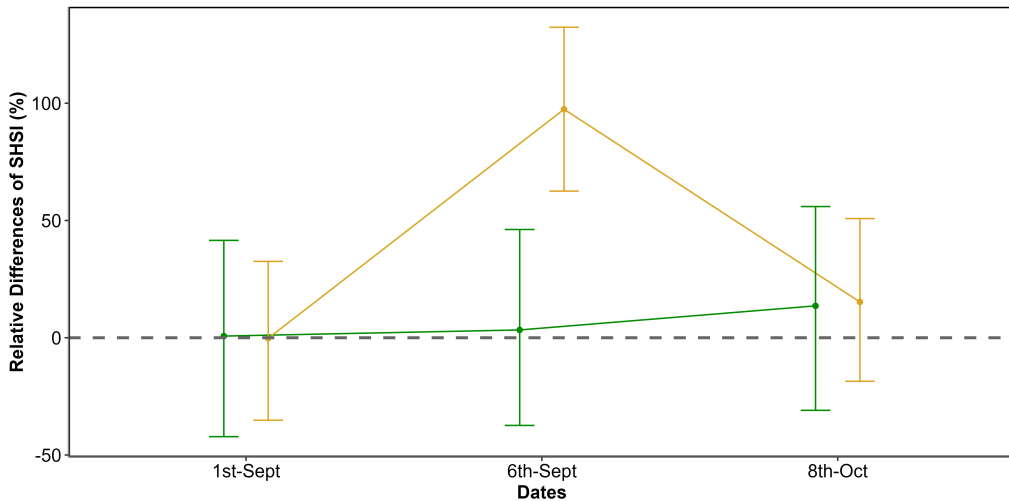


FIGURE 5.10: Changes in the relative Seagrass Heat Shock Index (SHSI) estimated from Sentinel-2, before (1st of September 2021), during (6th of September 2021) and after (8th of October 2021) a HW in the seagrass meadow of Quiberon (South Brittany, France). The relative SHSI difference was calculated using the 1st of September as a reference. SHSI was calculated for two categories of Quadrat Points (QPs; Figure 5.9): unimpacted seagrass (green) and impacted seagrass (orange). Points represent the predicted value of the metric using a Generalized Linear Model (GLM), while the error bar represents the 89% confidence interval.

distribution of darkened patches with the site's topography revealed that 94.6 % of darkened areas were located above a bathymetric level of 3.9 m (Figure 5.11, A and B). One month later, on the 8th of October, some of the previously darkened areas regained their green colour (Figure 5.11 C).

Additionally, seagrass emersion time revealed a clear relationship between the duration of air exposure and seagrass darkening (Figure 5.12). During the HW, no significant darkening occurred with less than 13 hours of daily exposure. However, above 13 hours, seagrasses began to darken, reaching peak darkening at around 14.5 hours of daily exposure.

5.4 Discussion

5.4.1 Physiological impacts of heatwaves on seagrasses

Although extensive research exists on MHWs' effects on subtidal seagrasses, little attention has been given to intertidal habitats and even less to the interaction between atmospheric extreme events and intertidal meadows. This study initiates an

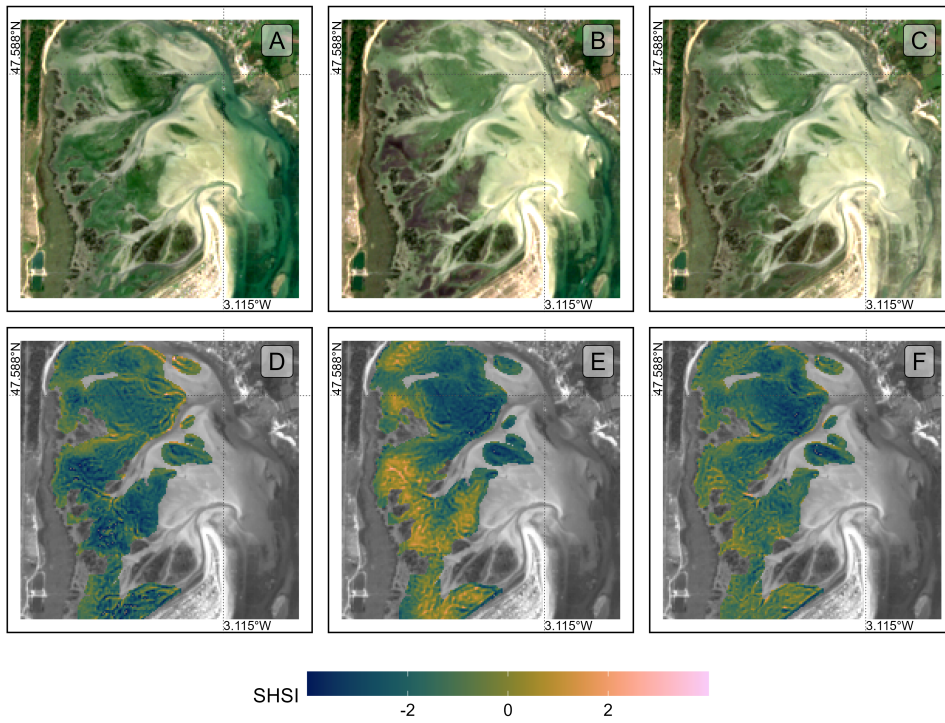


FIGURE 5.11: Sentinel-2 colour composition of the seagrass meadow of Quiberon, South Brittany, France, Before (A), During (B) and After (C) the HW Seagrass Heat Shock Index applied on Sentinel-2 images Before (D), During (E) and After (F) the HW.

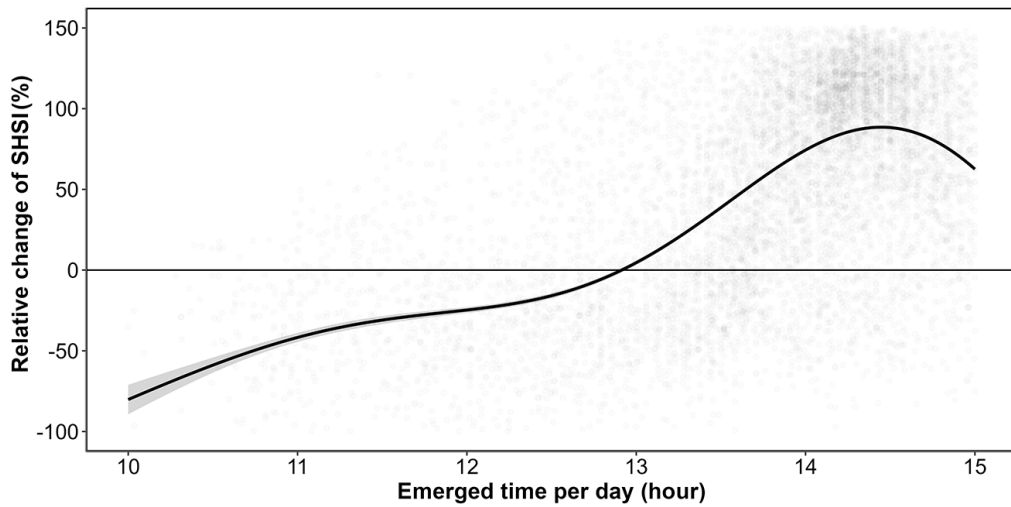


FIGURE 5.12: Relative change of the Seagrass Heat Shock Index (SHSI) before and during the HW events as a function of the daily emersion time of seagrass. The line represents a Generalized Additive Model (GAM) prediction, and the shaded area indicates the standard error. Shaded points represent raw data, each corresponding to a single pixel of the meadow.

exploration of how intertidal seagrasses respond to the dual influence of MHWs and AHWs, underscoring the need for further investigation in this under explored area.

In the present study, significant changes in the reflectance of seagrasses exposed to HWs were observed experimentally. These changes mainly include a drop in reflectance around 560 nm and another drop around 740 nm in the NIR part of the spectrum (Figure 5.7). The second derivative at 665 nm ($R''665$), NDVI, and GLI (Figure 5.7 B, C, and D) all demonstrated a clear decline over the experimental period (days 1-3). These changes suggest a progressive reduction in photosynthetic activity as well as structural or physiological changes in the leaves, such as degraded pigmentation or altered light absorption in the treatment group relative to the control as a consequence of the simulated HW event. In contrast, SHSI shows a marked increase, reaching up to 600% for some samples by day 3 (Figure 5.7 E). This positive trend in SHSI demonstrates its effectiveness as an index to quantify darkening of seagrass. While the general trends are consistent across experimental runs, there is some variability, particularly evident in the confidence intervals, which are wider for SHSI than for the other indices. This suggests that while darkening is a consistent response, it may vary in intensity between individual samples or experimental runs. Furthermore, the contrasting magnitudes of change—especially the pronounced increases in SHSI versus the declines in other indices—highlight the sensitivity of SHSI to changes associated with seagrass darkening, which could be indicative of stress or adaptation responses specific to the treatment conditions.

The change in colour can be multifactorial and has been documented in plants under various stress conditions, including thermal stress (Dascalciuc et al., 2007; Jones and Clayton-Greene, 1992). Leaf blackening in angiosperms, as observed in *Protea nerifolia*, is primarily driven by oxidative processes involving the enzyme polyphenol oxidase (PPO) and the oxidation of phenolic compounds. When photosynthesis is inhibited by factors such as low light, chemical interference, or thermal stress, the plant's production of essential carbohydrates and antioxidants diminishes, increasing oxidative stress and leading to darkening. Experimental essays have proved that low-oxygen environments and the addition of antioxidants like diphenylamine (DPA), have been effective in reducing these oxidative reactions. In the absence of photosynthesis, membrane integrity is also compromised, allowing PPO to interact with

phenolic compounds, thereby accelerating darkening. Furthermore, high temperatures can destabilize membranes, especially in chloroplasts, disrupting photosystem II and impairing recovery of photosynthetic function. As Chla degrades, the ratio of pigments shift; with pigments like carotenoids becoming more prominent, leading to a darkening of the leaves.

Zostera noltei, as a species inhabiting the intertidal zone and regularly exposed to air, has developed adaptations to minimize hydric stress. For example, it exhibits smaller, narrower leaves compared to species residing lower in the intertidal zone, such as *Zostera marina*, which helps reduce water loss during air exposure periods (Cabaço et al., 2009). However, during intense warming events and under high light conditions, desiccation can occur in certain parts of the meadow, particularly where seagrass leaves are exposed for prolonged periods (Figure 5.12). Under such hydric stress, cellular turgor pressure decreases (the internal cell water pressure that maintains cell shape), and concentrations of ions like Na⁺ and Cl⁻ can reach toxic levels. These effects can impair cellular functions, enzymatic activity, and membrane stability.

High IR reflectance in healthy plant leaves is primarily due to the internal cellular structure that scatters light. Once sunlight enters the leaf, it is diffused through various layers, particularly the spongy mesophyll, which contains air spaces and cell walls with different refractive indices. This scattering effect is intensified because there is minimal absorption in the NIR range (700 - 1300 nm), allowing light to reflect back through the leaf surface. Once the membranes (chloroplasts, thylakoids, cell walls) are destroyed due to oxidative stress, the reflectance in the Red Edge and the NIR regions of the spectrum (> 700 nm) decreases significantly (Knippling, 1970).

These unique reflectance properties of seagrasses under heat stress enable the detection of this darkening through RS techniques. The SHSI (Equation 5.2) index developed in this study leverages key reflectance bands (560, 740 and 840 nm) to detect reductions in the green and the Red-Edge regions. SHSI can be used to assess the extent and severity of darkening events across intertidal seagrass meadows from space. Current multi-spectral satellite missions, including Sentinel-2, Pleiades-Neo, WorldView-3, SkySat, and GeoSat-2 along with upcoming missions (Sentinel-2 Next Generation and Landsat Next), capture reflectance in the three wavelengths used as input for SHSI. As climate change advances, RS becomes a crucial tool for monitoring cumulative ecological impacts on seagrass meadows due to HWs. Although these

physiological and structural changes occur at the cellular level over short temporal scales, their synchronously manifest across the entire meadow cause changes in large spatial extensions. RS, with its synoptic views and real-time acquisition capabilities, enables the monitoring of these rapid biological responses to natural stressors. However, cloud coverage can limit continuous observations, necessitating the integration of alternative tools, such as multi-spectral drone platforms. Combined approaches allow for precise, localized monitoring of damaged seagrass meadows immediately after extreme events, which is critical for the early detection of ecosystem degradation, quick actions for habitat conservation and targeted management strategies. Moreover, uninterrupted, multi-year data acquisition would strengthen predictive ecological models for future HW impacts, enhancing the capacity for adaptive management and supporting long-term resilience planning for seagrass ecosystems.

5.4.2 Climate change and heatwaves

The rapid global escalation of HW frequency, intensity and duration is a defining characteristic of the current climate crisis, heavily influenced by anthropogenic activities and greenhouse gas emissions (Devi et al., 2024; Russo and Domeisen, 2023). Recent research suggests that the magnitude of these events has surged in the recent decades, with climate projections predicting a continuation of this trend. For example, HWs that were once considered rare are now up to ten times more likely to occur, with some regions experiencing events three times as intense as those in the early 20th century. Cumulative indices that quantify HW intensity are based on total temperature exceedances and offer a more comprehensive understanding of event severity than average temperature alone. This is because the cumulative impact of prolonged high temperatures imposes more extensive stress on ecosystems than isolated peak temperatures (Russo and Domeisen, 2023).

From a hazard analysis perspective, the concurrent evaluation of intensity, frequency, and duration of atmospheric HWs allows for a partial understanding of their likely impacts. Models like the HW Intensity Duration Frequency (HIDF) provide insights into various HW scenarios, indicating that both short intense and prolonged moderate events present unique risks depending on the region. For instance, in the Mediterranean, the frequency of high-intensity HWs has dramatically increased, leading to severe impacts on urban infrastructure, public health, energy consumption but also to terrestrial and intertidal ecosystems, such as seagrass meadows (Mazdiyasni et al.,

2019; Smale et al., 2019). Sharper increase in extreme heat events is expected in regions experiencing large daily thermic amplitude, which underscores the role of atmospheric variability in local HW dynamics. In mid-latitudes, where daily variability is expected to decrease, heat extremes may stabilize at elevated levels, reducing cold extremes while allowing for increasingly frequent hot days (Simolo and Corti, 2022).

In the ocean, similar trends were observed with MHWs, which have increased by more than 50% in the total number of days per year since the early 20th century, and projections suggest that a near-permanent state of MHW, based on nowadays baselines, could develop by the end of the century if greenhouse gas emissions remain high (Oliver et al., 2019). Events like the “Blob” in the northeast Pacific (2013–2016) have underscored the ecological ramifications of such heat anomalies, including shifts in species distributions, mass mortalities, and habitat degradation across vast oceanic regions. The physical mechanisms driving MHWs, such as altered ocean circulation and air-sea heat flux, further illustrate the interconnection of atmospheric and marine systems in the context of climate-driven thermal extremes (Smale et al., 2019).

The escalating frequency and intensity of HWs represent not only an atmospheric anomaly but a profound disruption to ecological stability across diverse ecosystems (Devi et al., 2024; Stillman, 2019). The temperature spikes associated with these events occur over very short timescales, with limited recovery periods—giving organisms little to no opportunity to acclimate to rapidly changing conditions and often exceeding their tolerance limits. The sustained high temperatures associated with both atmospheric and MHWs lead to physiological stress, habitat degradation, and increased mortality in many species, particularly those with limited thermal tolerance (Oliver et al., 2019; Simolo and Corti, 2022). Terrestrial and marine ecosystems experience shifts in species distributions, altered community dynamics, and reduced biodiversity as species are either forced to migrate or face local extinction under increasingly inhospitable conditions (Pansch et al., 2018). Similarly, in marine environments, prolonged heat stress from MHWs has cascading effects on foundational species, including corals, kelps, and seagrasses, all of which are crucial for providing habitat, food, and shelter to diverse marine life (Oliver et al., 2019; Smale et al., 2019). Seagrasses, in particular, play a vital role in carbon sequestration and coastal protection but are especially vulnerable to extreme heat events. Elevated temperatures can disrupt seagrass photosynthesis and metabolic processes, leading to reduced growth

and heightened susceptibility to disease (Deguette et al., 2022; Guerrero-Meseguer et al., 2020; Sawall et al., 2021; Winters et al., 2011). With repeated HW exposure and limited recovery periods, seagrass meadows may suffer severe declines, threatening their ability to deliver key ecosystem services such as carbon storage, sediment stabilization, and habitat provision (Mazdiyasni et al., 2019). The compounded impacts of atmospheric and MHWs thus pose an existential threat to intertidal seagrass ecosystems, highlighting the urgent need for targeted climate adaptation measures to mitigate these escalating thermal stresses and preserve the resilience of these essential marine habitats (Russo and Domeisen, 2023; Stillman, 2019).

5.4.3 Seagrass resilience to heatwaves

Seagrass resilience to HWs is a complex and multifaceted issue shaped by species-specific traits, geographical location, and concurrent environmental stressors (Berger et al., 2024; Canadell and Jackson, 2021; Hatum et al., 2024). As climate change drives the frequency and intensity of MHWs, understanding these dynamics becomes crucial, especially for temperate seagrass meadows composed of slow-growing, long-lived species like *Posidonia* spp., *Amphibolis* spp., and *Zostera* spp. These species, unlike their tropical counterparts, tend to be highly vulnerable to abrupt environmental changes, struggling to recover from disturbances due to their slower growth and longer lifespan. In contrast, colonizing species typical of tropical regions, such as *Halodule* spp., *Halophila* spp., and *Syringodium* spp., demonstrate greater resilience to warming events and MHWs due to their rapid growth and more flexible life strategies (O'Brien et al., 2018).

The impact of HWs on seagrass ecosystems is further intensified by tidal variations, especially in temperate regions with large tidal ranges that can exceed 10 m, such as Mont Saint Michel Bay, France. This pronounced tidal amplitude affects intertidal seagrasses like *Zostera noltei*, which experience varying durations of air exposure based on their position within the intertidal zone. During neap tides, seagrasses situated higher in the intertidal zone may remain exposed for extended periods, heightening their vulnerability to AHWs. Conversely, seagrasses in the lower intertidal zone experience prolonged immersion throughout the tidal cycle, making them susceptible to extreme MHWs. As a result, both marine and AHWs can increase stress on seagrass meadows, with effects that may be intensified by tidal timing and amplitude. In our study, we observed a darkening effect in the seagrasses, despite our experimental

setup simulating tides with consistent 6-hour exposure periods. In natural settings, however, bathymetry plays a significant role, and depending on depth variations, seagrasses may be exposed for even longer periods during low tides. This suggests that *in situ* exposure times could exacerbate the stress effects observed, as seagrasses may endure prolonged air exposure beyond what our controlled conditions have replicated.

Species like *Zostera noltei* display distinct seasonal patterns that become increasingly pronounced at higher latitudes (Davies et al., 2024b, 2024a). These patterns reflect the species' adaptation to seasonal variations in temperature and light, but they also make *Z. noltei* particularly sensitive to extreme events depending on their timing. For instance, if a HW coincides with early developmental stages or occurs after the biomass peak when leaf senescence has begun, the impact on meadow resilience can be severe.

Environmental conditions can moderate seagrass resilience to thermal stress. Seagrass meadows located in areas benefiting from tidal cooling or positioned further from the warmer edges of their geographical ranges often experience reduced heat stress, resulting in higher shoot densities and enhanced resilience (Berger et al., 2024; Canadell and Jackson, 2021). In these cooler areas, *Zostera noltei* exhibits high survival and photosynthetic performance up to 37°C, though temperatures above 39°C lead to near-total mortality within days, underscoring the species' sensitivity to temperature thresholds that may become increasingly common under climate change scenarios (Franssen et al., 2014). Moreover, the frequency, duration, and intervals between HWs significantly affect seagrass biomass and recovery; prolonged and frequent HWs reduce resilience and complicate recovery processes (Hatum et al., 2024).

The influence of other stressors, such as eutrophication and sulphide accumulation, complicates this resilience. Increased sediment sulphide levels, which often accompany nutrient enrichment, can be toxic to seagrasses, particularly under elevated temperatures that amplify sulphide toxicity. *Zostera noltei*, for example, has a mutualistic relationship with lucinid clams that helps detoxify sulphides. However, this interaction is compromised at high temperatures, reducing the efficacy of sulphide removal and further inhibiting nutrient uptake, growth, and overall resilience (De Fouw et al., 2022).

In a simulated HW experiment on *Zostera noltei*, resilience was evident under short-term moderate stress, with no significant changes in photosynthetic performance or

survival (Franssen et al., 2014; Massa et al., 2009). However, prolonged or more intense heat events posed a greater challenge, highlighting the species' limited capacity to withstand chronic thermal stress. The long-term impact of HWs is especially evident in changes to SC. Before the HW event on 1st September 2021, impacted seagrass patches exhibited higher SC than non-impacted areas. However, during the event on 6th September, the SC in the impacted patch experienced a sharp decline on impacted patches. By 8th October, one month post-event, the SC of impacted seagrasses, initially higher, had fallen below that of non-impacted seagrasses (Figure 5.10). The observed decrease in seagrass cover on 6th September was primarily due to leaf darkening. This darkening influenced the satellite NDVI measurements used to estimate SC (Zoffoli et al., 2020), creating an apparent decrease in SC in the impacted patch when, in reality, it remained stable (Figure 5.5). The bias introduced by RS in this instance reflects a limitation in accurately capturing true seagrass cover during stress events. It was only after the HW that leaves began to detach, leading to an actual decline in seagrass density. This delayed physical response underscores how extreme events can compromise seagrass resilience, leaving previously robust patches in a weakened state compared to less disturbed areas (Figure 5.10).

On a physiological level, seagrasses possess coping mechanisms such as photoprotective responses and heat-responsive gene expression, including the activation of heat-shock proteins (HSPs) and other stress-related genes (Hughes and Stachowicz, 2004; Reusch et al., 2005). *Zostera noltei*, in particular, has shown differential gene expression responses to heat stress, with a variety of genes involved in protein folding, membrane stability, and reactive oxygen species scavenging playing critical roles. However, the rapid pace of climate change raises concerns about whether these adaptations can keep up with the increasing frequency and severity of thermal events (Franssen et al., 2014).

5.4.4 Big picture

Given the combined pressures of temperature extremes, eutrophication, and other anthropogenic impacts, targeted management strategies are essential for enhancing seagrass resilience (Loarie et al., 2009). Approaches such as reducing local stressors, cultivating heat-tolerant genotypes, and investing in restoration initiatives are vital to supporting these ecosystems in a warming climate. Although challenges remain, the adaptability and potential resilience of certain seagrass species offer hope for their

persistence amid accelerating ecological shifts. In particular, regions that can buffer seagrasses from extreme stressors or provide cooler refuges may play a critical role in maintaining these valuable ecosystems in the face of global climate change (Canadell and Jackson, 2021; De Fouw et al., 2022).

Seagrass meadows function as foundational components of coastal ecosystems, sustaining diverse marine communities by providing essential habitats, nursery grounds, and trophic resources for fish, invertebrates, and migratory birds (Zoffoli et al., 2023). Their dense canopies stabilize sediment and protect shorelines from erosion, an increasingly crucial role as sea levels rise due to climate change (Folmer et al., 2012; Gacia et al., 1999). Recurrent HW events, which induce physiological stress like leaf darkening, can severely diminish seagrass density, thereby reducing their effectiveness in sediment stabilization and wave attenuation, ultimately increasing the risk of coastal erosion (Calleja et al., 2007). From a biodiversity perspective, degradation of these meadows disrupts intricate food webs, impacting commercially significant fish and shellfish populations that rely on seagrass for sustenance and refuge. This loss can reduce local fisheries' productivity and threaten the livelihoods of coastal communities (Unsworth and Cullen-Unsworth, 2014). Furthermore, as seagrass meadows decline, their capacity to act as a blue carbon sink—critical for climate mitigation—also diminishes, inadvertently contributing to increased atmospheric carbon levels (Armitage and Fourqurean, 2016; Samper-Villarreal et al., 2020)

5.5 Conclusion

This research has investigated the effects of both marine and atmospheric HWs on the intertidal seagrass *Zostera noltei*, a critical component of coastal ecosystems facing increased thermal stress due to climate change. By examining reflectance and pigment composition under controlled experimental conditions and validating these findings with satellite data, we aimed to understand how extreme heat events affect seagrass health and assess the potential of RS to monitor these impacts effectively. Our findings reveal that HWs lead to substantial declines in seagrass reflectance, particularly in the green and NIR regions, likely driven by pigment degradation and structural damage. This change is reflected in significant reductions in key vegetation indices such as NDVI and GLI. The Seagrass Heat Shock Index (SHSI), developed in this study, successfully detected seagrass darkening, a visible symptom of HW stress,

demonstrating the viability of spectral monitoring to capture early-stage impacts of heat events on intertidal ecosystems. By connecting our findings with satellite data, we have also confirmed the broader spatial impact of HWs on seagrass meadows in Quiberon, France. The correlation between HW exposure and darkening of seagrass suggests that RS, combined with targeted field observations, can enhance our understanding of ecosystem responses to climate-driven thermal events. These results advocate for integrating continuous spectral monitoring into conservation strategies, as it can help predict the resilience of these ecosystems and guide adaptive management practices. As climate change accelerates, with a predicted increase in the frequency and intensity of HWs, the vulnerability of intertidal zones to such events will likely intensify compromising meadows survival and their ecosystem functions. This study not only underscores the importance of seagrass meadows in coastal ecosystems but also highlights the urgency of protecting these critical habitats. Future work should focus on refining RS tools and examining the cumulative effects of repeated HW events to support the conservation of intertidal seagrass meadows in a warming world.

5.6 Annexes

5.6.1 Annexes A - Temperatures of the experiment

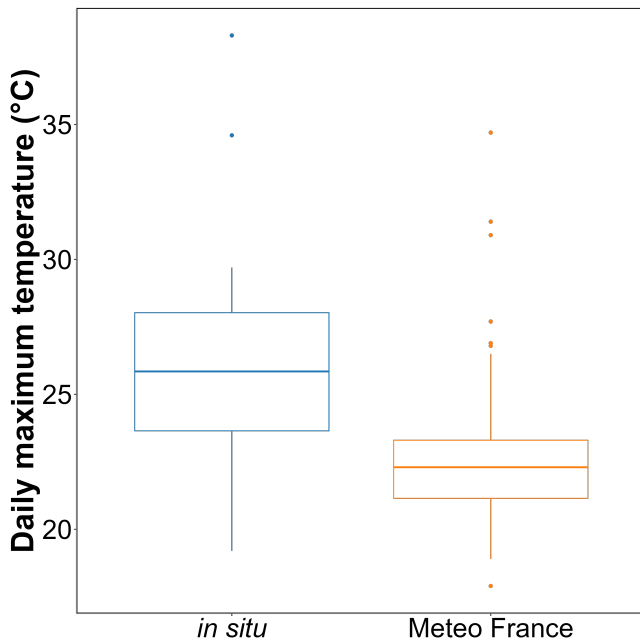
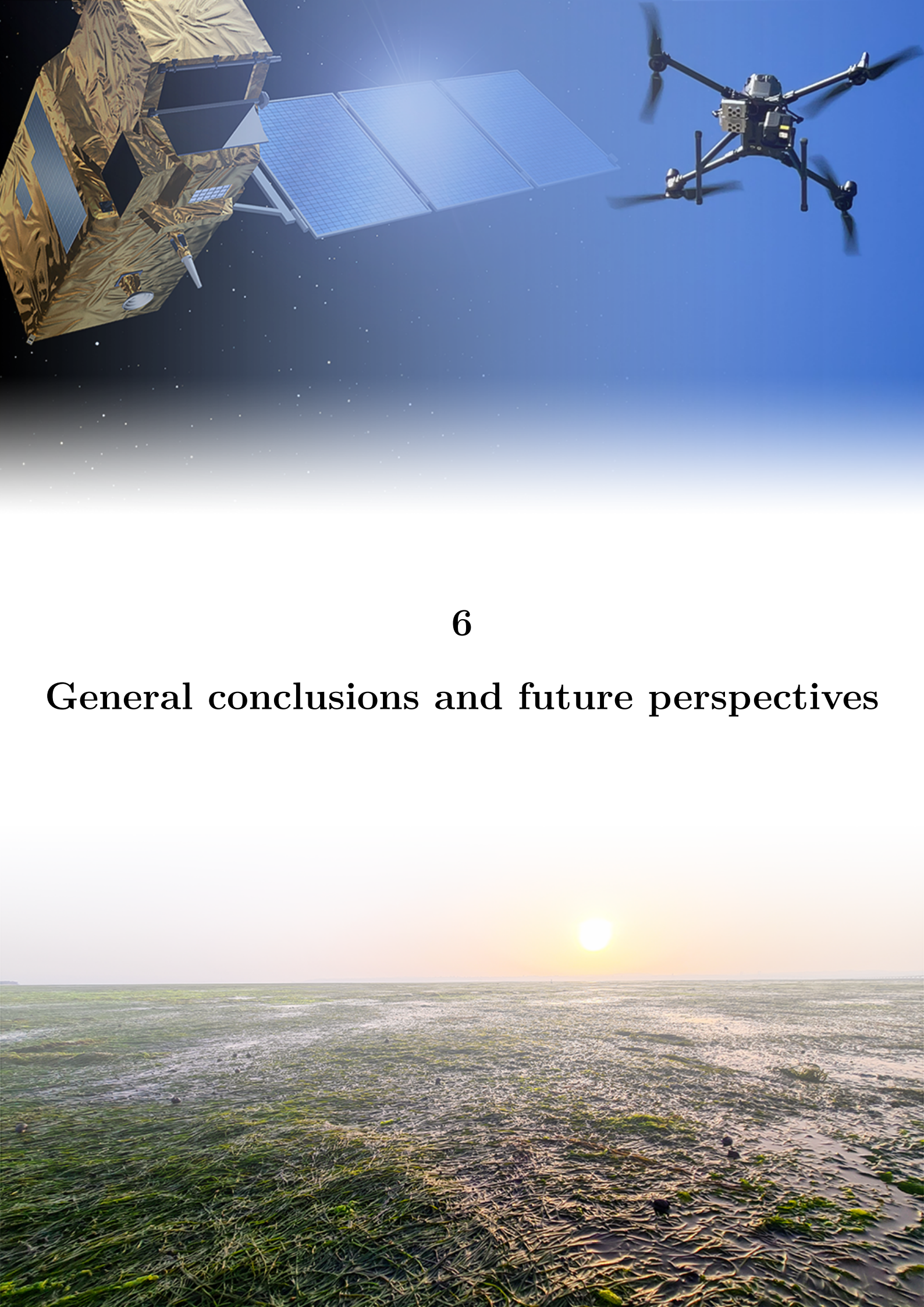


FIGURE 5.13: Annexe 5.1 - Comparison of daily maximum temperatures in August measured using an in-situ sensor (blue) and retrieved from Meteo France (orange). The solid line in the middle of the box-plot represents the median, the two ends of the box represent the 25th and 75th percentiles, and the whiskers represent values that are no more than 1.5 times the interquartile range.

On average, *in situ* temperatures were $3 \pm 3.2^\circ\text{C}$ higher than those recorded by Meteo France. Additionally, temperatures recorded by Meteo France were more stable than those from the *in situ* sensors, likely due to the sheltered and shaded location of the Meteo France equipment. This difference was used to adjust HW temperatures measured by Meteo France to better reflect the conditions experienced by the seagrasses.



6

General conclusions and future perspectives

This doctoral research successfully addressed its principal objectives, which were to: (1) demonstrate the effectiveness of RS for mapping intertidal habitats, (2) develop advanced methodologies for accurate vegetation classification and ecosystem monitoring, and (3) to investigate the capacity of RS to map ecosystem under biotic and abiotic pressures. This work underscore the potential of RS technologies in addressing ecological challenges in intertidal zones, including the impacts of climate change, anthropogenic pressures, and habitat fragmentation. By demonstrating improved accuracy in habitat classification, from seagrass discrimination to IAS mapping, this work highlights the critical role of multispectral and hyperspectral data in supporting biodiversity conservation and ecosystem resilience. The integration of ground-based, drone, and satellite observations proved pivotal in bridging spatial and temporal gaps, enabling a more comprehensive understanding of ecosystem dynamics. This concluding section reviews the key scientific advancements made through the application of RS to intertidal ecosystems, the challenges encountered, and future research directions.

6.1 Macrophytes discrimination and associated challenges.

This work has demonstrated the capability of multispectral RS when combined with sophisticated machine-learning techniques to differentiate between various types of intertidal vegetation, even among plants with similar pigment compositions. This capability was initially validated theoretically using a hyperspectral library degraded to the spectral resolution of several sensors. It was subsequently confirmed using a multispectral camera mounted on a drone. The distinction was particularly challenging between green macrophytes, such as seagrass and green macroalgae, which share similar pigment compositions and, consequently, spectral signatures. However, the slight variations in the spectral signatures of intertidal green macrophytes enabling this discrimination arises from differences in the proportions in which these pigments are present in each type of vegetation. Pigment concentrations and ratios are not static over time following phenological cycles and impacted by stress conditions or may not be uniform within a species due to phenotypic variability, limiting the application of the method developed here to certain conditions. Despite this limitation, a key strength of the method lies in its development across a wide geographical range,

open-source and use-case-driven design. The Drone Intertidal Substrate Classification of Vegetation (DISCOV) algorithm was developed to be dynamic and adaptable over time. The algorithm has been detailed in a scientific journal, with its complete code and training/validation dataset openly shared on GitHub (Oiry et al., 2024). This flexibility proved invaluable when applying the algorithm to a different use case: mapping the invasive *Gracilaria vermiculophylla*.

Interestingly, DISCOV v1.0 exhibited poor performance in identifying this red algae, despite its distinct and unique spectral signature attributed to the presence of phycocyanin and phycoerythrin. The algorithm's underperformance was traced to the lack of enough samples of this class in the original training dataset, causing confusion with other classes when encountering this specific spectral signature during prediction. This issue was promptly addressed by updating the model's training dataset to include more red algae samples. The updated model outperformed the original version on the new dataset while maintaining nearly the same accuracy on the original dataset. Including a more diverse training dataset improved DISCOV's performance across broader ecological contexts. Expanding the geographic and temporal range of data collection has been shown to enhance algorithm robustness and adaptability. By incorporating spectral data from multiple seasons and regions, the algorithm could better account for temporal variations in pigment concentrations and environmental factors, ensuring more reliable predictions across diverse conditions.

6.2 Drone and Satellite Interactions

UAVs provide high spatial resolution imagery, which is essential for capturing fine-scale heterogeneity, enabling the observation of subtle spatial patterns within habitats, and validating data derived from lower-resolution satellite imagery. High-resolution multispectral drones, when paired with classifier models, facilitate precise habitat mapping by identifying variations that may not be apparent otherwise. Furthermore, these drones produce large training datasets that are critical for enhancing the accuracy of ML models based on deep-learning architectures in satellite-based RS. By integrating UAV-derived observations with field-specific data, detailed assessments can be achieved, which are particularly relevant for complex environments such as intertidal zones.

Satellites, such as Sentinel-2, complement UAVs by offering broad spatial coverage and consistent temporal monitoring, facilitating the assessment of seasonal and inter-annual changes. This enables systematic analysis of long-term trends and spatial dynamics across expansive geographic areas and quantifying large surfaces. While drones excel in localized, high-resolution observations, satellites provide scalable and cost-effective solutions for monitoring intertidal ecosystems at regional and global scales. This integration ensures that monitoring programs benefit from detailed localized insights while maintaining broader ecological context.

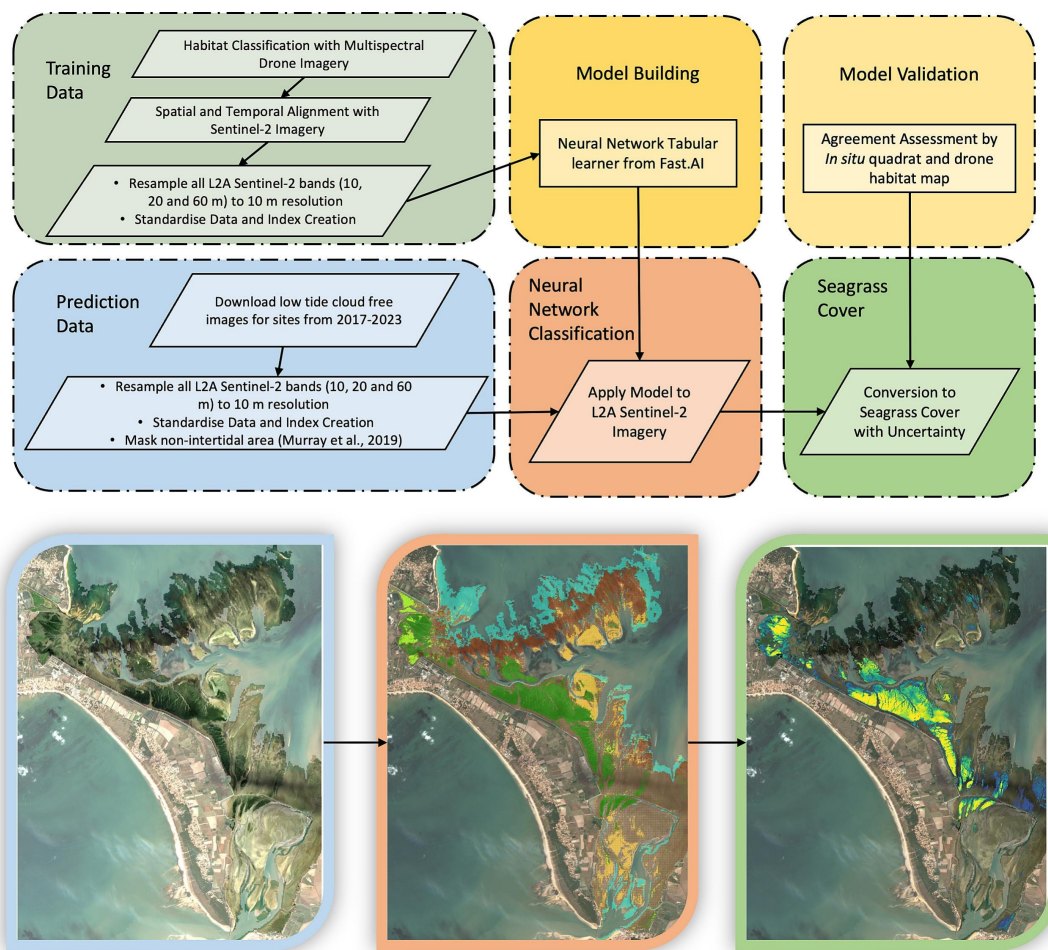


FIGURE 6.1: Workflow showing process for neural network classification model building and seagrass cover (%) from this classification, with example images showing process from Sentinel-2 Data to Habitat Classification to Seagrass Cover. From Davies et al. (2024a).

The combination of these technologies allows to leverage their respective strengths. For instance, UAV-acquired habitat data significantly enhance and validate satellite-based classifications, as demonstrated in the ICE CREAMS model (Davies et al., 2024a, 2024b), where UAV data were used to train and validate seagrass habitat classifications across Europe Figure 6.1. This hybrid methodology achieves a balance

between local accuracy and scalability, reducing the costs associated with large-scale monitoring while preserving the depth of localized observations necessary for comprehensive assessments.

This integration of drone and satellite technologies enhances the ability to monitor, analyse, and manage intertidal ecosystems effectively. By combining detailed precision with extensive coverage, these technologies address scientific and environmental challenges efficiently. They improve modelling accuracy, inform evidence-based conservation strategies, and provide critical tools for adaptive management in the context of environmental change.

6.3 Seagrass and Invasive Species Interactions

The interaction between seagrasses following HW events and the rapid growth capacity of *Gracilaria vermiculophylla* presents a complex dynamic shaped by environmental stressors, competition, and ecological resilience. These interactions are crucial for understanding the evolving structure and function of intertidal ecosystems under climate change.

Seagrasses, such as *Zostera noltei*, are integral to coastal ecosystems, offering essential services including sediment stabilization, carbon sequestration, and habitat provision. However, their health and resilience are highly vulnerable to environmental stressors, particularly MHWs and AHWs. These events induce physiological stress that manifests as leaf browning, chlorophyll degradation, and reduced photosynthetic efficiency. Observations reveal extensive browning and decreased seagrass coverage in intertidal zones subjected to prolonged high temperatures. The reduction in seagrass cover weakens its competitive edge, particularly in areas where other stressors, such as eutrophication or sediment disruption, are present.

IAS such as *Gracilaria vermiculophylla* exploit ecological disturbances to establish dominance. This red macroalga exhibits remarkable adaptability to varied environmental conditions, including fluctuations in temperature, salinity, and nutrient availability. Post-heatwave environments might provide ideal conditions for *G. vermiculophylla* or other IAS to expand. The degradation of seagrass meadows leads to increased light availability and free space making them more susceptible to biological invasions. Dense mats of *G. vermiculophylla* form on soft-bottom sediments,

where they can rapidly proliferate and monopolize space and resources. These mats can physically and chemically inhibit the recovery of seagrasses by reducing light penetration and altering sediment composition.

The competitive interplay between seagrasses and *G. vermiculophylla* is exacerbated in the aftermath of HW. Seagrasses' physiological stress limits their ability to recover quickly, creating a temporal window for *G. vermiculophylla* to expand. Furthermore, anthropogenic factors such as nutrient enrichment from agricultural runoff amplify this dynamic by promoting algal growth and suppressing seagrass resilience. The ecological consequences of *G. vermiculophylla* proliferation are multifaceted. While the algae can provide habitat and stabilize sediments, its dominance often disrupts existing trophic interactions and reduces biodiversity. Areas previously dominated by seagrasses may experience shifts in community composition, favouring species adapted to algal habitats. Additionally, the physical characteristics of dense algal mats can alter sediment dynamics and hydrology, further entrenching *G. vermiculophylla*'s presence.

Addressing the interaction between heatwave-stressed seagrasses habitats and IAS such as *G. vermiculophylla* requires integrated monitoring and management approaches. RS technologies, including multispectral and hyperspectral imaging, provide powerful tools for tracking changes in vegetation health and distribution. Monitoring metrics such as the SHSI developed in Chapter 5 enable early detection of thermal stress, allowing for timely interventions. Management strategies should focus on mitigating stressors that exacerbate competitive dynamics. Reducing nutrient inputs to coastal waters can limit the proliferation of *G. vermiculophylla* and other opportunistic species. Physical removal of algal mats, combined with restoration efforts to enhance seagrass resilience, can help reestablish ecological balance. Additionally, incorporating predictive models to assess the impacts of future HW scenarios can guide proactive conservation measures.

The possible interactions between seagrasses and IAS after extreme events might imply the complex interplay of environmental stressors, competition, and ecosystem resilience. Understanding these dynamics might be critical for preserving the ecological integrity of intertidal zones. By leveraging advanced monitoring techniques and implementing targeted management interventions, it is possible to mitigate the adverse effects of IAS and climate-induced stress, thereby supporting the long-term

sustainability of these vital coastal ecosystems.

References

- Abiodun, O.I., Jantan, A., Omolara, A.E., Dada, K.V., Mohamed, N.A., Arshad, H., 2018. State-of-the-art in artificial neural network applications: A survey. *Heliyon* 4.
- Abreu, M.H., Pereira, R., Buschmann, A., Sousa-Pinto, I., Yarish, C., 2011. Nitrogen uptake responses of *gracilaria vermiculophylla* (ohmi) papenfuss under combined and single addition of nitrate and ammonium. *Journal of Experimental Marine Biology and Ecology* 407, 190–199.
- Adade, R., Aibinu, A.M., Ekumah, B., Asaana, J., 2021. Unmanned aerial vehicle (UAV) applications in coastal zone management—a review. *Environmental Monitoring and Assessment* 193, 1–12.
- Agisoft, 2019. Agisoft metashape.
- Ahmed, N., Glaser, M., 2016. Coastal aquaculture, mangrove deforestation and blue carbon emissions: Is REDD+ a solution? *Marine Policy* 66, 58–66.
- Akbar, M., Arisanto, P., Sukirno, B., Merdeka, P., Priadhi, M., Zalessa, S., 2020. Mangrove vegetation health index analysis by implementing NDVI (normalized difference vegetation index) classification method on sentinel-2 image data case study: Segara anakan, kabupaten cilacap, in: IOP Conference Series: Earth and Environmental Science. IOP Publishing, p. 012069.
- Alongi, D.M., 2012. Carbon sequestration in mangrove forests. *Carbon management* 3, 313–322.
- Angnuureng, D.B., Brempong, K., Jayson-Quashigah, P., Dada, O., Akuoko, S., Frimpomaa, J., Mattah, P., Almar, R., 2022. Satellite, drone and video camera multi-platform monitoring of coastal erosion at an engineered pocket beach: A showcase for coastal management at elmina bay, ghana (west africa). *Regional Studies in Marine Science* 53, 102437.
- Arim, M., Abades, S.R., Neill, P.E., Lima, M., Marquet, P.A., 2006. Spread dynamics of invasive species. *Proceedings of the National Academy of Sciences* 103, 374–378.
- Arkema, K.K., Guannel, G., Verutes, G., Wood, S.A., Guerry, A., Ruckelshaus, M., Kareiva, P., Lacayo, M., Silver, J.M., 2013. Coastal habitats shield people and property from sea-level rise and storms. *Nature climate change* 3, 913–918.
- Armitage, A., Fourqurean, J.W., 2016. Carbon storage in seagrass soils: Long-term nutrient history exceeds the effects of near-term nutrient enrichment. *Biogeosciences* 13, 313–321.
- ASI, n.d. PRISMA products specification document issue 2.3 date 12/03/2020.
- Bajjouk, T., Zarati, I., Drumetz, L., Mura, M.D., 2019. Spatial Characterization of Marine Vegetation Using Semisupervised Hyperspectral Unmixing. 2019 10th Workshop on Hyperspectral Imaging and Signal Processing: Evolution in Remote Sensing (WHISPERS) 1–5.
- Bannari, A., Ali, T.S., Abahussain, A., 2022. The capabilities of sentinel-MSI (2A/2B) and landsat-OLI (8/9) in seagrass and algae species differentiation using spectral reflectance. *Ocean Science* 18, 361–388.

- Barbier, E.B., 2015. Valuing the storm protection service of estuarine and coastal ecosystems. *Ecosystem Services* 11, 32–38.
- Barbier, E.B., Hacker, S.D., Kennedy, C., Koch, E.W., Stier, A.C., Silliman, B.R., 2011. The value of estuarine and coastal ecosystem services. *Ecological monographs* 81, 169–193.
- Bargain, A., Robin, M., Le Men, E., Huete, A., Barillé, L., 2012. Spectral response of the seagrass *Zostera noltii* with different sediment backgrounds. *Aquatic Botany* 98, 45–56.
- Bargain, A., Robin, M., Méléder, V., Rosa, P., Le Menn, E., Harin, N., Barillé, L., 2013. Seasonal spectral variation of *Zostera noltii* and its influence on pigment-based Vegetation Indices. *Journal of Experimental Marine Biology and Ecology* 446, 86–94. <https://doi.org/10.1016/j.jembe.2013.04.012>
- Barillé, L., Mouget, J.L., Méléder, V., Rosa, P., Jesus, B., 2011. Spectral response of benthic diatoms with different sediment backgrounds. *Remote Sensing of Environment* 115, 1034–1042. <https://doi.org/10.1016/j.rse.2010.12.008>
- Barillé, L., Robin, M., Harin, N., Bargain, A., Launeau, P., 2010. Increase in seagrass distribution at Bourgneuf Bay (France) detected by spatial remote sensing. *Aquatic Botany* 92, 185–194. <https://doi.org/10.1016/j.aquabot.2009.11.006>
- Barillé-Boyer, A.-L., Gruet, Y., Barillé, L., Harin, N., 2004. Temporal changes in community structure of tide pools following the “erika” oil spill. *Aquatic living resources* 17, 323–328.
- Bastos, M., Roebeling, P., Alves, F.L., Villasante, S., Magalhães Filho, L., 2023. High risk water pollution hazards affecting aveiro coastal lagoon (portugal)—a habitat risk assessment using InVEST. *Ecological Informatics* 76, 102144.
- Beach, K., Borgeas, H., Nishimura, N., Smith, C., 1997. In vivo absorbance spectra and the ecophysiology of reef macroalgae. *Coral Reefs* 16, 21–28.
- Beltrand, M., Dineen, A., Hitzeroth, C., Baum, B., Cerff, C. de, Vos, C. de, Lewis, J., Zaroufis, S., Pillay, D., 2022. Warming Effects on Two Autogenic Engineers (*Zostera capensis* and *Gracilaria gracilis*): Consequences for Macrofaunal Assemblages and Benthic Heterogeneity in Intertidal Sandflat Ecosystems. *Estuaries and Coasts* 45, 247–259. <https://doi.org/10.1007/s12237-021-00949-8>
- BenDor, T.K., Metcalf, S.S., 2006. The spatial dynamics of invasive species spread. *System Dynamics Review: The Journal of the System Dynamics Society* 22, 27–50.
- Benyoucef, I., Blandin, E., Lerouxel, A., Jesus, B., Rosa, P., Méléder, V., Launeau, P., Barillé, L., 2014. Microphytobenthos interannual variations in a north-european estuary (loire estuary, france) detected by visible-infrared multispectral remote sensing. *Estuarine, Coastal and Shelf Science* 136, 43–52.
- Berger, A.C., Berg, P., McGlathery, K.J., Aoki, L.R., Kerns, K., 2024. Eelgrass meadow response to heat stress. II. Impacts of ocean warming and marine heatwaves measured by novel metrics. *Marine Ecology Progress Series* 736, 47–62. <https://doi.org/10.3354/meps14588>
- Besterman, A.F., McGlathery, K.J., Reidenbach, M.A., Wiberg, P.L., Pace, M.L., 2021. Predicting benthic macroalgal abundance in shallow coastal lagoons from geomorphology and hydrologic flow patterns. *Limnology and Oceanography* 66, 123–140.
- Blanchet, H., Gouillieux, B., Alizier, S., others, 2014. Multiscale patterns in the diversity and organization of benthic intertidal fauna among french atlantic estuaries. *Journal of Sea Research* 90, 95–110. <https://doi.org/10.1016/j.seares.2014.02.014>

- Blum, M.D., Roberts, H.H., 2009. Drowning of the mississippi delta due to insufficient sediment supply and global sea-level rise. *Nature geoscience* 2, 488–491.
- Bojinski, S., Verstraete, M., Peterson, T.C., Richter, C., Simmons, A., Zemp, M., 2014. The concept of essential climate variables in support of climate research, applications, and policy. *Bulletin of the American Meteorological Society* 95, 1431–1443.
- Borja, A., Elliott, M., Andersen, J.H., Cardoso, A.C., Carstensen, J., Ferreira, J.G., Heiskanen, A.-S., Marques, J.C., Neto, J.M., Teixeira, H., others, 2013. Good environmental status of marine ecosystems: What is it and how do we know when we have attained it? *Marine Pollution Bulletin* 76, 16–27.
- Bos, A.R., Bouma, T.J., Kort, G.L. de, Katwijk, M.M. van, 2007. Ecosystem engineering by annual intertidal seagrass beds: Sediment accretion and modification. *Estuarine, Coastal and Shelf Science* 74, 344–348.
- Boyer, M., Miller, J., Belanger, M., Hare, E., Wu, J., 1988. Senescence and spectral reflectance in leaves of northern pin oak (*quercus palustris muenchh.*). *Remote Sensing of Environment* 25, 71–87.
- Breiman, L., 2001. Random forests. *Machine learning* 45, 5–32.
- Brondízio, E.S., Settele, J., Díaz, S., Ngo, H.T.(eds.), 2019. IPBES (2019), Global assessment report of the Intergovernmental Science-Policy Platform on Biodiversity and Ecosystem Services.
- Brunier, G., Oiry, S., Gruet, Y., Dubois, S.F., Barillé, L., 2022a. Topographic analysis of intertidal polychaete reefs (*sabellaria alveolata*) at a very high spatial resolution. *Remote Sensing* 2022, Vol. 14, Page 307 14, 307. <https://doi.org/10.3390/RS14020307>
- Brunier, G., Tamura, T., Anthony, E.J., Dussouillez, P., Gardel, A., 2022b. Evolution of the french guiana coast from late pleistocene to holocene based on chenier and beach sand dating. *Regional Environmental Change* 22, 122.
- Bryndum-Buchholz, A., Tittensor, D.P., Blanchard, J.L., Cheung, W.W., Coll, M., Galbraith, E.D., Jennings, S., Maury, O., Lotze, H.K., 2019. Twenty-first-century climate change impacts on marine animal biomass and ecosystem structure across ocean basins. *Global change biology* 25, 459–472.
- Bürkner, P.-C., 2021. Bayesian item response modeling in R with brms and Stan. *Journal of Statistical Software* 100, 1–54. <https://doi.org/10.18637/jss.v100.i05>
- Bürkner, P.-C., 2018. Advanced Bayesian multilevel modeling with the R package brms. *The R Journal* 10, 395–411. <https://doi.org/10.32614/RJ-2018-017>
- Bürkner, P.-C., 2017. brms: An R package for Bayesian multilevel models using Stan. *Journal of Statistical Software* 80, 1–28. <https://doi.org/10.18637/jss.v080.i01>
- Cabaço, S., Machás, R., Santos, R., 2009. Individual and population plasticity of the seagrass *zostera noltii* along a vertical intertidal gradient. *Estuarine, Coastal and Shelf Science* 82, 301–308.
- Calleja, F., Galván, C., Silió-Calzada, A., Juanes, J.A., Ondiviela, B., 2017. Long-term analysis of *zostera noltei*: A retrospective approach for understanding seagrasses' dynamics. *Marine environmental research* 130, 93–105.
- Calleja, M.L., Marbà, N., Duarte, C.M., 2007. The relationship between seagrass (*posidonia oceanica*) decline and sulfide porewater concentration in carbonate sediments. *Estuarine, Coastal and Shelf Science* 73, 583–588.
- Canadell, J.G., Jackson, R.B., 2021. Ecosystem collapse and climate change. Springer.

- Cao, F., Yang, Z., Ren, J., Jiang, M., Ling, W.-K., 2017. Does Normalization Methods Play a Role for Hyperspectral Image Classification? 2–7.
- Cao, H., Wang, M., Su, S., Kang, M., 2022. Explicit quantification of coastal cultural ecosystem services: A novel approach based on the content and sentimental analysis of social media. *Ecological Indicators* 137, 108756.
- Cardoso, P., Pardal, M., Lillebø, A., Ferreira, S., Raffaelli, D., Marques, J., 2004. Dynamic changes in seagrass assemblages under eutrophication and implications for recovery. *Journal of Experimental Marine Biology and Ecology* 302, 233–248.
- Carlson, D.F., Yarbro, L.A., Scolaro, S., Poniatowski, M., McGee-Absten, V., Carlson Jr, P.R., 2018. Sea surface temperatures and seagrass mortality in florida bay: Spatial and temporal patterns discerned from MODIS and AVHRR data. *Remote Sensing of Environment* 208, 171–188.
- Carpenter, B., Gelman, A., Hoffman, M.D., Lee, D., Goodrich, B., Betancourt, M., Brubaker, M., Guo, J., Li, P., Riddell, A., 2017. Stan: A probabilistic programming language. *Journal of Statistical Software* 76, 1–32. <https://doi.org/10.18637/jss.v076.i01>
- Cartaxana, P., Cruz, S., Gameiro, C., Kühl, M., 2016. Regulation of intertidal microphytobenthos photosynthesis over a diel emersion period is strongly affected by diatom migration patterns. *Frontiers in microbiology* 7, 872.
- Casal, G., Kutser, T., Domínguez-Gómez, J.A., Sánchez-Carnero, N., Freire, J., 2013. Assessment of the hyperspectral sensor CASI-2 for macroalgal discrimination on the Ría de Vigo coast (NW Spain) using field spectroscopy and modelled spectral libraries. *Continental Shelf Research* 55, 129–140. <https://doi.org/10.1016/j.csr.2013.01.010>
- Casal, G., Sánchez-Carnero, N., Domínguez-Gómez, J.A., Kutser, T., Freire, J., 2012. Assessment of AHS (Airborne Hyperspectral Scanner) sensor to map macroalgal communities on the Ría de vigo and Ría de Aldán coast (NW Spain). *Marine Biology* 159, 1997–2013. <https://doi.org/10.1007/s00227-012-1987-5>
- Casella, E., Drechsel, J., Winter, C., Benninghoff, M., Rovere, A., 2020. Accuracy of sand beach topography surveying by drones and photogrammetry. *Geo-Marine Letters* 40, 255–268.
- Castaing, P., Guilcher, A., 1995. Morphosedimentary evolution of ria-type estuaries. *Earth Surface Processes and Landforms* 20, 361–376. <https://doi.org/10.1002/esp.3290200408>
- Chadwick, K.D., Brodrick, P.G., Grant, K., Goulden, T., Henderson, A., Falco, N., Wainwright, H., Williams, K.H., Bill, M., Breckheimer, I., others, 2020. Integrating airborne remote sensing and field campaigns for ecology and earth system science. *Methods in Ecology and Evolution* 11, 1492–1508.
- Chand, S., Bolland, B., 2021. Low altitude spatial assessment and monitoring of intertidal seagrass meadows beyond the visible spectrum using a remotely piloted aircraft system. *Estuarine, Coastal and Shelf Science* 255, 107299.
- Chang, W., Cheng, J., Allaire, J., Sievert, C., Schloerke, B., Xie, Y., Allen, J., McPherson, J., Dipert, A., Borges, B., 2024. Shiny: Web application framework for r.
- Chao Rodríguez, Y., Domínguez Gómez, J.A., Sánchez-Carnero, N., Rodríguez-Pérez, D., 2017. A comparison of spectral macroalgae taxa separability methods using an extensive spectral library. *Algal Research* 26, 463–473. <https://doi.org/10.1016/j.algal.2017.04.021>
- Charrier, B., Boscq, S., Nelson, B.J., Läubli, N.F., 2021. Growth and labelling of cell wall components of the brown alga ectocarpus in microfluidic chips. *Frontiers in Marine Science* 8, 745654.

- Chefaoui, R.M., Duarte, C.M., Serrão, E.A., 2018. Dramatic loss of seagrass habitat under projected climate change in the mediterranean sea. *Global change biology* 24, 4919–4928.
- Cheng, B., Titterington, D.M., 1994. Neural networks: A review from a statistical perspective. *Statistical science* 2–30.
- Christensen, T., Dixon, P.S., Irvine, L.M., 1977. *Seaweeds of the british isles: Tribophyceae (xanthophyceae)*. British Museum (Natural History).
- Cikoš, A.-M., Šubarić, D., Roje, M., Babić, J., Jerković, I., Jokić, S., 2022. Recent advances on macroalgal pigments and their biological activities (2016–2021). *Algal research* 65, 102748.
- CMEMS, 2024. European north west shelf/iberia biscay irish seas – high resolution ODYSSEA sea surface temperature multi-sensor L3 observations reprocessed, e.u. Copernicus marine service information (CMEMS). Marine data store (MDS). (Accessed on 17-10-2024). <https://doi.org/10.48670/moi-00311>
- Coffer, M.M., Graybill, D.D., Whitman, P.J., Schaeffer, B.A., Salls, W.B., Zimmerman, R.C., Hill, V., Lebrasse, M.C., Li, J., Keith, D.J., others, 2023. Providing a framework for seagrass mapping in united states coastal ecosystems using high spatial resolution satellite imagery. *Journal of Environmental Management* 337, 117669.
- Cognat, M., Ganty, F., Auby, I., Barraquand, F., Rigouin, L., Sottolichio, A., 2018. Environmental factors controlling biomass development of seagrass meadows of *zostera noltei* after a drastic decline (arcachon bay, france). *Journal of sea research* 140, 87–104.
- Collin, A., Dubois, S., James, D., Houet, T., 2019. Improving intertidal reef mapping using UAV surface, red edge, and near-infrared data. *Drones* 3, 67.
- Condal, F., Aguzzi, J., Sarda, F., Nogueras, M., Cadena, J., Costa, C., Del Río, J., Manuel, A., 2012. Seasonal rhythm in a mediterranean coastal fish community as monitored by a cabled observatory. *Marine Biology* 159, 2809–2817.
- Connor, R.F., Chmura, G.L., Beecher, C.B., 2001. Carbon accumulation in bay of fundy salt marshes: Implications for restoration of reclaimed marshes. *Global Biogeochemical Cycles* 15, 943–954.
- Cooley, S., Schoeman, D., Bopp, L., Boyd, P., Donner, S., Kiessling, W., Martinetto, P., Ojea, E., Racault, M., Rost, B., others, 2023. Oceans and coastal ecosystems and their services.
- Cornwall, C.E., Carlot, J., Branson, O., Courtney, T.A., Harvey, B.P., Perry, C.T., Andersson, A.J., Diaz-Pulido, G., Johnson, M.D., Kennedy, E., others, 2023. Crustose coralline algae can contribute more than corals to coral reef carbonate production. *Communications Earth & Environment* 4, 105.
- Cosby, A., Lebakula, V., Smith, C., Wanik, D., Bergene, K., Rose, A., Swanson, D., Bloom, D., 2024. Accelerating growth of human coastal populations at the global and continent levels: 2000–2018. *Scientific Reports* 14, 22489.
- Costa, V., Serôdio, J., Lillebø, A.I., Sousa, A.I., 2021. Use of hyperspectral reflectance to non-destructively estimate seagrass *zostera noltei* biomass. *Ecological Indicators* 121, 107018. <https://doi.org/https://doi.org/10.1016/j.ecolind.2020.107018>
- Cramer, W., Guiot, J., Fader, M., Garrabou, J., Gattuso, J.-P., Iglesias, A., Lange, M.A., Lionello, P., Llasat, M.C., Paz, S., others, 2018. Climate change and interconnected risks to sustainable development in the mediterranean. *Nature Climate Change* 8, 972–980.
- Crowl, T.A., Crist, T.O., Parmenter, R.R., Belovsky, G., Lugo, A.E., 2008. The spread of invasive species and infectious disease as drivers of ecosystem change.

- Frontiers in Ecology and the Environment 6, 238–246.
- Dascaliuc, A., Ralea, T., Cuza, P., 2007. Influence of heat shock on chlorophyll fluorescence of white oak (*quercus pubescens* willd.) leaves. *Photosynthetica* 45, 469–471. <https://doi.org/10.1007/s11099-007-0084-3>
- Davies, B.F., Holmes, L., Bicknell, A., Attrill, M.J., Sheehan, E.V., 2022. A decade implementing ecosystem approach to fisheries management improves diversity of taxa and traits within a marine protected area in the UK. *Diversity and Distributions* 28, 173–188.
- Davies, B.F., Holmes, L., Rees, A., Attrill, M.J., Cartwright, A.Y., Sheehan, E.V., 2021. Ecosystem approach to fisheries management works—how switching from mobile to static fishing gear improves populations of fished and non-fished species inside a marine-protected area. *Journal of Applied Ecology* 58, 2463–2478.
- Davies, B.F.R., Gernez, P., Geraud, A., Oiry, Simon, Rosa, P., Zoffoli, M.L., Barillé, L., 2023a. Multi- and hyperspectral classification of soft-bottom intertidal vegetation using a spectral library for coastal biodiversity remote sensing. *Remote Sensing of Environment* 290, 113554. <https://doi.org/10.1016/j.rse.2023.113554>
- Davies, B.F.R., Holmes, L., Attrill, M.J., Sheehan, E.V., 2022. Ecosystem benefits of adopting a whole-site approach to MPA management. *Fisheries Management and Ecology*.
- Davies, B.F.R., Oiry, S., Rosa, P., Zoffoli, M.L., Sousa, A.I., Thomas, O.R., Smale, D.A., Austen, M.C., Biermann, L., Attrill, M.J., others, 2024b. A sentinel watching over inter-tidal seagrass phenology across western europe and north africa. *Communications Earth & Environment* 5, 382. <https://doi.org/10.1038/s43247-024-01543-z>
- Davies, B.F.R., Oiry, S., Rosa, P., Zoffoli, M.L., Sousa, A.I., Thomas, O.R., Smale, D.A., Austen, M.C., Biermann, L., Attrill, M.J., others, 2024a. Intertidal seagrass extent from sentinel-2 time-series show distinct trajectories in western europe. *Remote Sensing of Environment* 312, 114340. <https://doi.org/10.1016/j.rse.2024.114340>
- Davies, B.F.R., Sousa, A.I., Figueira, R., Oiry, S., Gernez, P., Barillé, L., 2023b. Benthic intertidal vegetation from the tagus estuary and aveiro lagoon. <https://doi.org/10.15468/n4ak6x>
- Davis, T.A., Volesky, B., Mucci, A., 2003. A review of the biochemistry of heavy metal biosorption by brown algae. *Water research* 37, 4311–4330.
- Davoult, D., Surget, G., Stiger-Pouvreau, V., Noisette, F., Riera, P., Stagnol, D., Androuin, T., Poupart, N., 2017. Multiple effects of a *gracilaria vermiculophylla* invasion on estuarine mudflat functioning and diversity. *Marine Environmental Research* 131, 227–235.
- De Fouw, J., Rehlmeyer, K., Geest, M. van der, Smolders, A.J., Van Der Heide, T., 2022. Increased temperature reduces the positive effect of sulfide-detoxification mutualism on *zostera noltii* nutrient uptake and growth. *Marine Ecology Progress Series* 692, 43–52.
- De Jorge, V., Van Beusekom, J., 1995. Wind-and tide-induced resuspension of sediment and microphytobenthos from tidal flats in the ems estuary. *Limnology and oceanography* 40, 776–778.
- Decho, A.W., 2000. Microbial biofilms in intertidal systems: An overview. *Continental shelf research* 20, 1257–1273.
- Decottignies, P., Beninger, P.G., Rincé, Y., Robins, R.J., Riera, P., 2007. Exploitation of natural food sources by two sympatric, invasive suspension-feeders: *Crassostrea gigas* and *crepidula fornicata*. *Marine Ecology Progress Series*

- Progress Series 334, 179–192.
- Deguette, A., Barrote, I., Silva, J., 2022. Physiological and morphological effects of a marine heatwave on the seagrass *cymodocea nodosa*. *Scientific Reports* 12, 7950.
- Dekker, A.G., Pinnel, N., Gege, P., Briottet, X., Peters, S., Turpie, K.R., Sterckx, S., Costa, M., Giardino, C., Brando, V.E., others, 2018. Feasibility study for an aquatic ecosystem earth observing system version 1.2.
- Desai, R.M., Shambaugh, G.E., 2021. Measuring the global impact of destructive and illegal fishing on maritime piracy: A spatial analysis. *Plos one* 16, e0246835.
- Devi, R., Gouda, K., Lenka, S., 2024. Intensity duration and frequency of heat wave in different phases of MJO over india. *Atmospheric Research* 300, 107250.
- Devlin, M., Brodie, J., 2023. Nutrients and eutrophication, in: *Marine Pollution–Monitoring, Management and Mitigation*. Springer, pp. 75–100.
- Dierssen, H.M., Chlus, A., Russell, B., 2015. Hyperspectral discrimination of floating mats of seagrass wrack and the macroalgae *Sargassum* in coastal waters of Greater Florida Bay using airborne remote sensing. *Remote Sensing of Environment* 167, 247–258. <https://doi.org/10.1016/j.rse.2015.01.027>
- Dionisi, D., Bucci, S., Cesarini, C., Colella, S., D’Alimonte, D., Di Ciolo, L., Di Girolamo, P., Di Paolantonio, M., Franco, N., Gostinicchi, G., others, 2024. Exploring the potential of aeolus lidar mission for ocean color applications. Available at SSRN 4762423.
- Diruit, W., Le Bris, A., Bajjouk, T., Richier, S., Helias, M., Burel, T., Lennon, M., Guyot, A., Ar Gall, E., 2022. Seaweed habitats on the shore: Characterization through hyperspectral UAV imagery and field sampling. *Remote Sensing* 14. <https://doi.org/10.3390/rs14133124>
- Douay, F., Verpoorter, C., Duong, G., Spilmont, N., Gevaert, F., 2022. New hyperspectral procedure to discriminate intertidal macroalgae. *Remote Sensing* 14, 346.
- Douglas, T.J., Coops, N.C., Drever, M.C., Hunt, B.P., Martin, T.G., 2024. Linking microphytobenthos distribution and mudflat geomorphology under varying sedimentary regimes using unoccupied aerial vehicle (UAV)-acquired multispectral reflectance and photogrammetry. *Science of The Total Environment* 173675.
- Drouet, S., Turpin, V., Godet, L., Cognie, B., Cosson, R.P., Decottignies, P., 2015. Utilisation of intertidal mudflats by the dunlin *calidris alpina* in relation to microphytobenthic biofilms. *Journal of Ornithology* 156, 75–83.
- Duffy, J.E., Benedetti-Cecchi, L., Trinanes, J., Muller-Karger, F.E., Ambo-Rappe, R., Boström, C., Buschmann, A.H., Byrnes, J., Coles, R.G., Creed, J., others, 2019. Toward a coordinated global observing system for seagrasses and marine macroalgae. *Frontiers in Marine Science* 6, 317.
- Duffy, J.P., Pratt, L., Anderson, K., Land, P.E., Shutler, J.D., 2018. Spatial assessment of intertidal seagrass meadows using optical imaging systems and a lightweight drone. *Estuarine, Coastal and Shelf Science* 200, 169–180.
- Durou, C., Poirier, L., Amiard, J.-C., Budzinski, H., Gnassia-Barelli, M., Lemenach, K., Peluhet, L., Mouneyrac, C., Roméo, M., Amiard-Triquet, C., 2007. Biomonitoring in a clean and a multi-contaminated estuary based on biomarkers and chemical analyses in the endobenthic worm *nereis diversicolor*. *Environmental Pollution* 148, 445–458.
- Edgar, G., Bustamante, R., Farina, J.-M., Calvopina, M., Martinez, C., Toral-Granda, M., 2004. Bias in evaluating the effects of marine protected areas: The importance of baseline data for the galapagos marine reserve. *Environmental Conservation* 31, 212–218.

- Edwards, M., Beaugrand, G., Hays, G.C., Koslow, J.A., Richardson, A.J., 2010. Multi-decadal oceanic ecological datasets and their application in marine policy and management. *Trends in ecology & evolution* 25, 602–610.
- Eger, A.M., Marzinelli, E.M., Beas-Luna, R., Blain, C.O., Blamey, L.K., Byrnes, J.E., Carnell, P.E., Choi, C.G., Hessing-Lewis, M., Kim, K.Y., others, 2023. The value of ecosystem services in global marine kelp forests. *Nature communications* 14, 1894.
- Electric Blue, 2023. Intertidal chamber.
- El-Hacen, E.-H.M., Cheikh, M.A.S., Bouma, T.J., Olff, H., Piersma, T., 2020. Long-term changes in seagrass and benthos at banc d'arguin, mauritania, the premier intertidal system along the east atlantic flyway. *Global Ecology and Conservation* 24, e01364.
- Elliott, M., Whitfield, A.K., 2011. Challenging paradigms in estuarine ecology and management. *Estuarine, Coastal and Shelf Science* 94, 306–314.
- Elton, C.S., 2020. The ecology of invasions by animals and plants. Springer Nature.
- ESA, 2024b. Sen2Cor: Sentinel-2 atmospheric correction processor.
- ESA, 2024a. Copernicus open access hub.
- European-Commission, n.d. Official Journal of the European Communities L 327, 1–72.
- Eurostat, 2023. Tourism satellite accounts in europe - 2023 edition. Publications Office of the European Union, Luxembourg. <https://doi.org/10.2785/7794>
- Faber, J., Hanayama, S., Zhang, S., Pereda, P., Comer, B., Hauerhof, E., Schim van der Loeff, W., Smith, T., Zhang, Y., Kosaka, H., Adachi, M., Bonello, J.-M., Galbraith, C., Gong, Z., Hirata, K., Hummels, D., Kleijn, A., Lee, D.S., Liu, Y., Lucchesi, A., Mao, X., Muraoka, E., Osipova, L., Qian, H., Rutherford, D., Suárez de la Fuente, S., Yuan, H., Velandia Perico, C., Wu, L., Sun, D., Yoo, D.-H., Xing, H., 2021. Fourth IMO GHG study 2020: Executive summary. International Maritime Organization (IMO), 4 Albert Embankment, London SE1 7SR.
- Fairley, I., Williamson, B.J., McIlvenny, J., King, N., Masters, I., Lewis, M., Neill, S., Glasby, D., Coles, D., Powell, B., others, 2022. Drone-based large-scale particle image velocimetry applied to tidal stream energy resource assessment. *Renewable Energy* 196, 839–855.
- Farmery, A.K., Alexander, K., Anderson, K., Blanchard, J.L., Carter, C.G., Evans, K., Fischer, M., Fleming, A., Frusher, S., Fulton, E.A., others, 2022. Food for all: Designing sustainable and secure future seafood systems. *Reviews in fish biology and fisheries* 32, 101–121.
- Firth, L.B., Foggo, A., Watts, T., Knights, A.M., DeAmicis, S., 2024. Invasive macroalgae in native seagrass beds: Vectors of spread and impacts. *Annals of Botany* 133, 41–50.
- Foden, J., Brazier, D., 2007. Angiosperms (seagrass) within the EU water framework directive: A UK perspective. *Marine Pollution Bulletin* 55, 181–195.
- Folmer, E.O., Geest, M. van der, Jansen, E., Olff, H., Michael Anderson, T., Piersma, T., Gils, J.A. van, 2012. Seagrass–sediment feedback: An exploration using a non-recursive structural equation model. *Ecosystems* 15, 1380–1393.
- Fourqurean, J.W., Duarte, C.M., Kennedy, H., Marbà, N., Holmer, M., Mateo, M.A., Apostolaki, E.T., Kendrick, G.A., Krause-Jensen, D., McGlathery, K.J., others, 2012. Seagrass ecosystems as a globally significant carbon stock. *Nature geoscience* 5, 505–509.
- Fox, H.E., Barnes, M.D., Ahmadi, G.N., Kao, G., Glew, L., Haisfield, K., Hidayat, N.I., Huffard, C.L., Katz, L., Mangubhai, S., others, 2017. Generating

- actionable data for evidence-based conservation: The global center of marine biodiversity as a case study. *Biological Conservation* 210, 299–309.
- Franssen, S.U., Gu, J., Winters, G., Huylmans, A.-K., Wienpahl, I., Sparwel, M., Coyer, J.A., Olsen, J.L., Reusch, T.B., Bornberg-Bauer, E., 2014. Genome-wide transcriptomic responses of the seagrasses *zostera marina* and *nanozostera noltii* under a simulated heatwave confirm functional types. *Marine Genomics* 15, 65–73.
- Frick, H., Chow, F., Kuhn, M., Mahoney, M., Silge, J., Wickham, H., 2024. Rsample: General resampling infrastructure.
- Fyfe, S., 2003. Spatial and temporal variation in spectral reflectance: Are seagrass species spectrally distinct? *Limnology and Oceanography* 48, 464–479.
- Gacia, E., Granata, T., Duarte, C., 1999. An approach to measurement of particle flux and sediment retention within seagrass (*posidonia oceanica*) meadows. *Aquatic Botany* 65, 255–268.
- Gallardo, B., Clavero, M., Sánchez, M.I., Vilà, M., 2016. Global ecological impacts of invasive species in aquatic ecosystems. *Global change biology* 22, 151–163.
- Garbulsky, M.F., Peñuelas, J., Gamon, J., Inoue, Y., Filella, I., 2011. The photochemical reflectance index (PRI) and the remote sensing of leaf, canopy and ecosystem radiation use efficiencies: A review and meta-analysis. *Remote sensing of environment* 115, 281–297.
- García-Feced, C., Tempel, D.J., Kelly, M., 2011. LiDAR as a tool to characterize wildlife habitat: California spotted owl nesting habitat as an example. *Journal of Forestry* 109, 436–443.
- Gardner, R.C., Finlayson, C., 2018. Global wetland outlook: State of the world's wetlands and their services to people, in: Ramsar Convention Secretariat. pp. 2020–5.
- Garmendia, J.M., Valle, M., Borja, Á., Chust, G., Rodríguez, J.G., Franco, J., 2021. Estimated footprint of shellfishing activities in *Zostera noltei* meadows in a northern Spain estuary: Lessons for management. *Estuarine, Coastal and Shelf Science* 254. <https://doi.org/10.1016/j.ecss.2021.107320>
- Ginneken, V. van, Vries, E. de, others, 2018. The global dispersal of the non-endemic invasive red alga *gracilaria vermiculophylla* in the ecosystems of the euro-asia coastal waters including the wadden sea unesco world heritage coastal area: Awful or awesome? *Oceanography & Fisheries Open Access Journal* 8, 4–26.
- Gladstone-Gallagher, R.V., Hughes, R.W., Douglas, E.J., Pilditch, C.A., 2018. Biomass-dependent seagrass resilience to sediment eutrophication. *Journal of Experimental Marine Biology and Ecology* 501, 54–64.
- Gomes, I., Peteiro, L., Bueno-Pardo, J., Albuquerque, R., Perez-Jorge, S., Oliveira, E.R., Alves, F.L., Queiroga, H., 2018. What's a picture really worth? On the use of drone aerial imagery to estimate intertidal rocky shore mussel demographic parameters. *Estuarine, Coastal and Shelf Science* 213, 185–198.
- Green, A.E., Unsworth, R.K., Chadwick, M.A., Jones, P.J., 2021. Historical analysis exposes catastrophic seagrass loss for the united kingdom. *Frontiers in plant science* 12, 629962.
- Green, S.J., Grosholz, E.D., 2021. Functional eradication as a framework for invasive species control. *Frontiers in Ecology and the Environment* 19, 98–107.
- Greenwell, B.M., Boehmke, B.C., 2020. Variable importance plots—an introduction to the vip package. *The R Journal* 12, 343–366.
- Grizel, H., Heral, M., 1991. Introduction into france of the japanese oyster (*crassostrea gigas*). *ICES Journal of Marine Science* 47, 399–403.

- Guan, S., Brookens, T., 2023. An overview of research efforts to understand the effects of underwater sound on cetaceans. *Water Biology and Security* 2, 100141.
- Guerrero-Meseguer, L., Marín, A., Sanz-Lázaro, C., 2020. Heat wave intensity can vary the cumulative effects of multiple environmental stressors on posidonia oceanica seedlings. *Marine Environmental Research* 159, 105001.
- Gurgel, C.F.D., Norris, J.N., Schmidt, W.E., Le, H.N., Fredericq, S., 2018. Systematics of the gracilariales (rhodophyta) including new subfamilies, tribes, subgenera, and two new genera, agarophyton gen. Nov. And crassa gen. nov. *Phytotaxa* 374, 1–23.
- Guyot, G., 1990. Optical properties of vegetation canopies. *Optical properties of vegetation canopies.* 19–43.
- Hagger, V., Worthington, T.A., Lovelock, C.E., Adame, M.F., Amano, T., Brown, B.M., Friess, D.A., Landis, E., Mumby, P.J., Morrison, T.H., others, 2022. Drivers of global mangrove loss and gain in social-ecological systems. *Nature Communications* 13, 6373.
- Hallik, L., Kazantsev, T., Kuusk, A., Galmés, J., Tomás, M., Niinemets, Ü., 2017. Generality of relationships between leaf pigment contents and spectral vegetation indices in mallorca (spain). *Regional Environmental Change* 17, 2097–2109.
- Hanley, M.E., Firth, L.B., Foggo, A., 2024. Victim of changes? Marine macroalgae in a changing world. *Annals of Botany* 133, 1–16.
- Haro, S., Jimenez-Reina, J., Bermejo, R., Morrison, L., 2023. BioIntertidal mapper software: A satellite approach for NDVI-based intertidal habitat mapping. *SoftwareX* 24, 101520.
- Hassan, R., Scholes, R., Ash, N., 2005. Ecosystems and human well-being: Current state and trends.
- Hatum, P.S., McMahon, K., Mengersen, K., Kilminster, K., Wu, P.P.-Y., 2024. Predicting seagrass ecosystem resilience to marine heatwave events of variable duration, frequency and re-occurrence patterns with gaps. *Aquatic Conservation: Marine and Freshwater Ecosystems* 34, e4210. <https://doi.org/10.1002/aqc.4210>
- Hedley, J.D., Mirhakak, M., Wentworth, A., Dierssen, H.M., 2018. Influence of three-dimensional coral structures on hyperspectral benthic reflectance and water-leaving reflectance. *Applied Sciences* 8. <https://doi.org/10.3390/app8122688>
- Hestir, E.L., Brando, V.E., Bresciani, M., Giardino, C., Matta, E., Villa, P., Dekker, A.G., 2015. Measuring freshwater aquatic ecosystems: The need for a hyperspectral global mapping satellite mission. *Remote Sensing of Environment* 167, 181–195. <https://doi.org/10.1016/j.rse.2015.05.023>
- Hijmans, R.J., 2024. Terra: Spatial data analysis.
- Hobday, A.J., Alexander, L.V., Perkins, S.E., Smale, D.A., Straub, S.C., Oliver, E.C., BenthuySEN, J.A., Burrows, M.T., Donat, M.G., Feng, M., others, 2016. A hierarchical approach to defining marine heatwaves. *Progress in oceanography* 141, 227–238.
- Hobday, A.J., Oliver, E.C., Gupta, A.S., BenthuySEN, J.A., Burrows, M.T., Donat, M.G., Holbrook, N.J., Moore, P.J., Thomsen, M.S., Wernberg, T., others, 2018. Categorizing and naming marine heatwaves. *Oceanography* 31, 162–173.
- Hobohm, C., Schaminée, J., Rooijen, N. van, 2021. Coastal habitats, shallow seas and inland saline steppes: Ecology, distribution, threats and challenges. *Perspectives for biodiversity and ecosystems* 279–310.
- Holon, F., Marre, G., Parravicini, V., Mouquet, N., Bockel, T., Descamp, P., Tribot, A.-S., Boissery, P., Deter, J., 2018. A predictive model based on multiple coastal anthropogenic pressures explains the degradation status of a marine ecosystem:

- Implications for management and conservation. *Biological Conservation* 222, 125–135.
- Hope, J.A., Coco, G., Ladewig, S.M., Thrush, S.F., 2021. The distribution and ecological effects of microplastics in an estuarine ecosystem. *Environmental Pollution* 288, 117731. <https://doi.org/10.1016/j.envpol.2021.117731>
- Howard, J., others, 2018. Fastai.
- Hu, L., Hu, C., Ming-Xia, H.E., 2017. Remote estimation of biomass of *Ulva prolifera* macroalgae in the Yellow Sea. *Remote Sensing of Environment* 192, 217–227. <https://doi.org/10.1016/j.rse.2017.01.037>
- Hughes, A.R., Stachowicz, J.J., 2004. Genetic diversity enhances the resistance of a seagrass ecosystem to disturbance. *Proceedings of the National Academy of Sciences* 101, 8998–9002. <https://doi.org/10.1073/pnas.0402642101>
- IGN, 2024a. Institut national de l'information géographique et forestière (IGN).
- IGN, 2024b. Remonter le temps.
- Infantes, E., Hoeks, S., Adams, M.P., Heide, T. van der, Katwijk, M.M. van, Bouma, T.J., 2022. Seagrass roots strongly reduce cliff erosion rates in sandy sediments. *Marine Ecology Progress Series* 700, 1–12.
- IOC, n.d. Intergovernmental oceanographic commission ; sea level monitoring station - le conquet, france (LECY).
- Ismail, M.M., Alotaibi, B.S., El-Sheekh, M.M., 2020. Therapeutic uses of red macroalgae. *Molecules* 25, 4411.
- ITOPF, I.T.O.P.F., 2023. Statistics - ITOPF.
- Jamet, C., Ibrahim, A., Ahmad, Z., Angelini, F., Babin, M., Behrenfeld, M.J., Boss, E., Cairns, B., Churnside, J., Chowdhary, J., others, 2019. Going beyond standard ocean color observations: Lidar and polarimetry. *Frontiers in Marine Science* 6, 251.
- Jankowska, E., Michel, L.N., Lepoint, G., Włodarska-Kowalcuk, M., 2019. Stabilizing effects of seagrass meadows on coastal water benthic food webs. *Journal of Experimental Marine Biology and Ecology* 510, 54–63.
- Jesus, B., Rosa, P., Mouget, J.-L., Méléder, V., Launeau, P., Barillé, L., 2014. Spectral-radiometric analysis of taxonomically mixed microphytobenthic biofilms. *Remote sensing of environment* 140, 196–205.
- Jones, P.E., Tummers, J.S., Galib, S.M., Woodford, D.J., Hume, J.B., Silva, L.G., Braga, R.R., Garcia de Leaniz, C., Vitule, J.R., Herder, J.E., others, 2021. The use of barriers to limit the spread of aquatic invasive animal species: A global review. *Frontiers in Ecology and Evolution* 9, 611631.
- Jones, R.B., Clayton-Greene, K.A., 1992. The role of photosynthesis and oxidative reactions in leaf blackening of protea *neriifolia* r. Br. leaves. *Scientia Horticulturae* 50, 137–145. [https://doi.org/10.1016/S0304-4238\(05\)80016-0](https://doi.org/10.1016/S0304-4238(05)80016-0)
- Joyce, K.E., Belliss, S.E., Samsonov, S.V., McNeill, S.J., Glassey, P.J., 2009. A review of the status of satellite remote sensing and image processing techniques for mapping natural hazards and disasters. *Progress in Physical Geography* 33, 183–207. <https://doi.org/10.1177/0309133309339563>
- Joyce, K.E., Fickas, K.C., Kalamandeen, M., 2023. The unique value proposition for using drones to map coastal ecosystems. *Cambridge Prisms: Coastal Futures* 1, e6.
- Karakassis, I., Pitta, P., Krom, M.D., 2005. Contribution of fish farming to the nutrient loading of the mediterranean. *Scientia Marina* 69, 313–321.
- Kattenborn, T., Leitloff, J., Schiefer, F., Hinz, S., 2021. Review on convolutional neural networks (CNN) in vegetation remote sensing. *ISPRS journal of photogrammetry and remote sensing* 173, 24–49.

- Kelly, D.J., Clare, J.J., Bothwell, M.L., 2001. Attenuation of solar ultraviolet radiation by dissolved organic matter alters benthic colonization patterns in streams. *Journal of the North American Benthological Society* 20, 96–108.
- Kirk, J.T., 1994. Light and photosynthesis in aquatic ecosystems. Cambridge university press.
- Klemas, V., 2012. Remote sensing of algal blooms: An overview with case studies. *Journal of coastal research* 28, 34–43.
- Knippling, E.B., 1970. Physical and physiological basis for the reflectance of visible and near-infrared radiation from vegetation. *Remote Sensing of Environment* 1, 155–159. [https://doi.org/10.1016/S0034-4257\(70\)80021-9](https://doi.org/10.1016/S0034-4257(70)80021-9)
- Kovalenko, I., Zdyrko, B., Magasinski, A., Hertzberg, B., Milicev, Z., Burtovyy, R., Luzinov, I., Yushin, G., 2011. A major constituent of brown algae for use in high-capacity li-ion batteries. *Science* 334, 75–79.
- Krause-Jensen, D., Lavery, P., Serrano, O., Marbà, N., Masque, P., Duarte, C.M., 2018. Sequestration of macroalgal carbon: The elephant in the blue carbon room. *Biology letters* 14, 20180236.
- Krček, M., Král, K., Cushman, K.C., Missarov, A., Kellner, J.R., 2020. Supervised segmentation of ultra-high-density drone lidar for large-area mapping of individual trees. *Remote Sensing* 12, 3260.
- Krueger-Hadfield, S.A., Kollars, N.M., Strand, A.E., Byers, J.E., Shainker, S.J., Terada, R., Greig, T.W., Hammann, M., Murray, D.C., Weinberger, F., others, 2017. Genetic identification of source and likely vector of a widespread marine invader. *Ecology and evolution* 7, 4432–4447.
- Kruse, F.A., Lefkoff, A.B., Boardman, J.W., Heidebrecht, K.B., Shapiro, A.T., Barloon, P.J., Goetz, A.F.H., 1993. The spectral image processing system (SIPS)-interactive visualization and analysis of imaging spectrometer data 192, 192–201. <https://doi.org/10.1063/1.44433>
- Kuhn, M., Vaughan, D., Hvítfeldt, E., 2024. Yardstick: Tidy characterizations of model performance.
- Kuhn, M., Wickham, H., 2020. Tidymodels: A collection of packages for modeling and machine learning using tidyverse principles.
- Kutser, T., Vahtmäe, E., Martin, G., 2006. Assessing suitability of multispectral satellites for mapping benthic macroalgal cover in turbid coastal waters by means of model simulations. *Estuarine, Coastal and Shelf Science* 67, 521–529. <https://doi.org/10.1016/j.ecss.2005.12.004>
- Laignel, B., Vignudelli, S., Almar, R., Becker, M., Bentamy, A., Benveniste, J., Birol, F., Frappart, F., Idier, D., Salameh, E., others, 2023. Observation of the coastal areas, estuaries and deltas from space. *Surveys in Geophysics* 44, 1309–1356.
- Lakshmi, A., 2021. Coastal ecosystem services & human wellbeing. *Indian Journal of Medical Research* 153, 382–387.
- Launeau, P., Méléder, V., Verpoorter, C., Barillé, L., Kazemipour-Ricci, F., Giraud, M., Jesus, B., Le Menn, E., 2018. Microphytobenthos biomass and diversity mapping at different spatial scales with a hyperspectral optical model. *Remote Sensing* 10, 716.
- Le Bris, A., Rosa, P., Lerouxel, A., Cognie, B., Gernez, P., Launeau, P., Robin, M., Barillé, L., 2016. Hyperspectral remote sensing of wild oyster reefs. *Estuarine, Coastal and Shelf Science* 172, 1–12.
- Lee, J., Jo, H., Oh, J., 2023. Application of drone LiDAR survey for evaluation of a long-term consolidation settlement of large land reclamation. *Applied Sciences* 13, 8277.
- Légaré, B., Bélanger, S., Singh, R.K., Bernatchez, P., Cusson, M., 2022. Remote

- sensing of coastal vegetation phenology in a cold temperate intertidal system: Implications for classification of coastal habitats. *Remote Sensing* 14, 3000.
- Lehnert, L.W., Meyer, H., Bendix, J., 2017.
- Lengyel, S., Kobler, A., Kutnar, L., Framstad, E., Henry, P.-Y., Babij, V., Gruber, B., Schmeller, D., Henle, K., 2008. A review and a framework for the integration of biodiversity monitoring at the habitat level. *Biodiversity and Conservation* 17, 3341–3356.
- Lin, H., Sun, T., Zhou, Y., Gu, R., Zhang, X., Yang, W., 2018. Which genes in a typical intertidal seagrass (*Zostera japonica*) indicate copper-, lead-, and cadmium pollution? *Frontiers in Plant Science* 9, 1545.
- Liu, D., Ma, Q., Valiela, I., Anderson, D.M., Keesing, J.K., Gao, K., Zhen, Y., Sun, X., Wang, Y., 2020. Role of C4 carbon fixation in *Ulva prolifera*, the macroalgae responsible for the world's largest green tides. *Communications Biology* 3, 494.
- Livore, J.P., Mendez, M.M., Miloslavich, P., Rilov, G., Bigatti, G., 2021. Biodiversity monitoring in rocky shores: Challenges of devising a globally applicable and cost-effective protocol. *Ocean & Coastal Management* 205, 105548.
- Lizcano-Sandoval, L., Anastasiou, C., Montes, E., Raulerson, G., Sherwood, E., Muller-Karger, F.E., 2022. Seagrass distribution, areal cover, and changes (1990–2021) in coastal waters off west-central Florida, USA. *Estuarine, Coastal and Shelf Science* 108134.
- Loarie, S.R., Duffy, P.B., Hamilton, H., Asner, G.P., Field, C.B., Ackerly, D.D., 2009. The velocity of climate change. *Nature* 462, 1052–1055.
- Los Santos, C.B. de, Krause-Jensen, D., Alcoverro, T., Marbà, N., Duarte, C.M., Van Katwijk, M.M., Pérez, M., Romero, J., Sánchez-Lizaso, J.L., Roca, G., others, 2019. Recent trend reversal for declining European seagrass meadows. *Nature Communications* 10, 3356.
- Los Santos, C.B. de, Olivé, I., Moreira, M., Silva, A., Freitas, C., Luna, R.A., Quental-Ferreira, H., Martins, M., Costa, M.M., Silva, J., others, 2020. Seagrass meadows improve inflowing water quality in aquaculture ponds. *Aquaculture* 528, 735502.
- Louhaichi, M., Borman, M.M., Johnson, D.E., 2001. Spatially located platform and aerial photography for documentation of grazing impacts on wheat. *Geocarto International* 16, 65–70.
- Louime, C., Fortune, J., Gervais, G., 2017. Sargassum invasion of coastal environments: A growing concern. *American Journal of Environmental Sciences* 13, 58–64.
- Lovelock, C.E., Feller, I.C., Reef, R., Hickey, S., Ball, M.C., 2017. Mangrove dieback during fluctuating sea levels. *Scientific Reports* 7, 1680.
- MacIntyre, H.L., Geider, R.J., Miller, D.C., 1996. Microphytobenthos: The ecological role of the “secret garden” of unvegetated, shallow-water marine habitats. I. Distribution, abundance and primary production. *Estuaries* 19, 186–201.
- Mahrad, B.E., Newton, A., Icely, J.D., Kacimi, I., Abalansa, S., Snoussi, M., 2020. Contribution of remote sensing technologies to a holistic coastal and marine environmental management framework: A review. *Remote Sensing* 12, 2313.
- Malekmohamadi Faradonbe, S., Safi-Esfahani, F., Karimian-Kelishadrokhi, M., 2020. A review on neural turing machine (NTM). *SN Computer Science* 1, 333.
- Malvern Panalytical, 2023. RS3 software.
- Manca, F., Benedetti-Cecchi, L., Bradshaw, C.J., Cabeza, M., Gustafsson, C., Norkko, A.M., Roslin, T.V., Thomas, D.N., White, L., Strona, G., 2024.

- Projected loss of brown macroalgae and seagrasses with global environmental change. *Nature Communications* 15, 5344.
- Marbà, N., Duarte, C.M., 2010. Mediterranean warming triggers seagrass (*posidonia oceanica*) shoot mortality. *Global change biology* 16, 2366–2375.
- Mariën, B., Balzarolo, M., Dox, I., Leys, S., Lorène, M.J., Geron, C., Portillo-Estrada, M., AbdElgawad, H., Asard, H., Campioli, M., 2019. Detecting the onset of autumn leaf senescence in deciduous forest trees of the temperate zone. *New Phytologist* 224, 166–176.
- Marquet, P.A., Buschmann, A.H., Corcoran, D., Díaz, P.A., Fuentes-Castillo, T., Garreaud, R., Pliscoff, P., Salazar, A., 2024. Global change and acceleration of anthropic pressures on patagonian ecosystems, in: *Conservation in Chilean Patagonia: Assessing the State of Knowledge, Opportunities, and Challenges*. Springer International Publishing Cham, pp. 33–65.
- Martínez, M.L., Intralawan, A., Vázquez, G., Pérez-Maqueo, O., Sutton, P., Landgrave, R., 2007. The coasts of our world: Ecological, economic and social importance. *Ecological economics* 63, 254–272.
- Massa, S., Arnaud-Haond, S., Pearson, G., Serrão, E., 2009. Temperature tolerance and survival of intertidal populations of the seagrass *zostera noltii* (hornemann) in southern europe (ria formosa, portugal). *Hydrobiologia* 619, 195–201.
- Massé, C., Viard, F., Humbert, S., Antajan, E., Auby, I., Bachelet, G., Bernard, G., Bouchet, V.M.P., Burel, T., Dauvin, J.-C., Delegrange, A., Derrien-Courtel, S., Droual, G., Gouillieux, B., Goulletquer, P., Guérin, L., Janson, A.-L., Jourde, J., Labrune, C., Lavesque, N., Leclerc, J.-C., Le Duff, M., Le Garrec, V., Noël, P., Nowaczyk, A., Pergent-Martini, C., Pezy, J.-P., Raoux, A., Raybaud, V., Ruitton, S., Sauriau, P.-G., Spilmont, N., Thibault, D., Vincent, D., Curd, A., 2023. An overview of marine non-indigenous species found in three contrasting biogeographic metropolitan french regions: Insights on distribution, origins and pathways of introduction. *Diversity* 15. <https://doi.org/10.3390/d15020161>
- Masson-Delmotte, V., Zhai, P., Pirani, A., Connors, S.L., Péan, C., Berger, S., Caud, N., Chen, Y., Goldfarb, L., Gomis, M., others, 2021. Climate change 2021: The physical science basis. Contribution of working group I to the sixth assessment report of the intergovernmental panel on climate change 2.
- Mazdiyasni, O., Sadegh, M., Chiang, F., AghaKouchak, A., 2019. Heat wave intensity duration frequency curve: A multivariate approach for hazard and attribution analysis. *Scientific Reports* 9, 14117. <https://doi.org/10.1038/s41598-019-50643-w>
- McCulloch, W.S., Pitts, W., 1943. A logical calculus of the ideas immanent in nervous activity. *The bulletin of mathematical biophysics* 5, 115–133.
- Mcilwaine, B., Casado, M.R., Leinster, P., 2019. Using 1st derivative reflectance signatures within a remote sensing framework to identify macroalgae in marine environments. *Remote Sensing* 11. <https://doi.org/10.3390/rs11060704>
- McKenzie, L.J., Nordlund, L.M., Jones, B.L., Cullen-Unsworth, L.C., Roelfsema, C., Unsworth, R.K., 2020. The global distribution of seagrass meadows. *Environmental Research Letters* 15, 074041.
- McRoy, C.P., McMillan, C., 1977. Production ecology and physiology of seagrasses. Méléder, V., Barillé, L., Launeau, P., Carrère, V., Rincé, Y., 2003a. Spectrometric constraint in analysis of benthic diatom biomass using monospecific cultures. *Remote Sensing of Environment* 88, 386–400.
- Méléder, V., Barillé, L., Rincé, Y., Morançais, M., Rosa, P., Gaudin, P., 2005. Spatio-temporal changes in microphytobenthos structure analysed by pigment composition in a macrotidal flat (bourgneuf bay, france). *Marine Ecology Progress Series* 300, 1–12.

- Progress Series 297, 83–99.
- Méléder, V., Jesus, B., Barnett, A., Barillé, L., Lavaud, J., 2018. Microphytobenthos primary production estimated by hyperspectral reflectance. *PloS one* 13, e0197093.
- Méléder, V., Launeau, P., Barillé, L., Rincé, Y., 2003b. Cartographie des peuplements du microphytobenthos par télédétection spatiale visible-infrarouge dans un écosystème conchylicole. *Comptes rendus. Biologies* 326, 377–389.
- Méléder, V., Laviale, M., Jesus, B., Mouget, J.L., Lavaud, J., Kazemipour, F., Launeau, P., Barillé, L., 2013. In vivo estimation of pigment composition and optical absorption cross-section by spectroradiometry in four aquatic photosynthetic micro-organisms. *Journal of Photochemistry and Photobiology B: Biology* 129, 115–124. <https://doi.org/10.1016/j.jphotobiol.2013.10.005>
- Mendoza-Segura, C., Fernández, E., Beca-Carretero, P., 2023. Predicted changes in the biogeographical range of *gracilaria vermiculophylla* under present and future climate scenarios. *Journal of Marine Science and Engineering* 11. <https://doi.org/10.3390/jmse11020367>
- Ménèsguen, A., 2018. Les marées vertes: 40 clés pour comprendre. Editions Quae.
- Michel, G., Le Bot, S., Lesourd, S., Lafite, R., 2021. Morpho-sedimentological and dynamic patterns in a ria type estuary: The belon estuary (south brittany, france). *Journal of Maps* 17, 389–400. <https://doi.org/10.1080/17445647.2021.1925170>
- Mienye, I.D., Swart, T.G., Obaido, G., 2024. Recurrent neural networks: A comprehensive review of architectures, variants, and applications. *Information* 15, 517.
- Miller, D.C., Geider, R.J., MacIntyre, H.L., 1996. Microphytobenthos: The ecological role of the “secret garden” of unvegetated, shallow-water marine habitats. II. Role in sediment stability and shallow-water food webs. *Estuaries* 19, 202–212.
- Miloslavich, P., Bax, N.J., Simmons, S.E., Klein, E., Appeltans, W., Aburto-Oropeza, O., Garcia, M.A., Batten, S.D., Benedetti-Cecchi, L., Checkley, D.M., Chiba, S., Duffy, J.E., Dunn, D.C., Fischer, A., Gunn, J., Kudela, R., Marsac, F., Muller-Karger, F.E., Obura, D., Shin, Y.J., 2018. Essential ocean variables for global sustained observations of biodiversity and ecosystem changes. *Global Change Biology* 24, 2416–2433. <https://doi.org/10.1111/GCB.14108>
- Minderhoud, P., Middelkoop, H., Erkens, G., Stouthamer, E., 2020. Groundwater extraction may drown mega-delta: Projections of extraction-induced subsidence and elevation of the mekong delta for the 21st century. *Environmental Research Communications* 2, 011005.
- Momota, K., Hosokawa, S., 2021. Potential impacts of marine urbanization on benthic macrofaunal diversity. *Scientific Reports* 11, 1–12. <https://doi.org/10.1038/s41598-021-83597-z>
- Moore, K.A., Jarvis, J.C., 2008. Environmental factors affecting recent summertime eelgrass diebacks in the lower chesapeake bay: Implications for long-term persistence. *Journal of Coastal Research* 135–147.
- Moreira, A., Cruz, S., Marques, R., Cartaxana, P., 2022. The underexplored potential of green macroalgae in aquaculture. *Reviews in Aquaculture* 14, 5–26.
- Mouritsen, K.N., Poulin, R., 2002. Parasitism, community structure and biodiversity in intertidal ecosystems. *Parasitology* 124. <https://doi.org/10.1017/s0031182002001476>
- Moussa, R.M., Bertucci, F., Jorissen, H., Gache, C., Waqalevu, V.P., Parravicini, V., Lecchini, D., Galzin, R., 2020. Importance of intertidal seagrass beds as

- nursery area for coral reef fish juveniles (mayotte, indian ocean). *Regional Studies in Marine Science* 33, 100965.
- Mudd, S.M., D'Alpaos, A., Morris, J.T., 2010. How does vegetation affect sedimentation on tidal marshes? Investigating particle capture and hydrodynamic controls on biologically mediated sedimentation. *Journal of Geophysical Research: Earth Surface* 115.
- Mukhopadhyay, A., Dasgupta, R., Hazra, S., Mitra, D., 2012. Coastal hazards and vulnerability: A review. *International journal of geology, earth and environmental sciences* 2, 57–69.
- Muller-Karger, F.E., Hestir, E., Ade, C., Turpie, K., Roberts, D.A., Siegel, D., Miller, R.J., Humm, D., Izenberg, N., Keller, M., Morgan, F., Frouin, R., Dekker, A.G., Gardner, R., Goodman, J., Schaeffer, B., Franz, B.A., Pahlevan, N., Mannino, A.G., Concha, J.A., Ackleson, S.G., Cavanaugh, K.C., Romanou, A., Tzortziou, M., Boss, E.S., Pavlick, R., Freeman, A., Rousseaux, C.S., Dunne, J., Long, M.C., Klein, E., McKinley, G.A., Goes, J., Letelier, R., Kavanaugh, M., Roffer, M., Bracher, A., Arrigo, K.R., Dierssen, H., Zhang, X., Davis, F.W., Best, B., Guralnick, R., Moisan, J., Sosik, H.M., Kudela, R., Mouw, C.B., Barnard, A.H., Palacios, S., Roesler, C., Drakou, E.G., Appeltans, W., Jetz, W., 2018. Satellite sensor requirements for monitoring essential biodiversity variables of coastal ecosystems. *Ecological Applications* 28, 749–760.
<https://doi.org/10.1002/eap.1682>
- Murray, N.J., Phinn, S.R., DeWitt, M., Ferrari, R., Johnston, R., Lyons, M.B., Clinton, N., Thau, D., Fuller, R.A., 2019. The global distribution and trajectory of tidal flats. *Nature* 565, 222–225. <https://doi.org/10.1038/s41586-018-0805-8>
- Nebel, S., Beege, M., Schneider, S., Rey, G.D., 2020. A review of photogrammetry and photorealistic 3D models in education from a psychological perspective, in: *Frontiers in Education*. Frontiers Media SA, p. 144.
- Nguyen, H.M., Ralph, P.J., Marín-Guirao, L., Pernice, M., Procaccini, G., 2021. Seagrasses in an era of ocean warming: A review. *Biological Reviews* 96, 2009–2030.
- Nicholls, R.J., others, 2007. Impacts of climate change and sea-level rise on coastal systems, in: Parry, M., others (Eds.), *Climate Change 2007: Impacts, Adaptation and Vulnerability*. Cambridge University Press, Cambridge, pp. 315–356.
- Nijland, W., Reshitnyk, L., Rubidge, E., 2019. Satellite remote sensing of canopy-forming kelp on a complex coastline: A novel procedure using the landsat image archive. *Remote Sensing of Environment* 220, 41–50.
- Nixon, S.W., 1981. Remineralization and nutrient cycling in coastal marine ecosystems, in: *Estuaries and Nutrients*. Springer, pp. 111–138.
- Nordlund, L.M., Unsworth, R.K., Wallner-Hahn, S., Ratnarajah, L., Beca-Carretero, P., Boikova, E., Bull, J.C., Chefaoui, R.M., Santos, C.B. de los, Gagnon, K., others, 2024. One hundred priority questions for advancing seagrass conservation in europe. *Plants, People, Planet*.
- Nowacek, D.P., Thorne, L.H., Johnston, D.W., Tyack, P.L., 2007. Responses of cetaceans to anthropogenic noise. *Mammal Review* 37, 81–115.
- N-Uptake, A., 1999. Primary production by phytoplankton and microphytobenthos in estuaries. *Estuaries* 29, 93.
- Nurdin, N., Alevizos, E., Syamsuddin, R., Asis, H., Zainuddin, E.N., Aris, A., Oiry, S., Brunier, G., Komatsu, T., Barillé, L., 2023. Precision aquaculture drone mapping of the spatial distribution of *kappaphycus alvarezii* biomass and carrageenan. *Remote Sensing* 15, 3674.

- Nyberg, C.D., 2007. Introduced marine macroalgae and habitat modifiers: Their ecological role and significant attributes. Department of Marine Ecology.
- Nyberg, C.D., Thomsen, M.S., Wallentinus, I., 2009. Flora and fauna associated with the introduced red alga *gracilaria vermiculophylla*. European Journal of Phycology 44, 395–403.
- O'Brien, K.R., Waycott, M., Maxwell, P., Kendrick, G.A., Udy, J.W., Ferguson, A.J., Kilminster, K., Scanes, P., McKenzie, L.J., McMahon, K., others, 2018. Seagrass ecosystem trajectory depends on the relative timescales of resistance, recovery and disturbance. Marine Pollution Bulletin 134, 166–176.
- Oh, J., Kim, D., Lee, H., 2017. Use of a drone for mapping and time series image acquisition of tidal zones. Journal of the Korean Institute of Intelligent Systems 27, 119–125.
- OHMI, H., 1956. CONTRIBUTIONS TO THE KNOWLEDGE OF GRACILARIACEAE FROM JAPAN: . On a new species of the genus *gracilaria*, with some considerations on its ecology. 6, 271–279.
- Oiry, S., 2024. Shiny app for validation dataset building.
- Oiry, S., Barillé, L., 2021. Using sentinel-2 satellite imagery to develop microphytobenthos-based water quality indices in estuaries. Ecological Indicators 121, 107184.
- Oiry, S., Davies, B.F.R., Sousa, A.I., Rosa, P., Zoffoli, M.L., Brunier, G., Gernez, P., Barillé, L., 2024. Discriminating seagrasses from green macroalgae in european intertidal areas using high-resolution multispectral drone imagery. Remote Sensing 16. <https://doi.org/10.3390/rs16234383>
- Oksanen, J., Simpson, G.L., Blanchet, F.G., Kindt, R., Legendre, P., Minchin, P.R., O'Hara, R.B., Solymos, P., Stevens, M.H.H., Szoecs, E., Wagner, H., Barbour, M., Bedward, M., Bolker, B., Borcard, D., Carvalho, G., Chirico, M., De Caceres, M., Durand, S., Evangelista, H.B.A., FitzJohn, R., Friendly, M., Furneaux, B., Hannigan, G., Hill, M.O., Lahti, L., McGlinn, D., Ouellette, M.-H., Ribeiro Cunha, E., Smith, T., Stier, A., Ter Braak, C.J.F., Weedon, J., 2024. Vegan: Community ecology package.
- Oliver, E.C.J., Burrows, M.T., Donat, M.G., others, 2019. Projected marine heatwaves in the 21st century and the potential for ecological impact. Frontiers in Marine Science 6, 734. <https://doi.org/10.3389/fmars.2019.00734>
- Olmedo-Masat, O.M., Raffo, M.P., Rodríguez-Pérez, D., Arijón, M., Sánchez-Carnero, N., 2020. How far can we classify macroalgae remotely? An example using a new spectral library of species from the south west atlantic (argentine patagonia). Remote Sensing 12, 3870.
- Ortega, T., Ponce, R., Forja, J., Gómez-Parra, A., 2005. Fluxes of dissolved inorganic carbon in three estuarine systems of the cantabrian sea (north of spain). Journal of Marine Systems 53, 125–142.
- Orth, R.J., Carruthers, T.J., Dennison, W.C., Duarte, C.M., Fourqurean, J.W., Heck, K.L., Hughes, A.R., Kendrick, G.A., Kenworthy, W.J., Olyarnik, S., others, 2006. A global crisis for seagrass ecosystems. Bioscience 56, 987–996.
- Otrachshenko, V., Bosello, F., 2017. Fishing for answers? Impacts of marine ecosystem quality on coastal tourism demand. Tourism Economics 23, 963–980.
- Pansch, C., Scotti, M., Barboza, F.R., others, 2018. Heat waves and their significance for a temperate benthic community: A near-natural experimental approach. Global Change Biology 24, 4357–4367. <https://doi.org/10.1111/gcb.14282>
- Papathanasopoulou, E., Simis, S., Alikas, K., Ansper, A., Anttila, J., Barillé, A., Barillé, L., Brando, V., Bresciani, M., Bučas, M., others, 2019. Satellite-assisted

- monitoring of water quality to support the implementation of the water framework directive. EOMORES white paper.
- Papathanasopoulou, Eleni, Simis, S.G.H., Alikas, K., Ansper, A., Anttila, S., Jenni, A., Barillé, A.-L., Barillé, L., Brando, V., Bresciani, M., Bučas, M., Gernez, P., Giardino, C., Harin, N., Hommersom, A., Kangro, K., Kauppila, P., Koponen, S., Laanen, M., Neil, C., Papadakis, D., Peters, S., Poikane, S., Kathrin Poser, K., Pires, M.D., Riddick, C., Spyarakos, E., Tyler, A., Vaičiūtė, D., Warren, M., Zoffoli, M.L., 2019. Satellite-assisted monitoring of water quality to support the implementation of the Water Framework Directive. EOMORES white paper 28. <https://doi.org/10.5281/zenodo.3463051>
- Papenfuss, G.F., 1967. Notes on algal nomenclature - v. Various chlorophyceae and rhodophyceae. *Phykos* 5, 95–105.
- Parliament, E., Council, E., 2008. Directive 2008/56/ce du parlement européen et du conseil du 17 juin 2008 établissant un cadre d'action communautaire dans le domaine de la politique pour le milieu marin (directive-cadre «stratégie pour le milieu marin»)[en ligne]. Journal Officiel de l'Union EuropéenneRécupéré de: <http://eur-lex.europa.eu/legal-content/FR/TXT/PDF>.
- Parliament, E., Council, E., 2001. Directive 2000/60/CE du parlement européen et du conseil du 23 octobre 2000 établissant un cadre pour une politique communautaire dans le domaine de l'eau. Journal officiel, n L 327, 0001–0073.
- Passeri, D.L., Hagen, S.C., Medeiros, S.C., Bilskie, M.V., Alizad, K., Wang, D., 2015. The dynamic effects of sea level rise on low-gradient coastal landscapes: A review. *Earth's Future* 3, 159–181.
- Peidro-Devesa, M.J., Martínez-Movilla, A., Rodríguez-Somoza, J.L., Sánchez, J.M., Román, M., 2024. Quantifying intertidal macroalgae stocks in the NW iberian peninsula using unmanned aerial vehicle (UAV) multispectral imagery. *Regional Studies in Marine Science* 103621.
- Peñuelas, J., Munné-Bosch, S., Llusià, J., Filella, I., 2004. Leaf reflectance and photo-and antioxidant protection in field-grown summer-stressed *phillyrea angustifolia*. Optical signals of oxidative stress? *New Phytologist* 162, 115–124.
- Pereira, H.M., Ferrier, S., Walters, M., Geller, G.N., Jongman, R.H., Scholes, R.J., Bruford, M.W., Brummitt, N., Butchart, S.H., Cardoso, A., others, 2013. Essential biodiversity variables. *Science* 339, 277–278.
- Perera-Valderrama, S., Cerdeira-Estrada, S., Martell-Dubois, R., Rosique-de la Cruz, L., Caballero-Aragón, H., Valdez-Chavarin, J., López-Perea, J., Ressl, R., 2020. A new long-term marine biodiversity monitoring program for the knowledge and management in marine protected areas of the mexican caribbean. *Sustainability* 12, 7814.
- Perkins, S.E., Alexander, L.V., 2013. On the measurement of heat waves. *Journal of climate* 26, 4500–4517.
- Phinn, S.R., Kovacs, E.M., Roelfsema, C.M., Canto, R.F., Collier, C.J., McKenzie, L., 2018. Assessing the potential for satellite image monitoring of seagrass thermal dynamics: For inter-and shallow sub-tidal seagrasses in the inshore great barrier reef world heritage area, australia. *International Journal of Digital Earth* 11, 803–824.
- Piaser, E., Berton, A., Bolpagni, R., Caccia, M., Castellani, M.B., Coppi, A., Dalla Vecchia, A., Gallivanone, F., Sona, G., Villa, P., 2023. Impact of radiometric variability on ultra-high resolution hyperspectral imagery over aquatic vegetation: Preliminary results. *IEEE Journal of Selected Topics in Applied Earth Observations and Remote Sensing*.

- Pitts, W., 1943. The linear theory of neuron networks: The dynamic problem. *The bulletin of mathematical biophysics* 5, 23–31.
- QGIS Development Team, 2024. QGIS geographic information system. QGIS Association.
- R Core Team, 2023. R: A language and environment for statistical computing. R Foundation for Statistical Computing, Vienna, Austria.
- Ralph, P., Polk, S., Moore, K., Orth, R., Smith Jr, W., 2002. Operation of the xanthophyll cycle in the seagrass *zostera marina* in response to variable irradiance. *Journal of Experimental Marine Biology and Ecology* 271, 189–207.
- Ramesh, C., Mohanraju, R., 2020. Seagrass ecosystems of andaman and nicobar islands: Status and future perspective. *Environmental & Earth Sciences Research Journal* 7.
- Ramus, A.P., Silliman, B.R., Thomsen, M.S., Long, Z.T., 2017. An invasive foundation species enhances multifunctionality in a coastal ecosystem. *Proceedings of the national academy of sciences* 114, 8580–8585.
- Ranjan, D., Verma, P., Kshatri, A.S., Patel, A., Gupta, V., Chaudhary, V., Yadav, B., 2023. Destructive fishing practices and their impacts on fisheries. *Latest trends in Fisheries and Aquatic Animal Health* 3.
- Rasheed, M.A., Unsworth, R.K., 2011. Long-term climate-associated dynamics of a tropical seagrass meadow: Implications for the future. *Marine Ecology Progress Series* 422, 93–103.
- Ratnarajah, L., Abu-Alhaija, R., Atkinson, A., Batten, S., Bax, N.J., Bernard, K.S., Canonico, G., Cornils, A., Everett, J.D., Grigoratou, M., others, 2023. Monitoring and modelling marine zooplankton in a changing climate. *Nature Communications* 14, 564.
- Reddin, C.J., Decottignies, P., Bacouillard, L., Barillé, L., Dubois, S.F., Echappé, C., Gernez, P., Jesus, B., Méléder, V., Näscher, P.S., others, 2022. Extensive spatial impacts of oyster reefs on an intertidal mudflat community via predator facilitation. *Communications biology* 5, 1–11.
- Reeves, R.R., Ewins, P.J., Agbayani, S., Heide-Jørgensen, M.P., Kovacs, K.M., Lydersen, C., Suydam, R., Elliott, W., Polet, G., Dijk, Y. van, others, 2014. Distribution of endemic cetaceans in relation to hydrocarbon development and commercial shipping in a warming arctic. *Marine Policy* 44, 375–389.
- Reimann, L., Vafeidis, A.T., Honsel, L.E., 2023. Population development as a driver of coastal risk: Current trends and future pathways. *Cambridge Prisms: Coastal Futures* 1, e14.
- Repolho, T., Duarte, B., Dionísio, G., Paula, J.R., Lopes, A.R., Rosa, I.C., Grilo, T.F., Caçador, I., Calado, R., Rosa, R., 2017. Seagrass ecophysiological performance under ocean warming and acidification. *Scientific Reports* 7, 41443.
- Reusch, T.B., Ehlers, A., Häggerli, A., Worm, B., 2005. Ecosystem recovery after climatic extremes enhanced by genotypic diversity. *Proceedings of the National Academy of Sciences* 102, 2826–2831. <https://doi.org/10.1073/pnas.0500008102>
- Reuters, 2024. Aquafarming becomes main global source of fish, UN food agency says [WWW Document]. URL <https://www.reuters.com/business/environment/aquafarming-becomes-main-global-source-fish-un-food-agency-says-2024-06-07/>
- Roca, M., Dunbar, M.B., Román, A., Caballero, I., Zoffoli, M.L., Gernez, P., Navarro, G., 2022. Monitoring the marine invasive alien species *rugulopteryx okamurae* using unmanned aerial vehicles and satellites. *Frontiers in Marine Science* 9, 1004012.
- Rodrigues-Filho, J.L., Macêdo, R.L., Sarmento, H., Pimenta, V.R., Alonso, C.,

- Teixeira, C.R., Pagliosa, P.R., Netto, S.A., Santos, N.C., Daura-Jorge, F.G., others, 2023. From ecological functions to ecosystem services: Linking coastal lagoons biodiversity with human well-being. *Hydrobiologia* 850, 2611–2653.
- Román, A., Oiry, S., Davies, B.F., Rosa, P., Gernez, P., Tovar-Sánchez, A., Navarro, G., Méléder, V., Barillé, L., 2024. Mapping intertidal microphytobenthic biomass with very high-resolution remote sensing imagery in an estuarine system. *Science of The Total Environment* 177025.
- Román, A., Prasyad, H., Oiry, S., Davies, B.F., Brunier, G., Barillé, L., 2023. Mapping intertidal oyster farms using unmanned aerial vehicles (UAV) high-resolution multispectral data. *Estuarine, Coastal and Shelf Science* 291, 108432.
- Román, A., Tovar-Sánchez, A., Olivé, I., Navarro, G., 2021. Using a UAV-mounted multispectral camera for the monitoring of marine macrophytes. *Frontiers in Marine Science* 8, 722698.
- Romero, M., Andrés, A., Alonso, R., Viguri, J., Rincón, J.M., 2008. Sintering behaviour of ceramic bodies from contaminated marine sediments. *Ceramics International* 34, 1917–1924.
- Rossiter, T., Furey, T., McCarthy, T., Stengel, D.B., 2020. UAV-mounted hyperspectral mapping of intertidal macroalgae. *Estuarine, Coastal and Shelf Science* 242, 106789.
- Rouse, J.W., Haas, R.H., Schell, J.A., Deering, D.W., others, 1974. Monitoring vegetation systems in the great plains with ERTS. *NASA Spec. Publ* 351, 309.
- Rueness, J., 2005. Life history and molecular sequences of *gracilaria vermiculophylla* (gracilariales, rhodophyta), a new introduction to european waters. *Phycologia* 44, 120–128.
- Russo, E., Domeisen, D.I.V., 2023. Increasing intensity of extreme heatwaves: The crucial role of metrics. *Geophysical Research Letters* 50, e2023GL103540. <https://doi.org/10.1029/2023GL103540>
- Saderne, V., Geraldi, N.R., Macreadie, P.I., Maher, D.T., Middelburg, J.J., Serrano, O., Almahasheer, H., Arias-Ortiz, A., Cusack, M., Eyre, B.D., others, 2019. Role of carbonate burial in blue carbon budgets. *Nature communications* 10, 1106.
- Sage, R.F., 2020. Global change biology: A primer. *Global Change Biology* 26, 3–30.
- Samper-Villarreal, J., Bolaños, R.C., Heidemeyer, M., Vargas, M.M., Vargas, R.M., 2020. Characterization of seagrasses at two new locations in the eastern tropical pacific (el jobo and matapalito, costa rica). *Aquatic botany* 165, 103237.
- Sanabria-Fernández, J.A., Génin, A., Dakos, V., 2024. Unveiling functional linkages between habitats and organisms: Macroalgal habitats as influential factors of fish functional traits. *Marine Environmental Research* 194, 106305.
- Santos, R.O., Varona, G., Avila, C.L., Lirman, D., Collado-Vides, L., 2020. Implications of macroalgae blooms to the spatial structure of seagrass seascapes: The case of the *anadyomene* spp.(chlorophyta) bloom in biscayne bay, florida. *Marine pollution bulletin* 150, 110742.
- Sarker, I.H., 2021. Machine learning: Algorithms, real-world applications and research directions. *SN computer science* 2, 160.
- Savelli, R., Dupuy, C., Barillé, L., Lerouxel, A., Guizien, K., Philippe, A., Bocher, P., Polseñaere, P., Le Fouest, V., 2018. On biotic and abiotic drivers of the microphytobenthos seasonal cycle in a temperate intertidal mudflat: A modelling study. *Biogeosciences* 15, 7243–7271.
- Savitzky, A., Golay, M.J., 1964. Smoothing and differentiation of data by simplified least squares procedures. *Analytical chemistry* 36, 1627–1639.

- Sawall, Y., Ito, M., Pansch, C., 2021. Chronically elevated sea surface temperatures revealed high susceptibility of the eelgrass *Zostera marina* to winter and spring warming. *Limnology and Oceanography* 66, 4112–4124.
- Schibalski, A., Kleyer, M., Maier, M., Schröder, B., 2022. Spatiotemporally explicit prediction of future ecosystem service provisioning in response to climate change, sea level rise, and adaptation strategies. *Ecosystem Services* 54, 101414.
<https://doi.org/https://doi.org/10.1016/j.ecoser.2022.101414>
- Schiel, D.R., Gerrity, S., Orchard, S., Alestra, T., Dunmore, R.A., Falconer, T., Thomsen, M.S., Tait, L.W., 2021. Cataclysmic Disturbances to an Intertidal Ecosystem: Loss of Ecological Infrastructure Slows Recovery of Biogenic Habitats and Diversity. *Frontiers in Ecology and Evolution* 9.
<https://doi.org/10.3389/fevo.2021.767548>
- Schlegel, R.W., Smit, A.J., 2018. heatwaveR: A central algorithm for the detection of heatwaves and cold-spells. *Journal of Open Source Software* 3, 821.
<https://doi.org/10.21105/joss.00821>
- Schmidt, K., Skidmore, A., 2003. Spectral discrimination of vegetation types in a coastal wetland. *Remote sensing of Environment* 85, 92–108.
- Schneider, C.A., Rasband, W.S., Eliceiri, K.W., 2012. NIH image to ImageJ: 25 years of image analysis. *Nature methods* 9, 671–675.
- Schreyers, L., Emmerik, T. van, Biermann, L., Le Lay, Y.-F., 2021. Spotting green tides over brittany from space: Three decades of monitoring with landsat imagery. *Remote Sensing* 13, 1408.
- Scott, A.L., York, P.H., Duncan, C., Macreadie, P.I., Connolly, R.M., Ellis, M.T., Jarvis, J.C., Jinks, K.I., Marsh, H., Rasheed, M.A., 2018. The role of herbivory in structuring tropical seagrass ecosystem service delivery. *Frontiers in Plant Science* 9, 127.
- Sedano, F., Pavón-Paneque, A., Navarro-Barranco, C., Guerra-García, J.M., Digenis, M., Sempere-Valverde, J., Espinosa, F., 2021. Coastal armouring affects intertidal biodiversity across the Alboran Sea (Western Mediterranean Sea). *Marine Environmental Research* 171.
<https://doi.org/10.1016/j.marenvres.2021.105475>
- Sfriso, A., Wolf, M.A., Maistro, S., Sciuto, K., Moro, I., 2012. Spreading and autoecology of the invasive species *Gracilaria vermiculophylla* (Gracilariales, Rhodophyta) in the lagoons of the north-western Adriatic sea (Mediterranean sea, Italy). *Estuarine, Coastal and Shelf Science* 114, 192–198.
- Sheehan, E., Holmes, L., Davies, B., Cartwright, A., Rees, A., Attrill, M., 2021. Rewilding of protected areas enhances resilience of marine ecosystems to extreme climatic events. *Frontiers in Marine Science* 8.
- SHOM, n.d. Service hydrographique et océanographique de la marine ; bathymétrie Litto3D® Bretagne 2018-2021.
- SHOM, 2024. Service hydrographique et océanographique de la marine (SHOM).
- SHOM, 2022. Service hydrographique et océanographique de la marine ; références altimétriques maritimes: Ports de France métropolitaine et d'outre-mer, cotes du zéro hydrographique et niveaux caractéristiques de la marée. Shom, Brest, France.
- Simberloff, D., 2021. Maintenance management and eradication of established aquatic invaders. *Hydrobiologia* 848, 2399–2420.
- Simic Milas, A., Cracknell, A.P., Warner, T.A., 2018. Drones—the third generation source of remote sensing data. *International Journal of Remote Sensing*.
- Simolo, C., Corti, S., 2022. Quantifying the role of variability in future intensification of heat extremes. *Nature Communications* 13.

- <https://doi.org/10.1038/s41467-022-35571-0>
- Skendzic, S., 2023. Drought stress in winter wheat-physiological responses and detection using remote and proximal sensing techniques, in: Smart Life Sciences and Technology for Sustainable Development. pp. 39–39.
- Skidmore, A.K., Pettorelli, N., Coops, N.C., Geller, G.N., Hansen, M., Lucas, R., Mücher, C.A., O'Connor, B., Paganini, M., Pereira, H.M., others, 2015. Environmental science: Agree on biodiversity metrics to track from space. *Nature* 523, 403–405.
- Slaton, M.R., Raymond Hunt Jr., E., Smith, W.K., 2001. Estimating near-infrared leaf reflectance from leaf structural characteristics. *American Journal of Botany* 88, 278–284. [https://doi.org/https://doi.org/10.2307/2657019](https://doi.org/10.2307/2657019)
- Smale, D.A., Wernberg, T., Oliver, E.C.J., others, 2019. Marine heatwaves threaten global biodiversity and the provision of ecosystem services. *Nature Climate Change* 9, 306–312. <https://doi.org/10.1038/s41558-019-0412-1>
- Soissons, L.M., Haanstra, E.P., Van Katwijk, M.M., Asmus, R., Auby, I., Barillé, L., Brun, F.G., Cardoso, P.G., Desroy, N., Fournier, J., others, 2018. Latitudinal patterns in european seagrass carbon reserves: Influence of seasonal fluctuations versus short-term stress and disturbance events. *Frontiers in Plant Science* 9, 88.
- Sotka, E.E., Baumgardner, A.W., Bippus, P.M., Destombe, C., Duermit, E.A., Endo, H., Flanagan, B.A., Kamiya, M., Lees, L.E., Murren, C.J., others, 2018. Combining niche shift and population genetic analyses predicts rapid phenotypic evolution during invasion. *Evolutionary Applications* 11, 781–793.
- Sousa, A.I., Santos, D.B., Silva, E.F. da, Sousa, L.P., Cleary, D.F., Soares, A.M., Lillebø, A.I., 2017. ‘Blue carbon’and nutrient stocks of salt marshes at a temperate coastal lagoon (ria de aveiro, portugal). *Scientific reports* 7, 41225.
- Sousa, A.I., Silva, J.F. da, Azevedo, A., Lillebø, A.I., 2019. Blue carbon stock in zostera noltei meadows at ria de aveiro coastal lagoon (portugal) over a decade. *Scientific reports* 9, 14387.
- Speth, S., Goncalves, A., Rigault, B., Suzuki, S., Bouazizi, M., Matsuo, Y., Prendinger, H., 2022. Deep learning with RGB and thermal images onboard a drone for monitoring operations. *Journal of Field Robotics* 39, 840–868.
- Stan Development Team, C., others, 2020. RStan: The r interface to stan. R package version 2.21. 2.
- Steinmetz, F., Deschamps, P.-Y., Ramon, D., 2011. Atmospheric correction in presence of sun glint: Application to MERIS. *Optics express* 19, 9783–9800.
- Stévant, P., Schmedes, P.S., Le Gall, L., Wegeberg, S., Dumay, J., Rebours, C., 2023. Concise review of the red macroalga dulse, palmaria palmata (l.) weber & mohr. *Journal of Applied Phycology* 35, 523–550.
- Stillman, J.H., 2019. Heat waves, the new normal: Summertime temperature extremes will impact animals, ecosystems, and human communities. *Physiology* 34, 86–100. <https://doi.org/10.1152/physiol.00040.2018>
- Strydom, S., Murray, K., Wilson, S., Huntley, B., Rule, M., Heithaus, M., Bessey, C., Kendrick, G.A., Burkholder, D., Fraser, M.W., others, 2020. Too hot to handle: Unprecedented seagrass death driven by marine heatwave in a world heritage area. *Global change biology* 26, 3525–3538.
- Sun, Y., Yao, L., Liu, J., Tong, Y., Xia, J., Zhao, X., Zhao, S., Fu, M., Zhuang, M., He, P., others, 2022. Prevention strategies for green tides at source in the southern yellow sea. *Marine Pollution Bulletin* 178, 113646.
- Suomalainen, J., Oliveira, R.A., Hakala, T., Koivumäki, N., Markelin, L., Näsi, R., Honkavaara, E., 2021. Direct reflectance transformation methodology for drone-based hyperspectral imaging. *Remote Sensing of Environment* 266,

- 112691.
- Surget, G., 2017. Processus adaptatifs des végétaux marins face au changement climatique à différentes échelles de temps et d'espace: Dynamique de populations, métabolomique, écophysiologie et potentiels de valorisation (PhD thesis). Université de Bretagne occidentale-Brest.
- Sutton, M.A., Van Grinsven, H., Billen, G., Bleeker, A., Bouwman, A., Oenema, O., 2011. European nitrogen assessment-summary for policy makers, in: The European Nitrogen Assessment. Sources, Effects and Policy Perspectives. pp. xxiv–xxxiv.
- Sweet, D.D., Tirado, S.B., Springer, N.M., Hirsch, C.N., Hirsch, C.D., 2022. Opportunities and challenges in phenotyping row crops using drone-based RGB imaging. *The Plant Phenome Journal* 5, e20044.
- Tallam, K., Nguyen, N., Ventura, J., Fricker, A., Calhoun, S., O'Leary, J., Fitzgibbons, M., Robbins, I., Walter, R.K., 2023. Application of deep learning for classification of intertidal eelgrass from drone-acquired imagery. *Remote Sensing* 15, 2321.
- Tankoua, O.F., Buffet, P.-E., Amiard, J.-C., Amiard-Triquet, C., Mouneyrac, C., Berthet, B., 2011. Potential influence of confounding factors (size, salinity) on biomarkers in the sentinel species *scrobicularia plana* used in programmes monitoring estuarine quality. *Environmental Science and Pollution Research* 18, 1253–1263. <https://doi.org/10.1007/s11356-011-0479-3>
- Terada, R., Yamamoto, H., 2002. Review of *gracilaria vermiculophylla* (ohmi) papenfuss and other species in japan and asia. *Taxonomy of economic seaweeds, with special reference to Pacific species* 8, 225–230.
- Thomsen, E., Herbeck, L.S., Viana, I.G., Jennerjahn, T.C., 2023. Meadow trophic status regulates the nitrogen filter function of tropical seagrasses in seasonally eutrophic coastal waters. *Limnology and Oceanography* 68, 1906–1919.
- Thomsen, M.S., McGlathery, K., Schwarzschild, A., Silliman, B., 2009. Distribution and ecological role of the non-native macroalga *gracilaria vermiculophylla* in virginia salt marshes. *Biological Invasions* 11, 2303–2316.
- Thomsen, M.S., Staehr, P.A., Nyberg, C.D., Schwærter, S., Krause-Jensen, D., Silliman, B.R., 2007. *Gracilaria vermiculophylla* (ohmi) papenfuss, 1967 (rhodophyta, graciliaceae) in northern europe, with emphasis on danish conditions, and what to expect in the future. *Aquatic invasions* 2, 83–94.
- Thomsen, M.S., Staehr, P.A., Nejrup, L., Schiel, D.R., 2013. Effects of the invasive macroalgae *gracilaria vermiculophylla* on two co-occurring foundation species and associated invertebrates. *Aquatic Invasions* 8, 133–145.
- Thomson, J.A., Burkholder, D.A., Heithaus, M.R., Fourqurean, J.W., Fraser, M.W., Statton, J., Kendrick, G.A., 2015. Extreme temperatures, foundation species, and abrupt ecosystem change: An example from an iconic seagrass ecosystem. *Global change biology* 21, 1463–1474.
- Thorhaug, A., Richardson, A., Berlyn, G., 2007. Spectral reflectance of the seagrasses: *Thalassia testudinum*, *halodule wrightii*, *syringodium filiforme* and five marine algae. *International Journal of Remote Sensing* 28, 1487–1501.
- Tragano, D., Reinartz, P., 2018. Mapping mediterranean seagrasses with sentinel-2 imagery. *Marine Pollution Bulletin* 134, 197–209. <https://doi.org/10.1016/j.marpolbul.2017.06.075>
- Tuya, F., Hernandez-Zerpa, H., Espino, F., Haroun, R., 2013. Drastic decadal decline of the seagrass *cymodocea nodosa* at gran canaria (eastern atlantic): Interactions with the green algae *caulerpa prolifera*. *Aquatic Botany* 105, 1–6.
- Underwood, A., 1992. Beyond BACI: The detection of environmental impacts on

- populations in the real, but variable, world. *Journal of experimental marine biology and ecology* 161, 145–178.
- Union, M., 2025. How much trade is maritime? [WWW Document]. URL <https://maritime-union.org/how-much-trade-is-maritime>
- Unsworth, R., Cullen-Unsworth, L.C., 2014. Biodiversity, ecosystem services, and the conservation of seagrass meadows. *Coast. Conserv* 19, 95.
- Unsworth, R.K., Butterworth, E.G., 2021. Seagrass meadows provide a significant resource in support of avifauna. *Diversity* 13, 363.
- Unsworth, R.K., Cullen-Unsworth, L.C., Jones, B.L., Lilley, R.J., 2022. The planetary role of seagrass conservation. *Science* 377, 609–613.
- Unsworth, R.K., McKenzie, L.J., Collier, C.J., Cullen-Unsworth, L.C., Duarte, C.M., Eklöf, J.S., Jarvis, J.C., Jones, B.L., Nordlund, L.M., 2019a. Global challenges for seagrass conservation. *Ambio* 48, 801–815.
- Unsworth, R.K., Nordlund, L.M., Cullen-Unsworth, L.C., 2019b. Seagrass meadows support global fisheries production. *Conservation Letters* 12, e12566.
- Ustin, S.L., Jacquemoud, S., 2020. How the optical properties of leaves modify the absorption and scattering of energy and enhance leaf functionality. *Remote sensing of plant biodiversity* 349–384.
- Ustin, S.L., Roberts, D.A., Gamon, J.A., Asner, G.P., Green, R.O., 2004. Using imaging spectroscopy to study ecosystem processes and properties. *BioScience* 54, 523–534.
[https://doi.org/10.1641/0006-3568\(2004\)054%5B0523:UITSTSE%5D2.0.CO;2](https://doi.org/10.1641/0006-3568(2004)054%5B0523:UITSTSE%5D2.0.CO;2)
- Valderrama, D., Cai, J., Hishamunda, N., Ridler, N., 2013. Social and economic dimensions of carrageenan seaweed farming.
- Valle, M., Katwijk, M.M. van, Jong, D.J. de, Bouma, T.J., Schipper, A.M., Chust, G., Benito, B.M., Garmendia, J.M., Borja, Á., 2013. Comparing the performance of species distribution models of *zostera marina*: Implications for conservation. *Journal of Sea Research* 83, 56–64.
- Valle, M., Pala, V., Lafon, V., Dehouck, A., Garmendia, J.M., Borja, A., Chust, G., 2015. Mapping estuarine habitats using airborne hyperspectral imagery, with special focus on seagrass meadows. *Estuarine, Coastal and Shelf Science* 164, 433–442.
- Van Der Maarel, E., 2003. Some remarks on the functions of European coastal ecosystems. *Phytocoenologia* 33, 187–202.
<https://doi.org/10.1127/0340-269X/2003/0033-0187>
- Van Katwijk, M., 2003. Reintroduction of eelgrass (*zostera marina* l.) in the dutch wadden sea: A research overview and management vision, in: Challenges to the Wadden Sea Area. In: Proceedings of the 10th International Scientific Wadden Sea Symposium, Groningen, the Netherlands. pp. 173–195.
- Vanhellemont, Q., Ruddick, K., 2018. Atmospheric correction of metre-scale optical satellite data for inland and coastal water applications. *Remote sensing of environment* 216, 586–597.
- Veettil, B.K., Ward, R.D., Lima, M.D.A.C., Stankovic, M., Hoai, P.N., Quang, N.X., 2020. Opportunities for seagrass research derived from remote sensing: A review of current methods. *Ecological Indicators* 117, 106560.
- Villalobos Perna, P., Di Febbraro, M., Carranza, M.L., Marzialetti, F., Innangi, M., 2023. Remote sensing and invasive plants in coastal ecosystems: What we know so far and future prospects. *Land* 12, 341.
- Villares, R., Puente, X., Carballeira, A., 1999. Nitrogen and phosphorus in *ulva* sp. In the galician rias bajas (northwest spain): Seasonal fluctuations and influence on growth. *Boletin-Instituto Español de Oceanografia* 15, 337–342.

- Walker, D.I., McComb, A.J., 1992. Seagrass degradation in australian coastal waters. *Marine Pollution Bulletin* 25, 191–195.
- Wang, Y., Fang, H., 2020. Estimation of LAI with the LiDAR technology: A review. *Remote Sensing* 12, 3457.
- Wang, Z., Fang, Z., Liang, J., Song, X., 2022. Assessment of global habitat suitability and risk of ocean green tides. *Harmful Algae* 119, 102324.
- Waycott, M., Duarte, C.M., Carruthers, T.J., Orth, R.J., Dennison, W.C., Olyarnik, S., Calladine, A., Fourqurean, J.W., Heck Jr, K.L., Hughes, A.R., others, 2009. Accelerating loss of seagrasses across the globe threatens coastal ecosystems. *Proceedings of the national academy of sciences* 106, 12377–12381.
- Wei, P., Lu, Z., Song, J., 2015. Variable importance analysis: A comprehensive review. *Reliability Engineering and System Safety* 142, 399–432.
<https://doi.org/https://doi.org/10.1016/j.ress.2015.05.018>
- Wei, Y.-J., Fang, R.-E., Liu, J.-S., Chen, Y.-C., Lin, H.-T.V., Pan, C.-L., Huang, C.-H., 2023. Influence of porphyra-derived polysaccharides and oligosaccharides on attenuating food allergy and modulating enteric microflora in mice. *Food and Agricultural Immunology* 34, 2248419.
- Weinberger, F., Buchholz, B., Karez, R., Wahl, M., 2008. The invasive red alga *gracilaria vermiculophylla* in the baltic sea: Adaptation to brackish water may compensate for light limitation. *Aquatic Biology* 3, 251–264.
- Werbos, P., 1974. Beyond regression: New tools for prediction and analysis in the behavioral sciences. PhD thesis, Committee on Applied Mathematics, Harvard University, Cambridge, MA.
- Williams, S.L., Smith, J.E., 2007. A global review of the distribution, taxonomy, and impacts of introduced seaweeds. *Annu. Rev. Ecol. Evol. Syst.* 38, 327–359.
- Winters, G., Nelle, P., Fricke, B., Rauch, G., Reusch, T.B., 2011. Effects of a simulated heat wave on photophysiology and gene expression of high-and low-latitude populations of *zostera marina*. *Marine Ecology Progress Series* 435, 83–95.
- Wolff, W.J., Reise, K., 2002. Oyster imports as a vector for the introduction of alien species into northern and western european coastal waters, in: *Invasive Aquatic Species of Europe. Distribution, Impacts and Management*. Springer, pp. 193–205.
- Wright, M.N., Ziegler, A., 2017. ranger: A fast implementation of random forests for high dimensional data in C++ and R. *Journal of Statistical Software* 77, 1–17. <https://doi.org/10.18637/jss.v077.i01>
- Xu, S., Xu, S., Zhou, Y., Yue, S., Zhang, X., Gu, R., Zhang, Y., Qiao, Y., Liu, M., 2021. Long-term changes in the unique and largest seagrass meadows in the bohai sea (china) using satellite (1974–2019) and sonar data: Implication for conservation and restoration. *Remote Sensing* 13, 856.
- Xue, J., Su, B., 2017. Significant remote sensing vegetation indices: A review of developments and applications. *Journal of Sensors* 2017.
<https://doi.org/10.1155/2017/1353691>
- Ye, N., Zhang, X., Mao, Y., Liang, C., Xu, D., Zou, J., Zhuang, Z., Wang, Q., 2011. “Green tides” are overwhelming the coastline of our blue planet: Taking the world’s largest example. *Ecological Research* 26, 477–485.
- Yuan, X., Shi, J., Gu, L., 2021. A review of deep learning methods for semantic segmentation of remote sensing imagery. *Expert Systems with Applications* 169, 114417.
- Zahoor, I., Mushtaq, A., 2023. Water pollution from agricultural activities: A critical global review. *Int. J. Chem. Biochem. Sci* 23, 164–176.

- Zenetos, A., Tsiamis, K., Galanidi, M., Carvalho, N., Bartolotti, C., Canning-Clode, J., Castriota, L., Chainho, P., Comas-González, R., Costa, A.C., Dragičević, B., Dulčić, J., Faasse, M., Florin, A.-B., Gittenberger, A., Jakobsen, H., Jelmert, A., Kerckhof, F., Lehtiniemi, M., Livi, S., Lundgreen, K., Macic, V., Massé, C., Mavrič, B., Naddafi, R., Orlando-Bonaca, M., Petovic, S., Png-Gonzalez, L., Carbonell Quetglas, A., Ribeiro, R.S., Cidade, T., Smolders, S., Stæhr, P.A.U., Viard, F., Outinen, O., 2022. Status and trends in the rate of introduction of marine non-indigenous species in european seas. *Diversity* 14, <https://doi.org/10.3390/d14121077>
- Zhu, T., 2020. Analysis on the applicability of the random forest, in: *Journal of Physics: Conference Series*. IOP Publishing, p. 012123.
- Zoffoli, M.L., Gernez, P., Godet, L., Peters, S., Oiry, S., Barillé, L., 2021. Decadal increase in the ecological status of a north-atlantic intertidal seagrass meadow observed with multi-mission satellite time-series. *Ecological Indicators* 130, 108033.
- Zoffoli, M.L., Gernez, P., Oiry, S., Godet, L., Dalloyau, S., Davies, B.F.R., Barillé, L., 2023. Remote sensing in seagrass ecology: Coupled dynamics between migratory herbivorous birds and intertidal meadows observed by satellite during four decades. *Remote Sensing in Ecology and Conservation* 9, 420–433.
- Zoffoli, M.L., Gernez, P., Rosa, P., Le Bris, A., Brando, V.E., Barillé, A.-L., Harin, N., Peters, S., Poser, K., Spaias, L., others, 2020. Sentinel-2 remote sensing of *zostera noltei*-dominated intertidal seagrass meadows. *Remote Sensing of Environment* 251, 112020.